Estimation of inherent optical properties and phytoplankton community structure from hyperspectral in-water radiometry

Eric C. Rehm

A dissertation

submitted in partial fulfillment of the

requirements for the degree of

Doctor of Philosophy

University of Washington

2013

Reading Committee:

Eric A. D'Asaro, Chair

Norman J. McCormick

Curtis D. Mobley

Mary Jane Perry

Program Authorized to Offer Degree:

School of Oceanography

University of Washington

Abstract

Estimation of inherent optical properties and phytoplankton community structure from hyperspectral in-water radiometry

Eric C. Rehm

Chair of the Supervisory Committee:

Professor Eric A. D'Asaro

School of Oceanography

Inverse algorithms are developed to retrieve hyperspectral absorption and backscattering coefficients from measurements of hyperspectral upwelling radiance and downwelling irradiance in vertically homogeneous waters. The first inversion algorithm solves the radiative transfer equation using a simplified phase function to produce estimates of the ratio of the backscattering to absorption coefficients at depths where the light field is in the asymptotic regime. These estimates can be used as a starting point in the second implicit inversion algorithm, where the azimuthally-averaged radiative transfer equation is repeatedly evaluated using the Ecolight radiative transfer model, varying absorption and backscattering coefficients until modeled radiance and irradiance spectra match measurements within a specified criterion. Although this inversion problem is ambiguous for the retrieval of total scattering coefficients, unique and stable solutions can be found for absorption and backscattering coefficients when the inversion is constrained using the attenuation coefficient at one wavelength. A comprehensive error budget for absorption and backscattering estimates details the contributions from forward model parameter error, random and systematic radiometric error, and inversion noise. Both algorithms are tested using simulated light fields from a chlorophyll-based case I bio-optical model and

radiometric field data. The second algorithm is then applied to a 51 d record of hyperspectral radiometric measurements to measure the evolution of phytoplankton community structure during the North Atlantic spring bloom continuously over 51 days from a Lagrangian float. The retrieved absorption spectra are of sufficient accuracy, bandwidth, and resolution to estimate bio-optical signatures of phytoplankton community structure including overall biomass, the fraction of small phytoplankton, and the absorption due to colored detrital material. Size fraction estimates based on the effect of pigment packaging on the phytoplankton absorption spectrum are found to be ambiguous in the presence of vertical mixing, also a consideration for ocean satellite retrievals of this parameter. Derivative spectroscopy is employed to detect and estimate the relative contribution to absorption of individual phytoplankton pigments, specifically chlorophyll *a*, fucoxanthin and mycosporine-like amino acids. The time series of these two estimates of community composition show the growth of a diatom bloom which then rapidly disappears and is replaced by a community of smaller cells. This description is consistent with nearby ship-based measurements that rely on water samples and laboratory measurements. We conclude that observations of phytoplankton functional types are possible from low-power, autonomous platforms.

Acknowledgments

This work was funded by the National Science Foundation, NASA, the University of Washington, Theodore and Marie Sarchin Fellowship, Henry Bryant Bigelow Visiting Graduate Student Fellowship, and (twice) the National Defense Industries Association Fellowship.

I owe special thanks to Eric D'Asaro for agreeing to take me on as his graduate student, securing funds for the research I wanted to carry out and the equipment I needed to do so, for numerous enjoyable discussions, and always always urging me to go further with my ideas. Eric provided support when I was unsure of where to go, provided insight into ocean physics, bio-optics and statistics, and continually believed that I was capable of the work at hand. I have learned much from Eric that I will continue to discover for years to come. Eric was sure to provide me with the oceanographic field work opportunities that I sought from the day we met.

I would like to thank my PhD Advisory Committee, Eric D'Asaro, Mary Jane Perry, Curt Mobley, Norm McCormick, Ginger Armbrust, and Susan Hautala for their support, intellectual encouragement, patience, and perseverance as I have made this journey, introducing me to a world of new ideas in which I take much delight.

My field work during the 2008 North Atlantic Bloom Experiment (NAB08) would not have been possible without the help of Emily Kallin, who assisted with the collection of all of the NAB08 bio-optical profiles from the *R/V Knorr,* and Mary Jane Perry and Emmanuel Boss who loaned their bio-optical and radiometric profilers. Special thanks are due to the crews of the NAB08 research vessels, the *R/S Bjarni Sæmundsson* and the *R/V Knorr*. I owe a great debt to other NAB08 participants for the numerous discussions about the physics and biogeochemistry of the North Atlantic including the principal investigators (Eric D'Asaro, Mary Jane Perry, Craig

Lee, Katja Fennel), fellow scientists (Richard Lampitt, Katherine Richardson, Tatiana Rynearson), postdoctoral investigators (Matthew Alkire, Ivona Cetinić, Amala Mahadevan, Giorgio Dall'Olmo, Toby Westberry) and fellow graduate students (Nathan Briggs, Amanda Gray, Patrick Martin, Nicole Bale, Mike Sauer).

My turn to oceanography from software engineering was directly influenced by my desire to engage in field research. This was initially inspired by the passion and delight expressed by my daughter, Jora Fogg, in her ornithological field work as a student and seasonal field research assistant. Further, my interest in phytoplankton community composition was partly inspired by Jora's Master's thesis titled "Community Composition and Influence of Forest Structure on Birds in the Evergreen State Forest Reserve" (Rehm-Lorber, J., 2009).

Finally I would like to thank my wife Mary Geary, my daughter Jora Fogg and all of my friends for always being by my side, continually supporting me, cheering me on to the finish, and for frequently reminding me to remember the value of the journey as well as the destination.

Table of Contents

Chapter 1: Motivation and Summary of Results

Motivation

The formative idea of this thesis is that oceanic inherent optical properties and phytoplankton community composition can be retrieved from autonomous, in-water hyperspectral radiometric measures. This idea resulted from two events closely situated in time. First, in April 2004, I began work as a graduate student, advised by Dr. Eric D'Asaro at University of Washington's School of Oceanography. For the past 20 years, Dr. D'Asaro has focused on exploiting the unique capabilities of "Lagrangian Floats," a class of instruments that try to accurately follow the three dimensional motion of water parcels, particularly in regions of strong mixing [*D'Asaro*, 2003]. Langrangian floats have become a novel but effective way to measure turbulence in regions of strong mixing [*Harcourt and D'Asaro*, 2010]. They are also an ideal platform from which to study ocean biogeochemistry, in particular, phytoplankton. After all, the word plankton is derived from the Greek πλαγκτός (planktos), meaning "wandering, roaming," and by extension "drifter". By 2002, Dr. D'Asaro already had begun to experiment with bio-optical measurements in the Lagrangian reference frame in Puget Sound; these observations would later become the subject of my Master's work [*Rehm*, 2006a; b]. Dr. D'Asaro and I agreed that his float, a mechanical plankton if you will, would be a fruitful platform for autonomous bio-optical studies of phytoplankton dynamics.

The second formative event was my participation in the Summer 2004 Ocean Optics Class held at University of Maine's Darling Marine Center. The major theme of this cross-disciplinary, graduate-level course was the application of ocean optical methods to ocean biogeochemistry. The underlying rationale is that optical measurements serve as proxies for

important biogeochemical entities – including marine phytoplankton, dissolved organics, and suspended sediment particles. Topics covered included the principles of radiative transfer, the role of inherent optical properties (IOPs) in describing how light is absorbed or scattered independent of the ambient light field, and the particular role of photosynthetic and accessory phytoplankton pigments in contributing to the spectral quality of the underwater light field.

During the Ocean Optics Class, some of the instructors explored the topic of ocean color inversion, i.e., the estimation of IOPs from hyperspectral measurements of surface reflectance (e.g., *Roesler and Perry* [1995]). In one lecture, Dr. Collin Roesler demonstrated the sensitivity of hyperspectral ocean color observations in the Benguela Upwelling System to the variability in IOPs based on phytoplankton biomass, species composition and cell size [*Roesler et al.*, 2003]. In a subsequent laboratory exercise, Dr. Roesler provided a MATLAB-based non-linear inversion code that repeatedly solved an analytical forward reflectance model [*Gordon et al.*, 1988] to estimate spectral phytoplankton absorption modeled as a linear combination of phytoplankton absorption "basis functions" (assumed spectral shapes) for various phytoplankton taxonomical groups. From this exercise, a path can be found from ocean color to phytoplankton community composition. Recognizing that in-water spectral radiometric measurements might be possible from Dr. D'Asaro's Lagrangian platform, I discovered substantial literature on the topic of the estimation of IOPs from in-water radiometric measurements (for a review, see *Gordon* [2002]), but found that a) very little field verification of such approaches had been carried out (exceptions include *Stramska et al.* [2000], *Leathers et al.* [1999] and *Gordon et al.* [2009]) and b) there had been no autonomous observations of time-varying phytoplankton community structure using in situ radiometry.

Global Carbon Cycle

Anthropogenic carbon dioxide (CO_2) is released to the atmosphere by burning fossil fuels, land-use change such as deforestation, or cement production (Figure 1). Anthropogenic CO_2 has three possible fates: it may be absorbed by the terrestrial ecosystem, it may be absorbed by the ocean, or it may continue to reside in the atmosphere. According to *Le Quéré et al.* [2012], 26% is absorbed in the ocean and 28% on land on an annual basis. The ocean, therefore, plays a major role in the planetary carbon cycle. In the face of concern about the global warming induced by an increased radiative forcing by CO_2 emissions and ocean acidification resulting from increased CO_2 uptake by the oceans, oceanographers model the ocean carbon cycle in order to predict how it might be affected by climate change. Developers of these models are, therefore, required to consider the phytoplankton component(s) in terms of their roles in the cycling of CO_2 and other important biogeochemical parameters.

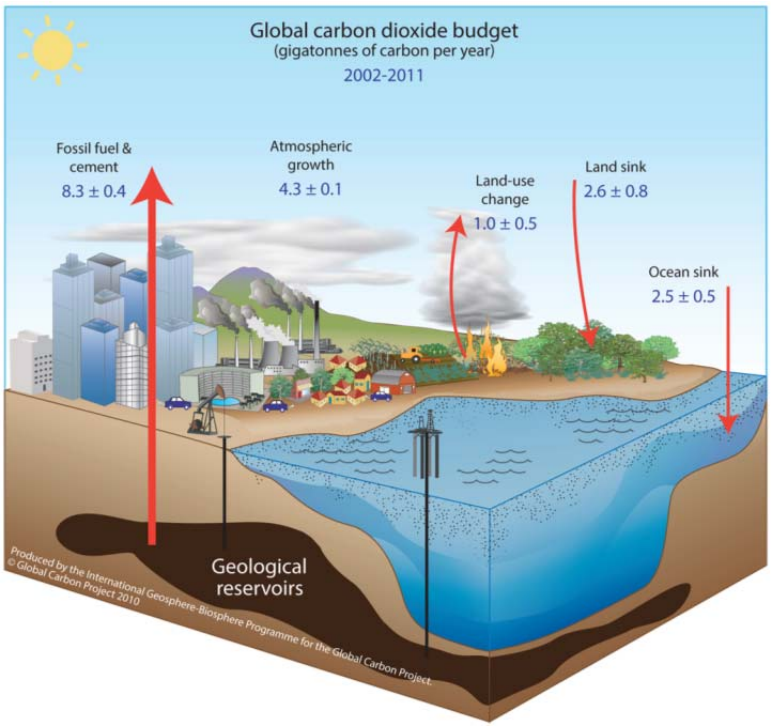

Figure 1 Perturbation of the global carbon cycle caused by anthropogenic activities, averaged globally for the decade 2002–2011 (PgC/yr)**.** Based on data from *Le Quéré et al.* [2012]. © Global Carbon Project 2010. Used by permission of the Global Carbon Project, www.globalcarbonproject.org .

Phytoplankton Functional Types

It is natural, then, to consider groups of phytoplankton species which have a common ecological function in biogeochemical cycles, or "Phytoplankton Functional Types (PFTs)". For instance, diatoms carry out one fifth of total global carbon fixation [*Nelson et al.*, 1995] and are major contributors to the biogeochemical cycling of silicon [*Falciatore et al.*, 2000]. Diatoms can be detected in the environment via microscopy, flow imaging , and by isolating their primary accessory pigment, fucoxanthin using high performance liquid chromatography (HPLC) techniques, albeit with some ambiguity because other phytoplankton may also contain fucoxanthin (e.g., dinoflagellates and Prymnesiophytes).

According to *Sieburth et al.* [1978], cell size is another approach to broadly classify phytoplankton according to biogeochemical function , where three size classes are created for picoplankton (<2 μm), associated with recycled production; nanoplankton (2–20 μm); and microplankton (>20 μm), associated with new production and the export of organic matter towards the deep ocean. While cell size functional classification may not be fully satisfactory from a biogeochemical perspective (see *Nair et al.* [2008]), many ecological and biogeochemical processes are related to cell size. These processes include light absorption, as influenced by the cellular pigment composition and packaging effect [*Bricaud et al.*, 1995; *Bricaud et al.*, 2004; *Duyens*, 1956; *Morel and Bricaud*, 1981; *Prieur and Sathyendranath*, 1981], nutrient uptake [*Probyn*, 1985; *Sunda and Huntsman*, 1997], and sinking rate and export [*Bagniewski et al.*, 2011; *Boyd and Newton*, 1999; *Laws et al.*, 2000; *Michaels and Silver*, 1988].

Recently, a variety of bio-optical methods have been established that use satellite data to identify and differentiate between phytoplankton functional types, including specific pigments

and cell size. The current PFT satellite algorithms can be categorized into three groups [*Brewin et al.*, 2011] :

- Spectral-response approaches which rely on the covariation between spectral features of optical properties and the dominant PFT or particle size distribution [*Alvain et al.*, 2005; *Alvain et al.*, 2008; *Bracher et al.*, 2009; *Brewin et al.*, 2010a; *Bricaud et al.*, 2012; *Ciotti and Bricaud*, 2006; *Kostadinov et al.*, 2009; *Mouw and Yoder*, 2010; *Sathyendranath et al.*, 2004],
- Abundance-based approaches which rely on observed relationships between phytoplankton and the trophic status, e.g., chlorophyll concentration or magnitude of phytoplankton absorption. [*Aiken et al.*, 2007; *Brewin et al.*, 2010b; *Devred et al.*, 2006; *Hirata et al.*, 2008; *Hirata et al.*, 2011; *Pan et al.*, 2010; *Sathyendranath et al.*, 2001; *Uitz et al.*, 2006] ,
- Ecological approaches which blend physical, spatial, and temporal data and bio-optical information to help detect different phytoplankton groups. [*Raitsos et al.*, 2008]

A unique contribution of this work is the application of selected PFT techniques to IOPs retrieved from autonomous, in situ measurements of radiometric data.

An Algorithm for Radiometric Inversion

During this 2004 Ocean Optics class, Dr. Curtis Mobley presented the lectures on radiative transfer theory, based on his book "Light and Water" [*Mobley*, 1994]. Laboratory exercises included using the HydroLight radiative transfer model [*Mobley et al.*, 1993] to compute in-water light fields given specified IOPs. At the time, Dr. Mobley was pursuing a look-up table approach to extract environmental information from remote sensing reflectance (R_{rs}) [*Mobley et al.*, 2005]. In this approach, a database of R_{rs} spectra is pre-computed based on a range of IOPs

and other pertinent parameters (e.g., bottom depths and reflectances, solar angles, and viewing directions) with numerous forward solutions of the radiative transfer equation (RTE). Then, when presented with an observed spectrum, the database is searched for the best least squares spectral match, which gives the IOPs and other parameters that generated that spectrum. This approach is ideally suited to environmental classification problems where the objective is retrieval from a tractable set of alternatives. However, for general IOP retrieval, there is a combinatorial explosion in the size of the database as the desired IOP resolution increases, and database generation and search becomes computationally expensive.

In this thesis, I develop an online algorithm that dynamically estimates IOPs without prior computation of a database or a priori assumptions about the values of the IOPs. A similar non-linear optimization approach as that presented by Dr. Roesler in the Ocean Optics Class exercise is employed, and the forward reflectance model is replaced with HydroLight's solution of RTE at each iteration. Computational performance is optimized by using Dr. Mobley's implementation of EcoLight which solves the azimuthally-averaged version of the RTE [*Mobley*, 2011], resulting in $\mathcal{O}(10^2)$ times faster performance than HydroLight. The limitation of EcoLight solutions to downwelling and upwelling irradiances (E_d, E_u) and nadir and zenith radiances (L_u, L_d) matches the capabilities of commercially available hyperspectral radiometers. (In this work, the marine light field is characterized by downwelling irradiance E_d and upwelling irradiance L_u.) EcoLight was integrated into MATLAB as a callable function, allowing the use of MATLAB's Optimization Toolbox [*Mathworks*, 2010], resulting in a framework that retrieves IOPs (in particular, the absorption and backscattering coefficients) from radiometric data at any spectral resolution. Characterization and propagation of errors from random and systematic sources is treated carefully using multivariate statistics. The computational and error analysis

framework of this approach is presented in Chapter 3. Ultimately, given hyperspectral measurements of $L_u(z, \lambda)$, $E_d(z, \lambda)$ and a single wavelength measurement of beam attenuation c, I show that this approach can estimate hyperspectral absorption with the same accuracy as a commercial in situ absorption meter [*Rehm and Mobley*, 2012].

A simpler but less accurate inversion algorithm in presented in Chapter 1, based on the fact that the in-water radiance distribution becomes asymptotic at large optical depths in homogeneous waters [*Rehm and McCormick*, 2011]. Combined with a simplified semi-analytic model for how light is scattered, a quick inverse solution for IOPs can be found. This solution can, if needed, be used as a starting point (initial guess) for the optimization scheme presented in Chapter 3. Ultimately (see Chapter 3), these inversions are found to work well at wavelengths where the in-water light field is dominated by elastic scattering and the ratio of particulate absorption to pure water absorption is not too small However, the performance is poor where Raman scattering, chlorophyll fluorescence dominate the light field, or where pure water dominates the absorption signal by two or more orders of magnitude.

Assessing phytoplankton community composition from in situ radiometry

In Chapter 4, two distinct spectral response approaches are applied to hyperspectral absorption spectra retrieved from hyperspectral radiometric measurements carried out on the Lagrangian float as part of the 2008 North Atlantic Bloom experiment. To assess the dominant cell size of phytoplankton, I employ the approach of *Ciotti et al.* [2002], where phytoplankton absorption is expressed as a spectral mixture of two basis functions defined by laboratory absorption measurements of natural communities of microphytoplankton and picophytoplankton from surface waters. To estimate the abundance of diatoms, spectral derivative analysis [*Tsai and*

Philpot, 1998] is applied to retrieved absorption spectra from which the concentration of the photosynthetic accessory pigment fucoxanthin is estimated. Both approaches are compared to size class assessed from water samples via HPLC analysis [*Uitz et al.*, 2006] and flow cytometry and flow imaging [*Sieracki et al.*, 2010].

The 2008 North Atlantic Bloom Experiment

The methods presented in this thesis are validated from observations carried out in the context of the 2008 North Atlantic Bloom Experiment. The broad objectives of this experiment were two-fold: 1) to study one of the largest and quickest explosions of life on the planet, the North American Bloom – responsible for > 20% of the annual ocean CO_2 uptake, and 2) to study this explosion of life from the perspective of autonomous robotic platforms, capable of observations at time and space scales not possible (or affordable) from ship-based sampling.

A Lagrangian float capable of accurate water following in the horizontal and vertical dimensions was outfitted with hyperspectral radiometers ($L_u(\lambda)$, $E_d(\lambda)$ at 3.3 nm resolution from 320 – 950 nm), beam attenuation ($c(653)$), backscattering ($b_b(700)$) and chlorophyll fluorescence. It was deployed at 59ºN, 20ºW near the JGOFS North Atlantic Bloom site by the *R/S Bjarni Sæmundsson* on 4 April 2008 and sampled for 51 days until the end of its mission on 25 May 2008 (Figure 2).

The *R/V Knorr* made extensive surveys near the float between 2 and 21 May 2008. At six stations, calibration casts were made within 1 km of the float, providing accurate CTD and bottle data as well as hyperspectral radiometric and bio-optical profiles (including absorption, attenuation, and backscattering). These measurements, part of the larger North Atlantic Bloom experiment [*Alkire et al.*, 2012; *Bagniewski et al.*, 2011; *Briggs et al.*, 2011; *Cetinić et al.*, 2012;

Mahadevan et al., 2012], allowed a) intercalibration of the bio-optical sensors deployed on both ship and autonomous platforms, as well as b) calibration of these sensors with the biogeochemical parameters under study.

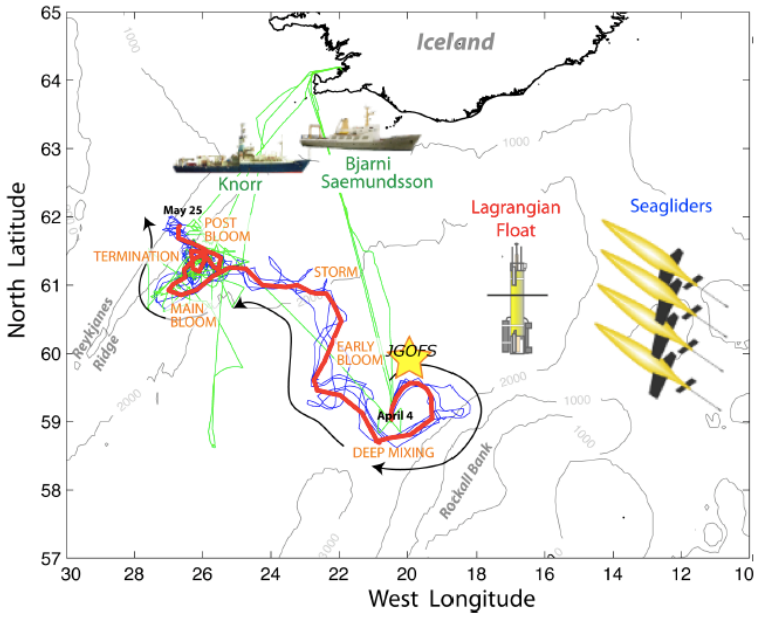

Figure 2. Map of the 2008 North Atlantic Bloom Experiment study area. The tracks of Float48 drift (red), Seagliders (blue), and supporting cruises (green) of the *R/V Knorr* and *R/V Bjarni Sæmundsson* are plotted as colored lines. The direction of the float drift, April 4 to May 25, is illustrated using black arrows. The various bloom periods presented in Chapter 4 (Deep Mixing, Early Bloom, Storm, Main Bloom, Termination, and Post-Bloom) are also noted. The location of the JGOFS 1989 North Atlantic Bloom Experiment is plotted as a yellow star**.**

Summary of Findings

- **Chapter 2:** Based on a simplified scattering phase function and the asymptotic eigenmode, the ratio of the backscattering to absorption coefficients (b_b/a) can be estimated from the ratio of measurements upwelling radiance (L_u) and the downward planar irradiance (E_d) in vertically homogeneous waters at depths where the light field is in the asymptotic regime.
- **Chapter 3:** Hyperspectral measurements of downwelling irradiance and upwelling radiance, with a single-wavelength measurement of attenuation, can be used to estimate hyperspectral absorption to an accuracy of ±0.01 m^{-1} and hyperspectral backscattering to an accuracy of

± 0.0005 m^{-1} over wavelengths for which the contributions of inelastic scattering are small (350 to 575 nm)

- **Chapter 4:** Hyperspectral estimates of particulate plus detrital absorption are retrieved from hyperspectral measurements of upwelling radiance and downwelling irradiance and beam attenuation at one wavelength. Knowledge of surface solar radiation is not necessary. The retrievals are found to be robust to spectrally-neutral biofouling.
- **Chapter 4:** These absorption spectra are of sufficient accuracy, bandwidth, and resolution to estimate bio-optical signatures of phytoplankton community structure including overall biomass, the fraction of small phytoplankton, and the absorption due to colored detrital material.
- **Chapter 4:** Size fraction estimates based on packaging effects on the flatness of the absorption spectrum are found to be ambiguous in the presence of vertical mixing, also a consideration for ocean satellite retrievals of this parameter.
- **Chapter 4:** Derivative spectroscopy applied to the retrieved absorption spectra can detect and estimate the relative contribution to absorption of individual phytoplankton pigments, specifically chlorophyll *a*, fucoxanthin and other carotenoids
- **Chapter 4:** The time series of these estimates show the growth of a diatom bloom which then rapidly disappears and is replaced by a community of smaller cells. This description is consistent with nearby ship-based measurements from the 2008 North Atlantic Bloom Experiment that rely on water samples and laboratory measurements.
- **Chapters 2,3,4:** Observations of hyperspectral IOPs and phytoplankton functional types are possible from low-power, autonomous platforms.

References

Aiken, J., J. Fishwick, S. Lavender, R. Barlow, G. Moore, H. Sessions, S. Bernard, J. Ras, and N. Hardman-Mountford (2007), Validation of MERIS reflectance and chlorophyll during the BENCAL cruise October 2002: preliminary validation of new demonstration products for phytoplankton functional types and photosynthetic parameters, *Int. J. Remote Sens.*, *28*(3-4), 497-516.

Alkire, M., E. D'Asaro, C. Lee, M. Jane Perry, A. Gray, I. Cetinić, N. Briggs, E. Rehm, E. Kallin, J. Kaiser, and A. González-Posada (2012), Estimates of net community production and export using high-resolution, Lagrangian measurements of O2, NO3−, and POC through the evolution of a spring diatom bloom in the North Atlantic, *Deep Sea Res., Part I*, *64*, 157-174, doi:10.1016/j.dsr.2012.01.012.

Alvain, S., C. Moulin, Y. Dandonneau, and F. M. Bréon (2005), Remote sensing of phytoplankton groups in case 1 waters from global SeaWiFS imagery, *Deep Sea Res., Part I*, *52*(11), 1989-2004.

Alvain, S., C. Moulin, Y. Dandonneau, and H. Loisel (2008), Seasonal distribution and succession of dominant phytoplankton groups in the global ocean: A satellite view, *Global Biogeochemical Cycles*, *22*(3), GB3001.

Bagniewski, W. J., K. Fennel, M. J. Perry, and E. A. D'Asaro (2011), Optimizing models of the North Atlantic spring bloom using physical, chemical and bio-optical observations from a Lagrangian float, *Biogeosciences*, *8*(5), 1291-1307, doi:10.5194/bg-8-1291-2011.

Boyd, P., and P. Newton (1999), Does planktonic community structure determine downward particulate organic carbon flux in different oceanic provinces?, *Deep-Sea Research Part I*, *46*(1), 63-91.

Bracher, A., M. Vountas, T. Dinter, J. Burrows, R. Röttgers, and I. Peeken (2009), Quantitative observation of cyanobacteria and diatoms from space using PhytoDOAS on SCIAMACHY data, *Biogeosciences*, *6*, 751-764.

Brewin, R. J. W., S. J. Lavender, N. J. Hardman-Mountford, and T. Hirata (2010a), A spectral response approach for detecting dominant phytoplankton size class from satellite remote sensing, *Acta Oceanol Sin*, *29*(2), 14-32.

Brewin, R. J. W., S. Sathyendranath, T. Hirata, S. J. Lavender, R. M. Barciela, and N. J. Hardman-Mountford (2010b), A three-component model of phytoplankton size class for the Atlantic Ocean, *Ecol. Model.*, *221*(11), 1472-1483.

Brewin, R. J. W., N. J. Hardman-Mountford, S. J. Lavender, D. E. Raitsos, T. Hirata, J. Uitz, E. Devred, A. Bricaud, A. Ciotti, and B. Gentili (2011), An intercomparison of bio-optical techniques for detecting dominant phytoplankton size class from satellite remote sensing, *Remote Sens. Environ.*, *115*(2), 325-339.

Bricaud, A., A. Ciotti, and B. Gentili (2012), Spatial-temporal variations in phytoplankton size and colored detrital matter absorption at global and regional scales, as derived from twelve years of SeaWiFS data (1998–2009), *Global Biogeochemical Cycles*, *26*(1), GB1010.

Bricaud, A., M. Babin, A. Morel, and H. Claustre (1995), Variability in the chlorophyll-specific absorption coefficients of natural phytoplankton: Analysis and parameterization, *J. Geophys. Res. (C Oceans)*, *100*(C7), 13321-13332.

Bricaud, A., H. Claustre, J. Ras, and K. Oubelkheir (2004), Natural variability of phytoplanktonic absorption in oceanic waters: Influence of the size structure of algal populations, *J. Geophys. Res*, *109*(C11), C11010.

Briggs, N., M. J. Perry, I. Cetinić, C. Lee, E. A. D'Asaro, A. M. Gray, and E. Rehm (2011), High-resolution observations of aggregate flux during a sub-polar North Atlantic spring bloom, *Deep Sea Res., Part I*, *58*(10), 1031-1039, doi:10.1016/j.dsr.2011.07.007.

Cetinić, I., M. J. Perry, N. T. Briggs, E. Kallin, E. A. D'Asaro, and C. M. Lee (2012), Particulate organic carbon and inherent optical properties during 2008 North Atlantic Bloom Experiment, *J. Geophys. Res. (C Oceans)*, *117*(C6), C06028, doi:10.1029/2011JC007771.

Ciotti, A. M., and A. Bricaud (2006), Retrievals of a size parameter for phytoplankton and spectral light absorption by colored detrital matter from water-leaving radiances at SeaWiFS channels in a continental shelf region off Brazil, *Limnol. Oceanogr. Methods*, *4*, 237-253.

Ciotti, A. M., M. R. Lewis, and J. J. Cullen (2002), Assessment of the relationships between dominant cell size in natural phytoplankton communities and the spectral shape of the absorption coefficient, *Limnol. Oceanogr.*, *47*(2), 404-417.

D'Asaro, E. A. (2003), Performance of autonomous Lagrangian floats, *J. Atmos. Oceanic Technol.*, *20*(6), 896-911.

Devred, E., S. Sathyendranath, V. Stuart, H. Maass, O. Ulloa, and T. Platt (2006), A two-component model of phytoplankton absorption in the open ocean: Theory and applications, *J. Geophys. Res*, *111*(C03011), 1-11.

Duyens, L. N. M. (1956), The flattening of the absorption spectrum of suspensions, as compared to that of solutions, *Biochim Biophys Acta*, *19*(0), 1-12, doi:10.1016/0006-3002(56)90380-8.

Falciatore, A., M. R. d'Alcalà, P. Croot, and C. Bowler (2000), Perception of Environmental Signals by a Marine Diatom, *Science*, *288*(5475), 2363-2366, doi:10.1126/science.288.5475.2363.

Gordon, H. R. (2002), Inverse methods in hydrologic optics, *Oceanologia*, *44*(1), 9-58.

Gordon, H. R., O. B. Brown, R. H. Evans, J. W. Brown, R. C. Smith, K. S. Baker, and D. K. Clark (1988), A Semianalytic Radiance Model of Ocean Color, *J. Geophys. Res.*, *93*(D9), 10909-10924.

Gordon, H. R., M. R. Lewis, S. D. McLean, M. S. Twardowski, S. A. Freeman, K. J. Voss, and G. C. Boynton (2009), Spectra of particulate backscattering in natural waters, *Opt. Express*, *17*(18), 16192-16208.

Harcourt, R. R., and E. A. D'Asaro (2010), Measurement of Vertical Kinetic Energy and Vertical Velocity Skewness in Oceanic Boundary Layers by Imperfectly Lagrangian Floats, *J. Atmos. Oceanic Technol.*, *27*(11), 1918-1935.

Hirata, T., J. Aiken, N. Hardman-Mountford, T. Smyth, and R. Barlow (2008), An absorption model to determine phytoplankton size classes from satellite ocean colour, *Remote Sens. Environ.*, *112*(6), 3153-3159.

Hirata, T., N. J. Hardman-Mountford, R. J. W. Brewin, J. Aiken, R. Barlow, K. Suzuki, T. Isada, E. Howell, T. Hashioka, M. Noguchi-Aita, and Y. Yamanaka (2011), Synoptic relationships between surface Chlorophyll-a and diagnostic pigments specific to phytoplankton functional types, *Biogeosciences*, *8*(2), 311-327, doi:10.5194/bg-8-311-2011.

Kostadinov, T., D. Siegel, and S. Maritorena (2009), Retrieval of the particle size distribution from satellite ocean color observations, *J. Geophys. Res.*, *114*(C9), C09015.

Laws, E. A., P. G. Falkowski, W. O. Smith, H. Ducklow, and J. J. McCarthy (2000), Temperature effects on export production in the open ocean, *Global Biogeochemical Cycles*, *14*(4), 1231-1246.

Le Quéré, C., R. J. Andres, T. Boden, T. Conway, R. A. Houghton, J. I. House, G. Marland, G. P. Peters, G. van der Werf, A. Ahlström, R. M. Andrew, L. Bopp, J. G. Canadell, P. Ciais, S. C. Doney, C. Enright, P. Friedlingstein, C. Huntingford, A. K. Jain, C. Jourdain, E. Kato, R. F. Keeling, K. Klein Goldewijk, S. Levis, P. Levy, M. Lomas, B. Poulter, M. R. Raupach, J. Schwinger, S. Sitch, B. D. Stocker, N. Viovy, S. Zaehle, and N. Zeng (2012), The global carbon budget 1959–2011, *Earth Syst. Sci. Data Discuss.*, *5*(2), 1107-1157, doi:10.5194/essdd-5-1107-2012.

Leathers, R. A., C. S. Roesler, and N. J. McCormick (1999), Ocean inherent optical property determinationfrom in-water light field measurements, *Appl. Opt.*, *38*(24), 5096-5103.

Mahadevan, A., E. D'Asaro, C. Lee, and M. J. Perry (2012), Eddy-Driven Stratification Initiates North Atlantic Spring Phytoplankton Blooms, *Science*, *337*(6090), 54-58, doi:10.1126/science.1218740.

Mathworks (2010), *MATLAB Optimization Toolbox™ 5 User's Guide*, The MathWorks, Inc., Natick, MA.

Michaels, A. F., and M. W. Silver (1988), Primary production, sinking fluxes and the microbial food web, *Deep Sea Research Part A. Oceanographic Research Papers*, *35*(4), 473-490.

Mobley, C. D. (1994), *Light and water: radiative transfer in natural waters*, 592 pp., Academic Press, San Diego.

Mobley, C. D. (2011), Fast light calculations for ocean ecosystem and inverse models, *Opt. Express*, *19*(20), 18927-18944.

Mobley, C. D., B. Gentili, H. R. Gordon, Z. Jin, G. W. Kattawar, A. Morel, P. Reinersman, K. Stamnes, and R. H. Stavn (1993), Comparison of numerical models for computing underwater light fields, *Appl. Opt.*, *32*(36), 7484-7504.

Mobley, C. D., L. K. Sundman, C. O. Davis, J. H. Bowles, T. V. Downes, R. A. Leathers, M. J. Montes, W. P. Bissett, D. D. R. Kohler, and R. P. Reid (2005), Interpretation of hyperspectral remote-sensing imagery by spectrum matching and look-up tables, *Appl. Opt.*, *44*(17), 3576-3592.

Morel, A., and A. Bricaud (1981), Theoretical results concerning light absorption in a discrete medium, and application to specific absorption of phytoplankton, *Deep Sea Research Part A. Oceanographic Research Papers*, *28*(11), 1375-1393.

Mouw, C. B., and J. A. Yoder (2010), Optical determination of phytoplankton size composition from global SeaWiFS imagery, *J. Geophys. Res.*, *115*(C12), C12018, doi:10.1029/2010jc006337.

Nair, A., S. Sathyendranath, T. Platt, J. Morales, V. Stuart, M. H. Forget, E. Devred, and H. Bouman (2008), Remote sensing of phytoplankton functional types, *Remote Sens. Environ.*, *112*(8), 3366-3375.

Nelson, D. M., P. Tréguer, M. A. Brzezinski, A. Leynaert, and B. Quéguiner (1995), Production and dissolution of biogenic silica in the ocean: revised global estimates, comparison with regional data and relationship to biogenic sedimentation, *Global Biogeochemical Cycles*, *9*, 359-359.

Pan, X., A. Mannino, M. E. Russ, S. B. Hooker, and L. W. Harding (2010), Remote sensing of phytoplankton pigment distribution in the United States northeast coast, *Remote Sens. Environ.*, *114*(11), 2403-2416.

Prieur, L., and S. Sathyendranath (1981), An optical classification of coastal and oceanic waters based on the specific spectral absorption curves of phytoplankton pigments, dissolved organic matter, and other particulate materials, *Limnol. Oceanogr.*, *26*(4), 19, doi:10.4319/lo.1981.26.4.0671.

Probyn, T. A. (1985), Nitrogen uptake by size-fractionated phytoplankton populations in the southern Benguela upwelling system, *Mar. Ecol. Prog. Ser.*, *22*(3), 249-258.

Raitsos, D. E., S. J. Lavender, C. D. Maravelias, J. Haralabous, A. J. Richardson, and P. C. Reid (2008), Identifying Four Puhytoplankton Functional Types from Space: An Ecological Approach, *Limnol. Oceanogr.*, 605-613.

Rehm, E. (2006a), Measurements and Modelling in a Coastal Inlet, poster presented at AGU Fall Meeting, San Francisco, California.

Rehm, E. (2006b), In-Situ Measurement of Primary Productivity from a Lagrangian Float, poster presented at ASLO Ocean Sciences, Honolulu, Hawaii.

Rehm, E., and N. J. McCormick (2011), Inherent optical property estimation in deep waters, *Opt. Express*, *19*(25), 24986-25005.

Rehm, E., and C. D. Mobley (2012), Estimation of hyperspectral inherent optical properties from in-water radiometry: error analysis and application to in situ data, *Appl. Opt.*, In press.

Roesler, C. S., and M. J. Perry (1995), In situ phytoplankton absorption, fluorescence emission, and particulate backscattering spectra determined from reflectance, *J. Geophys. Res. (C Oceans)*, *100*(C7), 13279-13294.

Roesler, C. S., S. M. Etheridge, and G. C. Pitcher (2003), Application of an ocean color algal taxa detection model to red tides in the Southern Benguela, paper presented at Proceedings of the Xth International Conference on Harmful Algae, Florida Fish and Wildlife Conservation Commission and Intergovernmental Oceanographic Commission of UNESCO, St. Petersburg, FL, USA.

Sathyendranath, S., G. Cota, V. Stuart, H. Maass, and T. Platt (2001), Remote sensing of phytoplankton pigments: a comparison of empirical and theoretical approaches, *Int. J. Remote Sens.*, *22*(2-3), 249-273.

Sathyendranath, S., L. Watts, E. Devred, T. Platt, C. Caverhill, and H. Maass (2004), Discrimination of diatoms from other phytoplankton using ocean-colour data, *Mar. Ecol. Prog. Ser.*, *272*, 59-68.

Sieburth, J. M., V. Smetacek, and J. Lenz (1978), Pelagic ecosystem structure: heterotrophic compartments of the plankton and their relationship to plankton size fractions, *Limnol. Oceanogr.*, *23*(6), 1256-1263.

Sieracki, M. E., N. Poulton, E. Kallin, B. Thompson, E. A. D'Asaro, C. M. Lee, and M. J. Perry (2010), Plankton Succession and Biomass during the 2008 North Atlantic Spring Bloom, paper presented at Proceedings from the 2010 AGU Ocean Sciences Meeting, AGU, Portland, Oregon, 22-26 Feb 2010.

Stramska, M., D. Stramski, B. G. Mitchell, and C. D. Mobley (2000), Estimation of the absorption and backscattering coefficients from in-water radiometric measurements, *Limnol. Oceanogr.*, *45*(3), 628-641.

Sunda, W. G., and S. A. Huntsman (1997), Interrelated influence of iron, light and cell size on marine phytoplankton growth, *Nature*, *390*(6658), 389-392.

Tsai, F., and W. Philpot (1998), Derivative analysis of hyperspectral data, *Remote Sens. Environ.*, *66*(1), 41-51.

Uitz, J., H. Claustre, A. Morel, and S. B. Hooker (2006), Vertical distribution of phytoplankton communities in open ocean: An assessment based on surface chlorophyll, *J. Geophys. Res.*, *111*(C8), C08005.

Chapter 2

Rehm, E., and N. J. McCormick (2011), Inherent optical property estimation in deep waters, *Optics Express*, 19(25), 24986-25005.

Inherent optical property estimation in deep waters

Eric Rehm[1,*] **and Norman J. McCormick**[2]

[1]*Applied Physics Laboratory, University of Washington, Seattle, WA 98105-6698, USA*

[2]*Department of Mechanical Engineering, University of Washington,*

Seattle, WA 98195-2600, USA

[*]*erehm@u.washington.edu*

Abstract: We develop two algorithms for determining two inherent optical properties (IOPs) from radiometric measurements in vertically homogeneous waters. The first algorithm is for estimation of the ratio of the backscattering to absorption coefficients from measurements of only the vertically upward radiance and the downward planar irradiance at depths where the light field is in the asymptotic regime. The second algorithm enables estimation of the absorption coefficient from measurement of the diffuse attenuation coefficient in the asymptotic regime after use of the first algorithm. Multiplication of the two estimates leads to an estimate for the backscattering coefficient. The algorithms, based upon the use of a simplified phase function and the asymptotic eigenmode, are shown to potentially provide good starting conditions for iteratively determining the absorption and backscattering coefficients of a wide variety of waters. The uncertainty in the estimates defines a subspace for IOPs that may reduce ambiguity in such iterative solutions. Because of the ease of estimating the backscattering to absorption ratio from in-water measurements, this IOP deserves further investigation as a proxy for biogeochemical quantities in the open ocean.

OCIS codes: (010.0010) Atmospheric and ocean optics; (010.4450) Ocean optics; (010.7340) Water; (030.5620) Radiative transfer; (100.3190) Inverse problems; (160.4760) Optical properties; (290.4210) Multiple scattering.

References and links

1. H. R. Gordon, "Inverse methods in hydrologic optics," Oceanologia **44**, 9–58 (2002).
2. N. J. McCormick, "Inverse Radiative Transfer Problems: A Review," Nucl. Sci. Eng. **112**, 185–198 (1992).
3. C. D. Mobley, *Light and Water: Radiative Transfer in Natural Waters* (Academic, New York, 1994).
4. H. R. Gordon, O. B. Brown, and M. M. Jacobs, "Computed relationships between the inherent and apparent optical properties of a flat homogeneous ocean," Appl. Opt. **14**, 417–427 (1975).

5. H. Gordon, "Simple Calculation of the Diffuse Reflectance of the Ocean," Appl. Opt. **12**, 2803–2804 (1973).
6. N. J. McCormick, "Analytical transport theory applications in optical oceanography," Ann. Nucl. Energy **23**, 381–395 (1996).
7. H. Loisel and D. Stramski, "Estimation of inherent optical properties of natural waters from the irradiance attenuation coefficient and reflectance in the presence of Raman scattering," Appl. Opt. **39**, 3001-3011 (2000).
8. M. Stramska, D. Stramski, B. G. Mitchell, and C. D. Mobley, "Estimation of the absorption and backscattering coefficients from in-water radiometric measurements," Limnol. Oceanogr. **45**, 628-641 (2000).
9. H. R. Gordon and G. C. Boynton, "A radiance–irradiance inversion algorithm for estimating the absorption and backscattering coefficients of natural waters: homogeneous waters," Appl. Opt. **36**, 26362641 (1997).
10. G. C. Boynton and H. R. Gordon, "Irradiance inversion algorithm for estimating the absorption and backscattering coefficients of natural waters: Raman-scattering effects," Appl. Opt. **39**, 3012-3022 (2000).
11. E. Rehm, "Inverting Light with Constraints," Poster session presented at Ocean Optics XIX, Barga, Italy (2008).
12. R. A. Leathers, C. S. Roesler, and N. J. McCormick, "Ocean inherent optical property determination from in-water light field measurements," Appl. Opt. **38**, 5096–5103 (1999).
13. B. D. Piening and N. J. McCormick, "Asymptotic optical depths in source-free ocean waters," Appl. Opt. **42**, 5382–5387 (2003).
14. S. Maritorena, D. A. Siegel, and A. R. Peterson, "Optimization of a semianalytical ocean color model for global scale applications," Appl. Opt. **41**, 2705-2714 (2002).
15. IOCCG, "Remote Sensing of Inherent Optical Properties: Fundamentals, Tests of Algorithms, and Applications," *Reports of the International Ocean-Colour Coordinating Group*, **5**, Lee, Z.-P., ed. (IOCCG, Dartmouth, Canada, 2006).
16. T. G. Peacock, K. L. Carder, C. O. Davis, and R. G. Steward, "Effects of fluorescence and water Raman scattering on models of remote sensing reflectance," in *Ocean Optics X*, R. W. Spinrad, ed., Proc. SPIE **1302**, 303-319 (1990).
17. H. R. Gordon, "Contribution of Raman scattering to water-leaving radiance: a reexamination," Appl. Opt. **38**, 3166-3174 (1999).
18. A. Morel and L. Prieur, "Analysis of variations in ocean color," Limnol. Oceanogr. **22**, 709–722 (1977).
19. J. H. Joseph, W. J. Wiscombe, and J. A. Weinman, "The delta-Eddington approximation for radiative flux transfer," J. Atmos. Sci. **33**, 2452–2459 (1976).
20. C. D. Mobley, L. K. Sundman, and E. Boss, "Phase function effects on oceanic light fields," Appl. Opt. **41**, 1035–1050 (2002).
21. C. D. Mobley and L. K. Sundman, *Hydrolight 5.0, Ecolight 5.0 Technical Documentation* (Sequoia Scientific, Inc., Redmond, WA, 2008).
22. N. J. McCormick, "Analytic inverse radiative transfer equations for atmospheric and hydrologic optics," J. Opt. Soc. Am. A **21**, 1009–1017 (2004).
23. K. M. Case and P. F. Zweifel, *Linear Transport Theory* (Addison-Wesley, Reading, MA, 1967).
24. N. J. McCormick and I. Kuščer, "Singular eigenfunction expansions in neutron transport theory," in *Advances in Nuclear Science and Technology* **7**, E. J. Henley and J. Lewins, eds. (Academic, New York, 1973), pp. 181–282.
25. N. J. McCormick, "Asymptotic optical attenuation," Limnol. Oceanogr. **37**, 1570–1578 (1992).
26. J. R. V. Zaneveld, "An asymptotic closure theory of irradiance in the sea and its inversion to obtain the vertical structure of inherent optical properties," Limnol. Oceanogr. **34**, 1442–1452 (1989).
27. G. R. Fournier and J. L. Forand, "Analytic phase function for ocean water," in *Ocean Optics XII*, J. S. Jaffe (ed), Proc. SPIE **2258**, 194–201 (1994).
28. T. J. Petzold, "Volume Scattering Functions for Selected Ocean Waters," Tech. Rep. SIO 72-78 (Scripps Institution of Oceanography, La Jolla, Calif., 1972), pp. 1-78.
29. E. A. D'Asaro, C. Lee, M. Perry, K. Fennel, E. Rehm, A. Gray, N. Briggs, and K. Gudmundsson, "The 2008 North Atlantic Bloom Experiment I: Overview and Strategy," Eos, Transactions, American Geophysical Union **89**(53), Fall Meeting Supplement, Abstract OS24A-08 (2008), http://adsabs.harvard.edu/abs/2008AGUFMOS24A..08D.
30. W. S. Pegau, D. Gray, and J. R. V. Zaneveld, "Absorption and attenuation of visible and near-infrared light in water: dependence on temperature and salinity," Appl. Opt. **36**, 6035-6046 (1997).
31. J. R. V. Zaneveld, J. C. Kitchen, and C. C. Moore, "Scattering error correction of reflecting tube absorption meter," in *Ocean Optics XII*, J. S. Jaffe (ed), Proc. SPIE **2258**, 44-55 (1994).
32. B. Efron and G. Gong, "A Leisurely Look at the Bootstrap, the Jackknife, and Cross-Validation," Am. Stat. **37**, 36–48 (1983).
33. *MATLAB® Optimization Toolbox™ 5 User's Guide*, (The MathWorks Inc., Natick, MA, 2010).
34. M. Defoin-Platel and M. Chami, "How ambiguous is the inverse problem of ocean color in coastal waters?," J. Geophys. Res. **112**, C03004, doi:10.1029/2006JC003847 (2007).
35. C. D. Mobley, "Fast light calculations for ocean ecosystem and inverse models," Opt. Express, submitted (2011).
36. H. R. Gordon and O. B. Brown, "Irradiance Reflectivity of a Flat Ocean as a Function of Its Optical Properties," Appl. Opt. **12**, 1549–1551 (1973).
37. G. E. Thomas and K. Stamnes, *Radiative Transfer in the Atmosphere and Ocean* (Cambridge University Press, 1999).

38. G. DallOlmo, T. K. Westberry, M. J. Behrenfeld, E. Boss, and W. H. Slade, "Significant contribution of large particles to optical backscattering in the open ocean," Biogeosciences **6**, 947-967 (2009).
39. J. J. Duderstadt and W. R. Martin, *Transport Theory* (Wiley, New York, 1979).
40. G. I. Bell and S. Glasstone, *Nuclear Reactor Theory* (Van Nostrand-Reinhold, Princeton, New Jersey, 1970).
41. Q. Min and L. C. Harrison "An adjoint formulation of the radiative transfer method," J. Geophys. Res. **101**, pp. 1635-1640 (1996).
42. A. B. Davis and Y. Knyazikhin, "A Primer in Three-Dimensional Radiative Transfer," in *Three-Dimensional Radiative Transfer in the Cloudy Atmosphere*, A. Davis and A. Marshak, eds. (Springer-Verlag, 2005), pp. 153-242.
43. H. Loisel, J. Nicolas, P. Deschamps, and R. Frouin, "Seasonal and inter-annual variability of particulate organic matter in the global ocean," Geophys. Res. Lett. **29**(24), 2196, doi:10.1029/2002GL015948 (2002).
44. D. Stramski, R. A. Reynolds, M. Babin, S. Kaczmarek, M. R. Lewis, R. Röttgers, A. Sciandra, M. Stramska, M. S. Twardowski, B. A. Franz, and H. Claustre, "Relationships between the surface concentration of particulate organic carbon and optical properties in the eastern South Pacific and eastern Atlantic Oceans," Biogeosciences **5**, 171-201 (2008).
45. L. Prieur and S. Sathyendranath, "An optical classification of coastal and oceanic waters based on the specific spectral absorption curves of phytoplankton pigments, dissolved organic matter, and other particulate materials," Limnol. Oceanogr. **26**(4), 671-689 (1981).
46. A. Morel,"Light and marine photosynthesis: a spectral model with geochemical and climatological implications," Prog. Oceanogr. **26**, 263–306 (1991).
47. M. J. Behrenfeld and E. Boss, "The beam attenuation to chlorophyll ratio: an optical index of phytoplankton physiology in the surface ocean?," Deep-Sea Research I **50** 1537-1549 (2003).

1. Introduction

The estimation of ocean inverse optical properties (IOPs) from radiometric measurements is a long-standing and important problem in ocean optics [1], forming the basis of remote sensing of ocean water constituents and biogeochemical properties. The solution for one or more IOPs from apparent optical properties (AOPs) is an example of such a problem. Using just the knowledge of the in-water light field, the inverse problem for IOPs can be solved by closed-form (explicit) methods or iterative (implicit) methods [2, 3].

Explicit methods do this by manipulation of the radiative transfer equation (RTE) or analytic solutions to derive formulas that estimate IOPs from AOPs. The explicit method is illustrated by the early work of Gordon *et al.* [4] who showed, assuming quasi-single scattering [5] and employing Monte Carlo simulations, that remote sensing reflectance was strongly correlated with the ratio of the backscattering to absorption coefficients, b_b/a. Explicit algorithms also can be derived from solutions to the RTE expressed as a linear combination of eigenfunctions [6], or by carrying out a large number of radiative transfer simulations in order to parameterize relationships between IOPs and AOPs [7, 8].

Implicit methods estimate IOPs by repeatedly solving the RTE, starting with an initial estimate or guess of the IOPs. At each iteration, radiometric measurements (or AOPs derived therein) are compared to the RTE solution and then an objective function is computed that expresses the difference between the RTE solution and the measured values. The IOPs are then adjusted to reduce the objective function. Iteration is complete when the objective function is reduced to an acceptably small value. Implicit approaches to estimating absorption and backscattering in homogeneous waters have been developed that estimate IOPs from surface illumination and depth profiles of easily-measured radiometric quantities, while allowing for general multiple scattering as well as inelastic scattering [9, 10, 11].

Two inversion algorithms are developed here, one for estimating the b_b/a ratio and the other for the absorption coefficient a. For estimating b_b/a, we use a hybrid approach where we iteratively solve a system of equations derived from an explicit eigenfunction formulation of the RTE. Our algorithm for b_b/a requires one fitted parameter F that corrects for an oversimplification of our assumed phase function. That phase function enables us to use a simplified solution of the radiative transfer equation which depends only on a and b_b. We also assume that the optical measurements are made in the asymptotic regime. (The depths at which the light reaches an asymptotic distribution depends on the IOPs and the surface illumination and occurs at shallower depths when the incident light is more diffuse [3, 12, 13].) With the values of F and b_b/a, our second algorithm can be used to estimate a from measurement of the in-water downward diffuse attenuation coefficient. Combination of the two estimates directly leads to an estimate of the backscattering coefficient b_b. Alternatively, a can be estimated from b_b/a, measurements of b_b at one or more wavelengths, and a model for the spectral behavior of $b_b(\lambda)$.

The resulting estimates of a and b_b can be used, for example, as the initial starting estimate, instead of a guess, for any implicit method, such as one using a nonlinear global optimization technique [11]. Furthermore, uncertainty in estimates from our algorithms can be used as

inversion constraints [11, 14, 15].

2. Radiative transfer equation

For our investigation the radiance $L(z,\mu,\varphi)$ for $z \geq 0$ is taken to be a function of the direction cosine μ, measured with respect to the depth z in the water, and ϕ, the azimuthal angle measured in the plane perpendicular to the z-axis. The water is taken to be spatially uniform and deep enough that bottom effects can be neglected. For scattering given by the phase function $\tilde{\beta}(\mu_0) = \tilde{\beta}(\mu',\varphi',\mu,\varphi)$ for μ_0 the cosine of the angle between $\{\mu',\varphi'\}$ and $\{\mu,\varphi\}$, the radiative transfer equation for the semi-infinite medium is [3]

$$\mu \frac{\partial}{\partial z} L(z,\mu,\varphi) + cL(z,\mu,\varphi) = b \int_0^{2\pi} \int_{-1}^{1} \tilde{\beta}(\mu',\varphi',\mu,\varphi) L(z,\mu',\varphi') \mathrm{d}\mu' \mathrm{d}\varphi' \ , \ z \geq 0 \ . \tag{1}$$

Here $c = a + b$ is the sum of the absorption and scattering coefficients. Notice that this formulation and subsequent algorithm development ignores inelastic scattering. As a result, the algorithm developed here will not be applied to spectral regions in which inelastic scattering can make a significant contribution to the upward radiance [10, 16, 17].

Because the objective here is to develop algorithms for measurements done with a planar irradiance detector and a radiance detector aimed in the vertically upward direction for which $\mu = -1$, there is no azimuthal dependence of the data so the analysis will be done for the azimuthally averaged radiance

$$L(z,\mu) = (2\pi)^{-1} \int_0^{2\pi} L(z,\mu,\varphi) \mathrm{d}\varphi \tag{2}$$

with

$$\mu \frac{\partial}{\partial z} L(z,\mu) + cL(z,\mu) = b \int_{-1}^{1} \tilde{\beta}(\mu',\mu) L(z,\mu') \mathrm{d}\mu' \ , \quad z \geq 0 \ , \tag{3}$$

and

$$\tilde{\beta}(\mu',\mu) = \int_0^{2\pi} \tilde{\beta}(\mu',\varphi',\mu,\varphi = 0) \mathrm{d}\varphi' . \tag{4}$$

We will derive an approximate equation for determining b_b/a from data for the vertically upward radiance $L_u(z_m) = L(z_m, -1)$ at measurement depth z_m and the downward planar irradiance $E_d(z_m)$,

$$E_d(z_m) \quad = \quad 2\pi \int_0^1 \mu L(z_m, \mu) \mathrm{d}\mu. \tag{5}$$

This will be done by developing an algorithm for determining b_b/a that is expressed in terms of the in-water remote sensing ratio,

$$r_{rs}(z_m) = L_u(z_m)/E_d(z_m). \tag{6}$$

Following that we will obtain the algorithm for determining a from the estimated value of b_b/a and multiple measurements of $E_d(z_m)$. Both algorithms will be developed with a value of F that is obtained by fitting data from previous calculations or experiments to situations where b_b and a are known.

There are two assumptions needed to develop the algorithms. The first is that water beneath measurement depth z_m is sufficiently spatially uniform and deep enough that z_m is approaching the so-called "asymptotic regime" where the angular distribution of the radiance will not perceptibly change with increasing depth. Another interpretation of this first assumption is that z_m must be deep enough that the directional nature of the incident surface illumination does not affect the directional nature of the underwater light field. The second assumption is that the angular distribution of the volume scattering function is so strongly forward that an "isotropic plus delta forward" synthetic scattering phase function model can be used,

$$\tilde{\beta}(\mu', \mu) = \frac{1}{2}\left[\frac{\tilde{b}_b}{F} + 2\left(1 - \frac{\tilde{b}_b}{F}\right)\delta(\mu' - \mu)\right] \tag{7}$$

where $\tilde{b}_b = b_b/b$ is the backscattering ratio and F is the adjustment factor to be determined from numerical simulations or experimental data. Our phase function satisfies the proper normalization condition

$$\int_{-1}^{1} \tilde{\beta}(\mu', \mu) \mathrm{d}\mu = 1. \tag{8}$$

A primary advantage of this phase function is that it leads directly to a radiative transfer equation that depends only on a and b_b, but not b, which has been shown to be a significant advantage for remote sensing applications [4, 18].

The phase function of Eq. (7) is a slight extension of the simplest form of the classic "delta-Eddington" scattering model [19] to which it degenerates if $F = 1$. Although this elementary model for the scattering phase function does not account for the directional dependence of backscattering, such a dependence has been shown to give errors in underwater radiances and planar irradiances on the order of 10% or less [20].

Substitution of the phase function of Eq. (7) into Eq. (3), followed by changes in the variables to obtain a dimensionless optical distance,

$$\tau = (c - b + b\tilde{b}_b/F)z = az\left[1 + \frac{b_b/a}{F}\right], \tag{9}$$

results in the radiative transfer equation

$$\mu \frac{\partial}{\partial \tau} L(\tau,\mu) + L(\tau,\mu) = \frac{\varpi}{2} \int_{-1}^{1} L(\tau,\mu')d\mu', \quad \tau \geq 0 \tag{10}$$

where

$$\varpi = \frac{b_b/a}{b_b/a + F}. \tag{11}$$

We also note that

$$\frac{\varpi}{1-\varpi} = \frac{b_b/a}{F}. \tag{12}$$

It is the parameter F that first must be obtained from either Hydrolight [21] calculations with known values of b_b/a or from experimental data in which both $r_{rs}(z_m)$ and b_b/a have been measured. Once obtained, the resulting F subsequently can be used in the algorithm for determining b_b/a for waters where no or limited IOP measurements are available. Notice that with this model the objective is to avoid the dependence on b by having the scattering depend instead on b_b, which is consistent with the quasi-single-scattering approximation [3, 4, 5].

3. Algorithm for backscattering-to-absorption ratio

The initial step in the derivation of the algorithm for b_b/a follows by combining Eq. (10) written for μ and for $-\mu$ in a way that the derivative with respect to τ can be eliminated [22]. This is done by first multiplying the equation for μ by $\mu L(\tau,-\mu)$ and the one written for $-\mu$ by $\mu L(\tau,\mu)$, integrating both equations over $-1 \le \mu \le 1$, and subtracting the results to obtain

$$\frac{\mathrm{d}}{\mathrm{d}\tau}\int_{-1}^{1}\mu^2 L(\tau,\mu)L(\tau,-\mu)\mathrm{d}\mu = -\varpi\int_{-1}^{1}\mu L(\tau,\mu)\mathrm{d}\mu\int_{-1}^{1}L(\tau,\mu')\mathrm{d}\mu'. \tag{13}$$

To simplify this equation, multiply Eq. (10) by μ, integrate over $-1 \le \mu \le 1$, and rearrange the result to obtain the so-called diffusion equation,

$$\int_{-1}^{1}L(\tau,\mu)\mathrm{d}\mu = -(1-\varpi)^{-1}\frac{\mathrm{d}}{\mathrm{d}\tau}\int_{-1}^{1}\mu L(\tau,\mu)\mathrm{d}\mu. \tag{14}$$

Substitution of this result into Eq. (13) gives

$$\frac{\mathrm{d}G(\tau)}{\mathrm{d}\tau} = \frac{\mathrm{d}}{\mathrm{d}\tau}\left[4\int_0^1\mu^2 L(\tau,\mu)L(\tau,-\mu)\mathrm{d}\mu - \frac{\varpi}{1-\varpi}\left(\int_{-1}^{1}\mu L(\tau,\mu)\mathrm{d}\mu\right)^2\right] = 0. \tag{15}$$

Integration of $\mathrm{d}G(\tau)/\mathrm{d}\tau$ over τ from an arbitrary measurement depth τ_m or z_m to infinity, where the light field vanishes, allows us to write

$$\frac{\varpi}{1-\varpi}\left[\int_{-1}^{1}\mu L(z_m,\mu)\mathrm{d}\mu\right]^2 = 4\int_0^1\mu^2 L(z_m,\mu)L(z_m,-\mu)\mathrm{d}\mu. \tag{16}$$

After division by $[E_d(z_m)/2\pi]^2$ and with Eqs. (5) and (12), Eq. (16) can be written as

$$\frac{b_b/a}{F}\left[1-2\pi\int_0^1\frac{\mu L(z_m,-\mu)}{E_d(z_m)}\mathrm{d}\mu\right]^2 = 16\pi^2\int_0^1\frac{\mu L(z_m,\mu)}{E_d(z_m)}\frac{\mu L(z_m,-\mu)}{E_d(z_m)}\mathrm{d}\mu. \tag{17}$$

The integrals in Eq. (17) involve radiance data that are not available because $L(z_m,\mu)$ is not measured, so we introduce two new radiometric functions

$$\Lambda(z_m) = 2\pi\int_0^1\mu\frac{L(z_m,-\mu)}{L_u(z_m)}\mathrm{d}\mu = \frac{E_u(z_m)}{L_u(z_m)}, \tag{18}$$

$$\Omega(z_m) = 16\pi^2\int_0^1\mu^2\frac{L(z_m,\mu)}{E_d(z_m)}\frac{L(z_m,-\mu)}{L_u(z_m)}\mathrm{d}\mu, \tag{19}$$

where the upward planar irradiance is

$$E_u(z_m) = 2\pi \int_0^1 \mu L(z_m, -\mu) \mathrm{d}\mu. \tag{20}$$

With the help of Eqs. (5), (6), (18) and (19), Eq. (17) then can be written in terms of the measured $r_{rs}(z_m)$ value as

$$\frac{b_b/a}{F} = \frac{\Omega(z_m) r_{rs}(z_m)}{[1 - \Lambda(z_m) r_{rs}(z_m)]^2} \ . \tag{21}$$

Equations (18) and (19) can be evaluated by invoking the second assumption for the algorithm that the measurements are made at any *asymptotic* depth z_{as}. With the approximation of $L(z_{as}, \mu)$ to evaluate $\Omega(z_m)$ and $\Lambda(z_m)$, from Eq. (21) the final form for the b_b/a algorithm is

$$\frac{b_b/a}{F} = \frac{\Omega(z_{as}) r_{rs}(z_m)}{[1 - \Lambda(z_{as}) r_{rs}(z_m)]^2} \tag{22}$$

where

$$\Lambda(z_{as}) = 2\pi \int_0^1 \mu \frac{L(z_{as}, -\mu)}{L_u(z_{as})} \mathrm{d}\mu = \frac{E_u(z_{as})}{L_u(z_{as})} \tag{23}$$

$$\Omega(z_{as}) = \frac{16\pi^2 \int_0^1 \mu^2 L(z_{as}, \mu) L(z_{as}, -\mu) \mathrm{d}\mu}{E_d(z_{as}) L_u(z_{as})}. \tag{24}$$

To evaluate $L(z_{as}, \mu)$ in Eqs. (23) and (24), an analytic representation can be used for the radiance at depths where it is asymptotic. The eigenmode expansion method [23, 24] shows that the asymptotic radiance far from the surface or bottom consists of only the dominant eigenmode [25] corresponding to the dominant eigenvalue ν_0,

$$L(\tau_{as}, \mu) = A(\nu_0) \phi(\nu_0, \mu) \exp(-\tau_{as}/\nu_0), \quad -1 \le \mu \le 1, \tag{25}$$

or, from Eq. (9),

$$L(z_{as}, \mu) = A(\nu_0) \phi(\nu_0, \mu) \exp\{-[1 + b_b/(aF)] a z_{as}/\nu_0\}, \quad -1 \le \mu \le 1. \tag{26}$$

(The $A(\nu_0)$ is a constant that depends on the surface illumination.) Substitution of Eq. (25) into Eq. (10) gives

$$(1 - \mu/\nu_0) \phi(\nu_0, \mu) = (\varpi/2) \int_{-1}^1 \phi(\nu_0, \mu') \mathrm{d}\mu'. \tag{27}$$

Because this equation is homogeneous and the dominant eigenvalue satisfies $1 < \nu_0 \leq \infty$, the eigenfunction $\phi(\nu_0, \mu)$ can be normalized with

$$\int_{-1}^{1} \phi(\nu_0, \mu) \mathrm{d}\mu = 1 \tag{28}$$

so from Eqs. (27) and (28),

$$\phi(\nu_0, \mu) = \frac{\varpi \nu_0 / 2}{\nu_0 - \mu}, \quad -1 \leq \mu \leq 1. \tag{29}$$

Substitution of Eq. (29) into Eq. (28) gives the eigenvalue ν_0 as the positive root of the transcendental equation

$$1 - \frac{\varpi \nu_0}{2} \ln\left(\frac{\nu_0 + 1}{\nu_0 - 1}\right) = 0. \tag{30}$$

From Eq. (11) it follows that ϖ depends on F, so ν_0 determined from Eq. (30) also does. Another very useful equation from the eigenfunction method is obtained by integrating Eq. (27) over $-1 \leq \mu \leq 1$ to obtain, after use of Eqs. (11) and (28),

$$\int_{-1}^{1} \mu \phi(\nu_0, \mu) \mathrm{d}\mu = \nu_0 (1 - \varpi) = \nu_0 [1 + b_b/(aF)]^{-1}. \tag{31}$$

With $L(z_{as}, \mu)$ from Eqs. (26) and (29) it follows from Eq. (18) that

$$\begin{aligned} \Lambda(z_{as}) &= 2\pi(\nu_0 + 1) \int_0^1 \mu (\nu_0 + \mu)^{-1} \mathrm{d}\mu \\ &= 2\pi(\nu_0 + 1) \left[1 - \nu_0 \ln\left(\frac{\nu_0 + 1}{\nu_0}\right)\right]. \end{aligned} \tag{32}$$

In a similar way it follows from Eq. (19) that

$$\begin{aligned} \Omega(z_{as}) &= \frac{16\pi^2(\nu_0 + 1) \int_0^1 \mu^2 (\nu_0^2 - \mu^2)^{-1} \mathrm{d}\mu}{\int_0^1 \mu (\nu_0 - \mu)^{-1} \mathrm{d}\mu} \\ &= 8\pi^2(\nu_0 + 1) \left[-1 + \nu_0 \ln\left(\frac{\nu_0}{\nu_0 - 1}\right)\right]^{-1} \int_{-1}^{1} \mu (\nu_0 - \mu)^{-1} \mathrm{d}\mu \\ &= \frac{F}{b_b/a} 16\pi^2(\nu_0 + 1) \left[-1 + \nu_0 \ln\left(\frac{\nu_0}{\nu_0 - 1}\right)\right]^{-1}, \end{aligned} \tag{33}$$

where Eqs. (12) and (31) have been used.

To summarize, for a specified value of b_b/a, F must be determined consistent with Eqs. (11), (22), (30), (32), and (33).

4. Algorithm for absorption and backscattering coefficients

The algorithm for determining the absorption coefficient a ultimately follows from the Gershun equation

$$a = K_E(z_m)\overline{\mu}(z_m), \tag{34}$$

where the diffuse attenuation coefficient and mean cosine of the radiance are

$$K_E(z_m) = -\mathrm{d}\left[\ln\int_{-1}^{1}\mu L(z_m,\mu)\mathrm{d}\mu\right]/\mathrm{d}z_m = -\mathrm{d}\{\ln[E_d(z_m)-E_u(z_m)]\}/\mathrm{d}z_m \tag{35}$$

$$\overline{\mu}(z_m) = \left[\int_{-1}^{1}\mu L(z_m,\mu)\mathrm{d}\mu\right]/\left[\int_{-1}^{1}L(z_m,\mu)\mathrm{d}\mu\right]. \tag{36}$$

Because $K_d(z_m)$ is measured instead of $K_E(z_m)$, it is again necessary to invoke the assumption that measurements are made at depths $z_m \rightarrow z_{as}$ where $K_E(z_{as}) = K_d(z_{as})$. Thus an algorithm for determining a can be obtained from

$$a = \widehat{K}_d(z_{as})\overline{\mu}(z_{as}), \tag{37}$$

where $\widehat{K}_d(z_{as})$, an estimate of the diffuse attenuation coefficient, follows from Eq. (35) as

$$\widehat{K}_d(z_{as}) \approx \frac{\Delta[\ln E_d(z_{as})]}{\Delta z_{as}}. \tag{38}$$

Alternatively, from values of $K_d(z_n)$, $n = 1$ to 3, where the depths z_n are such that the radiance is approaching the asymptotic regime, an estimate of $\widehat{K}_d(z_{as})$ can be obtained from [6, 26]

$$\widehat{K}_d(z_{as}) = \frac{K_d(z_1)K_d(z_3)-[K_d(z_2)]^2}{K_d(z_1)+K_d(z_3)-2K_d(z_2)} \tag{39}$$

provided $z_2 = 2^{-1}(z_1+z_3)$.

To estimate $\overline{\mu}(z_{as})$ in order to obtain the absorption coefficient from Eq. (37), it follows from Eqs. (26), (28), and (31) that

$$\overline{\mu}(z_{as}) = \left[\int_{-1}^{1}\mu\phi(\nu_0,\mu)\mathrm{d}\mu\right]/\left[\int_{-1}^{1}\phi(\nu_0,\mu)\mathrm{d}\mu\right] = \nu_0[1+(b_b/(aF)]^{-1}. \tag{40}$$

Thus, the algorithm for determining the absorption coefficient from Eq. (37) then becomes

$$a = \widehat{K}_d(z_{as})\nu_0[1+(b_b/(aF)]^{-1}, \tag{41}$$

where b_b/a has been obtained from Eq. (22) and used, along with the previously determined F, to compute the ν_0.

A second approach for determining the absorption coefficient from knowledge of b_b/a and F is to take the ratio of measurements in the asymptotic regime at two locations z_1 and z_2 and to use

$$L(z_{as},-1) = L_u(z_{as}) = A(\nu_0)\phi(\nu_0,-1)\exp[-az_{as}[1+b_b/(aF)]/\nu_0]. \tag{42}$$

For z_1 and z_2 in the asymptotic radiance regime this leads to the approximation

$$a = \frac{\nu_0}{(z_2-z_1)[1+b_b/(aF)]}\ln\left[\frac{L_u(z_1)}{L_u(z_2)}\right]. \tag{43}$$

Because of the small magnitude of $L_u(z_{as})$, however, this algorithm is expected to be prone to numerical difficulties. Another possibility, of course, is if b_b is measured or can be estimated at the wavelengths of interest, then a can be directly estimated from b_b/a as

$$a = \frac{b_{b,meas}}{b_b/a}. \tag{44}$$

Finally, the estimated values of b_b/a from Eq. (22) and a from Eq. (41) or (43) can be combined to give an estimated value of b_b from

$$b_b = (b_b/a)a. \tag{45}$$

5. Data and methods

5.1. Synthetic data sets

We assessed the ability of our extended delta-Eddington model to estimate the scattering phase function using synthetic data. Radiometric quantities L_u and E_d were simulated at 490 nm using a simple Case 1 chlorophyll-based bio-optical model embedded in Hydrolight [21] to generate inherent optical properties. Simulations were performed using chlorophyll concentrations *Chl* (0.01, 0.03, 0.1, 0.3, 1, 3, 10 mg m^{-3}) and three zenith angles ($15^\circ, 30^\circ, 60^\circ$), yielding 7x3 =

21 total simulations. While simulation output was requested every 5 m from 0 m to 50 m, radiometric data for three output depths (5, 10, 30 m) from each simulation was included in this synthetic data set, resulting in 63 simulated data points.

One synthetic data set was created allowing Hydrolight to select a Fournier-Forand scattering phase function $\tilde{\beta}_{\mathrm{FF}}$ [27] based on a specified particle backscattering ratio $\tilde{b}_{bp} = b_{bp}/b_p$, which resulted in a distinct scattering phase function selection for each chlorophyll concentration. To assess the ability of our algorithm to retrieve b_b/a in the absence of measurement noise and natural variability, the entire first synthetic data set was used both as a *training set* to determine the fitted parameter F and also as a *validation set* to compare values of b_b/a generated by the Case 1 bio-optical model to those estimated from corresponding simulated values of $r_{rs} = L_u/E_d$.

A second, somewhat independent, synthetic validation set was created using the same cross product of chlorophyll concentrations, depths, and zenith angles, but using a single Petzold scattering phase function $\tilde{\beta}_{\mathrm{P}}$ [28] for all simulations of radiometric quantities. This second synthetic data set was used solely as a validation set to test the sensitivity of our algorithm's estimates of b_b/a to any assumed phase function effects in the parameter F fitted using the first training set.

5.2. NAB08 data set

We also tested our algorithm's performance using depth profiles of $L_u(z)$, $E_d(z)$, $a(z)$, and $b_b(z)$ from a calibration campaign carried out as part of the 2008 North Atlantic Bloom Experiment (NAB08) in support of long term (51 d) autonomous physical, optical, and radiometric measurements from a Lagrangian float [29]. The data were obtained at eight process cruise stations during the spring bloom of May 2008, representing two distinct phytoplankton bloom communities: a large diatom-dominated community ($Chl \sim 2-5$ mg m^{-3}) during the bloom

and mixed ciliate/picoeukaryote community ($Chl < 1$ mg m^{-3}) following the bloom peak.

5.2.1. NAB08 data collection and processing

Temperature, salinity, pressure (CTD), and bio-optical profiles to approximately 80 m depth were performed during a cruise on the R/V Knorr from 1-22 May 2008. A Satlantic free-falling optical profiler was used to measure downward spectral irradiance, $E_d(z,\lambda)$, and upward spectral radiance, $L_u(z,\lambda)$ at 3.3 nm increments from 350 to 800 nm with a spectral accuracy of 0.3 nm and a spectral resolution of 10 nm. Profiles were taken within 1.5 h of local noon. Radiometric data was processed using 1 m bins with ProSoft 8-RC5 software (Satlantic, Inc.) to determine of $E_d(z,\lambda)$, $L_u(z,\lambda)$, and $K_d(z,\lambda)$.

In situ IOPs were obtained within 15 minutes of radiometric measurements. An AC-9 measured $a(z)$; a BB2F measured $b_b(z)$ at 470 and 700 nm (both WET Labs, Inc.); a Sea-Bird Electronics SBE25 CTD measured temperature, salinity, and pressure. The instruments were factory calibrated prior to field deployment. Manufacturer recommended protocols were used to track instrument calibration during the process cruise. Daily clean water calibrations were conducted whenever possible; however, sampling schedules did not consistently allow for daily calibration. Under these cases, the most recent water calibration was used. The maximum period without a calibration was three days. The drift during this study was negligible ($< 4\%$) and the precision of the AC-9 data was ± 0.01 m^{-1}, which corresponds to an average uncertainty of about 17% in the waters under consideration. Absorption data were subsequently corrected for temperature and salinity [30] and the absorption coefficient was corrected for scattering using the wavelength-dependent method [31]. Absorption and backscattering data were binned into 1 m intervals and then averaged within each bin. Backscattering at wavelengths other than those measured was estimated by fitting the particulate fraction b_{bp} using a power-law $b_{bp}(\lambda) = b_{bp}(\lambda_0)(\lambda_0/\lambda)^{\gamma}$ wavelength dependence [14]. Measured IOPs were typically homo-

geneous from 0 to 30 m (e.g., Fig. 1A). Some IOP profiles showed sharp changes deeper than 30 m, corresponding to the bottom of the mixed layer; outliers from these regions with different IOPs appeared as outliers in IOP estimates.

For each profile, radiometric and IOP data were sampled at eight depths (5, 10, 15, 20, 25, 30, 35, 40 m) at AC-9 wavelengths (412, 440, 488, 510, 532 and 555 nm). For wavelengths ≥ 555 nm we expect our algorithms to work poorly because our formulation of the radiative transfer equation (Eq. 1) does not include inelastic scattering [10, 17]. The 40 m depth was omitted for two profiles where radiometric measurements were below the noise level of the radiometer. Example contemporaneous radiometric and IOP profiles at 488 nm for a single station are shown in Fig. 1; $b_b(488)$ is estimated from $b_b(470)$ and $b_b(700)$ as described above and b_b/a is computed from $a(488)$ and the estimated $b_b(488)$.

When processing the measured data, no attempt was made to incorporate possible instrumentation inaccuracies. Radiometric measurements were discarded for $L_u(z) < 10^{-4}$ μW cm^{-2} sr^{-1} or $E_d(z) < 10^{-2}$ μW cm^{-2}.

5.2.2. Cross-validation approach

We used the NAB08 data set to both determine the fitted parameter F as well as test the algorithm. We were also interested in answering the question: "How many calibration profiles are needed to determine F for a specified accuracy?" To answer this question as fairly as possible, we employed a cross-validation approach [32] to estimate error in our predictions of IOPs from F, r_{rs} and $K_d(z_{as})$. Cross-validation is a resampling technique used to estimate how accurately a predictive model will perform in practice. Our cross-validation scheme iteratively partitions the $n = 8$ profiles into a *training set* used to determine the fitted parameter F and a *validation set* used to estimate the IOPs. A training set consists of a k-element subset of profiles, $k = 1 \ldots 7$, chosen from the set of eight profiles, resulting in $M_k = \binom{n}{k}$ possible training set combinations

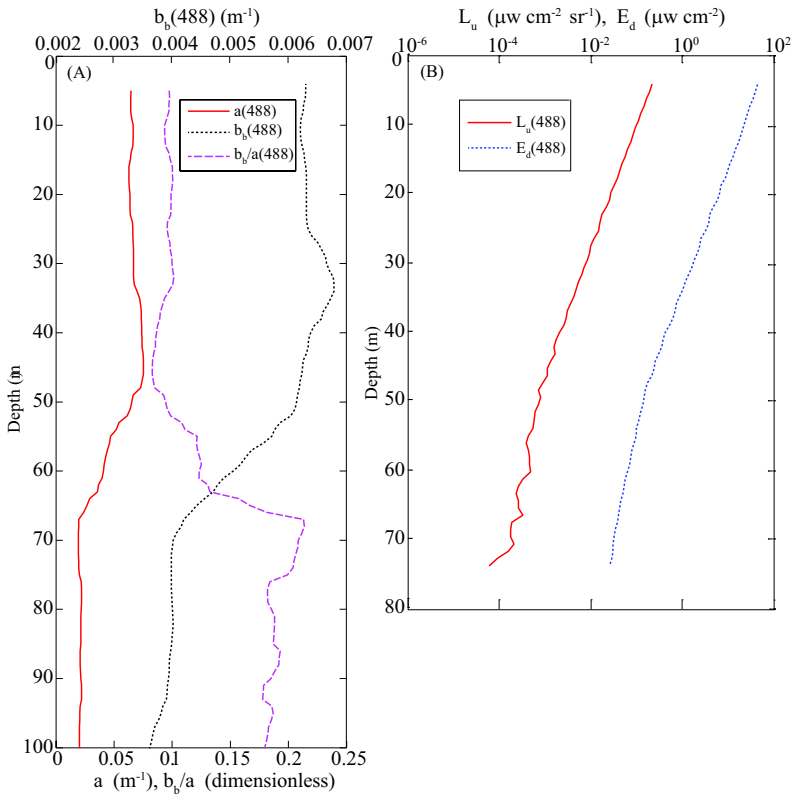

Fig. 1. An IOP and a radiometric profile from the NAB08 dataset. (A) Typical IOPs were nearly homogeneous in the lit portion of the water column. (B) Radiometric profiles of L_u and E_d at 488 nm show little curvature until 40 m, another indication of vertically homogeneous water.

for a given k. A validation set of profiles is simply the complementary set of profiles for any training set combination, assuring that training data is never used as validation data. Examples for profile numbers included for $k = 1,2$ are shown in Table 1.

Traditional cross-validation yields a nearly unbiased estimate of prediction error by removing one data point at a time from the data set used for prediction. A weakness of our approach is that the number of members of each set and the number of sets vary with each iteration k.

Table 1. Example training and validation sets of NAB08 calibration profiles for $k = 1, 2$ used for cross validation.

k	M_k	i	Training set	Validation set
1	8	1	1	2,3,4,5,6,7,8
		2	2	1,3,4,5,6,7,8
		3	3	1,2,4,5,6,7,8
		...	...	...
		8	8	1,2,3,4,5,6,7
2	28	1	1,2	3,4,5,6,7,8
		2	1,3	2,4,5,6,7,8
		3	2,3	1,4,5,6,7,8
		...	...	...
		28	7,8	1,2,3,4,5,6

5.3. Determination of fitted parameter F

For each training set, F was found using the contemporaneous values of $r_{rs} = L_u/E_d, b_b$, and a available from Hydrolight simulation or field measurement. The problem was solved as a system of three equations $\mathbf{G_F} = \mathbf{0}$ with three unknowns $\mathbf{X_F}$, where

$$\mathbf{X_F} = \begin{bmatrix} v_0 \\ b_b/a \\ F \end{bmatrix}. \tag{46}$$

A nonlinear least squares equation solver (function fsolve in MATLAB [33]) provides a solution $\mathbf{X_F}$ that minimizes the cost function $g_F = \mathbf{G_F}^{\mathrm{T}}\mathbf{G_F}$, where the first two elements of $\mathbf{G_F}$ correspond to Eqs. (22) and (30), and the final element provides the necessary third constraint

by matching the estimated and measured values of b_b/a:

$$\mathbf{G_F} = \begin{bmatrix} 1 - \frac{\varpi v_0}{2} \ln\left(\frac{v_0+1}{v_0-1}\right) \\ \frac{b_b/a}{F} - \frac{\Omega(z_{as}) r_{rs}(z_m)}{[1-\Lambda(z_{as}) r_{rs}(z_m)]^2} \\ (b_b/a) - (b_b/a)_{measured} \end{bmatrix}. \tag{47}$$

The required initial point for the solver, $\mathbf{X_F}^0$, was chosen as

$$\mathbf{X_F}^0 = \begin{bmatrix} 1.0005 \\ 0.2 \\ 0.2 \end{bmatrix}. \tag{48}$$

Finally, using the results for all the depths of given profile and wavelength, a simple linear least squares fit was made to estimate F as a linear function of b_b/a,

$$F(b_b/a) = p_1(b_b/a) + p_2. \tag{49}$$

5.4. Determination of b_b/a

The validation sets of profiles were used to test the algorithm. The linear equation Eq. (49) for the fitted parameter $F(b_b/a)$ determined from the training set and $r_{rs} = L_u/E_d$ computed from simulated or field radiometric data were used to estimate b_b/a. The contemporaneous measured or simulated values of b_b and a were reserved for subsequent error analysis (see section 5.5). Similar to the approach used to determine fitted parameter F in section 5.3, this problem was solved as a system of two equations $\mathbf{G} = \mathbf{0}$ and two unknowns $\mathbf{X}$, where

$$\mathbf{X} = \begin{bmatrix} v_0 \\ b_b/a \end{bmatrix}. \tag{50}$$

The same nonlinear least squares equation solver was used to minimize the cost function $g = \mathbf{G}^{\mathrm{T}}\mathbf{G}$, where the first two elements of $\mathbf{G}$ again correspond to Eqs. (22) and (30):

$$\mathbf{G} = \begin{bmatrix} 1 - \frac{\varpi v_0}{2} \ln\left(\frac{v_0+1}{v_0-1}\right) \\ \frac{b_b/a}{F} - \frac{\Omega(z_{as}) r_{rs}(z_m)}{[1-\Lambda(z_{as}) r_{rs}(z_m)]^2} \end{bmatrix}. \tag{51}$$

The required initial point for the solver, $\mathbf{X}^0$, was chosen as

$$\mathbf{X}^0 = \begin{bmatrix} 1.0005 \\ \\ 0.2 \end{bmatrix}. \tag{52}$$

5.5. Error analysis

Assessment of systematic biases and typical uncertainty between estimated IOPs and measured IOPs is made using relative percent difference ψ and its absolute value $|\psi|$, respectively. In the formulation of the relative percent differences, measured IOP data are considered the reference values, so for a paired estimate and measurement the relative error is

$$\psi_i(z_j) = 100\frac{IOP_{i,est}(z_j) - IOP_{i,meas}(z_j)}{IOP_{i,meas}(z_j)}, \tag{53}$$

where an IOP may be b_b/a, a, or b_b, $IOP_{i,est}(z_j)$ is an estimated value, and $IOP_{i,meas}(z_j)$ is the corresponding measured value for a given validation set $i = 1 \ldots M_k$ at depth z_j. Similarly, the average absolute percent difference is computed with $|\psi_i(z_j)|$. Outliers were excluded to prevent biased estimates by removing single $\psi_i(z_j)$ values exceeding the average plus or minus three times the standard deviation σ of the total number of values within each average.

The error analysis was carried out using the NAB08 radiometric and IOP profile data for the M_k validation sets complementing the M_k training sets used to determine fitting factor F. We summarize estimation of the errors in three ways for an implicitly denoted k:

1. Average absolute error $\overline{|\psi(z_j)|}$ of all M_k validation set combinations at each depth z_j

$$\overline{|\psi(z_j)|} = \frac{1}{M_k}\sum_{i=1}^{M_k} |\psi_i(z_j)| \tag{54}$$

   in order to explore our assumption of asymptotic radiance.

2. Depth-averaged absolute error $\overline{|\psi_i|}$ and relative error $\overline{\psi_i}$ for each validation set i

$$\overline{|\psi_i|} = \frac{1}{8}\sum_{j=1}^{8} |\psi_i(z_j)|, \tag{55a}$$

$$\overline{\psi_i} = \frac{1}{8}\sum_{j=1}^{8} \psi_i(z_j) \tag{55b}$$

with which to explore the variability of the M_k different validation set combinations, assuming a vertically homogeneous regime.

3. Average absolute error $|\psi|$ and average relative error ψ

$$\overline{|\psi|} = \frac{1}{8M_k}\sum_{i=1}^{M_k}\sum_{j=1}^{8} |\psi_i(z_j)|, \tag{56a}$$

$$\overline{\psi} = \frac{1}{8M_k}\sum_{i=1}^{M_k}\sum_{j=1}^{8} \psi_i(z_j) \tag{56b}$$

is used to explore the algorithm's average performance across all depths and validation set combinations.

For the two synthetic data sets, $\overline{\psi}$ and $\overline{|\psi|}$ were computed as averages of individual errors $\psi_i(z_j)$ and $|\psi_i(z_j)|$ in IOPs estimated from the 63 simulated data points.

6. Results

6.1. Synthetic data sets

The results for the first synthetic data set constructed using $\tilde{\beta}_{\mathrm{FF}}$ are shown in Table 2. For each value of chlorophyll concentration *Chl*, IOPs at 490 nm were generated. The parameter F was fitted for values of b_b/a using all the simulated radiometric and IOP data and was essentially constant, varying from 0.074 to 0.076 while b_b/a varied from 0.037 to 0.11. Using the simulated radiometric data to test our b_b/a algorithm, the average relative and absolute errors were found to be small, demonstrating that once the fitted parameter F was determined, recovery of the original data is possible to within $\sim$4%. This implies that the variation of $\tilde{\beta}_{\mathrm{FF}}$ due to changes in the backscattering ratio $\tilde{b}_{bp}$ was insignificant with respect to the phase function we assumed.

When we replaced the validation set by repeating the simulation except for a change from $\tilde{\beta}_{\mathrm{FF}}$ to $\tilde{\beta}_{\mathrm{P}}$ for all values of *Chl*, there was a greater error in the estimates of b_b/a (right half

Table 2. Average relative error $\overline{\psi}$ and absolute error $\overline{|\psi|}$ (in percent) for estimates of b_b/a from radiative transfer simulations at 490 nm. *Chl* in mg m^{-3}. Parenthetical values indicate the range of $\overline{|\psi|}$ over all depths.

	Fournier-Forand $\tilde{\beta}_{\mathrm{FF}}$ selected by $\tilde{b}_{bp}$			Petzold $\tilde{\beta}_{\mathrm{P}}$		
Chl	$\tilde{b}_{bp}$	$\overline{\psi}$	$\overline{\|\psi\|}$	$\tilde{b}_{bp}$	$\overline{\psi}$	$\overline{\|\psi\|}$
0.01	0.0965	0.84	0.84 (0.13 - 1.3)	0.0183	3.0	3.02 (1.6 - 4.0)
0.03	0.0596	-0.20	0.26 (0.12 - 0.49)	0.0183	0.88	0.88 (0.23 - 1.3)
0.10	0.0353	-0.38	0.74 (0.21 - 1.3)	0.0183	-0.49	0.77 (0.16 - 1.6)
0.30	0.0225	0.24	0.99 (0.13 - 1.9)	0.0183	-0.03	1.13 (0.03 - 2.0)
1.00	0.0142	1.00	1.44 (0.03 - 3.2)	0.0183	1.7	1.96 (0.15 - 3.9)
3.00	0.0096	0.97	1.40 (0.19 - 3.5)	0.0183	3.2	3.24 (0.89 - 5.3)
10.00	0.0065	0.01	0.73 (0.01 - 2.8)	0.0183	4.2	4.23 (3.1 - 5.5)

of Table 2). As one might expect, the smallest errors corresponded to $Chl = 0.10$ to 1.0 mg m^{-3} where $\tilde{b}_{bp}$ was closest in both data sets. This is because F has been "tuned" to the set of Fournier-Forand scattering phase functions used in the first data set. The Petzold data set represents a different bio-optical regime determined by a different scattering phase function; we should not expect F tuned to one bio-optical regime to do as well in another.

6.2. NAB08 data set

For the field data at 488 nm, Fig. 2A shows the evolution of the fitted parameter F as the number of training profiles k increases. The slope and intercept of $F(488)$ show convergence towards stable mean values, as one would expect as more of the data set is used to determine F; more of the natural variability of b_b/a is captured as additional profiles cover the experimental area and duration of the bloom. A linear model of $F(b_b/a)$ as in Eq. (49), using data for all $k = 6$ training set combinations at each wavelength, demonstrates the wavelength dependence of F

beyond 488 nm (Fig. 2B, Table 3).

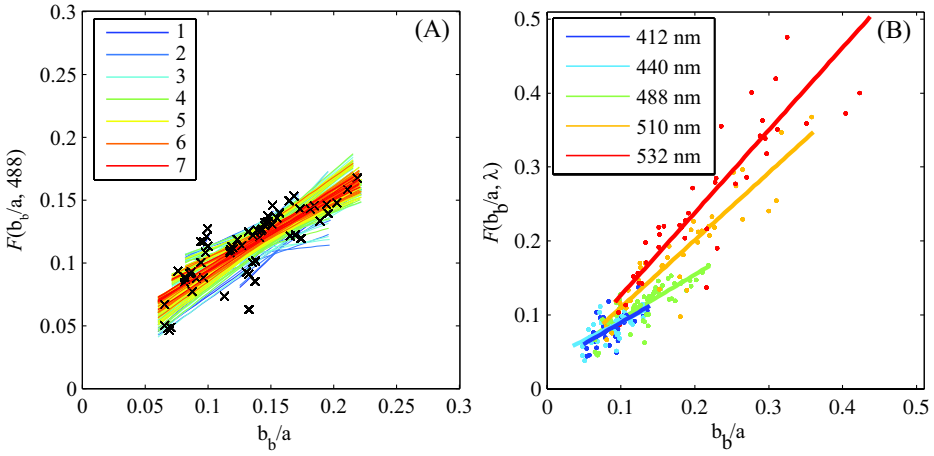

Fig. 2. Estimates of F using $r_{rs} = L_u/E_d$ and IOP measurements from the NAB08 dataset. A) Values of fitted parameter F at 488 nm for all training set combinations (black x's) and the linear fit for each value of k. Color indicates number of profiles k used in the training set. (B) fitted parameter F at selected wavelengths (color), created by linear fit for all k = 6 training set combinations.

Figure 3 shows the evolution of the estimates of b_b/a and average retrieval errors at 488 nm for $k = 1 \ldots 7$. As the number of training profiles increases, estimated values of b_b/a converge toward their measured values (Fig. 3A, Table 4) with a corresponding decrease in average absolute error $\overline{|\psi|}$ (Fig. 3B, Table 4). For b_b/a, the average retrieval error $\overline{|\psi|}$ for $k \geq 4$ is approximately $\pm 20\%$, with some retrieval errors $\overline{|\psi_i|}$ as high as 100%. The range of relative error $\overline{\psi_i}$ for each validation set combination i remains large across all values of k, but the relative errors show little bias when averaged as $\overline{\psi}$ (Fig. 3C, Table 5). As expected, we can conclude that taking multiple measurements within a vertically homogeneous water column will reduce the average absolute error in the IOP estimates.

The average absolute error at each depth $\overline{|\psi(z_j)|}$ is shown in Fig. 3D and decreases markedly after 25 m; this depth represents 3-5 optical depths for most profiles. This indicates that the

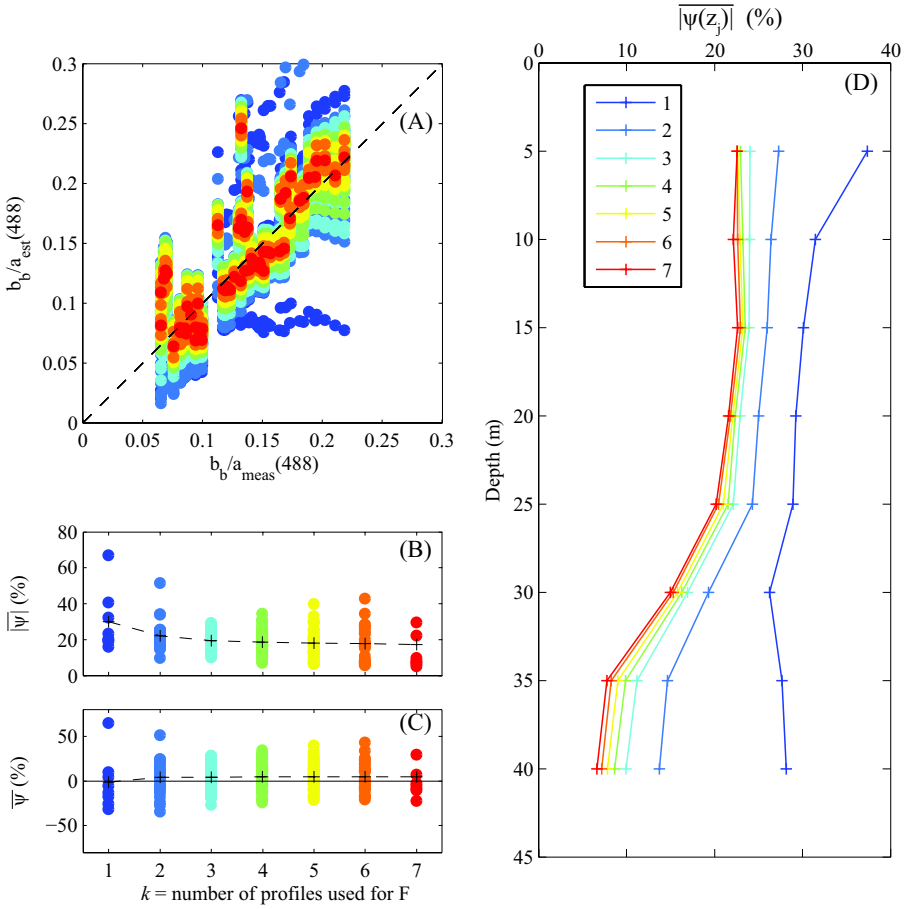

Fig. 3. (A) Matchups of estimated and measured b_b/a values show convergence towards 1:1 line (black dashed line) as k increases; each colored dot represents a single matchup. (B) Depth-averaged absolute error for each validation set ($\overline{|\psi_i|}$, colored dots) remains variable irrespective of the number of profiles k used to determine F. The overall average absolute error $\overline{|\psi|}$ for the algorithm (black dashed line) decreases most from k = 1 to 4. (C) Similarly, relative error depth-averaged for each validation set ($\overline{\psi_i}$, colored dots) shows variability but little average bias $\overline{\psi}$ (black dashed line). (D) Absolute error averaged across all validation set combinations at each depth $\overline{|\psi(z_j)|}$ decreases markedly in deep water.

Table 3. Slope, intercept and R^2 for fitted parameter $F = p_1(b_b/a) + p_2$ for AC-9 wavelengths ≤ 532 nm with a linear least squares fit using all $k = 6$ training set combinations.

λ (nm)	p_1	p_2	R^2
412	0.582	0.0313	0.69
440	0.496	0.0407	0.70
488	0.598	0.0348	0.68
510	0.911	0.0190	0.84
532	1.12	0.0145	0.82

radiance from 0-25 m is not necessarily in an asymptotic regime and a solution to the radiative transfer equation governed by the dominant eigenvalue ν_0 (Eq. 25) is therefore approximate. As the asymptotic regime is reached and its concomitant assumptions are satisfied, the average absolute error is less than 10% for $k \geq 4$. While these field results indicate that measurable radiance and irradiance data are available within the asymptotic regime, previous studies indicate that asymptotic optical depths vary with IOPs and the angular distribution of the surface illumination [3, 12, 13]. Therefore, a significant contributer to the variability in average absolute error $\overline{|\psi|}$ can be the failure to achieve an asymptotic light field in some surface illumination conditions; this is a limitation of our approach.

The estimates of absorption at 488 nm and average retrieval errors are shown in Fig. 4 for two different algorithms: (1) absorption $a_{K_d}(488)$ estimated from F, b_b/a, ν_0, and $K_d(z_{as})$ using Eq (41) (Fig. 4A-C) and (2) absorption $a_{est}(488)$ estimated from b_b/a and measurements of $b_b(470)$ and $b_b(700)$ using Eq. (44) and the bio-optical model to estimate $b_b(488)$ (Fig. 4D-E). As we saw with estimates of b_b/a, both absorption estimates improve as k increases, based on improved F and b_b/a estimates. The absorption estimate $a_{K_d}(488)$ (Fig. 4A-C) requires the estimation of the asymptotic quantity $K_d(z_{as})$ from E_d data; estimates of $K_d(z_{as})$ from radio-

metric profile samples below 25 m assured that we were close to the asymptotic regime, but in some cases IOPs changed below 30 m that challenge this assumption. Applying standard error propagation techniques, we can expect a 20% uncertainty in b_b/a and similar 20% uncertainty in $K_d(z_{as})$ to result in ~30% uncertainty in a_{K_d}; this is close to the average absolute error $\overline{|\psi|}$ shown in Fig. 4B for $k \geq 4$. The use of measured values of backscattering improve the estimation of $a(488)$ to a lower average absolute error $\overline{|\psi|}$ of 15% for $k \geq 4$. The improvements are most evident at lower values of absorption.

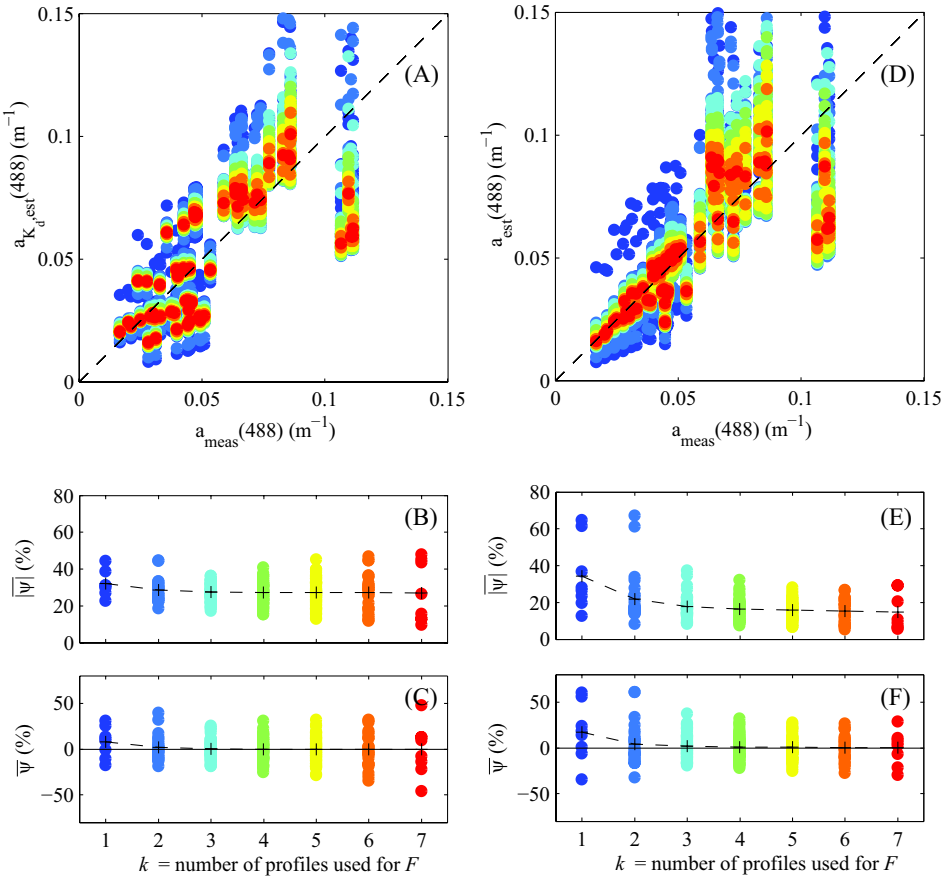

Fig. 4. Values of absorption a (A) and average error (B-C) at 488 nm, estimated from F, b_b/a, ν_0, and $K_d(z_{as})$, using Eq. (41), and (D-F) estimated from b_b/a and measurements of $b_b(470)$ and $b_b(700)$ using Eq. (44). Colors indicate the number of profiles k used to determine the value of F; remaining profiles are used to estimate b_b/a, $K_d(z_{as})$ and a.

Finally, estimates of backscattering at 488 nm are shown in Fig. 5. While the average absolute error is ∼20% (Fig. 5B), large individual errors can be seen in groups of matchups (Fig. 5A). Large overestimates in $b_b(488)$ are the result of overestimates in both b_b/a and a_{K_d}; these cases are found in profiles taken near the bloom peak where both higher values of absorption and backscattering were common.

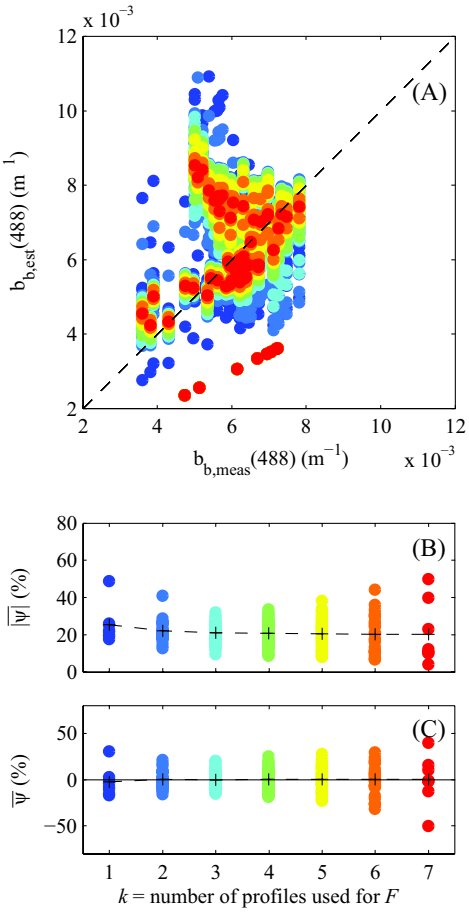

Fig. 5. Values of backscattering b_b (A) and average error (B) and (C) at 488 nm, estimated from b_b/a, F, and $K_d(z_{as})$. Colors indicate the number of profiles k used to determine the value of F; remaining profiles are used to estimate b_b/a, $K_d(z_{as})$ and a.

The estimates of average error for any given validation set $\overline{|\psi_i|}$ are roughly twice that of the average for all validation sets $\overline{|\psi|}$. For example, the estimate of absorption $a(488)$ has an

average uncertainty of $\overline{|\psi|} = 15 - 16\%$ for $k \geq 4$ (Table 5), with uncertainty for individual validation sets $\overline{|\psi_i|}$ exhibiting as much as 36% error (Fig. 4B). This information can be used to create a subspace of absorption values ranging from $0.64\overline{a}$ to $1.36\overline{a}$, where $\overline{a}$ represents the water column average absorption estimate. This water column average could be used as a starting point and the subspace values as bound constraints for a more sophisticated multi-parameter nonlinear inversion algorithm [11].

The validation results for other wavelengths below 555 nm are consistent with those at 488 nm (Tables 4, 5, 6): (1) little or no average bias $\overline{\psi}$ is evident in relative errors; (2) the average absolute error $\overline{|\psi|}$ in IOP estimates decreases as k increases, i.e., as more training profiles are used to estimate the fitted parameter F; (3) while parameterization of F as a function of b_b/a (Eq. 49) varies with wavelength (Fig. 2B), there is no discernible wavelength trend in IOP errors for wavelengths less than 555 nm; and (4) retrievals of absorption a nearly always improve when measurements of b_b are available, even when a bio-optical model is used to estimate $b_b(\lambda)$ at wavelengths other than the measurement wavelengths (470 and 700 nm) (Table 5).

The 555 nm retrieval of b_b/a is poor even when most of the profiles are used as training data (Table 4). This is due to Raman scattering which our algorithm does not incorporate. The slope of fitted parameter F (Eq. 49) does vary with wavelength (Fig. 2, Table 3). At wavelengths below 555 nm, we suspect F can help compensate for some Raman scattering at these wavelengths, while at 555 nm our assumption of no inelastic scattering in the formulation of the radiative transfer equation (Eq. 1) breaks down.

7. Discussion

We have developed a simple analytical algorithm that, when tuned using contemporaneous IOP and radiometric measurements, produces an IOP subspace defined by a mean IOP estimate and its associated uncertainty. Following the suggestion of Defoin-Platel and Chami [34],

Table 4. Relative and absolute error (in percent) for estimates of b_b/a using different numbers of profiles k in the training set for fitted parameter F

	$\overline{\psi}$			$\overline{\lvert\psi\rvert}$		
k	2	4	6	2	4	6
λ (nm)						
412	8.0	6.7	4.4	26	20	17
440	17	6.0	2.8	36	21	17
488	4.0	4.5	3.3	22	19	17
510	15	2.7	3.0	30	16	15
532	5.6	3.2	3.2	19	15	14
555	-5.3	5.4	-29	51	50	29

the resulting IOP subspace can be used as a divide and conquer strategy to reduce or eliminate ambiguities of IOPs estimated from a wider set of radiometric measurements in the same waters where IOP measurements are limited or not available. For example, the predicted IOP subspace can be used to constrain a more sophisticated inversion algorithm that incorporates, for example, models of Raman scattering and chlorophyll fluorescence and/or more accurate scattering phase functions as well as computationally efficient radiative transfer models (e.g., Ecolight-S [35]) that do not require the assumptions of an asymptotic light regime employed in the algorithms presented here.

Our single-parameter b_b/a algorithm converges quickly and reliably; no Monte Carlo simulations [36] or iterative solutions with forward problem solvers [3, 37] are required. The algorithm works best when light field measurements are made in the asymptotic regime and the parameter F is tuned to the local environment (Fig. 3). With simulations, we have shown that the b_b/a algorithm's performance degrades as the scattering phase function of the radiometric measure-

Table 5. Relative and absolute error (in percent) for estimates of a using Eqs. (41) and (44) using different numbers of profiles k in the training set for fitted parameter F

	$a_{K_d} = f(F, b_b/a, \nu_0, K_d(z_{as}))(m^{-1})$						$a = (b_b/a)b_{b,meas}(m^{-1})$					
	$\overline{\psi}$			$\overline{\lvert\psi\rvert}$			$\overline{\psi}$			$\overline{\lvert\psi\rvert}$		
k	2	4	6	2	4	6	2	4	6	2	4	6
λ (nm)												
412	-8.1	0.2	-0.1	42	18	17	6.2	-0.1	-0.7	30	19	17
440	0.7	-1.1	-1.4	22	20	19	4.5	0.8	-0.5	24	18	17
488	1.7	0.1	-0.3	29	27	27	4.3	0.9	-0.4	22	16	15
510	3.2	-1.5	-1.9	25	18	18	4.1	1.3	-0.7	26	15	14
532	0.3	0.5	0.4	23	20	20	0.3	0.3	-0.1	24	14	13

ments deviates from that used to generate the data (Table 2). Consistent with these results, we found that applying the parameterization of F developed for our synthetic data produced very poor estimates when applied to the NAB08 field data set. For the NAB08 calibration campaign, numerous radiometric and IOP profiles were available that adequately spanned the variability of waters. Estimating F directly from this calibration campaign data (Fig. 2) effectively tunes our simple scattering phase function $\tilde{\beta}$ (Eq. 7) to the North Atlantic waters under study. While we did not develop an algorithm to directly estimate the number of profiles k required for such a calibration campaign, the results presented here using the bio-optical data set (eight calibration profiles) from the NAB08 process cruise can be used as a guide.

If simple IOP measurements (e.g., $b_b(470)$ and $b_b(700)$) can be made at the time of radiometric measurements, we can improve the mean absorption estimate and decrease its overall uncertainty, further reducing potential ambiguity and increasing the performance of more computationally intensive IOP estimation approaches that benefit from reduced bound constraints.

Table 6. Relative and absolute error (in percent) for estimates of b_b using different numbers of profiles k in the training set for fitted parameter F

	$\overline{\psi}$			$\overline{\lvert\psi\rvert}$		
k	2	4	6	2	4	6
λ (nm)						
412	9.0	0.7	0.6	31	7.3	6.6
440	1.6	-1.8	-2.0	16	11	11
488	0.0	0.0	0.1	22	21	20
510	-29	0.9	0.9	53	16	16
532	3.0	1.8	1.7	17	17	17

This use of ancillary IOP data is an example of an "enrichment strategy" suggested by Defoin-Platel and Chami [34].

The results presented here do not account for instrument error. If there is an expected uncertainty of $\pm 17\%$ in backscattering [38] and $\pm 17\%$ in absorption, as mentioned previously, this results in a relative instrumental error of 34% in b_b/a, which is within the range of the average absolute errors shown in Table 4. Similarly, the resulting estimates for absorption and backscattering (Tables 5 and 6, respectively) are also comparable to the instrument error.

One might wonder, based on the assumptions introduced and the simplicity of the algorithm for b_b/a, why it works as well as it does. One interpretation is that the algorithm is a "bilinear inverse method" that weights the measured data for $r_{rs}(z_m)$ by the "importance" of the photons as given by the adjoint radiance $L^{\dagger}(z_m,\mu) \equiv L(z_m,-\mu)$ (e.g., Eq. 24) of the radiative transfer equation [39, 40]. Radiance, considered from the point of view of forward radiative transfer methods, conceptually traces every photon from the source to detector. Adjoint radiance can be visualized as tracing pseudo photons received by the detector backwards to the

source [41]; these pseudo photons provide insight to the importance of "how much a given position-direction matters for a given radiometric observation" [42].

As the ratio of two inherent optical properties (IOPs), b_b/a is itself an inherent optical property. Particulate backscattering b_{bp} has been shown to correlate to particulate organic carbon [38, 43, 44]; several bio-optical models relate chlorophyll concentration to particulate absorption [45, 46]. The ratio b_b/a might, therefore, be close to a proxy for a carbon-to-chlorophyll ratio [47], and thus be a diagnostic IOP for plankton community structure. Given the ease of estimating b_b/a from in-water measurements of L_u and E_d, this IOP deserves further investigation as a bio-optical proxy in the open ocean.

Acknowledgments

This work was supported by the National Science Foundation grants OCE0628379 and OCE0628107, and NASA grants NNX08AL92G and NNX-10AP29H. This work would not have been possible without the help of Emily Kallin, who assisted with the collection of all of the NAB08 bio-optical profile data used here and Mary Jane Perry and Emmanuel Boss who loaned their bio-optical and Satlantic radiometric profilers. We wish to thank Eric D'Asaro for statistical insight, Curtis Mobley for guidance with radiative transfer simulations, and the crew and technicians of the R.V. Knorr.

Chapter 3

Rehm, E., and C. D. Mobley (2012), Estimation of hyperspectral inherent optical properties from in-water radiometry: error analysis and application to in situ data, Accepted by *Applied Optics*, In revision.

Estimation of hyperspectral inherent optical properties from in-water radiometry: error analysis and application to *in situ* data

Eric Rehm[1,*] and Curtis D. Mobley[2]

[1]*Applied Physics Laboratory, University of Washington School of Oceanography,*

1013 NE 40th Street, Seattle, WA, 98105

[2]*Sequoia Scientific, Inc., 2700 Richards Road, Suite 107*

Bellevue, WA 98005

[*]*Corresponding author: erehm@earthlink.net*

An inverse algorithm is developed to retrieve hyperspectral absorption and backscattering coefficients from measurements of hyperspectral upwelling radiance and downwelling irradiance in vertically homogeneous waters. The forward model is the azimuthally-averaged radiative transfer equation, efficiently solved by the EcoLight radiative transfer model which includes the effects of inelastic scattering. Although this inversion problem is ill-posed (the solution is ambiguous for retrieval of total scattering coefficients), unique and stable solutions can be found for absorption and backscattering coefficients. The inversion uses the attenuation and backscattering coefficients at one wavelength to constrain the inversion, increasing the algorithm's stability and accuracy. Two complementary methods, Monte Carlo simulation and first-order error propagation, are used to develop uncertainty estimates for the retrieved absorption and backscattering coefficients. The algorithm is tested using both simulated light fields from a chlorophyll-based case I bio-optical model and radiometric field data from the 2008 North Atlantic Bloom Experiment. The influence of uncertainty in the radiometric quantities and

additional model parameters on the inverse solution for absorption and backscattering is studied using a Monte Carlo approach and an uncertainty budget is developed for retrievals. All of the required radiometric and IOP measurements can be made from power-limited autonomous platforms. We conclude that hyperspectral measurements of downwelling irradiance and upwelling radiance, with a single-wavelength measurement of attenuation, can be used to estimate hyperspectral absorption to an accuracy of ± 0.01 m^{-1} and hyperspectral backscattering to an accuracy of ± 0.0005 m^{-1} over wavelengths for which the contributions of inelastic scattering are small (350 to 575 nm).

OCIS codes: (010.0010) Atmospheric and ocean optics; (010.4450) Ocean optics; (010.7340) Water; (030.5620) Radiative transfer; (100.3190) Inverse problems; (160.4760) Optical properties; (280.0280) Remote sensing and sensors; (290.4210) Multiple scattering.

1. Introduction

Arrays of autonomous and Lagrangian sensors are being deployed in order to add a vertical dimension to the near -surface observations from satellite-based ocean color sensors [1]. As a result, methods for estimating inherent optical properties (IOPs) and other biogeochemically significant quantities from in-water radiometric measurements have gained renewed interest [2-5]. In addition to measurements of radiance and irradiance, measurements of chlorophyll fluorescence, backscattering, and beam attenuation are now possible from power-limited autonomous platforms [6-11]. Integrating contemporaneous measurements from multiple sensors enhances the type and quality of biogeochemical observations that can be achieved compared to single sensor measurements [3, 10, 12] and enhances validation of satellite-based ocean color products [5, 13, 14].

In the present study, we made hyperspectral radiometric measurements with the objective of subsequently assessing biologically relevant information about the natural phytoplankton community where the measurements are taken. For example, features of *in situ* absorption spectra resulting from photosynthetic and accessory pigments can be used to estimate ecologically relevant information about the phytoplankton community such as community composition [15], size structure [16] and photoadaptive status [17]. While deciphering the meaning of spectral variations in backscattering remains enigmatic [18, 19], increased spectral resolution of backscattering has recently confirmed a taxonomic relationship to algal cell size and cellular particular organic content [20]. Notably, hyperspectral measurements of backscattering are limited to those estimated from hyperspectral radiometry [21], and these estimates provide an opportunity for additional exploration.

The forward problem in hydrologic optics is defined by the radiative transfer equation (RTE): given measurements of in-water IOPs and boundary conditions at the sea surface and bottom, calculate the in-water light field (radiances and irradiances) [22]. The inverse problem estimates in-water IOPs given measurements of the in-water light field. Previous work shows that the inverse problem for IOPs can be solved by explicit (closed form) methods or implicit (iterative) methods [22-24]. Explicit methods manipulate the radiative transfer equation or approximate analytic solutions thereof to derive formulas that estimate IOPs from apparent optical properties (AOPs) such as reflectance and the diffuse attenuation coefficient of downwelling irradiance [25-31]. The explicit method is illustrated by the early work of Gordon et al. [32], who showed that reflectance is strongly correlated with the ratio of the backscattering to absorption coefficients, b_b/a. Explicit approaches essentially constrain solutions by virtue of the empirical relationships embedded within their semi-analytical models; these empirical relationships are developed based on regressions of numerous field measurements (e.g., [31]) or extensive forward modeling to cover the range of natural variability of interest (e.g., [26]). While errors in these relationships can be very carefully propagated through to IOP uncertainty estimates, (e.g., [33]), the statistical variability about the mean of these relationships [34] can limit their precision with respect to any single inversion. Garver and Siegel [35] developed a model-based inversion approach to retrieve IOPs from ocean color spectra. Uncertainty intervals were quantified for merged satellite ocean color products, resulting in a complete error budget that, as in the present study, characterizes sensor and forward model errors in order to develop statistically rigorous confidence intervals in the retrieved products, including IOPs [36, 37].

Implicit methods estimate IOPs by repeatedly solving the RTE, starting with an initial guess or an estimate based on *a priori* knowledge of the IOPs in the area of study. At each

iteration, radiometric measurements (or AOPs derived therefrom) are compared to the light field estimated by the RTE and an objective function is computed that expresses the difference between the estimated light field and the measured radiometric values. The IOPs are then modified to reduce the objective function. Iteration terminates when the objective function is reduced to an acceptably small value. Since no (or few) simplifying assumptions are made about the relationship between IOPs and the light field (or related AOPs), implicit methods can, in principle, be highly accurate. However, implicit methods incur the added computational cost of solving the RTE one or more times for each iteration. Some implicit approaches avoid the computational cost of solving the full RTE by employing simplifying assumptions, e.g., an asymptotic light field [31, 38]. Implicit approaches for which the resulting relation between IOPs and the estimated light field is exact (according to the RTE) are rare. Gordon and Boynton [39] have developed such an inverse algorithm where radiative transfer includes a coupled ocean-atmosphere model and a RTE solved by Monte Carlo methods. Their approach computes IOP estimates that reproduce AOP profiles that are consistent with the RTE to within experimental error. Their initial algorithm [31], addressing vertically homogenous waters, was subsequently extended to resolve vertical structure in IOPs [40]. An additional algorithmic update accommodates Raman scattering [41], although the algorithm was only tested with simulated data. Their approach was used to retrieve hyperspectral absorption and backscattering from oligotrophic Hawaiian waters as well as mesotrophic waters near San Diego, California, and validated using contemporaneous *in situ* measurements of multispectral absorption and backscattering [21]. Spurr et al. [42] have used a coupled atmosphere-ocean radiative transfer model (CAO-DISORT) to simultaneously retrieve atmospheric aerosol and ocean optical parameters using an optimization approach very similar to the one used in this study [43].

However, IOPs are not directly retrieved by their scheme; rather, they are parameterized using bio-optical models with assumed spectral shapes for phytoplankton and colored dissolved organic matter (CDOM) absorption as well as particulate backscattering. This explicit model has been used to successfully retrieve aerosol and ocean properties from ocean color satellite data [44] and produce a comprehensive error budget for retrievals [45].

An alternative to iterative implicit methods is a look-up table (LUT) approach: First, using the RTE, pre-compute a database of spectra representing radiometric quantities or AOPs (e.g., reflectance) based on a range of input values for IOPs and other pertinent parameters (e.g., bottom depths and reflectances, solar angles, and viewing directions) with numerous forward RTE simulations. Then, when presented with an observed spectrum, search the database for the best least squares spectral match and return the IOPs and other parameters that generated that spectrum. For this procedure, absolute radiometric calibration of radiometric sensors is required for the spectral matching scheme to be effective. This LUT approach was successfully used to extract IOPs and related environmental information from remotely sensed hyperspectral reflectance [46]; a small number of IOPs was used in database generation, based on a bio-optical model. This approach is ideally suited environmental classification problems where the objective is retrieval from a tractable set of alternatives. For general IOP retrieval, there is a combinatorial explosion in the size of the LUT as the desired IOP resolution increases, and database generation and search becomes computationally expensive. However, the LUT approach points to the value of using hyperspectral measurements: it was precisely the additional spectral information available in hyperspectral measurements that allowed the LUT algorithm to discriminate between the numerous combinations of IOPs and environmental parameters [47].

In this paper, we develop an implicit algorithm for estimating hyperspectral IOPs from in-water hyperspectral measurements of upwelling radiance $L_{\underline{u}}$ and downwelling plane irradiance E_d in a vertically well-mixed regime. The EcoLight radiative transfer software efficiently solves the forward radiative transfer problem [48]. As a result, there is an exact relationship between the retrieved IOPs and the estimated light field. We use an optimization approach that integrates contemporaneous measurements of chlorophyll fluorescence, backscattering b_b at one or two wavelengths and beam attenuation c at a single wavelength to constrain and stabilize the inversion (although only beam attenuation proves to matter). This combination of sensors matches both that of a ship-deployed optical package as well those mounted on an autonomous Lagrangian float as part of the 2008 North Atlantic Bloom Experiment (NAB08) [49]. We use the ship-based radiometric measurements that also include vertical profiles of IOPs for validation of our algorithm. The optimization procedure minimizes the least squares difference of log-transformed radiance and irradiance from numerous depths and returns a locally linear estimate of the RTE, allowing for propagation of uncertainty in radiometric measurements and other forward model parameters to the final estimates of IOPs. A core part of this study is the development of a detailed error analysis, including the effects of measurement errors, forward model parameter errors, and inversion noise, which extends previous oceanographic work [33, 36, 37, 50, 51]. We explore the uniqueness and stability of estimating IOPs from such a set of complementary radiometric and IOP measurements and test the general sensitivity of the IOP estimates to radiometric measurements. Finally, after fully understanding the retrieval algorithm, we apply our inversion and error analysis techniques to *in situ* data taken during the 2008 North Atlantic spring bloom.

2. Retrieval Methodology

In this work, we employ optimization techniques that require little *a priori* information about oceanic IOPs. While databases and large bio-optical data sets exist (WOOD [52], SeaBASS [53], NOMAD [54]), few data sets are available that provide useful priors for the data set used here, which represents a dynamical period of a spring phytoplankton bloom in the North Atlantic [55]. In addition, our approach does not require iterations other than those inherent in the optimization process and employs coincident IOP measurements as bound constraints (backscattering) or as forward model parameters (attenuation) that are supplied but not retrieved. With this approach, limited *a priori* information about forward model parameters is required to characterize uncertainty in the retrieved IOPs.

A. Additive Noise Model

1) Formulation: For each wavelength λ, radiance and irradiances are related to in-water IOPs, incident radiance and other model parameters via the radiative transfer equation through the following additive noise model [43]:

$$\mathbf{d} = \mathbf{G}(\mathbf{m}, \mathbf{b}) + \boldsymbol{\varepsilon} \tag{1}$$

where $\mathbf{d} \in \mathbb{R}^{2N}$ is a vector of radiance $L_u(z)$ and irradiance $E_d(z)$ calibrated measurements at depths $z_1, \ldots, z_N$ in the mixed layer

$$\begin{aligned} \mathbf{d} &= [d_1, \ldots, d_{2N}]^T \\ &= [L_u(z_1), \ldots, L_u(z_N), E_d(z_1), \ldots, E_d(z_N)]^T, \end{aligned} \tag{2}$$

$\mathbf{G}: \mathbb{R}^M \rightarrow \mathbb{R}^{2N}$ represents the radiative transfer equation for vertically homogeneous waters, and $\mathbf{m} \in \mathbb{R}^M$ represents the retrieval vector, i.e., the vertically homogeneous IOPs in the mixed layer to be estimated by the inversion algorithm

$$\begin{aligned} \mathbf{m} &= [m_1, m_2, m_3]^T \\ &= [a, b_b, b]^T. \end{aligned} \tag{3}$$

Absorption and scattering due to particles (phytoplankton, detritus) and colored dissolved organic matter (CDOM), a_{pg} and b_{pg} respectively, are derived from RTE solutions for the total absorption and scattering coefficients a and b by simply subtracting pure water absorption a_w and scattering b_w. Similarly particulate backscattering b_{bp} is derived from total backscattering by subtracting pure water backscattering b_{bw}:

$$\begin{aligned} a_{pg} &= a - a_w \\ b_{pg} &= b - b_w \\ b_{bp} &= b_b - b_{bw}. \end{aligned} \tag{4}$$

Vector **b** represents additional model parameters that influence the measurement but are not retrieved:

$$\begin{aligned} \mathbf{b} &= [b_1, \ldots, b_8]^T \\ &= [\tilde{\beta}(\theta', \theta, \lambda), a_w, b_w, E_s, \theta_s, cloud, U_{10}, Chl]^T. \end{aligned} \tag{5}$$

These additional model parameters include the scattering phase function $\tilde{\beta}$, pure water absorption a_w and scattering b_w, incident solar downwelling irradiance $E_s = E_d(0^+)$ onto the sea surface, solar zenith angle θ_s, cloud fraction *cloud* (which influences the incident radiance distribution), wind speed at 10 m U_{10} (which influences the transfer of radiance across the sea

surface), and chlorophyll concentration *Chl* (which is used to estimate chlorophyll fluorescence). Infinitely deep water is assumed; therefore no ocean bottom reflectance parameters are required. The noise term $\boldsymbol{\varepsilon} \in \mathbb{R}^{2N}$ represents radiometric error and is assumed to be zero-mean Gaussian noise with error covariance

$$\mathbf{S}_{\varepsilon} = E[\boldsymbol{\varepsilon}\boldsymbol{\varepsilon}'], \tag{6}$$

where $E[\cdot]$ is the expectation operator. The error covariance $\mathbf{S}_\varepsilon$ is operationally assumed to be diagonal with respect to depth, i.e., the error in radiance and irradiance at each depth are independent and identically distributed (i.i.d.) random variables.

2) Forward Model: The forward model **G** is the depth-dependent radiative transfer equation (RTE) for vertically homogenous waters

$$\begin{aligned} \cos\theta \frac{dL(z,\theta,\phi,\lambda)}{dz} &= -c(\lambda)L(z,\theta,\phi,\lambda) \\ &\quad + \int_0^{2\pi}\int_0^{\pi} \beta(\theta',\phi',\theta,\phi,\lambda)L(z,\theta',\phi',\lambda)\sin\theta' d\theta' d\phi' + S(z,\theta,\phi,\lambda). \end{aligned} \tag{7}$$

This equation can be solved for the full angular radiance distribution $L(z,\theta,\phi,\lambda)$ given the beam attenuation coefficient c, volume scattering function (VSF) β, source function S that represents the contributions from inelastic scattering at wavelength λ, and appropriate boundary conditions. The HydroLight radiative transfer software solves equation (7) in run time $\mathcal{O}(M_\theta^2 N_\phi^2)$ by discretizing the set of all available directions (θ, ϕ) in M_θ θ bins and N_ϕ ϕ bins [22, 56, 57]. Since we need only azimuthally-independent quantities L_u and E_d for our formulation of the inverse problem, we use the related EcoLight software [48], which reduces run time by a factor of N_ϕ^2 by solving the azimuthally integrated RTE

$$\cos\theta \frac{dL(z,\theta,\lambda)}{dz} = -c(\lambda)L(z,\theta,\lambda) + \int_0^{\pi} \beta(\theta',\theta,\lambda)L(z,\theta',\lambda)\sin\theta' d\theta' + S(z,\theta,\lambda), \quad (8)$$

where

$$\beta(\theta',\theta,\lambda) = \int_0^{2\pi} \beta(\theta',\phi',\theta,\phi=0,\lambda) d\phi' \quad (9)$$

is the azimuthally integrated VSF. Compared to the standard HydroLight with its default angular resolution of 15 deg in ϕ, i.e. $N_\phi = 24$, this gives a reduction of $(24)^2$ in run time. Equation (8) yields the azimuthally integrated radiance,

$$L(z,\theta,\lambda) = \int_0^{2\pi} L(z,\theta,\phi,\lambda) d\phi. \quad (10)$$

The azimuthally integrated RTE yields the same values for downwelling irradiance E_d

$$E_d(z,\lambda) = \int_0^{\pi/2} L(z,\theta,\lambda)\cos\theta d\theta \quad (11)$$

and nadir viewing radiance L_u

$$L_u(z,\lambda) = L(z,\theta=0,\lambda) \quad (12)$$

as HydroLight because neither quantity has any azimuthal dependence. Inelastic scattering effects $S(z,\theta,\lambda)$ (Raman scattering by water and chlorophyll fluorescence) are also modeled as azimuthally symmetric functions [56]. The backscatter fraction b_b/b is used by EcoLight to determine a depth- and wavelength-dependent Fournier-Forand [58] scattering phase function $\tilde{\beta}(\theta',\theta,\lambda)$ (the ratio of the VSF to the scattering coefficient) [59].

3) Radiometric Error: The radiometric error vector $\boldsymbol{\varepsilon}$ in equation (1) is in radiance and irradiance space and arises from both random (detector noise) and systematic errors, including calibration errors, uncorrected stray light (where light from one measurement channel scatters to other measurement channels), thermal changes in radiometric dark values, and errors in the immersion factor and cosine response function, and in-water self-shading [60]. Errors in L_u and E_d are taken as uncorrelated during optimization. For retrieval error analysis, the radiometric error covariance matrices of the random and systematic forward model parameter error are assessed *a posteriori* in Section 3.

B. Constrained Nonlinear Least Squares Estimation

We wish to find the optimal vector of IOPs **m** that yields an RTE solution for the in-water light field $\mathbf{d}^{est} = G(\mathbf{m}, \mathbf{b})$ that best fits our radiometric observations $\mathbf{d}^{meas}$. We find the best fit by minimizing the squared L_2 distance, in $\log_{10}$ space, between the measured radiometric variables $\mathbf{d}^{meas}$ and those estimated by the forward model $\mathbf{d}^{est} = \mathbf{G}(\mathbf{m}, \mathbf{b})$, subject to IOP lower (**l**) and upper (**u**) bound constraints:

$$\min_{\mathbf{l} \le \mathbf{m} \le \mathbf{u}} \left\| \log_{10}(\mathbf{d}^{meas}) - \log_{10}(\mathbf{d}^{est}) \right\|_2^2 = \min_{\mathbf{l} \le \mathbf{m} \le \mathbf{u}} F(\mathbf{m}) \tag{13}$$

where $\mathbf{d}^{est} = \mathbf{G}(\mathbf{m}, \mathbf{b})$ and the objective (or cost function) $F(\mathbf{m})$ is defined as

$$F(\mathbf{m}) = \mathbf{f}(\mathbf{m})^T \mathbf{f}(\mathbf{m}) \tag{14}$$

and

$$\mathbf{f}(\mathbf{m}) = \begin{bmatrix} f_1(\mathbf{m}) \\ \vdots \\ f_N(\mathbf{m}) \\ f_{N+1}(\mathbf{m}) \\ \vdots \\ f_{2N}(\mathbf{m}) \end{bmatrix} = \begin{bmatrix} \log_{10}\left[L_u^{meas}(z_1)\right] - \log_{10}\left[L_u^{est}(z_1)\right] \\ \vdots \\ \log_{10}\left[L_u^{meas}(z_N)\right] - \log_{10}\left[L_u^{est}(z_N)\right] \\ \log_{10}\left[E_d^{meas}(z_1)\right] - \log_{10}\left[E_d^{est}(z_1)\right] \\ \vdots \\ \log_{10}\left[E_d^{meas}(z_N)\right] - \log_{10}\left[E_d^{est}(z_N)\right] \end{bmatrix}. \quad (15)$$

Logarithmic transformation of radiometric quantities is justified because

- In-water radiances and irradiances decay roughly exponentially with depth, resulting in several orders of magnitude change between z_1 and z_N. Logarithmic transformation results in roughly equal contribution of error components $f_i(\mathbf{m})$ to the objective function $F = \mathbf{f}^T\mathbf{f}$ with depth and the expression of radiometric accuracy as a percentage of the total measurement [61, 62].
- Radiance and irradiance values, hence their errors, differ by two orders of magnitude. Logarithmic transformation scales these values to roughly the same range.

The underwater radiance distribution, $L(z,\theta,\phi,\lambda)$, along with derived quantities L_u and E_d, are nonlinear functions of IOPs. Therefore, to carry out a bound-constrained, nonlinear least squares optimization, we use an efficient trust-region reflective algorithm (MATLAB's `lsqnonlin` function [63]) and a version of EcoLight callable as a MATLAB function [64]. Given a starting point $\mathbf{m}_0$, the optimization procedure minimizes the objective function $F(\mathbf{m})$ by systematically choosing IOP values $\mathbf{m}$ within supplied bound constraints [$\mathbf{l}$,$\mathbf{u}$]. At each optimization step towards the solution, EcoLight is invoked several times in order to compute $\mathbf{d}^{est} = \mathbf{G}(\mathbf{m},\mathbf{b})$ and $\mathbf{f}(\mathbf{m})$, as well as to estimate the objective function gradient $\nabla F(\mathbf{m})$

$$\nabla F(\mathbf{m}) = 2\mathbf{J}(\mathbf{m})^T \mathbf{f}(\mathbf{m}) \tag{16}$$

where **J**(**m**) is the Jacobian

$$\mathbf{J}(\mathbf{m}) = \begin{bmatrix} \frac{\partial f_1(\mathbf{m})}{\partial m_1} & \frac{\partial f_1(\mathbf{m})}{\partial m_2} & \frac{\partial f_1(\mathbf{m})}{\partial m_3} \\ \vdots & \vdots & \vdots \\ \frac{\partial f_{2N}(\mathbf{m})}{\partial m_1} & \frac{\partial f_{2N}(\mathbf{m})}{\partial m_2} & \frac{\partial f_{2N}(\mathbf{m})}{\partial m_3} \end{bmatrix}, \tag{17}$$

representing the sensitivity of log-transformed estimates of L_u (first N rows) and E_d (last N rows) to each IOP m_i. The objective function gradient $\nabla F(\mathbf{m})$ is used to help determine the best direction to take in the IOP retrieval vector space **m** in order to reduce the objective function F(**m**). The Jacobian **J**(**m**) has further utility as a linear approximation for **G**(**m**) near **m**. Appling Taylor's theorem to the forward model **G**(**m**), we obtain the local first-order approximation

$$\mathbf{G}(\mathbf{m} + \Delta\mathbf{m}, \mathbf{b}) \approx \mathbf{G}(\mathbf{m}, \mathbf{b}) + \mathbf{K}_m \Delta\mathbf{m}, \tag{18}$$

where the retrieval Jacobian $\mathbf{K}_m$ takes into account the logarithm operation in equation (15):

$$\mathbf{K}_m = \log(10) \times diag\left[L_u^{est}(z_1), \ldots L_u^{est}(z_N), E_d^{est}(z_1), \ldots E_d^{est}(z_N) \right] \mathbf{J}(\mathbf{m}). \tag{19}$$

Therefore, $\mathbf{K}_m$ represents a locally linear approximation of the RTE around the current estimate of the IOP retrieval vector **m** and is useful for studying the stability and uncertainty of the final estimate $\hat{\mathbf{m}}$.

The optimization procedure uses several criteria to determine when to stop iteration (Table 1). At this point, the final solution $\hat{\mathbf{m}}$, the Jacobian $\mathbf{J}(\hat{\mathbf{m}})$ at this point, and the estimated light

field $\hat{\mathbf{d}} = \mathbf{G}(\hat{\mathbf{m}}, \mathbf{b})$ are retained as the solution. The final solution $\hat{\mathbf{m}}$ is optimal in the sense that if the errors $f_i(\mathbf{m})$ are normally distributed with equal variance σ_i, then minimizing $F(\mathbf{m})$ produces a maximum likelihood solution, i.e., the optimization procedure selects the mostly likely model, as characterized by the retrieval vector $\hat{\mathbf{m}}$, for the set of observations $\mathbf{d}^{meas}$ [65]. (The assumptions upon which such optimality is based will be discussed further in section 8.)

As we will show in section 4, our inverse problem is underdetermined, meaning multiple solutions are possible; we expect this ambiguity because we are attempting to estimate three parameters (a, b, b_b) from two radiometric measurements (L_u, E_d) at each wavelength. In light of this, the optimization procedure is aided by three additional features. First, we use a quick semi-analytic algorithm [31] to establish a starting point $\mathbf{m}_0(\lambda_1)$ at the initial solution wavelength $\lambda_1 = 350$ nm; this hybrid implicit/explicit inverse algorithm solves the RTE using a simplified phase function tuned using a few field measurements and estimates both a and b_b in the asymptotic light regime as well as broad error bounds. In section 4, we will examine just how close this starting point needs to be to assure we can achieve a global minimum for $F\left[\mathbf{m}(\lambda_1)\right]$. Retrievals of IOPs at subsequent wavelengths $\mathbf{m}(\lambda_j), j > 1,$ use the solution at the previous wavelength $\mathbf{m_0}(\lambda_j) = \hat{\mathbf{m}}(\lambda_{j-1})$ as the starting point. Second, we constrain any estimate $\mathbf{m}$ within the prescribed bounds [$\mathbf{l}$, $\mathbf{u}$] based on uncertainty estimates for a_{pg} and b_b from the semi-analytical algorithm based on contemporaneous measurement of backscattering $b_b(z)$ at 470 and 700 nm with a bio-optical model to estimate values of these IOPs at any solution wavelength. The wavelength-dependence of backscattering $b_b(\lambda)$ is represented as [66]

$$b_{bp}(\lambda) = b_{bp}(\lambda_0)\left(\frac{\lambda}{\lambda_0}\right)^{-\eta} \tag{20}$$

where $b_{bp} = b_b - b_{bw}$ and η are estimated using nonlinear regression of measurements of b_b at λ_0 = 470 and/or 700 nm.

For the third feature of the optimization procedure, we take a slightly different approach. As we will see in Section 4, the scattering coefficient b_{pg} is not practically retrievable, but if it is properly bounded, its value increases the accuracy of the estimates of a_{pg} and b_b. We proceed by assuming we have available one contemporaneous attenuation measurement $c(650, z)$, employ a bio-optical model for the wavelength dependence of $c(\lambda)$ and re-organize the inversion as a two parameter estimation problem $\mathbf{m} = [a_{pg}, b_b]$ augmenting the additional forward model parameter vector **b** with an estimate of b_{pg}, computed as

$$b_{pg}(\lambda) = c_p(\lambda) - a_{pg}(\lambda). \tag{21}$$

The wavelength dependence of particulate attenuation $c_p(\lambda)$ is represented as [67, 68]

$$c_p(\lambda) = c_p(650)\left(\frac{\lambda}{650}\right)^{-\gamma} \tag{22}$$

where $c_p(650) = c(650) - c_w(650)$ and $\gamma = 0.5$. While an approximation with fixed γ implies a fixed particle size distribution, we will see that it sufficiently constrains scattering $b_{pg}(\lambda)$ and sensitivity to choice of γ is small. Bootstrap statistics for b_{pg} are derived by a campaign of optical measurements carried out during the field experiment and error propagation methods via equations (21) and (22).

Inelastic scattering at wavelengths less than λ_e = 500 nm is negligible for the waters under study here, so single-wavelength solutions of the forward model **G(m**,**b**) can found quickly and discretely at each wavelength $\lambda_j \le \lambda_e$ during optimization. At wavelengths where inelastic scattering contributes to the light field, we follow an inductive approach to computing the forward model. During optimization for $\mathbf{m}(\lambda_j), \lambda_j > \lambda_e$, IOPs at shorter wavelengths $\mathbf{m}(\lambda_k), k = 1, \ldots, j-1$ have been previously estimated; the light field at these wavelengths is saved and is used to compute the source term for inelastic scattering at wavelength λ_j. The optimization proceeds at the current wavelength, varying only the IOPs $\mathbf{m}(\lambda_j)$ while minimizing the objective function $F\left[\mathbf{m}(\lambda_j)\right]$. When optimization at wavelength λ_j is complete, the light field at λ_j is also saved and is used to prime the optimization at λ_{j+1}, and so on. Thus, optimization at inelastically scattered wavelengths incurs only the small additional cost of computing the source functions for chlorophyll fluorescence and Raman scattering [22].

3. Error Characterization

A. Linear Retrieval

Here we follow the work in the atmospheric sounding community by Rodgers [43]. Omitting *a priori* knowledge of IOPs, if the estimate of vertically homogeneous IOPs $\hat{\mathbf{m}}$ is close to the actual values of IOPs **m**, the estimated IOPs can be expressed by a linearization about the actual value **m**:

$$\hat{\mathbf{m}} = \mathbf{m} + \mathbf{G}_m \boldsymbol{\varepsilon} + \mathbf{G}_m \mathbf{K}_{\mathbf{b}} (\mathbf{b} - \mathbf{b}_a) + \boldsymbol{\varepsilon}_r \tag{23}$$

where $\boldsymbol{\varepsilon}$ is the noise vector defined in equation (1), $\mathbf{m}$ is the state of the actual in-water IOPs, and $\boldsymbol{\varepsilon}_r$ is noise introduced by the optimization process. The gain matrix $\mathbf{G}_m$ is defined by

$$\mathbf{G}_m = \frac{\partial \mathbf{m}}{\partial \mathbf{G}} = (\mathbf{K}_m^T \mathbf{S}_\varepsilon^{-1} \mathbf{K}_m)^{-1} \mathbf{K}_m^T \mathbf{S}_\varepsilon^{-1}, \tag{24}$$

where $\mathbf{K}_m$ is the retrieval Jacobian, as defined in equation (19). The gain matrix $\mathbf{G}_m$ is essentially the ratio between statistical measures of the uncertainty in an IOP estimate and the uncertainty in a measurement [69]. Vector $\mathbf{b}$ is the true state of the additional forward model parameters that affect forward-modeled radiance L_u and irradiance E_d, (solar zenith angle, cloud fraction, etc.), and vector $\mathbf{b}_a$ is the *a priori* estimate of those parameters. The Jacobian

$$\mathbf{K}_\mathbf{b} = \frac{\partial \mathbf{G}(\mathbf{m}, \mathbf{b})}{\partial \mathbf{b}} \tag{25}$$

describes the sensitivity of L_u and E_d to changes in the additional forward model parameters.

B. Retrieval Error Analysis

From equation (23), the error in the estimated IOPs is the difference between the estimated and actual IOPs and is composed of measurement error and systematic errors [43],

$$\tilde{\mathbf{m}} = \hat{\mathbf{m}} - \mathbf{m} = \underbrace{\mathbf{G}_m \boldsymbol{\varepsilon}}_{\text{measurement error}} + \underbrace{\mathbf{G}_m \mathbf{K}_\mathbf{b} (\mathbf{b} - \mathbf{b}_a)}_{\text{forward model parameter error}} + \underbrace{\boldsymbol{\varepsilon}_r}_{\text{retrieval noise}} . \tag{26}$$

The first term transforms random and systematic errors in radiometric measurements to an error in the retrieved IOPs. The second term transforms errors from the additional forward model parameters into an error in the retrieved IOPs. Although these are described as systematic errors, many of the additional forward model parameters can change with each retrieval. The last term

represents errors systematically introduced by the optimization process and may be dependent on the magnitude of the retrieved values. Similarly, the total IOP retrieval error covariance matrix $\mathbf{S}_t$ is the sum of the measurement error, forward model parameter error, and retrieval noise covariance matrices [70]:

$$\mathbf{S}_t = \mathbf{S}_m + \mathbf{S}_f + \mathbf{S}_r \tag{27}$$

where the measurement error covariance is

$$\mathbf{S}_m = \mathbf{G}_m \mathbf{S}_\varepsilon \mathbf{G}_m^T \tag{28}$$

and the forward model error covariance is

$$\mathbf{S}_f = \mathbf{G}_m \mathbf{K}_\mathbf{b} \mathbf{S}_\mathbf{b} \mathbf{K}_b^T \mathbf{G}_m^T, \tag{29}$$

where $\mathbf{S_b}$ is the forward model parameter error covariance matrix. The retrieval noise covariance matrix $\mathbf{S}_r$ will be treated as diagonal and characterized through simulation under conditions where $\mathbf{S}_m$ and $\mathbf{S}_f$ are zero.

The 95% confidence intervals for individually retrieved IOPs can be estimated from the diagonal of the total retrieval error covariance matrix $\mathbf{S}_t$ as [71]

$$\hat{\mathbf{m}} \pm \boldsymbol{\delta}_{0.95}, \tag{30}$$

where $\hat{\mathbf{m}}$ is the mean retrieval estimate returned by the optimization, the individual (univariate) confidence interval is

$$\boldsymbol{\delta}_{0.95} = t_{0.975(2),N-p} \times \sqrt{\mathrm{diag}(\mathbf{S}_t)}, \tag{31}$$

and $t_{0.975(2),N-p}$ is the two-tailed Student's *t*-statistic for *N* observations (number of radiometric measurement depths) and *p* unknowns (the length of the IOP retrieval vector **m)**. However, when estimating more than one parameter simultaneously, the joint parameter confidence region should be examined to see the influence of correlation between the retrieved parameters, expressed by non-zero off-diagonal elements in $\mathbf{S}_t$. This correlation significantly reduces the region of uncertainty from a *p*-dimensional rectangular region (hypercube) expressed by equation (30) to a *p*-dimensional ellipsoid surrounding $\hat{\mathbf{m}}$**.** Assuming an inverse solution that is locally-linear about the final IOP estimate (an assumption we will test below)**,** the joint confidence region is defined by an ellipsoid [71]

$$N(\hat{\mathbf{m}}-\mathbf{m})^T\mathbf{S}_t^{-1}(\hat{\mathbf{m}}-\mathbf{m}) \le \frac{(N-1)p}{(N-p)}F_{p,N-p}(\alpha), \tag{32}$$

where $F_{p,n-p}(\alpha)$ is the upper α point of the *F(p,n-p)* distribution (implemented in MATLAB as the `finv` function) and α= 1-0.95 for a 95% confidence region. This ellipsoid can be drawn to evaluate the joint confidence region of IOPs and can be projected onto the retrieval parameter axes to get the following individual confidence intervals

$$\boldsymbol{\delta}_{0.95} = \frac{(N-1)p}{N-p}F_{p,N-p}(\alpha)\times\sqrt{\mathrm{diag}(\mathbf{S}_t)}, \tag{33}$$

which will be broader than those predicted by equation (31). When jointly estimating only the two IOPs a_{pg} and b_b, then $p = 2$ and the joint confidence region can be plotted as an "error ellipse". The error ellipse provides information about the combinations of IOP estimates that are "jointly reasonable" [72]. We will report the broader, more conservative individual intervals calculated using equation (33) and display the error ellipses at selected wavelengths in order to

visually assess correlation of estimated IOPs and this jointly reasonable region of IOP estimates. For less conservative assumptions, see Johnson and Wichern [71].

C. Relative Errors

Assessment of systematic biases and typical uncertainties between estimated and measured quantities can be made using the relative percent difference ψ and its absolute value |ψ|, respectively. In the formulation of the relative percent differences, measured data are considered the reference values, so for a paired estimate and measurement the residual and relative errors are

$$res_i(z_j) = X_i^{est}(\lambda_i, z_j) - X_i^{meas}(\lambda_i, z_j) \tag{34}$$

and

$$\psi_i(z_j) = 100\frac{res_i(z_j)}{X_i^{meas}(\lambda_i, z_j)}, \tag{35}$$

respectively, where an X may be an IOP or radiometric value, $X_i^{est}(\lambda_i, z_j)$ is an estimated value, and $X_i^{meas}(\lambda_i, z_j)$ is the corresponding measured value at wavelength λ_i and depth z_j. Similarly, the average absolute percent difference is computed with $|\psi_i(z_j)|$. We summarize estimation of the relative errors as follows:

1. Average absolute error $\overline{|\psi|}$ and average relative error $\bar{\psi}$

$$\overline{|\psi|} = \frac{1}{MN}\sum_{i=1}^{M}\sum_{j=1}^{N}\left|\psi_i(z_j)\right|, \tag{36}$$

and

$$\bar{\psi} = \frac{1}{MN} \sum_{i=1}^{M} \sum_{j=1}^{N} \psi_i(z_j) \tag{37}$$

are used to explore the algorithm's average performance across all depths and wavelengths.

2. Root mean square (RMS) error

$$\varepsilon_{RMS} = \sqrt{\frac{\sum_{i=1}^{M} \sum_{j=1}^{N} res_i^2(z_j)}{MN}}, \tag{38}$$

is used to explore average expected spectral error in IOPs $\hat{\mathbf{m}}$ and predicted light fields $\mathbf{d}^{\text{est}}$, in light of the fact that we have minimized the least square error in the log-transformed radiometric quantities according to equation (13).

D. Radiometric Error Covariance Matrix $\mathbf{S}_\varepsilon$

Radiometric errors $\boldsymbol{\varepsilon}$ are assumed to be uncorrelated and normally distributed random variables with zero means and variances $\sigma_{L_u}^2$ and $\sigma_{E_d}^2$. These variances are considered to be "combined standard uncertainties" of Type A errors (typically random errors where uncertainties are determined by statistical analysis, reduced by making additional measurements) and Type B errors (typically systematic errors where uncertainties are obtained by heuristic means, reduced by instrument characterization) [73]. For radiometry, a typical Type A error is due to sensor noise and its error variance is expressed as a manufacturer-supplied noise equivalent radiance. A typical Type B radiometric error is radiometric calibration error, due to, for example, mischaracterizations in the calibration lamp, cosine collector response, or immersion coefficient, and cannot be reduced by repeating a measurement. Components of radiometric uncertainty budgets, where Type B errors dominate, are presented as a percent error in the radiometric

measurement [60, 62, 74]. A common approach to expressing the magnitude of a Type B error is to assume that the error is a single realization draw from some statistical parent distribution of possible Type B errors[75]. Accordingly, we assume that relative radiometric uncertainties Δ_{L_u} % and Δ_{E_d} % can be represented as 95% confidence intervals $\delta_{L_u,0.95}$ and $\delta_{E_d,0.95}$ for systematic radiometric errors interpreted as random variables drawn from a normal distribution, i.e.,

$$\begin{aligned} \delta_{L_u,0.95} &= 1.96 \times \sigma_{L_u} = \Delta_{L_u} / 100 \times \bar{L}_u \\ \delta_{E_d,0.95} &= 1.96 \times \sigma_{E_d} = \Delta_{E_d} / 100 \times \bar{E}_d \end{aligned}, \tag{39}$$

where 95% of the area under the univariate normal distribution lies within ≈1.96 standard deviations of the mean. In this case, the radiometric error covariance matrix is

$$\mathbf{S}_{\varepsilon}^{sim} = \begin{bmatrix} \sigma_{L_u}^2 & 0 \\ 0 & \sigma_{E_d}^2 \end{bmatrix}, \tag{40}$$

where equation (39) is solved for $\sigma_{L_u}^2$ and $\sigma_{E_d}^2$. For field measurements with radiometric instruments where complete radiometric uncertainty budget is not available, we estimate the standard uncertainty of radiometric measurements at each wavelength λ_i from the residual errors res_i with [76]

$$\hat{\sigma}_i^2 = \frac{\sum_{j=1}^{N} res_i^2(z_j)}{\nu} \tag{41}$$

where $\nu = N - p$ is the number of degrees of freedom and the radiometric error covariance matrix is

$$\mathbf{S}_{\varepsilon}^{meas} = \begin{bmatrix} \hat{\sigma}_{L_u}^2 & 0 \\ 0 & \hat{\sigma}_{E_d}^2 \end{bmatrix}. \tag{41}$$

E. Measurement Error Covariance $\mathbf{S}_m$*: Estimates and Validation*

If the first-order linear approximation of RTE about the IOP estimate $\hat{\mathbf{m}}$ in equation (23) is valid, the measurement covariance matrix $\mathbf{S}_m$ can be calculated using an estimate of the radiometric error covariance matrix $\mathbf{S}_\varepsilon$ and a quick matrix computation with equation (28). To test the assumption of local linearity, we also estimate $\mathbf{S}_m$ using a Monte Carlo approach and compare this to a first-order estimate of $\mathbf{S}_m$ for the same data point [77]. The Monte Carlo estimate is trivial to implement but slow, and provides an uncertainty estimate that is specific to the particular inversion being performed. So, in the end, it is preferable to use the more efficient first-order error propagation method.

For this comparison, we identified a profile of vertically homogeneous IOPs found in the oligotrophic waters of the Korea Strait [78], available from the Worldwide Ocean Optics Database (WOOD [52]). IOPs (*a, b, b_b*), taken from a data point at 10 m from an optical profile vertically homogenous to 30 m, were used to compute mean (or "true") values $\overline{L}_u$ and $\overline{E}_d$ by a forward simulation using EcoLight (Table 2). To carry out the Monte Carlo method, we performed single-wavelength, single-depth unconstrained inversions using 10,000 uncorrelated, normally-distributed radiometric samples $\mathcal{N}(\overline{L}_u, \sigma_{L_u}^2)$ and $\mathcal{N}(\overline{E}_d, \sigma_{E_d}^2)$. Sample variances $\sigma_{L_u}^2$ and $\sigma_{E_d}^2$ were computed according to equation (39), based on an assumption of $\Delta_{L_u} = \Delta_{E_d} = 5\%$ radiometric error. From the Monte Carlo inversion results $\mathbf{m}_i$ for each random radiometric

sample, we estimated the mean of each retrieved IOP $\bar{\mathbf{m}}$ as well as the measurement error covariance matrix

$$\mathbf{S}_m^{MC} = \frac{1}{n} \sum_{i=1}^{10,000} \left(\mathbf{m}_i - \bar{\mathbf{m}}\right)\left(\mathbf{m}_i - \bar{\mathbf{m}}\right)^T . \tag{42}$$

Computed this way, the Monte Carlo estimate $\mathbf{S}_m^{MC}$ would normally include forward model parameter errors, but since we used the same model parameters **b** for both forward simulation of $\bar{L}_u$ and $\bar{E}_d$ as well as for retrievals of IOPs, forward model parameter error can be disregarded. For the first-order error propagation method, the measurement error covariance matrix $\mathbf{S}_\varepsilon^{sim}$ was populated with the same radiometric errors $\sigma_{L_u}^2$ and $\sigma_{E_d}^2$ that were used as sample variances in the Monte Carlo simulation. The inversion was carried out using $\bar{L}_u$ and $\bar{E}_d$ as radiometric input, and the retrieval Jacobian $\mathbf{K}_m(\hat{\mathbf{m}})$ was saved from the final optimization step. The first-order estimate of the measurement covariance matrix $\mathbf{S}_m^1$ was computed using equations (24) and (28). We ignored retrieval noise covariance S_r in both model error covariance estimates.

The Monte Carlo and first-order error propagation results are presented in Fig. 1 and Table 3. The elliptical colored region is a 2-D histogram of the IOP retrievals $\mathbf{m}_i$ from the Monte Carlo radiometric samples and is an estimate of the joint probability distribution $p(a_{pg},b_b)$, with histogram bin count shown by the color bar. The projection of this 2-D histogram onto each IOP axis is shown as the grey 1-D histograms, which are estimates of the marginal probability distributions $p(a_{gp})$ and $p(b_b)$. These marginal distributions are also normal, as shown by the fit of the grey histograms to univariate normal distributions (the blue line bounding each grey histogram). The resulting distributions for a_{pg} and b_b passed a normality test, consistent with

local linearity of the RTE. This implies that the probability distribution of the radiometric quantities $\mathbf{d}^{meas}$ is preserved by the inversion; alternative assumptions about the probability distributions of radiometric errors will similarly be reproduced in the probability distribution of IOP estimates.

To compare uncertainty estimates, we used equation (32) to plot the 95% joint confidence region for a_{pg} and b_b using each of the two covariance matrix estimates $\mathbf{S}_m^{MC}$ and $\mathbf{S}_m^1$, shown in Fig. 1 as the blue and red 95% confidence ellipses, respectively. The two error ellipses are very close, and the small relative error in estimated covariance matrices $\left\|\mathbf{S}_m^{MC} - \mathbf{S}_m^1\right\|_2 \Big/ \left\|\mathbf{S}_m^{MC}\right\|_2 = 11\%$ justifies the use of the first-order error propagation method. The resulting univariate 95% confidence intervals (Table 3) differ by 5% (a_{pg}) and 11% (b_b). That the first-order estimates of uncertainty are slightly larger than the Monte Carlo estimates means that the first-order approach, in this case, is conservative. The correlation coefficient for both covariance matrix estimates is $\rho = 0.86$, also demonstrated by the positive slope of the error ellipses' major axis. This indicates that uncertainties in IOPs found by our inversion approach are not independent. The resulting error ellipses show that the range of uncertainty in the two parameters retrieved jointly (area bounded by the ellipse) is much less than that if estimation errors where considered individually (area of a bounding box around the ellipses).

In summary, we have found that we can quickly and accurately estimate the 95% confidence intervals of IOP estimates using the first-order error propagation method. The results compare well with Monte Carlo simulation. The correct interpretation of the confidence ellipse is that there is a 95% probability that when we construct the confidence ellipse that this ellipse will contain the true mean of both IOP estimates. The correct interpretation of the univariate

confidence intervals is that there is a 95% probability that when we construct a confidence interval for one IOP *irrespective of the value of the other IOP,* that this interval will contain the true mean of that IOP. In practice, IOPs a_{pg} and b_{pg} are true quantities that we are estimating, not random variables; the measurements, mean values and confidence intervals are the random quantities. We have assumed that radiometric errors can be modeled as zero-mean, normal random variables (arising, for example, from random dark-current noise). However, radiometric errors can include systematic errors (e.g., from self-shading, immersion factor, or calibration lamp biases) resulting in non-zero means and/or non-normal error distributions.

F. Forward Model Parameter Sensitivity Matrix $\mathbf{K}_b$ *and Covariance Matrix* $\mathbf{S_b}$

Forward model error covariance $\mathbf{S}_f$ is derived by calculating $\mathbf{K_b}$, the Jacobian that expresses the sensitivity of radiometric measurements to the additional forward model parameters **b** and estimating the forward model parameter covariance matrix $\mathbf{S_b}$. The sensitivity matrix $\mathbf{K_b}$, equation (25), was obtained by evaluating the RTE using EcoLight. Each forward model parameter was varied individually over the range of values shown in Table 4, with L_u and E_d computed at 5 m intervals from 5 – 50 m. IOPs were selected from a known vertically homogeneous profile at 490 nm from the 10 m Korea Strait (Table 2). For each forward model parameter b_i at each depth, a linear fit was computed for L_u and E_d over the range of parameter (Fig. 2a-e shows the results at10 m); the resulting slope is the sensitivity coefficient $\partial L_u(z_k)/\partial b_i$ and $\partial E_d(z_k)/\partial b_i$. (Fig. 2f-j). The resulting sensitivities were found to be reasonably linear with parameter range and nonlinear with depth. Therefore, the sensitivities at all depths are retained and $\mathbf{K_b}(z)$ is evaluated at the depths used in the retrieval. At 490 nm, the light field has little or

no contribution from inelastic scattering, so the sensitivity coefficients can be applied to any retrieval wavelength dominated by elastic scattering.

The sensitivity coefficients show that L_u and E_d are most sensitive to changes in incident solar irradiance E_s and solar zenith angle is θ_s. For solar zenith angle θ_s, the light field estimates decrease as θ_s decreases because of photons lost due to the cosine law. We observe piecewise linear sections in the relationship based on EcoLight's partitioning of the radiance distribution into 10° polar angle bands; hard boundaries are at 35°, 45°, etc. (Fig. 2a). The sensitivity of the L_u and E_d to ±35% errors in the scattering coefficient is relatively small at depths below 15 m. The nonlinear relationship between L_u, E_d and *cloud* is a result of effects of cloud fraction in EcoLight's sky radiance [79] and cloud cover [80] models. In particular, the cloud cover model adjusts clear sky irradiances if the cloud fraction > 0.25. EcoLight uses the Cox-Munk wind speed – wave slope model [81, 82] and Monte Carlo simulations to estimate water surface roughness and slope, which result in air-water transmittances and reflectances that are parameterized by wind speed U_{10}. We found the sensitivity of the light field to wind is relatively small. Finally, as expected, the sensitivity of the in-water light field to the incident solar irradiance E_s is nearly 1:1.

The forward parameter error covariance matrix $\mathbf{S_b}$ was constructed as diagonal matrix, implying there is no correlation between errors in θ_s, *cloud*, U_{10}, E_s and scattering b:

$$\mathbf{S_b} = \mathrm{diag}(\sigma^2_{\theta_s}, \sigma^2_{cloud}, \sigma^2_{U_{10}}, \sigma^2_{E_s}, \sigma^2_b) \tag{43}$$

Estimates of all the diagonal entries, except σ^2_b. were based on assigning an assumed relative error as a 95% confidence interval of a normally distributed random variable. The relative error

for those entries is shown in Table 4. For the scattering coefficient *b*, multi-wavelength measurements from ten *in situ* IOP profiles from the NAB08 data (see section 6) were compared to estimates based on measurements at a single wavelength (650 nm) and the bio-optical model in equation (22), to produce residual errors at eight wavelengths λ_i = 412, 440, 510, 532, 555, 650 and 676 nm

$$\begin{aligned} res_{ijk} &= res_k(\lambda_i, z_j) \\ &= b_{ijk}^{meas} - b_{ijk}^{est} \\ &\approx (c_{p,ijk}^{meas} - a_{pg,ijk}^{meas}) - (c_{p,ijk}^{est} - a_{pg,ijk}^{meas}) \\ &= c_{p,ijk}^{meas} - c_{p,ijk}^{est} \end{aligned} \tag{44}$$

where equation (22) is used to compute $c_{p,ijk}^{est}$, *k* represents each of ten NAB08 process cruise stations where bio-optical profiles were taken, *j* represents the set of depths in the vertically homogenous region, and *i* represents wavelength. This yielded 245 residuals at each wavelength from which the mean variance $\overline{\sigma_b^2}(\lambda_i)$ was estimated via bootstrap analysis using 10,000 runs (Fig. 3). Estimates of σ_b^2 at other wavelengths were found by linear interpolation of $\overline{\sigma_b^2}(\lambda_i)$.

G. Estimation of Retrieval Noise $\mathbf{S}_r$

Numerical methods such as those used here have fast convergence properties but can oscillate around the objective function minimum within the supplied optimization tolerances (Table 1). Reducing tolerances in an attempt to increase numerical accuracy can result in local, rather than global, convergence. Analytical Jacobians are not available from the EcoLight model, therefore the Jacobian $\mathbf{J}(\mathbf{m})$ in our method is computed using finite-difference techniques and is less precise than that derived by analytical (typically linear) approximations to the RTE [42] or automatic differentiation [83]. The relative strength of the bio-optical absorption signal becomes

weak at longer wavelengths and may be difficult to detect. In this section, without prejudice to the source of inversion errors, we seek to establish the floor for noise generated by the inversion method itself.

To assess the ability of our algorithm to retrieve IOPs in the absence of measurement noise, natural variability, and forward model parameter errors, simulations were carried out to generate vertically homogeneous IOPs and an associated in-water light field. Then the inversion method was used to retrieve those very same IOPs from the simulated light field. Hyperspectral IOPs $\mathbf{m}^{sim}(Chl_i)$ were computed based on five chlorophyll concentrations Chl = 0.01, 0.1, 1, 3, 10 mg m^{-3} using EcoLight's simple Case 1 chlorophyll-based bio-optical model [84]. Using these IOPs, EcoLight was used to generate azimuthally symmetric light fields $L_u^{sim}(z,\lambda), E_d^{sim}(z,\lambda)$ at ten depths z = 5, 10, 20,…,90 m and wavelengths from 350 – 700 nm at 3.3 nm increments, with the scattering phase function selected using b_b/b. The EcoLight forward model used in the optimization was configured identically for retrieval, using the same forward model parameters $\mathbf{b}^{sim}$ for light field $\mathbf{d}^{sim}$ generation and estimation of light fields $\mathbf{d}^{est}$ (Table 4). During the optimization procedure, the simulated light field $\mathbf{d}^{sim}$ was compared to the estimated light field $\mathbf{d}^{est} = \mathbf{G}(\mathbf{m}, \mathbf{b}^{sim})$ using the objective function $F(\mathbf{m})$ described in equations (13), (14) and (15).

The resulting spectral estimates for absorption a_{pg} are shown in Fig. 4a-b. Spectral relative error $\psi_{a_{pg}}(\lambda)$ increases as the relative contribution of a_{pg} to pure water absorption a_w declines. This can be considered a signal detection problem for the optimization procedure: the a_{pg} signal at Chl = 0.01 mg m^{-3} varies from 6% to less than 0.2% of the large pure water a_w signal, i.e., there is an inherent lack of sensitivity of the light field at longer visible wavelengths to optical constituents. Relative and band-averaged RMS errors are presented in Table 5 and Fig.

5. In general, relative errors increase with decreasing *Chl* and increase markedly when wavelengths greater than 500 nm are considered. RMS error in retrieved IOPs increases with increasing *Chl*. The average relative errors in radiometric quantities $\overline{\psi_{L_u}}$ and $\overline{\psi_{E_d}}$ show some negative bias (-1% to -2%) at smaller *Chl* values, along with a similar bias in $\overline{\psi_{a_{pg}}}$; this is unexpected, as our sensitivity studies predict a negative correlation between radiometric errors and IOP estimation errors. Otherwise, no significant bias is evident in radiometric quantities or a_{pg} estimates. The average absolute error in absorption $\overline{\left|\psi_{a_{pg}}\right|}$ is 1 to 2% when considering wavelengths less than 500 nm; for wavelengths greater than 500 nm, it varies from 1 to 10%, increasing with lower values of *Chl.* This establishes the "noise floor" for our inversions of absorption. Spectral estimates for backscattering b_b show smaller retrieval errors under these ideal conditions (Fig. 6). The average error below 650 nm $\overline{\left|\psi_{b_b}\right|}$ is ≈1% except for *Chl = 0.1* between 350-500 nm (Table 5)**.** Above 650 nm, b_b estimates exhibit individual errors as large as 10% (see Fig. 6b). We estimate the retrieval noise covariance matrix $\mathbf{S}_r$ by assigning the square of RMS errors across two wavebands (< 500 nm, ≥ 500 nm) for each value of *Chl* and assigning them as the diagonal elements:

$$\mathbf{S}_r(Chl, \Delta\lambda_i) = \begin{bmatrix} \varepsilon_{RMS}^{a_{pg}}(Chl, \Delta\lambda_i)^2 & 0 \\ 0 & \varepsilon_{RMS}^{b_b}(Chl, \Delta\lambda_i)^2 \end{bmatrix}, \tag{45}$$

where $\Delta\lambda_1$ represents < 500 nm and $\Delta\lambda_2$ represents ≥ 500 nm; the RMS error values are given in Table 5.

To further explore the source of inversion errors for a_{pg}, we examined the matrix norm of the spectral Jacobians $\left\|\mathbf{J}(\lambda_i, \hat{\mathbf{m}})\right\|_2$, which provides a scalar measure of the magnitude of the elements of $\mathbf{J}(\lambda_i, \hat{\mathbf{m}})$. Recall from equation (17) that the elements of $\mathbf{J}(\lambda_i, \hat{\mathbf{m}})$ represent the sensitivity of RTE solutions (L_u, E_d) to changes in an IOP at λ_i; a larger value of $\left\|\mathbf{J}(\lambda_i, \hat{\mathbf{m}})\right\|_2$ indicates a larger sensitivity of the estimated light field to changes in the estimated IOPs $\hat{\mathbf{m}}(\lambda_i)$. The spectral Jacobians shown in Fig. 4c demonstrate two results consistent with our understanding of ocean optics. First, the spectral norm of the Jacobian decreases after 600 nm; this is consistent with the large increase in pure water absorption a_w at these wavelengths where changes in a_{pg} and b_b have much less effect on L_u and E_d. Second, the spectral norm of the Jacobian increases at wavelengths less than 500 nm for Chl = 0.01; under these conditions, pure water absorption is comparable to a_{pg}, thus changes in a_{pg} (see Fig. 4a) have a much larger influence on light field.

Since identical EcoLight Raman scattering and chlorophyll fluoresce models were used to generate the light field and carryout the inversions, we attribute little error in this exercise to uncertainty in estimating inelastic scattering. Indeed, the chlorophyll absorption peaks are reproduced at all Chl values in Fig. 4a. However, we expect at wavelengths greater than 500 nm (depending on chlorophyll concentration or equivalently, average a_{pg} at these wavelengths) that a_{pg} retrievals will be extremely sensitive to estimation of the true in-water light field.

4. Existence, Uniqueness, and Stability of IOP Estimates

A. Theory

The radiometric inverse problem is well-posed, in the Hadamard sense [85], if the entire radiance distribution and its depth derivative are known [86]. In this case, a complete IOP solution (absorption coefficient, VSF and its derived quantities, the scattering coefficient b and backscattering coefficient b_b) exists, is unique, and is stable. Instrumentation that directly measures $L(z,\theta,\phi,\lambda)$ has been used to directly recover the absorption coefficient [87] using Gershun's Law. In general, the irradiance distribution fails to fully specify the radiance distribution and therefore complete retrieval of IOPs is impossible from irradiance measurements alone [88]. However, Preisendorfer and Mobley [89] have shown that the absorption coefficient can be retrieved from depth-resolved measurements of the irradiance quartet [$E_d(z)$, $E_u(z)$, $E_{od}(z)$, $E_{ou}(z)$], but in this case a solution for backscattering coefficient b_b does not exist. When less than the full radiance distribution is available, we should expect one or more of the Hadamard conditions to fail. Indeed, Sydor, et al. [90] as well as Defoin-Platel and Chami [91] have shown that several combinations of IOPs (a, b_b) can reproduce the same subsurface reflectance spectrum $R_{rs} = L_u / E_d$, i.e., the inverse solution for this problem is not unique and limits the precision of IOP estimates. Observational and methodological errors (e.g., uncertainty in radiometric measurements and spectral matching criterion, respectively), may also contribute to ambiguity in the inversion of remote sensing ratio for IOPs [92]. Since we measure the irradiance distribution at only one orientation (E_d) and the radiance at only one direction (L_u), we cannot recover the radiance distribution, the problem is ill-posed, and one or more of the Hadamard conditions (existence, uniqueness, stability) will not be met. Let us consider Hadamard conditions in turn for our problem, i.e., the retrieval of the absorption coefficient from depth-resolved measurements of L_u and $E_{\underline{d}}$ in vertically homogeneous waters, along with measurements of several easily obtained IOPs.

B. Existence

Do we have a model that closely fits the data? As discussed in [22] and [91], the radiative transfer equation itself is well-posed and is a result of a phenomenological theory that adequately describes our macroscopic observations of light in water. We expect that at least one set of IOPs will come adequately close to the solution, within the limitations of the RTE implementation [56]. Our model, EcoLight, may be inadequate because additional model parameters **b** may not be adequately known. By creating sensitivity studies of solutions with respect to these parameters **b,** we can explore the limitations of model uncertainties with respect to IOP estimates **m (**see section 5**).**

C. Uniqueness (Elastic Scattering)

Are inverse solutions unique? We seek to determine if more than one set of IOPs (a, b_b b,) can produce a light field consistent with calibrated measurements of L_u and E_d assuming the incident solar irradiance E_s is known. Formally, we examine the forward model $\mathbf{G}(\mathbf{m},\mathbf{b})$ as a functional mapping and ask if the mapping is injective, i.e., does it satisfy

$$\mathbf{G}(\mathbf{m}_1,\mathbf{b}) = \mathbf{G}(\mathbf{m}_2,\mathbf{b}) \Rightarrow \mathbf{d}_1 = \mathbf{d}_2 \quad \text{for all } \mathbf{d}_1,\mathbf{d}_2 \in \mathcal{D},\ \mathbf{m} \in \mathcal{M}, \tag{46}$$

where $\mathcal{D}$ represents the space of naturally realizable combinations of L_u and E_d in natural waters and $\mathcal{M}$ represents all physically realistic oceanic IOPs? If **G** is not an injective mapping, then multiple sets of IOPs can produce the same in-water light field as characterized by L_u and E_d. We must then analyze how well one can characterize this lack of injectivity. Although we know the inverse RTE solution given L_u and E_d will not be unique, the quasi-single scattering approximation [93, 94] leads us to believe that two IOPs (a, b_b) may be retrieved.

To explore this semi-quantitatively, we examined two NAB08 data points (see section 6 and Table 2) representing measurements of L_u, E_d, a, b_b and b interpolated to 490 and 650 nm, both 20 m deep. A 3-D volume of IOPs values was created, representing $N_a \times N_{b_b} \times N_b = 41 \times 41 \times 41 = 68{,}921$ IOP combinations centered about the known data point. Forward RTE simulations were computed using EcoLight for each IOP value, yielding corresponding radiometric volumes for L_u and E_d. As shown in Fig. 7, isosurfaces were computed for constant values L_u (blue) and E_d (red) within the 3-D IOP volume, for $\lambda_1 = 490$ nm and $\lambda_2 = 650$ nm. A 3-D isosurface represents the subset of IOPs within the volume that give rise to the specified values of L_u and E_d. At 490 nm, the two isosurfaces and their intersection (shown in yellow) lie nearly parallel to the b_{pg}-axis, indicating the solution for the scattering coefficient b_{pg} is not unique; any value of b_{pg} on the yellow line yields the specified L_u and E_d values. The isosurfaces demonstrate that a_{pg} and b_b should be retrievable from simultaneous measurements of L_u and E_d, but scattering coefficient b_{pg} cannot be retrieved. However, the curvature of the isosurfaces (Fig. 7b) indicates some ambiguity in the retrieval of a_{pg} and b_b due to due the unknown scattering coefficient (black dashed lines).

If we reduce the measurement space from L_u and E_d to one AOP $R_L = L_u / E_d$, the effect on uniqueness of the inverse problem can be easily demonstrated by evaluating an objective function based on reflectance alone, i.e., by replacing equation (15) with

$$\mathbf{f}_R(\mathbf{m}) = \begin{bmatrix} \log_{10}\left[R_L^{meas}(z_1)\right] - \log_{10}\left[R_L^{est}(z_1)\right] \\ \vdots \\ \log_{10}\left[R_L^{meas}(z_N)\right] - \log_{10}\left[R_L^{est}(z_N)\right] \end{bmatrix} \tag{47}$$

and computing $F_R(\mathbf{m}) = \mathbf{f}_R(\mathbf{m})^T \mathbf{f}_R(\mathbf{m})$ over the same range of a and b_b as above. In Fig. 8, this reflectance-based objective function is compared to $F(\mathbf{m})$ computed using equations (14) and (15) with 50% error in b. (See online media for an animation of each surface over the range b = 0.1 to 1.0.) The objective function $F(\mathbf{m})$ using L_u and E_d (Fig. 8a) always has a single minimum (i.e., a unique solution) while the objective function $F_R(\mathbf{m})$ using R_L (Fig. 8b) always has multiple nearby local minima; the problem has become ill-posed again. This shows the value of basing retrievals on calibrated L_u and E_d spectra.

We conclude that 1) L_u and E_d provide distinct information regarding the radiance distribution, offering a nearly unique inverse solution for a and b_b, and 2) if the scattering coefficient b_{pg} can be bounded, even with substantial uncertainty, then we can restrict solutions to a smaller section along the line of intersection, yielding a smaller IOP subspace and less uncertainty in a_{pg} and b_b.

D. Uniqueness (Inelastic Scattering)

At 650 nm, Raman scattered photons contribute to the light field. In Fig. 7, we observe that the isosurfaces at λ_2 = 650 nm are folded closer together than at 490 nm, resolving a smaller subspace of IOPs. In the limit of an isotropic light field, the two surfaces merge with no unique intersection in the a_{pg}-b_b plane. We hypothesize that the light field is more isotropic at 650 nm than at 480 nm due to a greater number of photons that are inelastically scattered in a nearly isotropic manner. Fig. 9 demonstrates this phenomenon, based on HydroLight simulations of the full radiance distribution using a chlorophyll-based bio-optical model. As we expect, at shorter wavelengths (400, 500 nm), the radiance distribution broadens slightly with depth until an asymptotic radiance distribution is achieved; the light field is still dominated by downward

travelling photons even at 50 m. At longer wavelengths (600, 700 nm), where most of the solar photons have been absorbed in the first 5 m of water, the light field becomes dominated by photons generated by inelastic scattering. At 20 m, the radiance distribution at 700 nm becomes nearly isotropic. Note that even if the inelastic scattering is isotropic (e.g., chlorophyll fluorescence or Raman scattering), the radiance is still greater looking upward than downward because the source strength is stronger above than below the selected depth. At 600 to 700 nm, the radiance distribution shows significant broadening at 40 m. As shown above, as this broadening occurs, the isosurfaces begin to merge and the radiometric inversion problem becomes more ill-posed, reducing to that of nearly one measurement trying to resolve three IOPs. This exercise demonstrates that unique spatial information provided by L_u and E_d is lost at wavelengths where inelastic scattering contributes to the light field, limiting our ability to fully resolve two IOPs. As will be seen below, a dramatic increase in the IOP retrieval error occurs at wavelengths where inelastic scattering is important.

E. Stability

Is the inverse solution stable? Do our IOP estimates change dramatically when there is a) a slight change in the optimization starting point or b) a small change in measured radiometric quantities? We shall consider each type of change in turn. To study the effect of the optimization starting point, we again performed inversions for Korea Strait data point (Table 2) and varied the starting point $\mathbf{m}_0$ on a grid surrounding the known solution for a_{pg} and b_b; scattering b was fixed at 0.225 m^{-1}, representing a 50% relative error. The absolute error $\left|\psi_{a_{pg}}\right|$ in the resulting estimate of a_{pg} was computed at each grid point and mapped in Fig. 10a. All the starting points converge near the true value (a_{pg}, b_b) = (0.05, 0.00585) m^{-1} (shown with +), with absolute error shown by

the contour region color, ranging from very small (1e-6 %) to substantial (10%). Notice that starting points in the lower-left corner where both coordinates (a_{pg}, b_b) are smaller than the true value have the lowest average absolute error. Since it is not immediately obvious why this should be so, we also computed the value of the objective function $F(\mathbf{m})$ from equations (14) and (15) as well as its gradient $\nabla F(\mathbf{m})$ from equation (16), shown in Fig. 10b. The vectors in this figure illustrate magnitude and direction of objective function gradient. Of course, the minimum of $F(\mathbf{m})$ is found at the coordinates of the true value of a_{pg}, and b_b (+) and the gradient vectors point downhill in the direction of the true value. Starting points where both coordinates are in the lower-left corner have the largest gradients, i.e., have the largest "push" to the objective function minimum, reliably achieving estimates with the lowest absolute error. These results also show that we need very little *a priori* information about the true value; starting at the smallest coordinate (a_{pg}, b_b) = (0.01, 0.001) m^{-1} does just as well as any other estimate in that region. We also found that starting points slightly larger than the true value (within 10%) also achieved acceptably small errors in the a_{pg} estimate. These results were implemented as follows:

- The starting point for the first solution wavelength (350 nm) was derived from our ancillary inversion algorithm which returns an estimate of a and b_b as well as uncertainty intervals (typically ±30-40% of the estimated value) [31]. The 350 nm starting point is always chosen as the minimum coordinate within the individual uncertainty intervals for a_{pg} and b_b, i.e., the "lower left corner" of the IOP subspace defined by the ancillary algorithm.
- The starting point for subsequent solution wavelengths is simply chosen as the estimate from the previous wavelength.

Using these methods, we estimate that maximum uncertainty of IOP retrievals based on the choice of starting point is less than 1%.

While we more fully consider the sensitivity of estimated IOPs to radiometric measurements and forward model parameters in section 5, we can quickly assess the stability of the final estimate by considering the condition number of the Jacobian at our final estimate, $\mathbf{J}(\hat{\mathbf{m}})$. Recall from equation (18) that $\mathbf{J}(\hat{\mathbf{m}})$ represents a locally linear solution to the RTE. The condition number of $\mathbf{J}(\hat{\mathbf{m}})$ (or equivalently $\mathbf{K}_m(\hat{\mathbf{m}})$) is a scalar measure of the sensitivity of the estimated parameters $\hat{\mathbf{m}}$ (the retrieved IOPs) to changes in the measured data $\mathbf{d}^{meas}$ (L_u, E_d) [65]. For the inverse problem where we attempt to retrieve all three IOPs $\mathbf{m} = [a, b_b, b]^T$, the condition number of $\mathbf{J}(\hat{\mathbf{m}})$ is $\mathcal{O}(10^{10})$ indicating that the locally linear solution to the RTE behaves badly, i.e., is ill-conditioned. In contrast, for the reduced problem where $\mathbf{m} = [a, b_b]^T$ and scattering b is supplied as a forward model parameter, the condition number of $\mathbf{J}(\hat{\mathbf{m}})$ is $\mathcal{O}(10^1)$, indicating that the reduced problem is stable and locally continuous. Therefore, by transforming our radiometric inverse problem from a three-parameter estimation to a two-parameter estimation problem, the problem is much better posed.

5. IOP Sensitivity Analysis

An important source of errors in our inversion calculations arises from uncertainty in radiometric quantities $\mathbf{d}^{meas}$ and additional model parameters **b**. Uncertainty in additional model parameters arises from the observations, instruments or models that supply latitude, longitude, time, wind speed, cloud cover and incident solar irradiance. It is important to know how changes in these quantities can affect estimates of IOPs **m**.

A. Radiometric Sensitivity

The influence of radiometric measurement uncertainty on IOP estimation uncertainty can be expressed by the 'sensitivity coefficient', defined as the ratio of the relative standard deviation of an IOP estimate = a_{pg}^{est} or b_b^{est} to the relative standard deviation of the uncertain parameter

$$S_{IOP,R} = \frac{\sigma_{IOP} / \overline{IOP}}{\sigma_R / \bar{R}}, \tag{48}$$

where R is L_u, E_d, or E_s [95]. This measure is useful in that it expresses the fractional change in an estimated IOP to a given fractional change in a radiometric quantity. For radiometric sensitivity studies, 10,000 samples of each radiometric variable $R = L_u$, E_d, or E_s were generated as uncorrelated, normally-distributed random variables $\mathcal{N}(\bar{R}, \sigma_R^2)$ for 5%, 10%, 20% and 50% radiometric error for a light field (L_u, E_d) at 10 m, where uncertainty σ_R is estimated from relative error as in equation (39). Additionally, for 5% radiometric error, radiometric samples were also generated for 5, 10, 20 and 50 m, resulting in simulations from optical depths $\tau = 2.5$ to 25. The mean (or true) values for the IOPs were based on Korea Strait data (Table 2); forward simulations were used to establish the true values for L_u and E_d. To simulate a variety of independent radiometric errors in the in-water sensors, Monte Carlo inversions of L_u and E_d were carried out together: random combinations of L_u and E_d were produced for each inversion trial with constant values for all additional forward model parameters **b**, including E_s. Monte Carlo inversions for E_s were carried out for constant values of L_u and E_d to simulate radiometric errors in a surface-mounted downwelling solar irradiance sensor or uncertainty in E_s estimates from radiative transfer models of incoming solar radiation, when a surface-mounted E_s sensor is not available.

The inversion results for radiometric variables are shown in Fig. 11 and Tables 6 – 9. At 10 m, the sensitivity coefficients of a_{pg} retrievals $S_{a_{pg},L_u}, S_{a_{pg},E_d}, S_{a_{pg},E_s}$ are ≈1 for radiometric errors of 5 to 30% in L_u, E_d or E_s (Tables6 and 8). Thus a 5% radiometric uncertainty translates into 5% a_{pg} uncertainty. The sensitivity coefficients of b_b retrievals $S_{b_b,L_u} S_{b_b,E_d}$ at 10 m are approximately double (1.78 to 2.6) those for a_{pg}, while those for incoming solar radiation S_{b_b,E_s} are also ≈1. Thus, radiometric uncertainty translates directly into IOP uncertainty. Notice that changes in IOPs are strongly negatively correlated with errors in E_d, e.g., less absorption and backscattering are predicted with increasing errors in E_d. Absorption a_{pg} also shows a slight negative correlation increasing errors in L_u, but a slight positive correlation with backscattering, which tends to increase upwelling photons. Finally, errors in both IOPs are positively correlated with errors in incident solar irradiance as the inversion compensates for too many or too few source photons.

Sensitivity coefficients for a_{pg} and b_b are constant with increasing radiometric error, consistent with a locally linear inverse solution $\hat{\mathbf{m}}$ to the RTE for a_{pg} and b_b. However, the estimates of a_{pg} and b_b show a small increase in relative error ψ as radiometric error increases, indicating limits to this local linearity. Generally, there is a marked decrease in the sensitivity coefficients with depth (e.g., $S_{a_{pg},L_u}, S_{a_{pg},E_d}, S_{a_{pg},E_s}$ ≈ 2.5 to 0.2, see Tables 7 and 9). Thus, IOP uncertainty can be reduced by a) making deeper radiometric measurements and b) averaging IOP estimates from a number of radiometric measurements, if and only if radiometric error is due to random processes rather than systematic bias.

B. Forward Model Parameter Sensitivity

A similar Monte Carlo study was carried out to assess the sensitivity of retrieved IOPs to changes to forward model parameters. 1000 samples were computed and Monte Carlo inversions carried out separately for each parameter with $\theta_s = \mathcal{N}(45^\circ, (4.5^\circ)^2)$, $cloud = \mathcal{N}(50\%, (30\%)^2)$, $U_{10} = \mathcal{N}(7\ \mathrm{m\ s^{-1}}, (3\ \mathrm{m\ s^{-1}})^2)$ and $b = \mathcal{U}(0.2, 0.8)\ \mathrm{m^{-1}}$ using the same 10 m radiometric data used for other sensitivity analyses. In all cases, optimizations had bound constraints **l**, **u** for a_{pg}, b_b and b_{pg} from 0.1× to 10× the known value with the starting point $\mathbf{m}_0$ at the lower bound. All optimizations terminated with a global minimum in $F(\mathbf{m})$.

The relationships between IOPs and additional model parameters θ_s, *cloud*, and U_{10} are reasonably linear (Fig. 2k-o) over the range of simulation, while for the scattering coefficient b, the relationship is nonlinear. We observe many of the same features in the IOP sensitivity analysis as we did in the sensitivity analysis developed to develop the forward model parameter sensitivity matrix $\mathbf{K_b}$ (Fig. 2a-e). As with $\mathbf{K}_\mathrm{b}$, IOP estimates are most sensitive to uncertainty in solar zenith angle θ_s and incident solar irradiance E_s, although, as expected, b_b estimates are somewhat sensitive to errors in scattering b. The study also confirms the general understanding in ocean optics that uncertainty in scattering b has little influence on the ability to retrieve quality estimates of absorption a_{pg} (Fig. 2n).

For the purposes of computing sensitivity coefficients for these additional model parameters and comparing them to the radiometric sensitivity coefficients, we calculated simple linear fits to IOP-parameter relationships over parameter regions for which the sensitivity is significant, except a quadratic fit was computed for scattering b. The sensitivity coefficient is computed as

$$S_{IOP,b_i} = \frac{dIOP}{d\mathbf{b}_i}\frac{\bar{\mathbf{b}}_i}{\overline{IOP}}, \tag{49}$$

where IOP = a_{pg} or b_b and additional parameter $\mathbf{b}_i = \theta_s$, *cloud*, U_{10}, or scattering b. (The sensitivity to E_s was considered in the section above.) The $dIOP/d\mathbf{b}_i$ term is simply the slope of linear fit over the selected region and the $\bar{\mathbf{b}}_i / \overline{IOP}$ term is the ratio of the midpoints of the selected region. The sensitivity of retrieved IOPs to scattering b was evaluated over the range simulated b values. The resulting sensitivity coefficients are summarized in Table 10 and range in absolute value from 0.0012 to 0.34. Notice that all of the sensitivity coefficients for the selected ranges of additional model parameters are small compared to the radiometric sensitivity coefficients, which range from 0.22 to 3.36. The largest sensitivity coefficient is S_{a_{pg},θ_s} = -0.34, i.e., a 10% error in the solar zenith angle can lead to a 3.4% uncertainty in a_{pg}; this sensitivity coefficient is not truly linear and we expect even greater sensitivity when θ_s is greater than 60°. With GPS positioning and calibrated clocks, even autonomous instruments are able to minimize solar zenith angle estimation errors, so we expect IOP uncertainty from θ_s to be negligible despite the large sensitivity. It is comparatively difficult to estimate cloud cover accurately from manual observations or from 1-km resolution satellite products [96, 97]. With $S_{a_{pg},cloud}$ = 0.065, a 30% error in the estimation of cloud fraction > 0.25 can yield an additional 2% uncertainty in the estimation of a_{pg}. Average wind speed sensitivity coefficient $S_{a_{pg},U_{10}}, S_{b_b,U_{10}}$ are quite small (≈0.001) over the range of EcoLight sea surface files (U_{10} = 0-15 m s^{-1}). The sensitivity of retrieved a_{pg} to changes is dependent on the modeled value of the scattering coefficient *b;* values of $S_{a_{pg}}(b)$ are negative, ranging from -0.03 to -0.1; an overestimate of b as a forward model parameter will lead to a small underestimate in absorption. Since spectral b is derived from a

single-wavelength measurement of attenuation, this also implies that the sensitivity of a_{pg} to the choice of spectral slope for attenuation, γ in equation (22), is small. The range of sensitivity of estimates of b_b to the value of the scattering coefficient b, $S_{b_b}(b)$, was larger, ranging from -0.1 to -0.33. Errors in the scattering coefficient b also cause errors in the selection of the scattering phase function β, since EcoLight selects the Fournier-Forand phase function based on backscattering ratio b_{bp}/b .

6. The NAB08 Data Set

We tested our algorithm's performance using depth profiles of $L_u(z)$, $E_d(z)$, $a(z)$, and $b_b(z)$ from a calibration campaign carried out as part of the 2008 North Atlantic Bloom Experiment (NAB08) in support of long term (51 d) autonomous physical, optical, and radiometric measurements from a Lagrangian float [11, 49]. The data were obtained at six process cruise stations during the spring bloom of May 2008, representing two distinct phytoplankton bloom communities: a large diatom-dominated community (*Chl* ~2-5 mg m^{-3}) during the bloom and a small picoeukaryote-dominated community (*Chl* < 1 mg m^{-3}) following the bloom peak.

Temperature, salinity, pressure (CTD), and bio-optical profiles to approximately 80 m depth were performed during a cruise on the *R/V Knorr* from 1-22 May 2008. A Satlantic Profiler II free-falling optical profiler was used to measure downward spectral irradiance, $E_d(z,\lambda)$, and upward spectral radiance, $L_u(z,\lambda)$ at 3.3 nm increments from 350 to 800 nm with a spectral accuracy of 0.3 nm and a spectral bandwidth of 10 nm. Profiles were taken within 1.5 h of local noon. Hyperspectral radiometric data were processed using 1 m bins and 2 nm increments with ProSoft 8-RC5 software (Satlantic, Inc.) to determine $L_u(z,\lambda)$ and $E_d(z,\lambda)$, and subsequently

re-interpolated at M = 105 3.3 nm increments from 354.0 to 697.2 nm. Measured radiometric quantities were not corrected for out-of-band stray light or thermal responsivity; the water column temperature gradient was small (8.5-9.5° C in the top 50 m). Only small (<1%) changes were noted between pre- and post-cruise calibration files. Radiometric measurements were discarded for $E_d(z,\lambda) < 10^{-2}$ μW cm^{-2} nm^{-1}; below this level, L_u measurements were either below the noise equivalent radiance of the Satlantic HyperOCR upwelling radiance sensor or extremely noisy. Measurements were also discarded for tilt angles > 5°.

In situ IOPs were obtained within 15 minutes of radiometric measurements. In two separate casts, a WET Labs AC-9 measured total absorption $a_t^{ac-9}(z,\lambda)$ and 0.2μm filtered water absorption $a_g^{ac-9}(z,\lambda)$; a WET Labs BB2F measured $b_b(z)$ at 470 and 700 nm; a Sea-Bird Electronics SBE25 CTD measured temperature, salinity, and pressure. The instruments were factory calibrated prior to field deployment. Manufacturer-recommended protocols were used to track instrument calibration during the process cruise. Daily clean water AC-9 calibrations were conducted whenever possible; however, sampling schedules did not consistently allow for daily calibration. Under these cases, the most recent water calibration was used. The maximum period without a calibration was three days. The drift during this study was negligible ($< 4\%$) and the precision of the AC-9 data was ± 0.01 m^{-1}, which corresponds to an average uncertainty of about 17% in the waters under consideration. Absorption data were subsequently corrected for temperature and salinity [98] and the absorption coefficient was corrected for scattering using the wavelength-dependent method [99]. The precision of the backscattering data is no better than 0.0005 m^{-1}, based on NAB08 backscattering meter intercalibration [100]. Absorption and backscattering data were binned into 1 m intervals and then averaged within each bin. Measured

IOPs were typically homogeneous from 0 to 30 m (e.g., Fig. 12). Some IOP profiles showed sharp changes deeper than 30 m, corresponding to the bottom of the mixed layer; outliers from these regions with different IOPs appeared as outliers in IOP estimates. Example radiometric and IOP profiles at Station 34 are shown in Fig. 12.

During the optimization procedure, the measured light field $\mathbf{d}^{meas}$ was compared to the estimated light field $\mathbf{d}^{est} = \mathbf{G}(\mathbf{m}, \mathbf{b})$ using the objective function **F** described in equations (13), (14), and (15). The model parameters **b** used for estimation of NAB08 light fields $\mathbf{d}^{est}$ are shown in Table 11. The final light field estimate $\hat{\mathbf{d}}$ was compared to the observed light field $\mathbf{d}^{meas}$. The resulting optimal IOP estimates $\hat{\mathbf{m}}$ were compared to IOPs measured by the AC-9 and the BB2F and vertically averaged over the same depths as radiometric measurements. For example, for AC-9 absorption

$$\overline{a}_{pg}^{ac-9}(\lambda) = \frac{1}{N}\sum_{i=1}^{N}\left[a_t^{ac-9}(z_i,\lambda) - a_w(\lambda)\right]. \tag{50}$$

At three stations, water samples were collected using the ship's CTD rosette within an hour of the optical casts and subsequently ship-board measurements of spectrophotometric filter pad absorption were carried out with ~1 nm resolution [101]. Spectrophotometric measurements of absorption by chromophoric dissolved organic material (CDOM, 10 cm pathlength) were also made at two stations. To compare spectrophotometric absorption measurements to the absorption $a_{pg}(\lambda)$ retrieved from radiometry as well as AC-9 measurements, we compute

$$a_{pg}^{spec}(z,\lambda) = a_{part}^{spec}(z,\lambda) + a_{cdom}^{spec}(z,\lambda). \tag{51}$$

At one station where spectrophotometric CDOM absorption was not available, wavelength-dependent CDOM absorption was estimated by [102]

$$a_{CDOM}^{est}(\lambda) = a_g(\lambda_0)\exp\left[-S_g(\lambda-\lambda_0)\right], \tag{52}$$

where $a_g(\lambda_0)$ and S_g were estimated via linear regression of log-transformed, depth-averaged filtered water absorption data $\overline{a}_g^{ac-9}(\lambda)$ from the AC-9.

7. NAB08 Results

We applied our radiometric inversion methodology to the NAB08 data set. Only optimizations at wavelengths greater than 500 nm were run with EcoLight's inelastic scattering enabled. We used EcoLight's default value for the wavelength dependence of the Raman scattering coefficient. Estimates of chlorophyll concentration derived from the BB2F chlorophyll fluorometer were supplied to EcoLight to estimate wavelength-dependent chlorophyll fluorescence. Tight bound constraints for backscattering were not needed and resulting bounds were set from 0.5× to 2.0× the value modeled from BB2F measurements and equation (20). Scattering *b* is derived from a single-wavelength measurement of attenuation *c*(650) as described previously. Other forward model parameters and solution depths for each station are shown in Table 11.

Comparison of radiometric measurements and estimates across all wavelengths and depths at Station 34 are shown in Fig. 13 and summarized for all stations in Table 12. The results show that the optimization procedure does well matching the measured spectra between 350 and 575 nm but has difficulty in matching the measured light field beyond 575 nm at depths below 16 m for E_d (Fig. 13a) and at any depth for L_u (Fig. 13b). Given the poor radiometric matches at longer wavelengths, the summary statistics in Table 12 are confined to wavelengths less than 555

nm. Radiometric matches, other than Station 44, show little bias in L_u ($\overline{\psi} < 1\%$) and a slight positive bias for E_d ($\overline{\psi} < 5\%$). Average absolute error $\overline{|\psi|}$ in $L_{\underline{u}}$ and E_d are less than 6% and 9%, respectively, within the 350-575 nm region. Average relative error and absolute error in light field estimates are high at Station 44, indicating a large source estimation error, possibly ship shadowing during the radiometric cast. Examining the in-water reflectance $R_L = L_u / E_d$ for Station 34 (Fig. 13c), it is obvious that depth-dependent inelastic scattering contributions to the light field begin just after 575 nm, i.e., where R_L deviates from roughly a constant value with depth. EcoLight reproduces some features of the light field beyond 575 nm; both the initial increase at 575 (Raman scattering) and the chlorophyll fluorescence peak at 680 are reproduced, but with significant relative errors.

The IOP retrieval results for all six NAB08 stations are shown in Fig. 14 (absorption) and Fig. 15 (backscattering), and are also summarized in Table 12. The grey shaded areas around the mean IOP estimates (blue dots) represents the 95% confidence interval based on the error analysis presented in section 3; the varying widths from wavelength to wavelength and station to station are due to wavelength-dependent measurement and forward model parameter errors as well as lack of strict vertical homogeneity of IOPs at some stations. In general, a_{pg} and b_{bp} retrievals below wavelengths with significant contributions from inelastic scattering were very good, and retrievals above ≈575 nm were poor. Between 575 and 650 nm, the optimization procedure consistently drives absorption a_{pg} to zero and increases particulate backscattering b_{bp} in an attempt to match the measured light field; at these wavelengths, EcoLight often generates more light than was measured, perhaps because the assumed quantum efficiency of chlorophyll fluorescence was too high. Above 650 nm, inelastically scattered light from chlorophyll fluorescence generates a larger portion of the light field at the measured depths. While EcoLight

generates inelastically scattered light corresponding to chlorophyll fluorescence from 650 to 700 nm, nevertheless absorption is overestimated and particulate backscattering is underestimated. As a result, we will disregard the absorption and backscattering retrievals above 575 nm; uncertainty estimates in these regions should also be disregarded.

Absorption estimates compare well to AC-9 absorption measurements at wavelengths less than or equal to 575 nm, with an average absolute error $\overline{|\psi|}$ of 2-4%, except at Station 44 where $\overline{|\psi|}$ is almost 8%. The absorption estimates are biased 3 to 5% low at all stations but one (Station 80) relative to AC-9 measurements. Analysis of the *t*-statistic for comparing two independent sample means (our estimate vs. the depth-averaged AC-9 measurement) indicates that the overlapping confidence intervals are statistically significant [76]. At three stations (34, 94, and 128), spectrophotometric absorption measurements a_{pg}^{spec} was estimated according to equations (51) and (52); see Fig. 14. Note that the scan for each filter pad rotation is shown as a visual assessment of the variability in spectrophotometric absorption measurements; between 400 and 550 nm, the variability in spectrophotometric measurements is comparable to the standard deviation of absorption estimates derived from radiometry. (Remember that the grey contours in Fig. 14 indicate 95% confidence intervals, which are roughly *two* standard deviations wide about the mean estimate.) The average RMS error between radiometric absorption estimates and spectrophotometric absorption measurements is less than 0.01 m^{-1} at Station 34 and ≈0.003 m^{-1} at Stations 94 and 128. Matchups with spectrophotometric measurements interpolated to radiometric measurement wavelengths are shown in Fig. 16a and confirm the successful estimation of hyperspectral absorption from in-water radiometry at wavelengths without source contributions from inelastic scattering.

We have no means to directly measure hyperspectral backscattering; in fact no such instrumentation exists. The only validation of NAB08 particulate backscattering estimates (Fig. 15) are BB2F measurements at 470 and 700 nm; matchups are shown in Fig. 16b. In general, particulate backscattering b_{bp} is underestimated at 470 nm; the overlapping confidence intervals for $b_{bp}(470)$ at stations 80, 94, and 128 are statistically significant. Since the b_{bp} retrievals are not accurate above 575 nm, the comparison of retrievals to the 700 nm measurements can be disregarded. However, the observed decreasing trend of b_{bp} measurements at 470 and 700 nm are consistent with the decreasing trend of b_{bp} retrievals from 350 to 575 nm.

Detailed error budget for absorption and backscattering estimates for NAB08 Station 34 are shown in Fig. 17. The absorption error budget is dominated by forward model parameter error (red line in Fig. 17e); as we saw in Section 5, absorption estimates are most sensitive to incident solar irradiance E_s. Error ellipses generally show significant positive correlation between errors in a_{pg} and b_b below 500 nm and little correlation between 500-575 nm. Beyond 575 nm at Station 34, retrievals have failed and reversal in the orientation of the error ellipses may be used as a diagnostic for those failed retrievals. The backscattering error budget is more spectrally variable: below 450 nm, the error budget is dominated by forward model parameter error, while above 450 nm radiometric measurement error dominates. Backscattering error ellipses also show reversed correlation for failed backscattering retrievals above ≈555 nm. Note that the error ellipses show the same information in both Fig. 17d and Fig. 17e, because they are derived from the same total error covariance matrix $\mathbf{S}_t$ of equation (27). An unquantified source of error at each station is oceanic variability; there may have been advection and/or changes in ship position during sequential profiling for radiometry, IOPs, and water samples.

8. Discussion

In this paper, we have demonstrated that hyperspectral estimates of absorption and backscattering can be computed from hyperspectral radiometry, along with an error budget and confidence intervals based on estimates of errors in radiometry and additional forward model parameters. We have also shown that estimation of IOPs from radiometry is a mixed-determined problem [103], i.e., absorption and backscattering may be resolved, but total scattering may not and is ambiguous. Formally, we state that the scattering coefficient lies in the null space of our model $\mathbf{G}(\mathbf{m},\mathbf{b})$. A variety of strategies have been proposed by Defoin-Platel and Chami to "tackle the ambiguity problem" [91] and we applied some of them here. First, we followed the enrichment strategy, transforming the ill-posed problem into a well-posed problem by a) retaining the distinct information about the light field provided by both L_u and E_d in our spectral matching criterion and b) constraining the optimization with a single attenuation measurement $c(650)$ and a bio-optical model. The additional use of one or two wavelengths of backscattering and chlorophyll fluorescence was unneeded but provided reassurance during algorithm development as optimization stopping criteria (Table 1) were tuned. Second, following the divide and conquer strategy, we restricted the solution domain to realistic natural values of IOPs. Third, with a nod to the integration strategy, we studied the propagation of probability distributions of simulated radiometric data through our inverse algorithm to explore the linearity of our algorithm near the estimated IOPs.

A formal error analysis for IOP retrieval was carried out. The error was separated into three components: (1) random error in our radiometric measurements, (2) model error due to uncertain forward model parameters, and (3) noise introduced by the inversion process. Each of the components was evaluated using straightforward *a priori* model simulation. We found that

IOP estimates were largely insensitive to errors in wind speed, but errors in solar zenith angle θ_s and radiometry (L_u, E_d, E_s) do matter and are a large portion of the error budgets. Our success therefore relies on having calibrated radiometric measurements and sufficiently precise estimates of position and time. The resulting errors in our estimates of absorption are only mildly sensitive to uncertainty in the scattering estimate derived from the single attenuation measurement (Fig. 2n).

The comparison of spectrophotometric and AC-9 *in situ* measurements of particulate plus dissolved absorption $a_{pg}(\lambda)$ demonstrates that our retrieval method is valid between 350 and 575 nm. Below 575 nm, we can retrieve absorption with 95% confidence to approximately ± 0.01 m^{-1}, similar to the uncertainty of AC-9 measurements (± 0.01 m^{-1}). At very low levels of absorption $\mathcal{O}(10^{-3})$ m^{-1}, retrieval noise introduced by our algorithm noticeably increases to 2-3% of the IOP estimate. At wavelengths greater than 575 nm, absorption retrievals fail because the $a_{pg}(\lambda)$ signal becomes too weak for this method to detect in the presence of the pure water absorption that is two to three orders of magnitude larger. The failed absorption retrievals in turn cause complex artifacts in $b_b(\lambda)$ between 575 and 650 nm and underestimates $b_b(\lambda)$ from 650 – 700 nm.

A major assumption in our analysis was that errors in measurements and forward model parameters can be estimated as zero-mean normal random variables. Our error analysis demonstrated that near the IOP estimate, our model $\mathbf{G}(\mathbf{m}, \mathbf{b})$ (the RTE) is locally linear. With these two conditions, IOP estimates found by minimizing the least-square sum of differences of log-transformed measured and estimated radiometric quantities (equation (13)) is a maximum likelihood estimate, i.e., the optimized value for the IOPs maximize the probability that the observed light field was in fact observed [103]. If the least-square error criterion is retained for

other assumptions about the radiometric and/or forward model parameter error distributions, a Monte Carlo approach should first be taken to validate these maximum likelihood IOP estimates against the mean of the propagated error distribution. The total error covariance matrix revealed that errors in the IOP estimates are correlated. Care should be taken when interpreting the uncertainty intervals for jointly retrieved IOPs; the display of confidence regions as error ellipses helps to convey this information.

Even with a forward model that incorporates inelastic scattering via models of Raman scattering and chlorophyll fluorescence, we were unable to reliably retrieve IOPs at wavelengths where Raman scattering or fluorescence represents a significant fraction of the total light (e.g., greater than 575 nm in Fig. 17). Forward model parameters controlling Raman scattering are well known [104] and are not a likely culprit. It is possible that CDOM fluorescence was needed for closure, as it was not enabled in our EcoLight forward model. To test this idea, we enabled CDOM fluorescence in EcoLight and completed several inversions based on the NAB08 data. Concentrations of CDOM during the 2008 North Atlantic Bloom were nearly undetectable at wavelengths >600 nm [9],and there was little effect on our IOP retrievals when CDOM fluorescence was included in the EcoLight simulations. We believe that both a) inelastic processes and b) an increase in absorption by water make it difficult for our method to resolve IOPs when the a_{pg} signal is relatively small. Another cause for the failed retrievals at wavelengths beyond 575 nm is that the distinct information provided by L_u and E_d is lost as the light field becomes dominated by inelastic scattering, resulting in an increasingly isotropic light field, especially at depths below 30 m. (Remember the folding of the L_u and E_d isosurfaces at 650 nm in Fig. 7.) In other words, two degrees of freedom start to collapse to one degree of freedom, creating an ill-posed problem that is both computationally unstable and without guarantee of a

unique solution in this spectral region. Below these wavelengths, retaining L_u and E_d as separate measurements creates a well-posed problem (2 parameters, 2 unknowns) at the expense of requiring calibrated radiometric measurements.

The value of hyperspectral retrievals can be understood by examining the phytoplankton pigment absorption bands in the retrieved absorption spectra. To do so, we computed particulate absorption by removing CDOM absorption, i.e., $a_p(\lambda) = a_{pg}(\lambda) - a_g(\lambda)$, where hyperspectral $a_{\mathrm{pg}}(\lambda)$ was estimated from radiometry, and CDOM absorption a_g was estimated from AC-9 measurements, equation (52), interpolation and extrapolation. Plots of estimated $a_{\mathrm{pg}}(\lambda)$ for each of the six NAB08 stations are shown in Fig. 18, along with their second derivative spectra [105, 106]. We find many of the same distinct spectral absorption features that were found by Gordon [21] at a San Diego station: selective absorption by phytoplankton pigments, including chlorophyll *a* (370-387, 412-416, 437 nm), chlorophyll *c* (466 nm) and carotenoids (499-542 nm) the later perhaps indicative of the diatoms [107], known to be blooming in the study area [108]. There is even a hint of a absorption peak at 565 nm at a few stations, possibly associated with the marine cyanobacterium *Synechococcus*.

9. Conclusion

We conclude that hyperspectral retrievals of absorption and backscattering are possible when upwelling radiance L_u and downwelling irradiance E_d measurements are integrated with a single-wavelength measurement of attenuation c. We have shown that such retrievals are unambiguous, unlike retrievals from reflectance, which are inherently ambiguous. Retrievals fail at wavelengths and depths where the pure water absorption signal dominates and inelastic scattering reduces the distinct spatial information otherwise provided by L_u and E_d. Since low-power, hyperspectral

radiometers and single-wavelength attenuation meters are commercially available and the retrieval method can provide distinct information about the presence of specific phytoplankton pigments, this approach could be widely deployed on autonomous and Lagrangian platforms.

10. Acknowledgements

E. Rehm was supported in this work by the National Science Foundation grants OCE0628379 and OCE0628107, and NASA grants NNX08AL92G and NNX-10AP29H. C. Mobley was supported by HydroLight revenues. This work would not have been possible without the help of Emily Kallin, who assisted with the collection of all of the NAB08 bio-optical profile data and performed the spectrophotometric measurements used here and Mary Jane Perry and Emmanuel Boss who loaned their bio-optical and Satlantic radiometric profilers. This work is part of the lead author's doctoral research which would not have been possible without the insight and support of Eric D'Asaro. We wish to thank Andy Ganse and David Trossman for statistical insight and the captain, crew, and technicians of the R.V. Knorr.

11. References

1. K. S. Johnson, et al., "Observing biogeochemical cycles at global scales with profiling floats and gliders: Prospects for a global array," Oceanography **22**, 216-225 (2009).

2. D. Rudnick and M. Perry, eds., *ALPS: Autonomous and Lagrangian platforms and sensors, Worskshop Report* (2003), http://www.geo-prose.com/ALPS/.

3. C. A. Brown, et al., "Mapping coastal optical and biogeochemical variability using an autonomous underwater vehicle and a new bio-optical inversion algorithm," Limnol. Oceanogr. Methods **2**, 262-281 (2004).

4. H. Claustre, et al., "Bio-optical profiling floats as new observational tools for biogeochemical and ecosystem studies," in *Proceedings of the OceanObs '09: Sustained Ocean Observations and Information for Society Conference,* J. Hall, D. E. Harrison, and D. Stammer, eds. (**ESA Publ. WPP-306**, 2010).

5. IOCCG, "Bio-Optical Sensors on Argo Floats," in *Reports of the International Ocean-Colour Coordinating Group,* H. Claustre, ed. (IOCCG **11**, 2011).

6. B. Mitchell, M. Kahru, and J. Sherman, "Autonomous temperature-irradiance profiler resolves the spring bloom in the Sea of Japan," in *Proceedings, Ocean Optics XV,* (Monaco, 2000).

7. E. Boss, et al., "Observations of pigment and particle distributions in the western North Atlantic from an autonomous float and ocean color satellite," Limnol. Oceanogr. **53**, 2112-2122 (2008).

8. W. J. Bagniewski, et al., "Optimizing models of the North Atlantic spring bloom using physical, chemical and bio-optical observations from a Lagrangian float," Biogeosciences **8**, 1291-1307 (2011).

9. I. Cetinić, et al., "Particulate organic carbon and inherent optical properties during 2008 North Atlantic Bloom Experiment," J. Geophys. Res. (C Oceans) **117**, C06028 (2012).

10. X. Xing, et al., "Combined processing and mutual interpretation of radiometry and fluorimetry from autonomous profiling Bio-Argo floats: Chlorophyll a retrieval," J. Geophys. Res **116**, C06020 (2011).

11. M. Alkire, et al., "Estimates of net community production and export using high-resolution, Lagrangian measurements of O2, NO3−, and POC through the evolution of a spring diatom bloom in the North Atlantic," Deep Sea Res., Part I **64**, 157-174 (2012).

12. X. Xing, et al., "Combined processing and mutual interpretation of radiometry and fluorometry from autonomous profiling Bio-Argo floats: 2. Colored dissolved organic matter absorption retrieval," J. Geophys. Res. **117**, C04022 (2012).

13. IOCCG, *Remote sensing of inherent optical properties: fundamentals, tests of algorithms, and applications*, Reports of the International Ocean-Colour Coordinating Group (IOCCG, 2006), Vol. 5.

14. H. Lavigne, et al., "Towards a merged satellite and in situ fluorescence ocean chlorophyll product," Biogeosciences **9**, 2111-2125 (2012).

15. C. S. Roesler and M. J. Perry, "In situ phytoplankton absorption, fluorescence emission, and particulate backscattering spectra determined from reflectance," J. Geophys. Res. (C Oceans) **100**, 13279-13294 (1995).

16. A. M. Ciotti, M. R. Lewis, and J. J. Cullen, "Assessment of the relationships between dominant cell size in natural phytoplankton communities and the spectral shape of the absorption coefficient," Limnol. Oceanogr. **47**, 404-417 (2002).

17. R. J. Geider, H. L. MacIntyre, and T. M. Kana, "A dynamic model of photoadaptation in phytoplankton," Limnol. Oceanogr. **41**, 1-15 (1996).

18. D. Stramski, et al., "The role of seawater constituents in light backscattering in the ocean," Prog. Oceanogr. **61**, 27-56 (2004).

19. A. L. Whitmire, et al., "Spectral backscattering properties of marine phytoplankton cultures," Opt. Express **18**, 15073-15093 (2010).

20. W. Zhou, et al., "Variations in the optical scattering properties of phytoplankton cultures," Opt. Express **20**, 11189-11206 (2012).

21. H. R. Gordon, et al., "Spectra of particulate backscattering in natural waters," Opt. Express **17**, 16192-16208 (2009).

22. C. D. Mobley, *Light and water: radiative transfer in natural waters* (Academic Press, San Diego, 1994).

23. N. J. McCormick, "Inverse radiative transfer problems: a review," Nucl. Sci. Eng **112**, 185-198 (1992).

24. H. R. Gordon, "Inverse methods in hydrologic optics," Oceanologia **44**, 9-58 (2002).

25. A. H. Barnard, J. R. V. Zaneveld, and W. S. Pegau, "In Situ Determination of the Remotely Sensed Reflectance and the Absorption Coefficient: Closure and Inversion," Appl. Opt. **38**, 5108-5117 (1999).

26. M. Stramska, et al., "Estimation of the absorption and backscattering coefficients from in-water radiometric measurements," Limnol. Oceanogr. **45**, 628-641 (2000).

27. H. Loisel and D. Stramski, "Estimation of the Inherent Optical Properties of Natural Waters from the Irradiance Attenuation Coefficient and Reflectance in the Presence of Raman Scattering," Appl. Opt. **39**, 3001-3011 (2000).

28. Z. Lee, K. L. Carder, and R. A. Arnone, "Deriving Inherent Optical Properties from Water Color: a Multiband Quasi-Analytical Algorithm for Optically Deep Waters," Appl. Opt. **41**, 5755-5772 (2002).

29. D. McKee, A. Cunningham, and S. Craig, "Estimation of absorption and backscattering coefficients from in situ radiometric measurements: theory and validation in case II waters," Appl. Opt. **42**, 2804-2810 (2003).

30. V. Garg and I. Chaubey, "A computationally efficient inverse modelling approach of inherent optical properties for a remote sensing model," Int. J. Remote Sens. **31**, 4349-4371 (2010).

31. E. Rehm and N. J. McCormick, "Inherent optical property estimation in deep waters," Opt. Express **19**, 24986-25005 (2011).

32. H. R. Gordon, O. B. Brown, and M. M. Jacobs, "Computed Relationships Between the Inherent and Apparent Optical Properties of a Flat Homogeneous Ocean," Appl. Opt. **14**, 417-427 (1975).

33. Z. Lee, et al., "Uncertainties of optical parameters and their propagations in an analytical ocean color inversion algorithm," Appl. Opt. **49**, 369-381 (2010).

34. A. Morel, et al., "Natural variability of bio-optical properties in Case 1 waters: attenuation and reflectance within the visible and near-UV spectral domains, as observed in South Pacific and Mediterranean waters," Biogeosciences **4**, 913-925 (2007).

35. S. A. Garver and D. A. Siegel, "Inherent optical property inversion of ocean color spectra and its biogeochemical interpretation 1. Time series from the Sargasso Sea," J. Geophys. Res. (C Oceans) **102**, 18607-18618,18625 (1997).

36. S. Maritorena and D. A. Siegel, "Consistent merging of satellite ocean color data sets using a bio-optical model," Remote Sens. Environ. **94**, 429-440 (2005).

37. S. Maritorena, et al., "Merged satellite ocean color data products using a bio-optical model: Characteristics, benefits and issues," Remote Sens. Environ. **114**, 1791-1804 (2010).

38. Z. Tao, N. J. McCormick, and R. Sanchez, "Ocean source and optical property estimation from explicit and implicit algorithms," Appl. Opt. **33**, 3265-3275 (1994).

39. H. R. Gordon and G. C. Boynton, "Radiance-irradiance inversion algorithm for estimating the absorption and backscattering coefficients of natural waters: homogeneous waters," Appl. Opt. **36**, 2636-2641 (1997).

40. H. R. Gordon and G. C. Boynton, "Radiance–irradiance inversion algorithm for estimating the absorption and backscattering coefficients of natural waters: vertically stratified water bodies," Appl. Opt. **37**, 3886-3896 (1998).

41. G. C. Boynton and H. R. Gordon, "Irradiance Inversion Algorithm for Estimating the Absorption and Backscattering Coefficients of Natural Waters: Raman-Scattering Effects," Appl. Opt. **39**, 3012-3022 (2000).

42. R. Spurr, et al., "Simultaneous retrieval of aerosols and ocean properties: A classic inverse modeling approach. I. Analytic Jacobians from the linearized CAO-DISORT model," J. Quant. Spectrosc. Radiat. Transfer **104**, 428-449 (2007).

43. C. D. Rodgers, *Inverse methods for atmospheric sounding: theory and practice*, Series on atmospheric, oceanic and planetary physics (World Scientific, River Edge, N.J., 2000).

44. W. Li, et al., "Simultaneous retrieval of aerosol and ocean properties by optimal estimation: SeaWiFS case studies for the Santa Barbara Channel," Int. J. Remote Sens. **29**, 5689-5698 (2008).

45. R. Spurr, et al., "Error analysis for simultaneous retrieval of marine and aerosol properties from SeaWiFS," in *Proceedings of Ocean Optics XVIII,* (Montreal, Canada, 2006).

46. C. D. Mobley, et al., "Interpretation of hyperspectral remote-sensing imagery by spectrum matching and look-up tables," Appl. Opt. **44**, 3576-3592 (2005).

47. G. Chang, et al., "The new age of hyperspectral oceanography," Oceanography **17**, 22-29 (2004).

48. C. D. Mobley, "Fast light calculations for ocean ecosystem and inverse models," Opt. Express **19**, 18927-18944 (2011).

49. E. A. D'Asaro, et al., "The 2008 North Atlantic Spring Bloom Experiment I: Overview and Strategy," EOS Trans. Am. Geophys. Union **89**, Fall Meeting Supplement, Abstract OS24A-08 (2008).

50. R. A. Leathers and N. J. McCormick, "Ocean inherent optical property estimation from irradiances," Appl. Opt. **36**, 8685-8698 (1997).

51. P. Wang, E. S. Boss, and C. Roesler, "Uncertainties of inherent optical properties obtained from semianalytical inversions of ocean color," Appl. Opt. **44**, 4074-4085 (2005).

52. J. H. Smart, "World-wide ocean optics database (WOOD)," Oceanography **13**, 70-74 (2000).

53. P. J. Werdell, et al., "The SeaWiFS bio-optical archive and storage system (SeaBASS): Current architecture and implementation," (NASA Goddard Space Flight Center **NASA/TM-2002-211617**, Greenbelt, MD, 2002).

54. P. J. Werdell and S. W. Bailey, "An improved in-situ bio-optical data set for ocean color algorithm development and satellite data product validation," Remote Sens. Environ. **98**, 122-140 (2005).

55. A. Mahadevan, et al., "Eddy-Driven Stratification Initiates North Atlantic Spring Phytoplankton Blooms," Science **337**, 54-58 (2012).

56. C. D. Mobley, et al., "Comparison of numerical models for computing underwater light fields," Appl. Opt. **32**, 7484-7504 (1993).

57. C. D. Mobley, "Ocean Optics Web Book: Hydrolight" (2011), retrieved August 1, 2012, http://www.oceanopticsbook.info/view/radiative_transfer_theory/level_2/hydrolight.

58. G. R. Fournier and J. L. Forand, "Analytic phase function for ocean water," in *Ocean Optics XII,* J. S. Jaffe, ed. (Proc. SPIE **2258**, 1994), pp. 194-201.

59. C. D. Mobley, L. K. Sundman, and E. Boss, "Phase Function Effects on Oceanic Light Fields," Appl. Opt. **41**, 1035-1050 (2002).

60. S. B. Hooker, et al., *NASA strategic planning document: A comprehensive plan for the long-term calibration and validation of oceanic biogeochemical satellite data* (National Aeronautics and Space Administration, Goddard Space Flight Center, 2007).

61. J. L. Mueller, et al., "Ocean Optics Protocols for Satellite Ccean Color Sensor Validation, Revision 4, Volume II: Instrument Specifications, Characterization and Calibration," NASA Tech. Memo. NASA/TM-2003-21621 (2003).

62. K. J. Voss, et al., "An Example Crossover Experiment for Testing New Vicarious Calibration Techniques for Satellite Ocean Color Radiometry," J. Atmos. Oceanic Technol. **27**, 1747-1759 (2010).

63. *MATLAB Optimization Toolbox™ 5 User's Guide* (The MathWorks, Inc., Natick, MA, 2010).

64. The HydroLight/EcoLight software, as supplied by Sequioa Scientific, Inc., includes FORTRAN source code. Using the MATLAB MEX gateway (http://www.mathworks.com/help/techdoc/matlab_external/f33356.html), EcoLight software was modified to create a shared library that allows EcoLight to run from a MATLAB script or command line and return results as a MATLAB structure.

65. R. C. Aster, B. Borchers, and C. H. Thurber, *Parameter estimation and inverse problems,* 2nd ed. (Academic Press, 2012).

66. A. Morel, "Diffusion de la lumière par les eaux de mer: Résultats experimentaux et approach théoretique," in *Optics of the sea,* (AGARD Lect. Ser. **61**, 1973), pp. 3.1.1-3.1.76.

67. P. Diehl and H. Haardt, "Measurement of the spectral attenuation to support biological research in a “plankton tube” experiment," Oceanol. Acta **3**, 89-96 (1980).

68. E. Boss, M. S. Twardowski, and S. Herring, "Shape of the particulate beam attenuation spectrum and its inversion to obtain the shape of the particulate size distribution," Appl. Opt. **40**, 4885-4893 (2001).

69. A. Gelb, *Applied Optimal Estimation* (The Analytic Science Corporation, MIT Press, 1974).

70. J. Worden, et al., "Predicted errors of tropospheric emission spectrometer nadir retrievals from spectral window selection," J. Geophys. Res **109**, D09308 (2004).

71. R. A. Johnson and D. W. Wichern, *Applied multivariate statistical analysis,* 6th ed. (Prentice Hall, Upper Saddle River, NJ, 2006).

72. N. R. Draper and H. Smith, *Applied regression analysis* (Wiley, New York, 1998).

73. B. N. Taylor and C. E. Kuyatt, "Guidelines for Evaluating and Expressing the Uncertainty of NIST Measurement Results" (National Institute of Standards and Technology, 2009), retrieved October 20, 2012, http://www.nist.gov/pml/pubs/tn1297/index.cfm.

74. S. W. Brown, et al., "The marine optical buoy (MOBY) radiometric calibration and uncertainty budget for ocean color satellite sensor vicarious calibration," in *Proc. SPIE 6744, Sensors, Systems, and Next-Generation Satellites XI*, 2007), 67441M.

75. H. W. Coleman and W. G. Steele, *Experimentation, validation, and uncertainty analysis for engineers* (Wiley, 2009).

76. J. H. Zar, *Biostatistical analysis,* 4th ed. (Prentice Hall, Upper Saddle River, NJ, 1999).

77. J. C. Clarke, "Modelling uncertainty: A primer," University of Oxford. Dept. Engineering science, Tech. Rep **2161**, 1-21 (1998).

78. L. Li, et al., "Influence of submicron absorptive aerosol on Sea-viewing Wide Field-of-view Sensor (SeaWiFS)-derived marine reflectance during Aerosol Characterization Experiment (ACE)-Asia," J. Geophys. Res. **108**, 4472 (2003).

79. A. W. Harrison and C. A. Coombes, "An opaque cloud cover model of sky short wavelength radiance," Solar Energy **41**, 387-392 (1988).

80. F. Kasten and G. Czeplak, "Solar and terrestrial radiation dependent on the amount and type of cloud," Solar Energy **24**, 177-189 (1980).

81. C. Cox and W. Munk, "Measurement of the roughness of the sea surface from photographs of the sun's glitter," J. Opt. Soc. Am. **44**, 11838-11850 (1954).

82. C. Cox and W. Munk, "Statistics of the sea surface derived from sun glitter," J. Mar. Res **13**, 198-227 (1954).

83. M. Bücker, et al., eds., *Automatic differentiation: applications, theory and implementations*, Lecture Notes in Computational Science and Engineering (Springer-Verlag, Inc., New York, 2006), Vol. 50.

84. C. D. Mobley and L. K. Sundman, *HydroLight 5.0, EcoLight 5.0 Technical Documentation* (Sequoia Scientific, Inc., Bellevue, WA, 2008).

85. J. Hadamard, "Sur les problemes aux dérivées partielles et leur signification physique," Princeton University Bulletin **13**, 49-52 (1902).

86. R. W. Preisendorfer, *Hydrologic Optics* (NOAA Pacific Marine Environment Laboratories, Seattle, 1976), Vol. NTIS PB-259 793/8ST.

87. M. R. Lewis, et al., "Quantitative estimation of the underwater radiance distribution," J. Geophys. Res. **116**, C00H06 (2011).

88. R. Ramamoorthi and P. Hanrahan, "On the relationship between radiance and irradiance: determining the illumination from images of a convex Lambertian object," J. Opt. Soc. Am. A **18**, 2448-2459 (2001).

89. R. W. Preisendorfer and C. D. Mobley, "Direct and inverse irradiance models in hydrologic optics," Limnol. Oceanogr. **29**, 903-929 (1984).

90. M. Sydor, et al., "Uniqueness in Remote Sensing of the Inherent Optical Properties of Ocean Water," Appl. Opt. **43**, 2156-2162 (2004).

91. M. Defoin-Platel and M. Chami, "How ambiguous is the inverse problem of ocean color in coastal waters?," J. Geophys. Res. **112**, C03004 (2007).

92. D. Creanor and A. Cunningham, "Origins of ambiguity in the inversion of remote sensing reflectance signals by spectral matching in optically complex shelf seas," J. Europ. Opt. Soc. Rap. Public **5**, 10081S (2010).

93. H. R. Gordon, "Modeling and Simulating Radiative Transfer in the Ocean," in *Ocean Optics*, R. W. Spinrad, K. L. Carder, and M. J. Perry, eds. (Oxford University Press, USA, 1994), pp. 3-39.

94. C. D. Mobley, "Ocean Optics Web Book: The Single Scattering Approximation" (2011), retrieved August 1, 2012, http://www.oceanopticsbook.info/view/radiative_transfer_theory/level_2/the_singlescattering_approximation.

95. M. Williams and M. Eaton, "A probabilistic study of the influence of parameter uncertainty on solutions of the radiative transfer equation," J. Quant. Spectrosc. Radiat. Transfer **111**, 696-707 (2010).

96. Z. Li, et al., "Validation of MODIS-retrieved cloud fractions using whole sky imager measurements at the three ARM sites," in *14th Atmospheric Radiation Measurement (ARM) Science Team Meeting,* (Albuquerque, NM, 2004), pp. 1-6.

97. B. A. Baum and S. Platnick, "Introduction to MODIS cloud products," in *Earth Science Satellite Remote Sensing, Vol. 1: Science and instruments*, J. J. Qu, W. Gao, M. Kafatos, R. E. Murphy, and V. Salomonson, eds. (Springer-Verlag, Berlin, 2006), pp. 74-91.

98. W. S. Pegau, D. Gray, and J. R. V. Zaneveld, "Absorption and attenuation of visible and near-infrared light in water: dependence on temperature and salinity," Appl. Opt. **36**, 6035-6046 (1997).

99. J. R. V. Zaneveld, J. C. Kitchen, and C. C. Moore, "Scattering error correction of reflecting-tube absorption meters," in *Ocean Optics XII,* J. S. Jaffe, ed. (Proc. SPIE **2258**, 1994), pp. 44-55.

100. N. Briggs, "The 2008 North Atlantic Bloom Experiment Calibration Report #7: Intercalibration of the Backscatter sensors" (Biol. and Chem. Oceanogr. Data Manage. Off., 2011), retrieved July 21, 2012, http://data.bco-dmo.org/NAB08/Backscatter_Calibration-NAB08.pdf.

101. E. Kallin, et al., "Laboratory_analysis_report-NAB08" (Biol. and Chem. Oceanogr. Data Manage. Off., 2011), retrieved July 21, 2012, http://osprey.bcodmo.org/dataset.cfm?id=13820&flag=view.

102. A. Bricaud, A. Morel, and L. Prieur, "Absorption by dissolved organic matter of the sea (yellow substance) in the UV and visible domains," Limnol. Oceanogr. **26**, 43-53 (1981).

103. W. Menke, *Geophysical data analysis: discrete inverse theory*, International Geophysics Series (Academic Press, San Diego, 1989).

104. R. A. Desiderio, "Application of the Raman scattering coefficient of water to calculations in marine optics," Appl. Opt. **39**, 1893-1894 (2000).

105. F. Tsai and W. Philpot, "Derivative analysis of hyperspectral data," Remote Sens. Environ. **66**, 41-51 (1998).

106. E. Torrecilla, J. Piera, and M. Vilaseca, "Derivative analysis of hyperspectral oceanographic data," Advances in Geoscience and Remote Sensing, 1st ed., Gary Jedlovec, Ed. In-Tech, 597-618 (2009).

107. T. G. Owens and E. R. Wold, "Light-Harvesting Function in the Diatom Phaeodactylum tricornutum: I. Isolation and Characterization of Pigment-Protein Complexes," Plant Physiol. **80**, 732-738 (1986).

108. M. E. Sieracki, et al., "Plankton Succession and Biomass during the 2008 North Atlantic Spring Bloom," in *Proceedings from the 2010 AGU Ocean Sciences Meeting*, (AGU, 2010).

109. R. M. Pope and E. S. Fry, "Absorption spectrum (380-700 nm) of pure water. II. Integrating cavity measurements," Appl. Opt. **36**, 8710-8723 (1997).

110. F. M. Sogandares and E. S. Fry, "Absorption spectrum (340-640 nm) of pure water. I. Photothermal measurements," Appl. Opt. **36**, 8699-8709 (1997).

111. W. W. Gregg and K. L. Carder, "A simple spectral solar irradiance model for cloudless maritime atmospheres," Limnol. Oceanogr. **35**, 1657-1675 (1990).

Figures

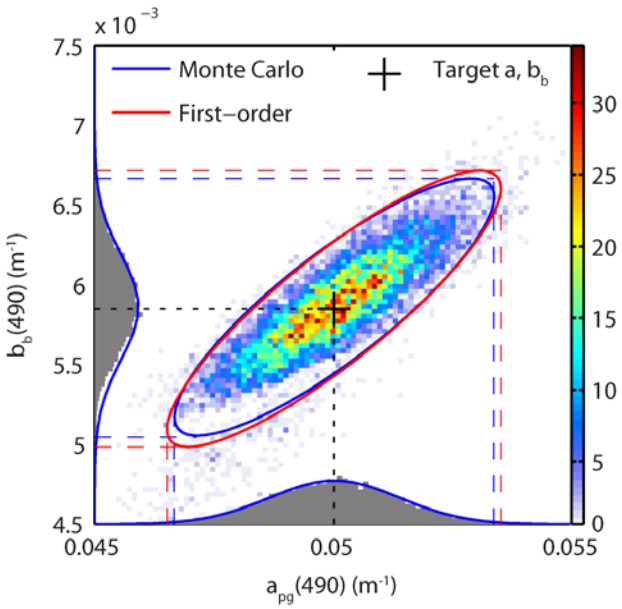

Fig. 1. Monte Carlo and first-order uncertainty analysis results for a single radiometric inversion. Center: Color 2-D histogram of IOP inversion results for 10,000 samples of $L_u(490)$ and $E_d(490)$ with added Gaussian random noise (see text). Target IOPs for the mean L_u and E_d are shown as the black cross at $a_{pg} = 0.05$ m^{-1}, $b_b = 0.00585$ m^{-1}. The color bar indicates sample count in each 2-D color histogram bin. Uncertainty ellipses show good agreement between Monte Carlo (blue) and first-order (red) uncertainty ellipses. Gray 1-D histograms show projected univariate (a_{pg}, b_b) sample distributions, with fit of a normal distribution to the projected data (blue line) and projected 95% confidence intervals (dashed lines). The elliptical shape and orientation of the 2-D histogram and resulting uncertainty ellipses indicate positive correlation $\rho_{a_{pg},b_b} = 0.86$ between errors in the absorption and backscattering coefficients, even though errors in the input L_u , E_d data are uncorrelated.

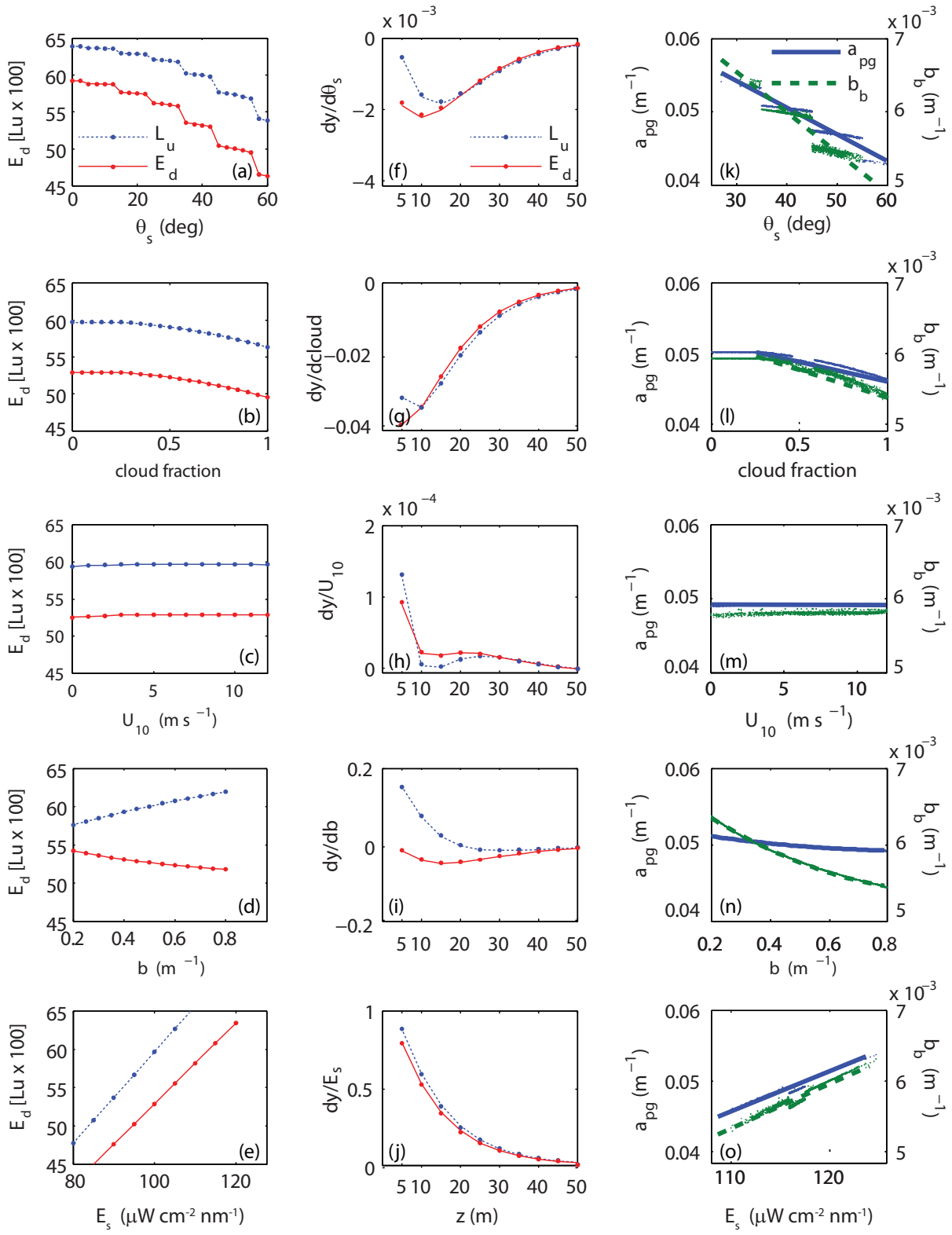

Fig. 2. Forward model parameter sensitivity study. (a-e) Sensitivity of L_u and E_d to forward model parameters **b** at 10 m. Vertical scales are identical on each plot (a-e), so relative

assessments of radiometric sensitivity can be made. Units for L_u (blue dashed) are $\mu W\ cm^{-2}\ sr^{-1}\ nm^{-1} \times 100$; units for E_d are $\mu W\ cm^{-2}\ nm^{-1}$. (f-j) Rows of the forward model sensitivity matrix $\mathbf{K_b}(z)$ versus depth, indicating sensitivity of radiometric measurement ($\partial y = \partial L_u$ or ∂E_d) to changes in forward model parameters ($\partial \mathbf{b}$) for a simulated radiometric profile based on the Korea Strait, with parameters listed in Table 4. The sensitivity is nonlinear with depth for all the parameters. Note that the units for each sensitivity coefficient $\partial y/\partial b$ are different for each parameter, e.g., $\mu W\ cm^{-2} \times 10^{-9}$ for $\partial E_d/\partial b$ (where b is scattering). Values for L_u (blue dashed lines) have been scaled by 100. (k-o) Sensitivity $\partial \mathbf{m}/\partial \mathbf{b}$ of retrieved IOPs $a_{pg}(490)$ and $b_b(490)$ to forward model parameters. Retrieval sensitivity coefficients are derived from (k-n) linear fits to indicated portions of data and (o) quadratic fit to all b_{pg} data. Vertical scales are identical on each plot (k-n), so relative assessments of IOP retrieval sensitivity can be made.

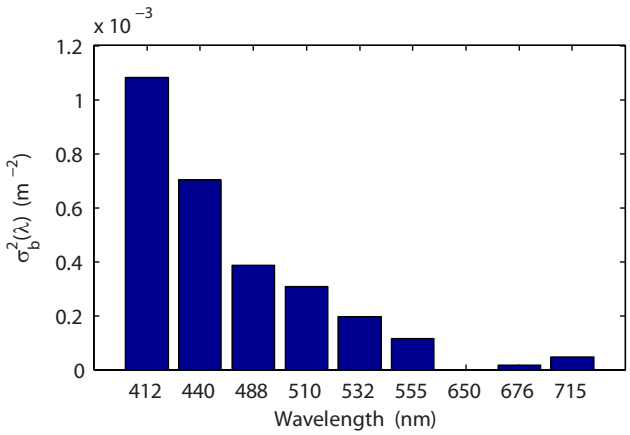

Fig. 3. Multi-wavelength bootstrap estimates of scattering error variance $\sigma_b^2(\lambda_i)$ used in the forward model error covariance matrix $\mathbf{S_b}$. Errors were derived from the difference between AC-9 measurements in vertically homogenous waters and estimates from a bio-optical model of equation (22).

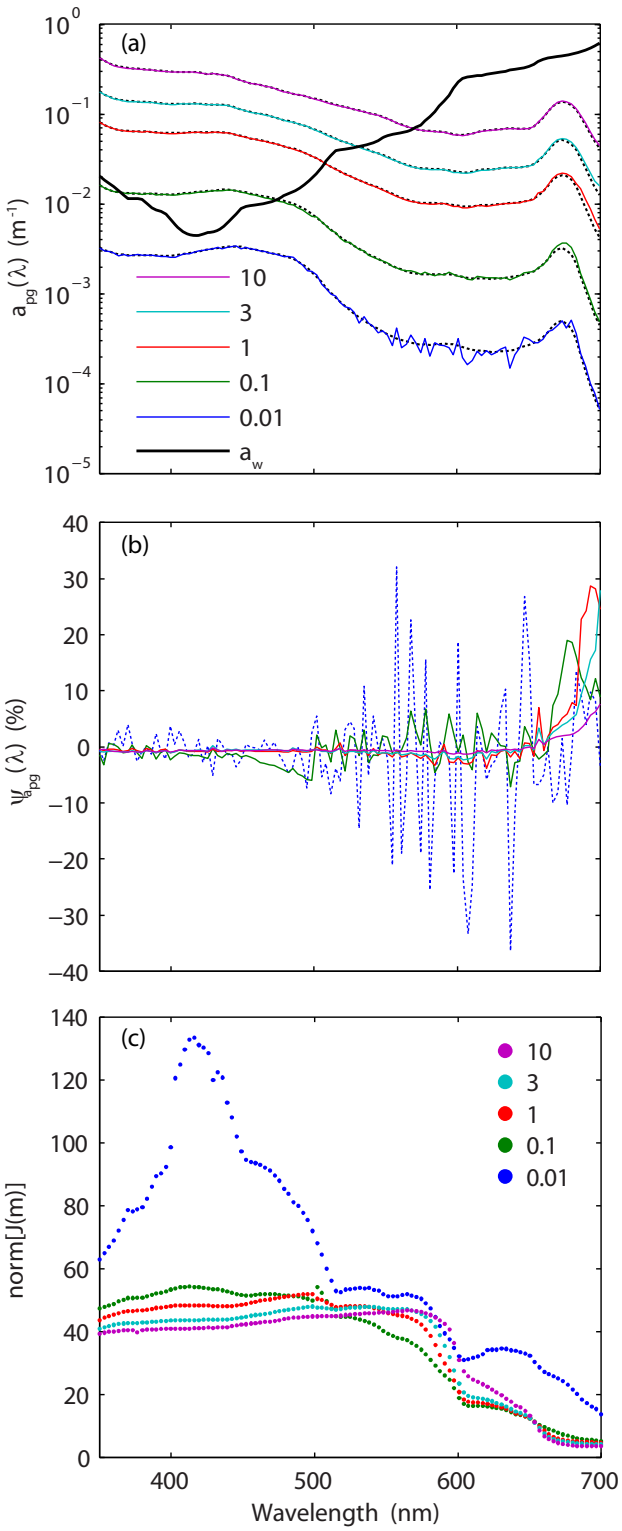

Fig. 4. Inversion noise study for absorption. (a) Hyperspectral (3.3 nm) retrievals of absorption $a_{pg}(\lambda)$ from simulated radiometric data for Chl = 0.01, 0.1, 1, 3, 10 mg m^{-3}. Black solid line shows pure water absorption $a_w(\lambda)$. Black dotted lines show true values, colored lines show

$a_{pg}(\lambda)$ retrievals. (b) Relative error $\psi_{a_{pg}}$ in absorption retrievals. $Chl = 0.01$ shown as blue dotted line. (c) The ℓ_2 matrix norm of spectral Jacobians $\mathbf{J}(\lambda, \hat{\mathbf{m}})$. A larger norm indicates greater sensitivity of L_u and E_d to estimated IOPs.

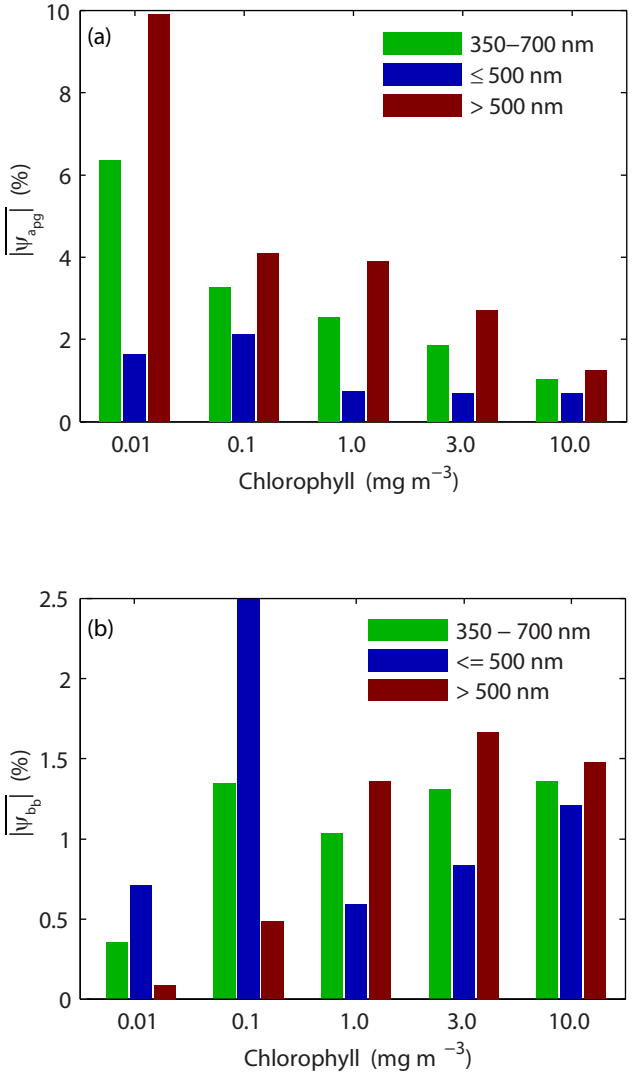

Fig. 5. Absolute average error for hyperspectral (3.3 nm) retrievals of (a) absorption $\overline{|\psi_{a_{pg}}|}$ and (b) backscattering $\overline{|\psi_{b_b}|}$ from simulated radiometric data.

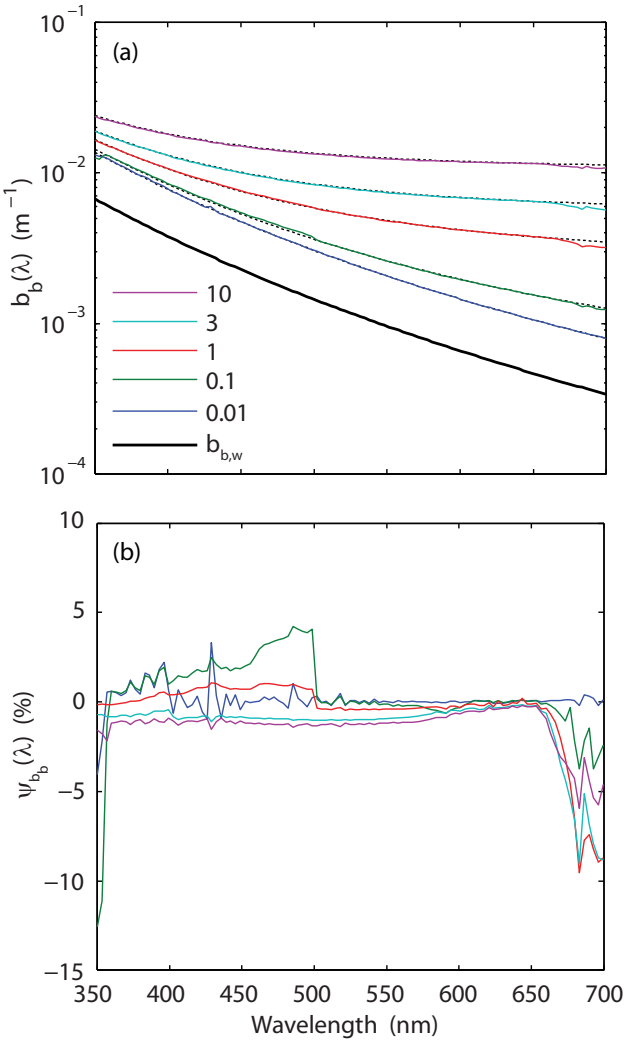

Fig. 6. Inversion noise study for backscattering. (a) Hyperspectral (3.3 nm) retrievals of backscattering $b_b(\lambda)$ from simulated radiometric data for Chl = 0.01, 0.1, 1, 3, 10 mg m^{-3}. Black solid line shows pure water backscattering $b_{b,w}(\lambda)$. Black dotted lines show true values, colored lines show $b_b(\lambda)$ retrievals. (b) Relative error ψ_{b_b} in backscattering retrievals. For the ℓ_2 matrix norm of spectral Jacobians $\mathbf{J}(\lambda, \hat{\mathbf{m}})$, see Fig. 4c.

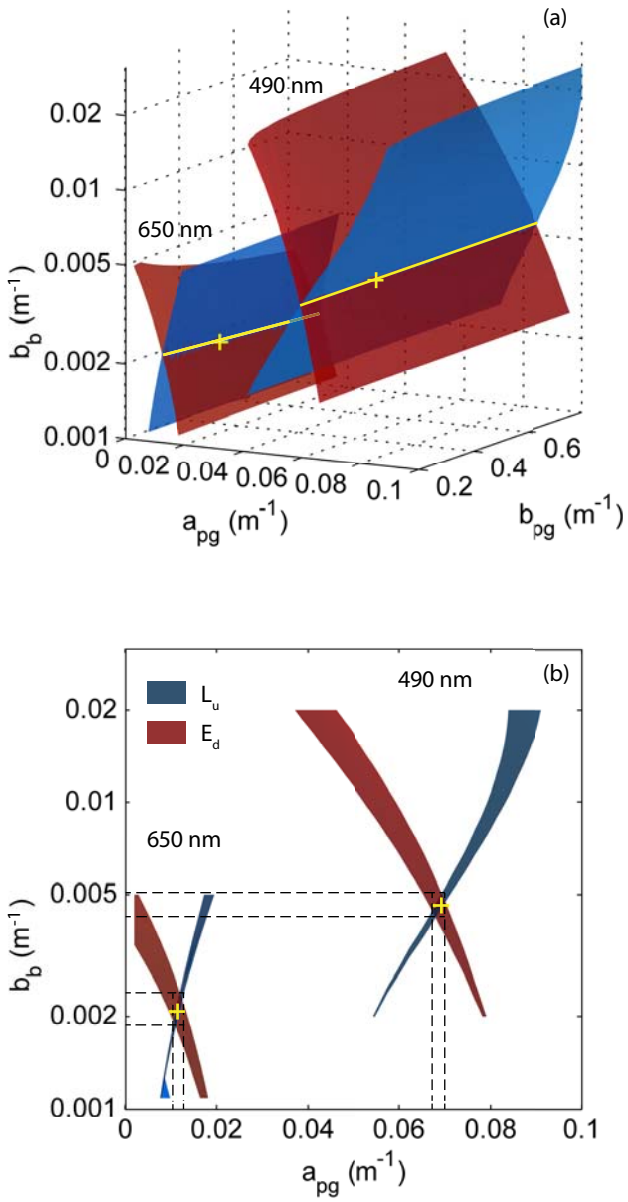

Fig. 7. Isosurfaces for L_u (blue) and E_d (red) at 490 and 650 nm, representing a subset of the domain of IOPs (a_{pg}, b_b, b_{pg}) that can produce given values of L_u or E_d. The yellow cross identifies the true value of the IOP triplet for the given L_u and E_d. Notice how isosurfaces at 650 nm have folded closer together than at 490 nm. (a) Isosurface intersection (yellow lines) indicates the range of possible inverse solutions when given both L_u and E_d, indicating that b is completely ambiguous. (b) The projected dashed lines show the range of uncertainty in the estimated IOPs a_{pg} and b_b if no value of b is specified.

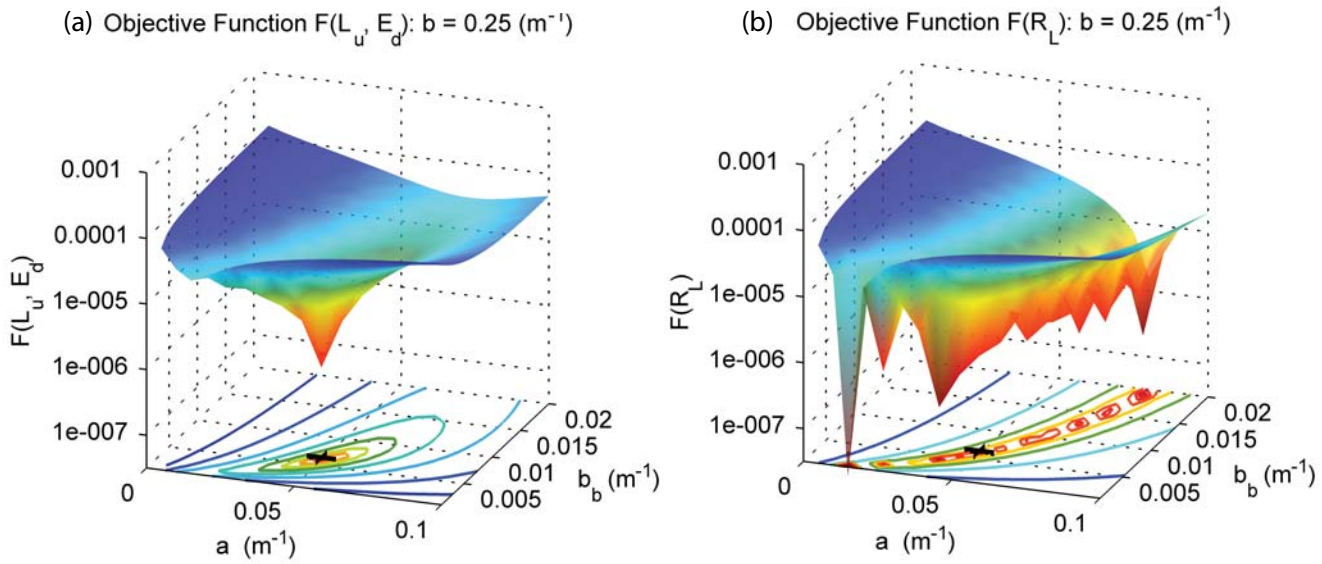

Fig. 8. Single-frame excerpts from animations of two objective function surfaces over a range of scattering b from 0.1 to 1.0 m^{-1}. (a) Objective function surface $F(L_u, E_d)$ used in this work shows a single minimum (Media 1). (b) Objective function surface $F(R_L) = (R_L^{meas} - R_L^{est})/R_L^{meas}$ shows multiple local minima (Media 2).

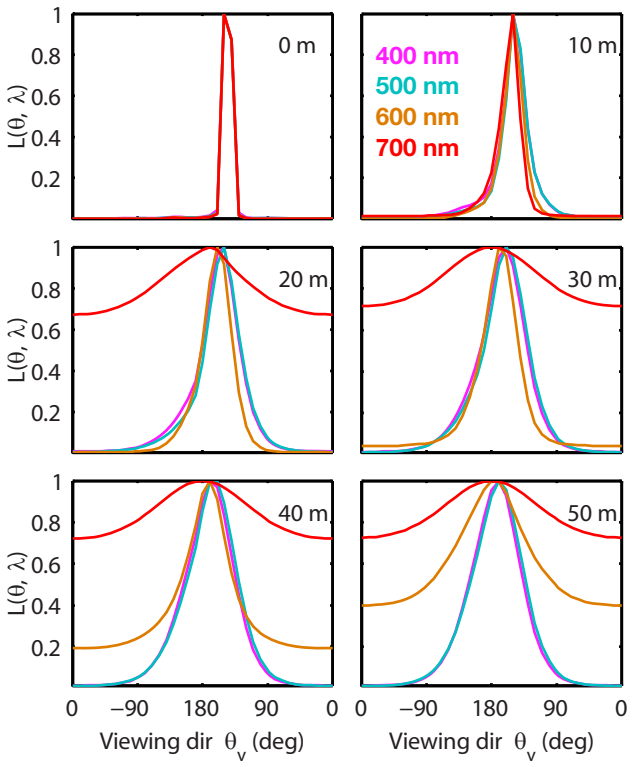

Fig. 9. Shape of normalized radiance distribution $L(\theta_v, \lambda)$ in the plane of the sun as a function of viewing direction θ_v and wavelength λ at six depths, as computed by HydroLight for vertically homogeneous waters, using a chlorophyll based model with Chl = 1 mg m^{-3}, θ_s = 50°, U_{10} = 5 m s^{-1}. Note broadening of shape at all wavelengths, and nearly isotropic shape for 700 nm at 30 m.

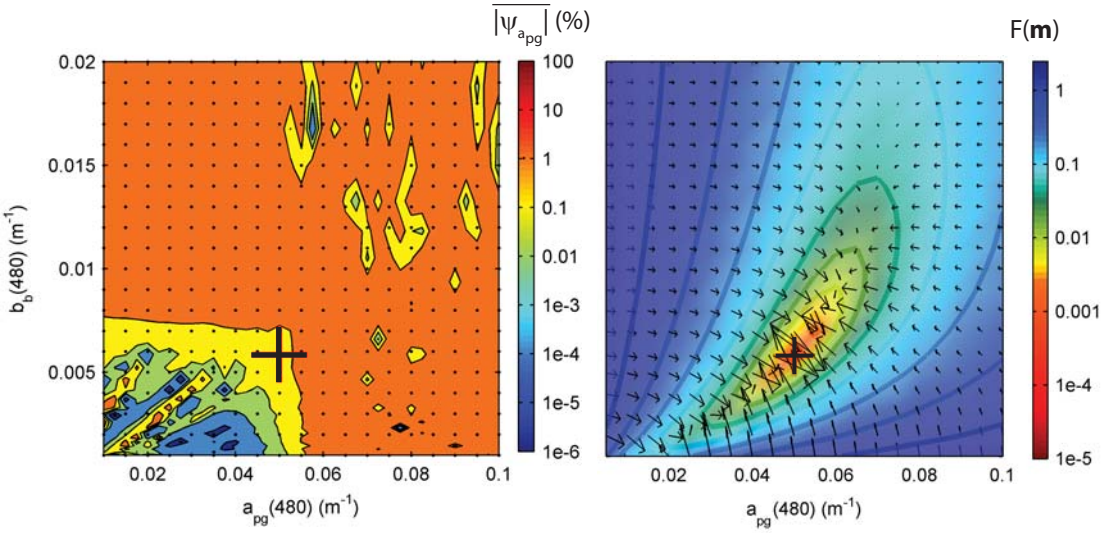

Fig. 10. Stability of optimization starting points $\mathbf{m}_0 = (a_{pg}, b_b, b_{pg})$ with b_{pg} fixed at 0.225 m^{-1} (50% error). (Left) Contours show influence of optimization starting point $\mathbf{m}_0$ on absolute error in absorption retrieval $\left|\psi_{a_{pg}}\right|$ at 480 nm. Starting points converge near the true value (a_{pg}, b_b) = (0.05, 0.00585) m^{-1} (shown with black +), with average absolute error shown by the contour region color bar. Dots indicate the computation grid, decimated by a factor of four for clarity. (Right) Contour plot of objective function $F(\mathbf{m}_0)$ at the same grid points. Color indicates value of the objective function $F(\mathbf{m})$. Vectors illustrate magnitude and direction of objective function gradient $\nabla F(\mathbf{m}_0)$. Notice that starting points in the lower-left corner where both coordinates are smaller than the true value have the lowest absolute error (left plot) and largest gradients (right plot).

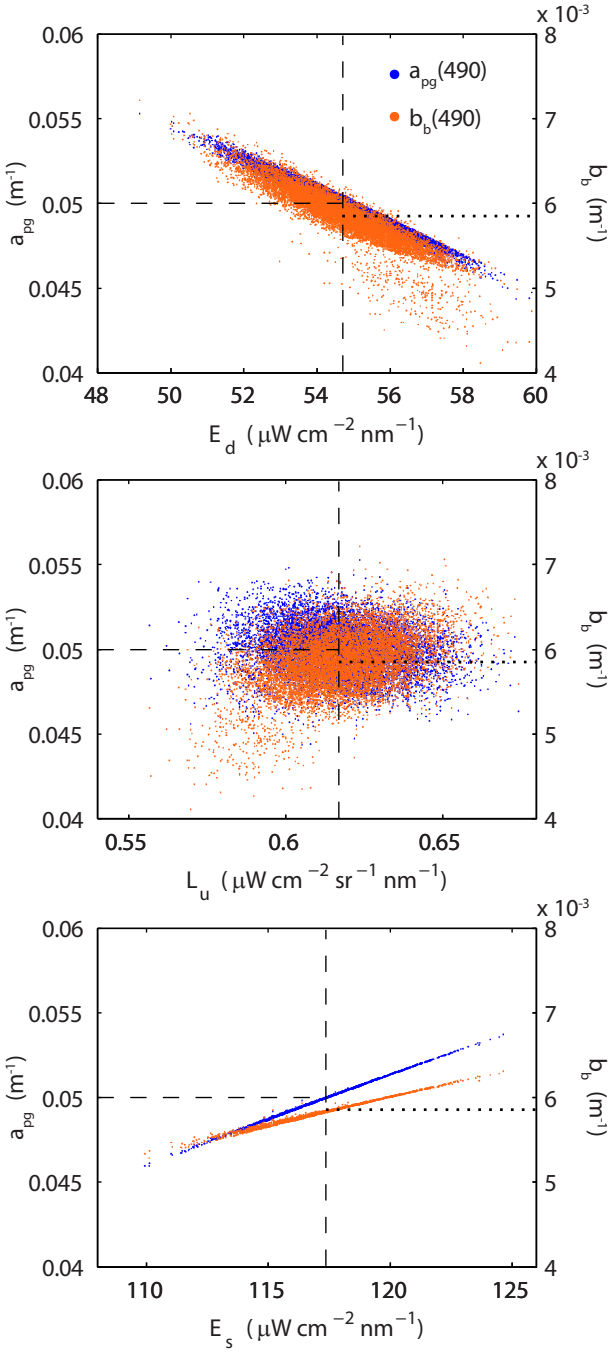

Fig. 11. Sensitivity studies of retrieved IOPs to L_u, E_d and E_s. Dashed lines indicate true values for E_d, L_u, E_s, and a_{pg}, dotted lines for b_b. (SensitivityLuEd.eps)

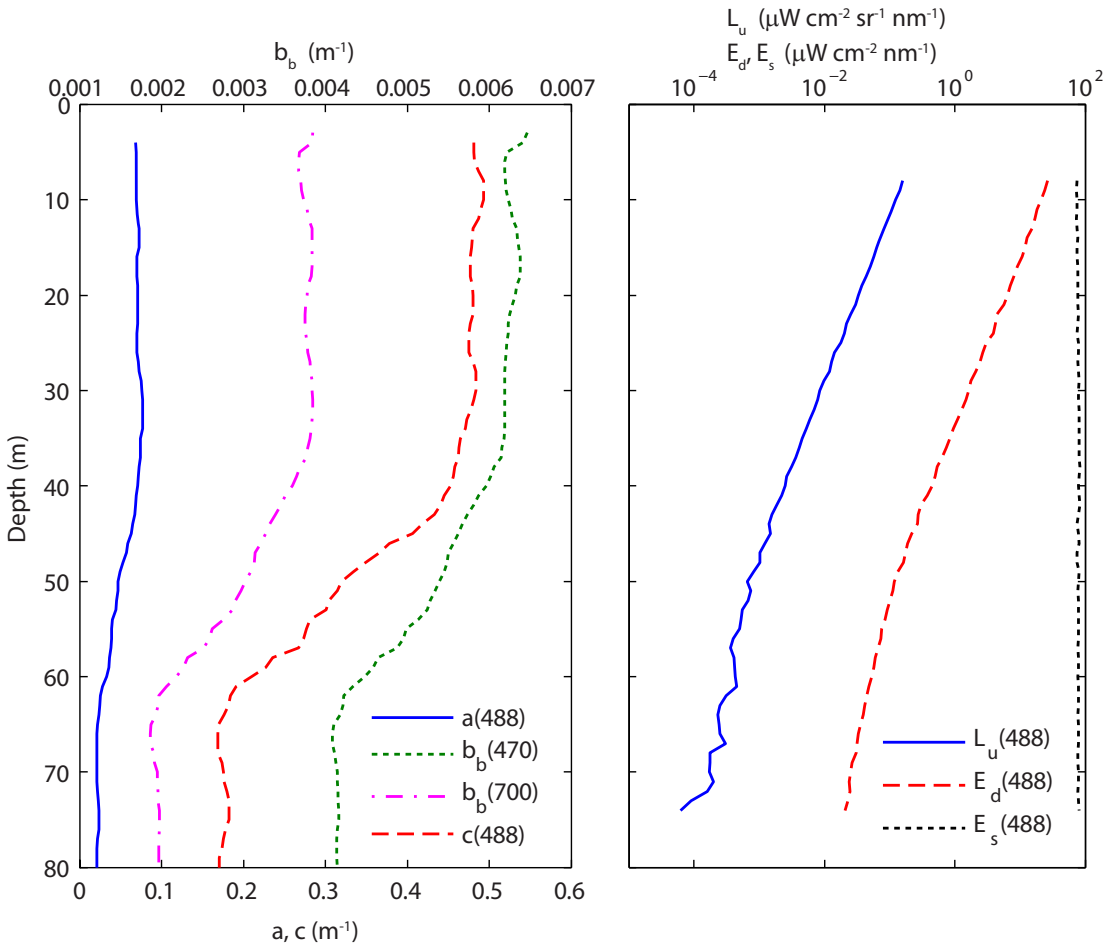

Fig. 12. IOP and radiometric profiles from Station 34 in the NAB08 dataset. Left Panel: Typical IOPs were nearly homogeneous in the lit portion of the water column. Right panel: Radiometric profiles of L_u, E_d, and E_s at 488 nm on log scale. L_u and E_d show little curvature until 40 m, another indication of vertically homogeneous water.

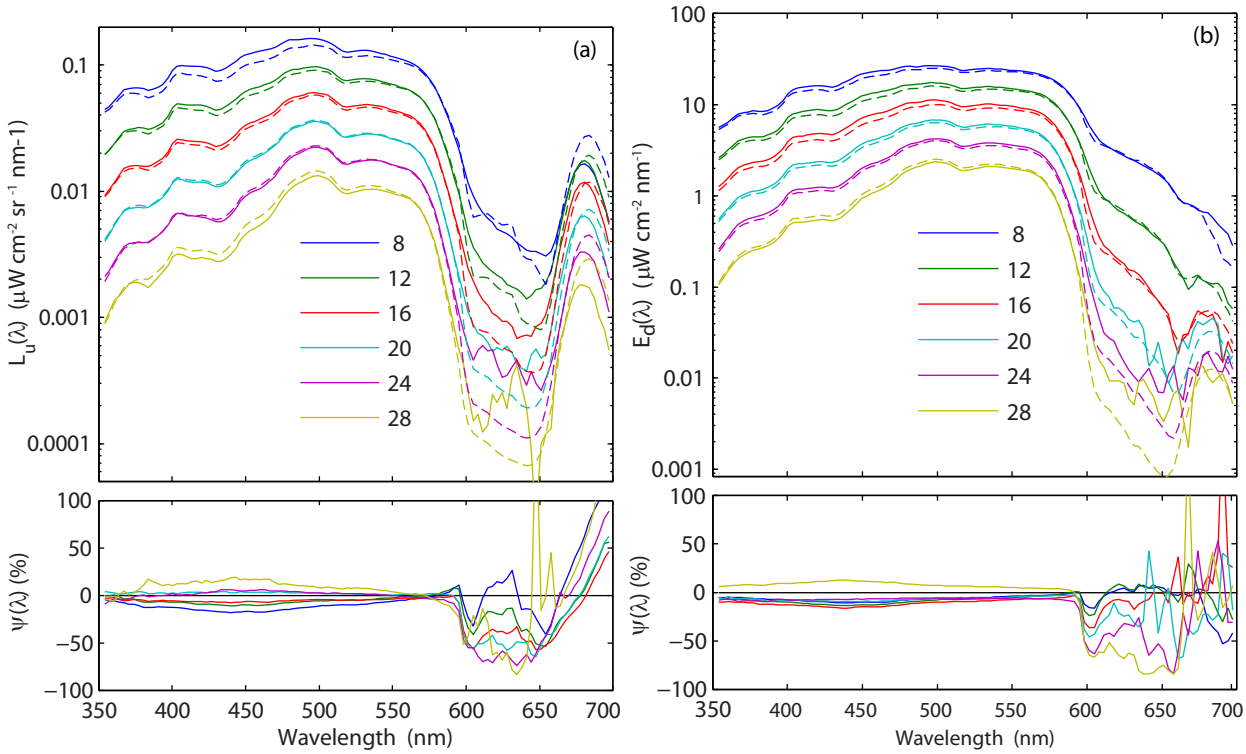
(a)
(b)
8
12
16
20
24
28
$L_u(\lambda)$ (μW cm^{-2} sr^{-1} nm-1)
$E_d(\lambda)$ (μW cm^{-2} nm^{-1})
$\psi(\lambda)$ (%)
Wavelength (nm)

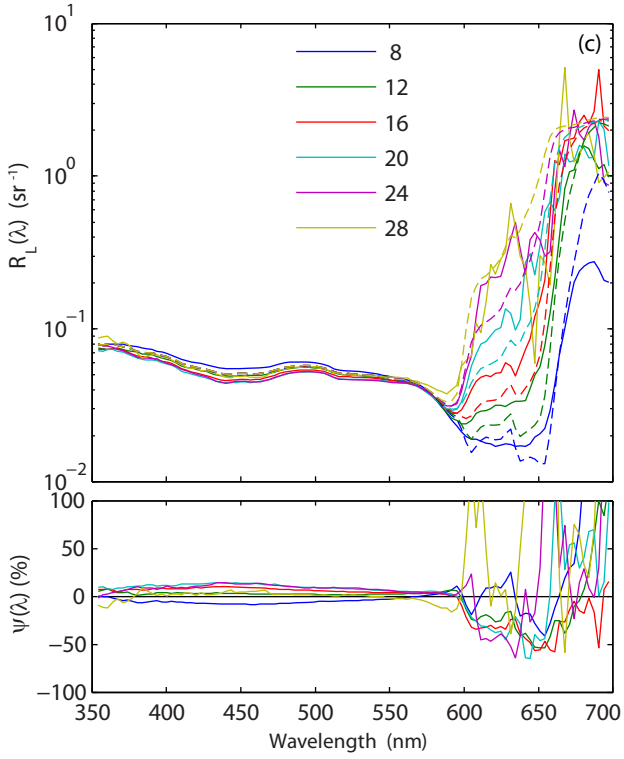
(c)
8
12
16
20
24
28
$R_L(\lambda)$ (sr^{-1})
$\psi(\lambda)$ (%)
Wavelength (nm)

Fig. 13. Radiometric measurements $\mathbf{d}^{meas}$ (dashed),least squares estimates $\mathbf{d}^{est}$ (solid) and relative error $\psi(\lambda)$ at selected depths for (a) $L_u(\lambda)$, (b) $E_d(\lambda)$, and (c) $R_L(\lambda)$ at NAB08 Station 34. Note solar-induced chlorophyll fluorescence near 680 nm and related depth effects in $R_L(\lambda)$ for $\lambda > 600$ nm.

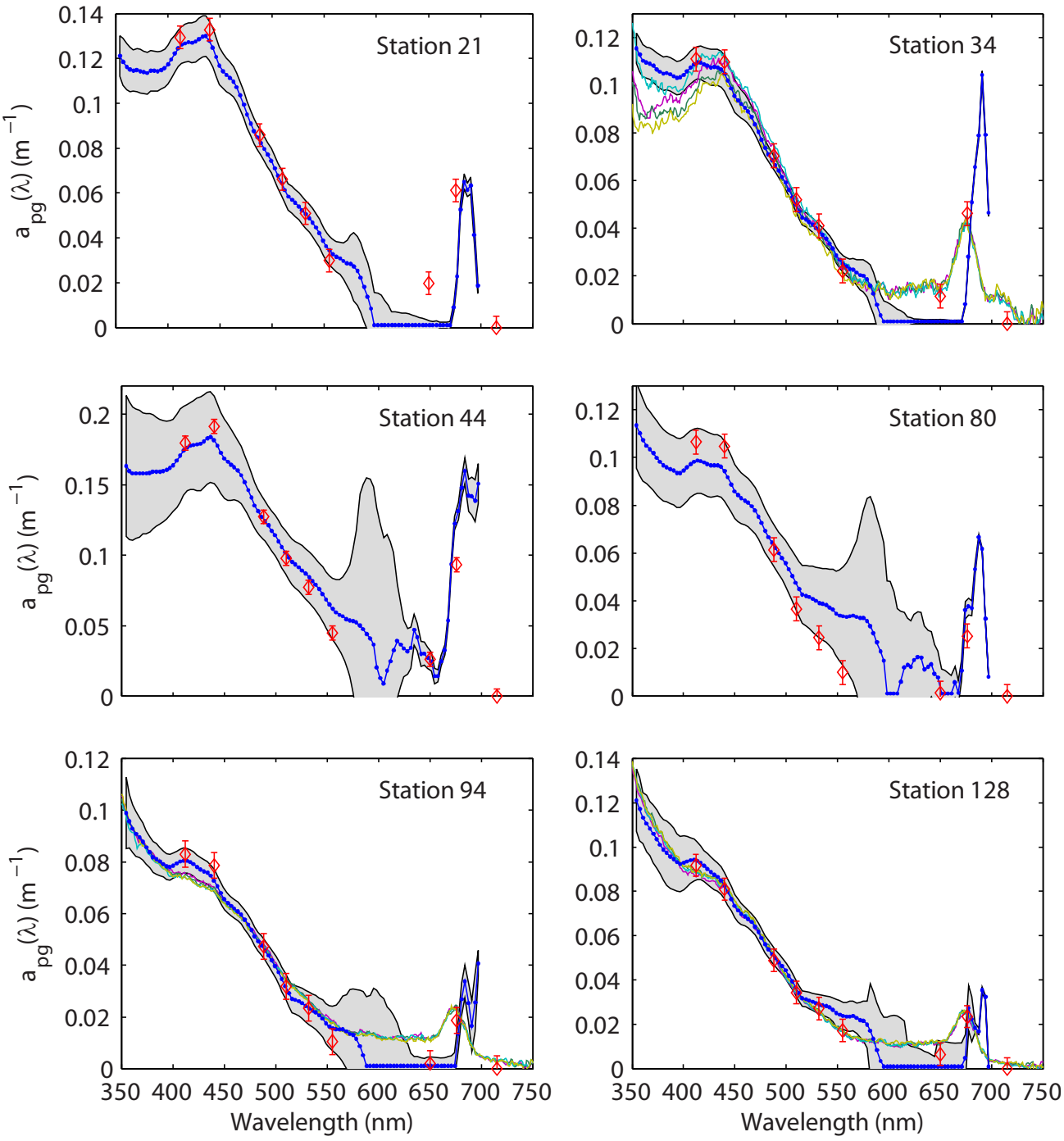

Fig. 14. Retrieved absorption $a_{pg}(\lambda)$ at 3.3 nm increments from NAB08 stations (blue lines and dots) with 95% confidence intervals based on first-order uncertainty analysis (gray shaded area). Retrieved quantities are averages over the mixed layer at each station (see Table 12). Measured AC-9 absorption (red diamonds). Spectrophotometric absorption replicates (fine colored lines, stations 34, 94, 128).

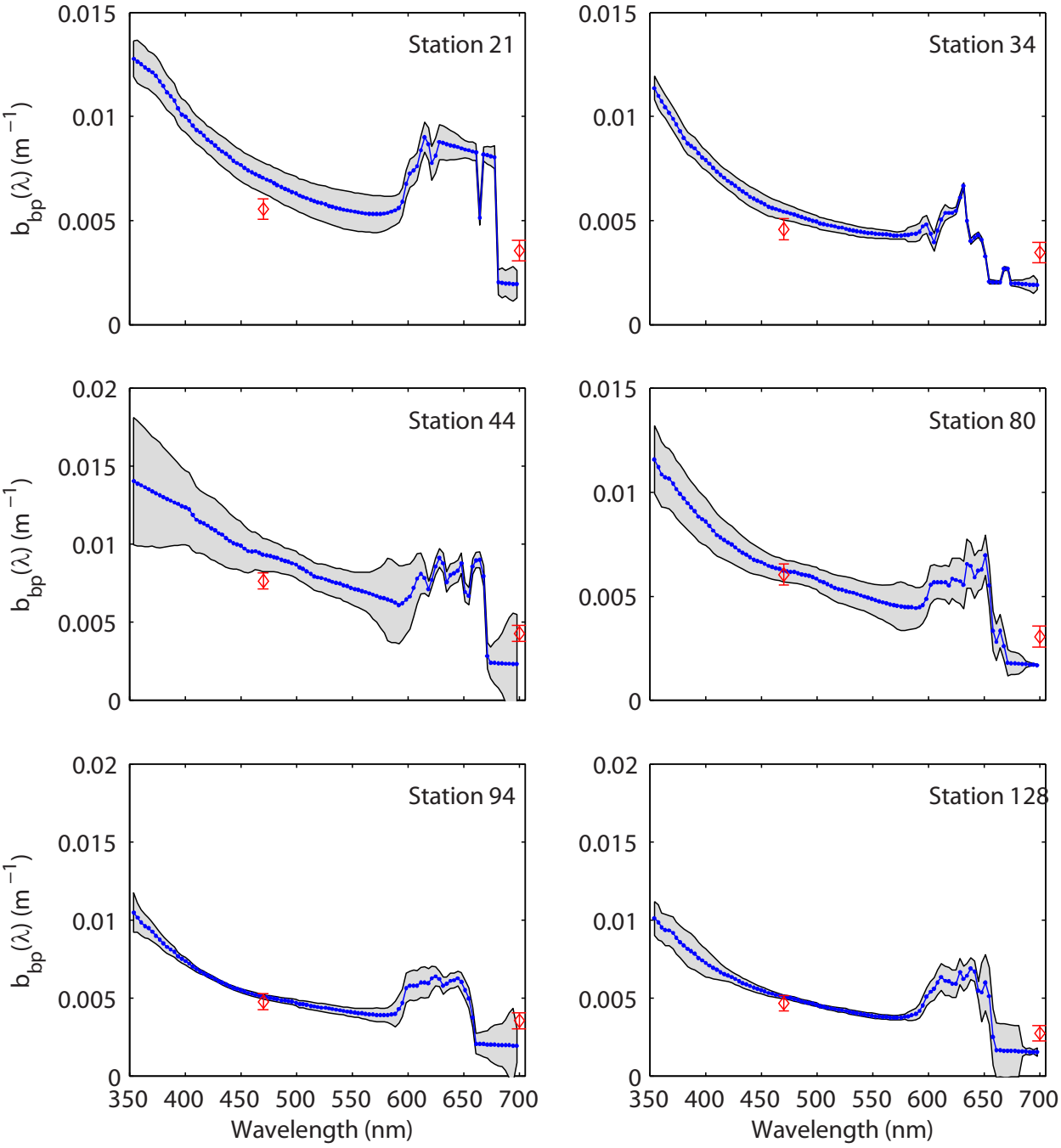

Fig. 15. Retrieved particulate backscattering $b_{bp}(\lambda)$ at 3.3 nm increments from NAB08 stations (blue lines and dots) with 95% confidence intervals based on first-order uncertainty analysis (gray shaded area). Retrieved quantities are averages over the mixed layer for each station. (See Table 12). Measured BB2F particulate backscattering (red diamonds).

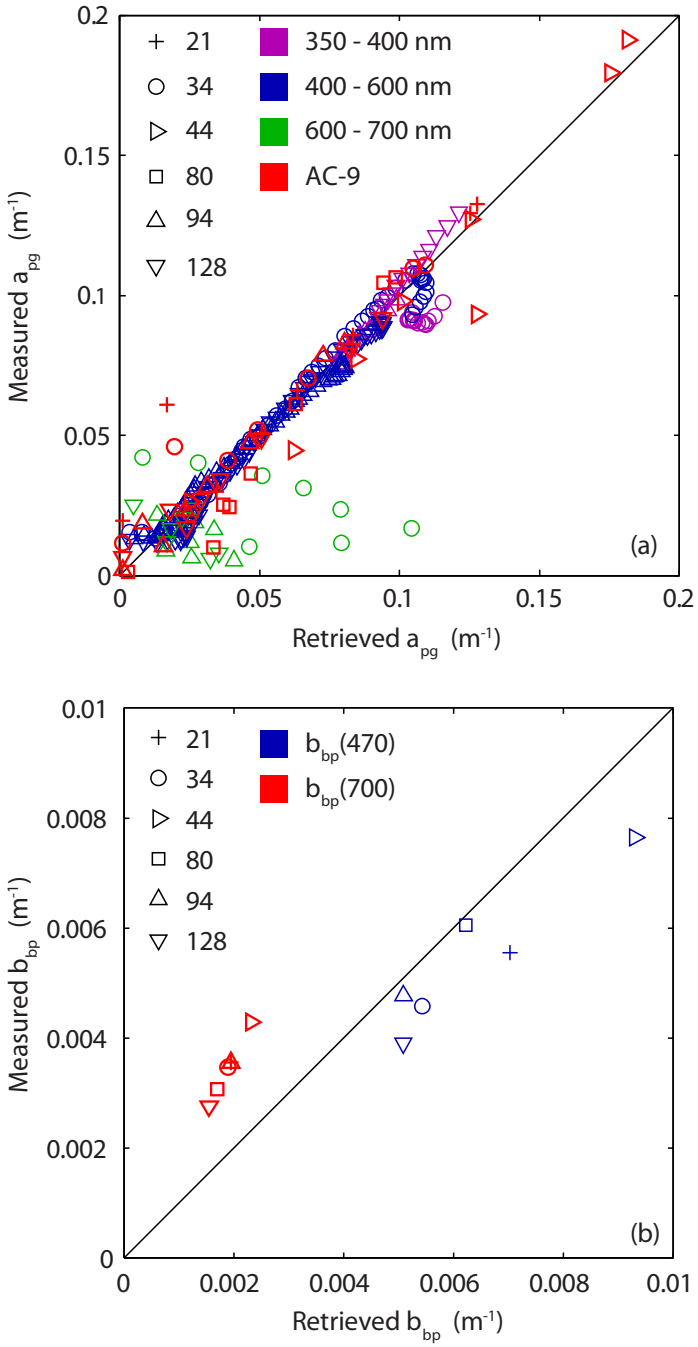

Fig. 16. Comparison of measured vs. retrieved IOPs at NAB08 process cruise stations, identified by the symbols. (a) Comparison of retrieved absorption $a_{pg}(\lambda)$ to AC-9 absorption (all stations) shown with red symbols. Comparison to spectrophotometric absorption (stations 34, 94 and 128 only): violet: $350 \le \lambda < 400$, blue: $400 \le \lambda \le 600$ nm, green: $600 < \lambda \le 700$ nm symbols. Note that most retrievals failed above 600 nm (green symbols). (b) Comparison of retrieved particulate backscattering $b_{bp}(\lambda)$ to that measured by the BB2F.

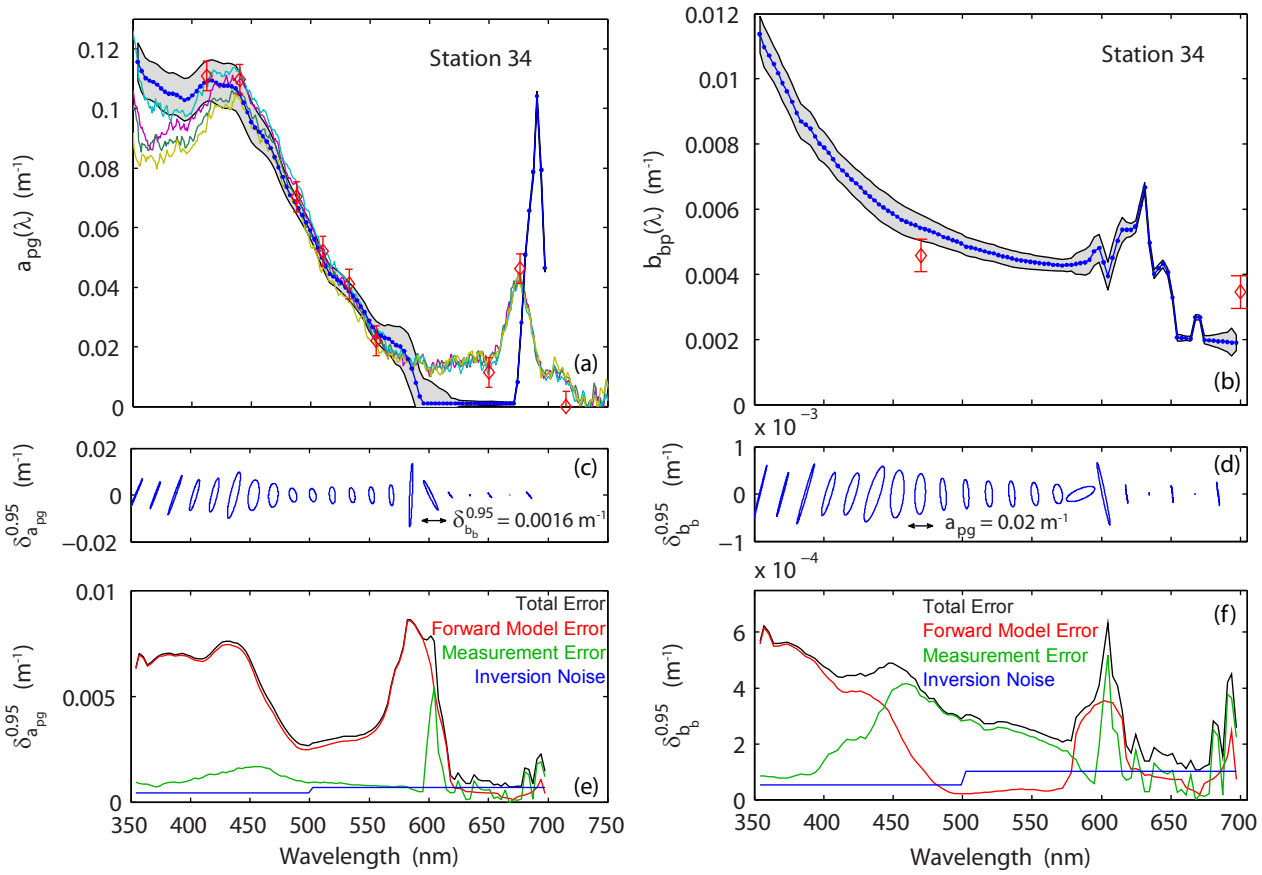

Fig. 17. Absorption and backscattering error budgets for NAB08 Station 34. (a-b) Retrieved absorption $a_{pg}(\lambda)$ and particulate backscattering $b_{bp}(\lambda)$ (blue), 95% confidence interval (grey shaded area), and spectrophotometric absorption replicates (fine colored lines, a only). (c-d) 95% confidence ellipses at ≈15 nm spacing showing positive (e.g., 350-450 nm), and generally negative (e.g., ≥ 575 nm) correlation between errors in a_{pg} and b_b. (e-f) Estimated errors for NAB08 Station 34 retrieval of $a_{pg}(\lambda)$ and $b_{bp}(\lambda)$. The final retrieval error (black) is composed of forward model parameter error (red), radiometric measurement error (green), and error from the inversion (optimization) process (blue).

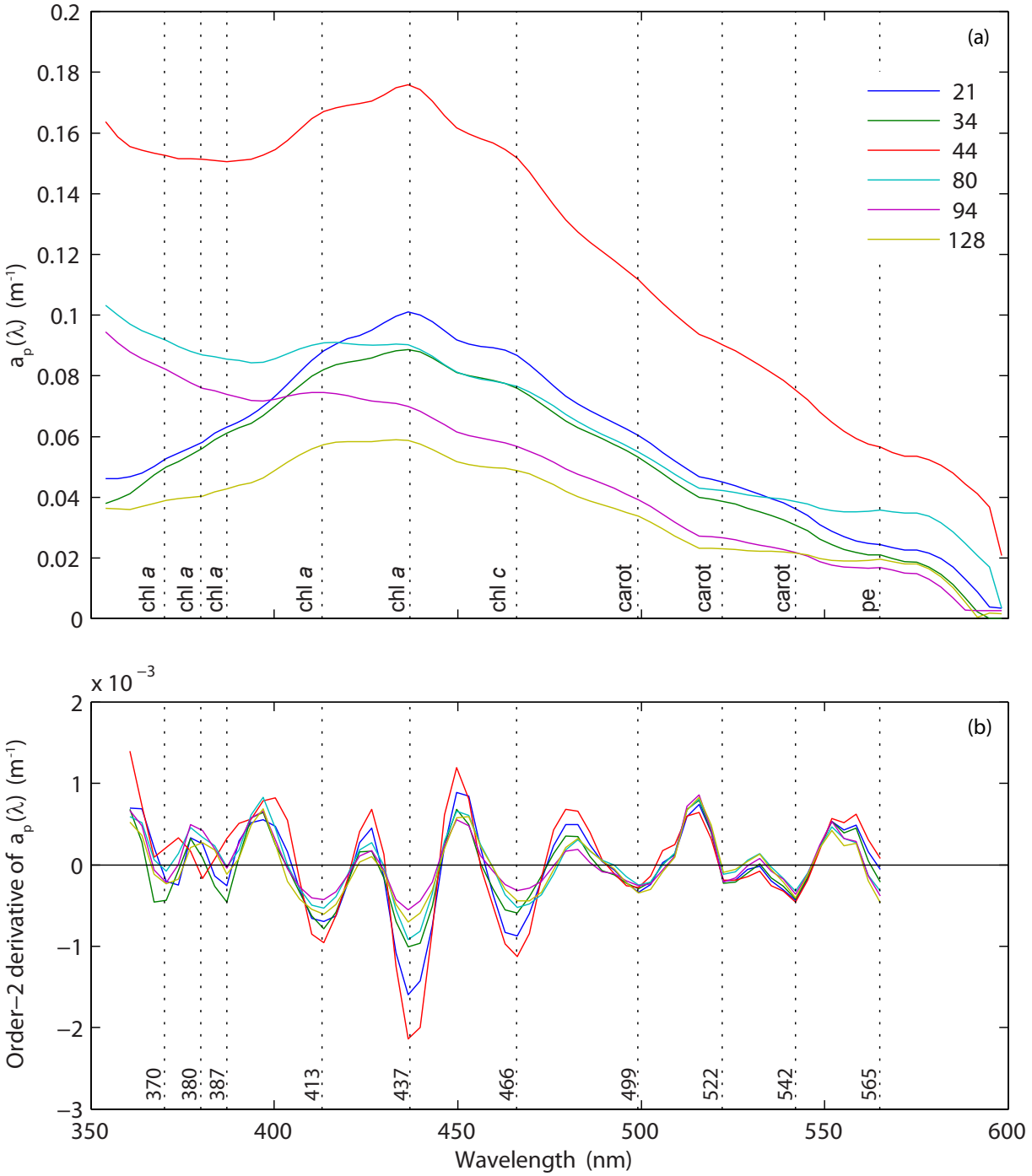

Fig. 18. (a) Estimates of particulate absorption $a_p(\lambda)$ derived by subtracting $a_g(\lambda)$ (filtered AC-9 measurements) from radiometric estimates of $a_{pg}(\lambda)$, averaged over the mixed layer at NAB08 stations. Vertical dotted lines indicate phytoplankton pigment absorption bands, including chl *a* (370-387, 413, 437 nm), chl *c* (466 nm) and carotenoids (499, 522, 542 nm). One phycoerithrin absorption peak is marked at 565 nm. (b) Second derivative of absorption spectra $a_{pg}(\lambda)$ calculated using Savitzky–Golay smoothing and derivative computation [105]. (Corresponding fourth derivatives are all positive at the minima noted in the second derivative curves.)

Tables

Table 1. Optimization stopping criteria and related evaluation parameters

	Criteria	Formal Definition	Associated Parameter[a]	Value
1.	Converged	Norm of gradient is close to zero, $\left\|\nabla F(\mathbf{m})\right\|_2 < tolFun$, and $F(\mathbf{m})$ has positive curvature.	*tolFun*	1e-6
2.	No change in **m**	Change in **m** at iteration *k*, $\left\|\mathbf{m}_k - \mathbf{m}_{k-1}\right\|_2 < tolX$. Can indicate a local minimum.	*tolX*	1e-7
3.	No change in $F(\mathbf{m})$	*Relative* change in $F(\mathbf{m})$ at iteration $k <$ *tolFun*, $\left\|F(\mathbf{m}_k) - F(\mathbf{m}_{k-1})\right\| < tolFun \times \left[1 + \left|F(\mathbf{m}_{k-1})\right|\right]$. Can indicate a local minimum.	*tolFun*	1e-6
	Minimum change in **m**	$\left\|\mathbf{m}_k - \mathbf{m}_{k-1}\right\|_2 \geq DiffMinChange$	*DiffMinChange*	5e-3

[a]While these parameters are specific to MATLAB's `lsqnonlin` routine, other nonlinear least square solvers have similar stopping and evaluation parameters.

Table 2. Radiometric and IOP data points used for simulations

λ nm	z m	θ_s *deg*	*cloud* %	U_{10} *m s^{-1}*	E_s μW cm^{-2} nm^{-1}	L_u μW cm^{-2} sr^{-1} nm^{-1}	E_d μW cm^{-2} nm^{-1}	a_{pg} m^{-1}	b_b m^{-1}	b_{pg} m^{-1}	*Source*
490	20	44	30	7	63.5	0.00384	7.50	0.0686	0.0046	0.389	NAB08 Sta. 34
650	20	44	30	7	49.1	3.29e-4	0.0159	0.0114	0.0021	0.424	NAB08 Sta. 34
480	5	43.8	0	5	120	1.30[a]	82.1	0.050[b]	0.00585	0.450	WOOD, ACE-103, Korea Strait Cast 30 [52]
480	10					0.617	54.7				
480	20					0.265	23.3				
480	50					0.00198	1.74				

[a]Simulated radiometric values. [b]Depth-averaged IOPs.

Table 3. IOP Uncertainty Estimates for IOP retrievals using the Monte Carlo and First-order Methods

Method	$\delta^{a_{pg}}_{0.95}$ m^{-1}	$\delta^{b_b}_{0.95}$ m^{-1}	ρ
Monte Carlo	3.34e-3	8.06e-4	0.86
First-order	3.51e-3	8.97e-4	0.86
ψ	-5.3%	-11.7%	0

Table 4. Additional model parameters supplied to EcoLight forward model G(m,b).

Forward Model parameter	Simulation $\mathbf{b}^{sim}$	NAB08 field data **b**	Range used to determine $\mathbf{K_b}$ entry	Assumed relative error to determine $\mathbf{S_b}$ entry
$\tilde{\beta}(\theta', \theta, \lambda)$	Fournier-Forand lookup using b_b/b [58, 59]	Fournier-Forand lookup using b_b/b [58, 59]		
a_w, b_w	Pope & Fry [109, 110]	Pope & Fry [109, 110]		
Chl	0.01, 0.1, 1, 3, 10 mg m^{-3}	Calibrated chlorophyll fluorometer (BB2F) measurement		
θ_s	15°	*R/V Knorr* latitude, longitude, date, time	0 – 60°	±0.42° (≈15 min time error)
cloud	30%	Field observations of cloud cover	0.0 – 1.0	±0.2
U_{10}	5 m s^{-1}	*R/V Knorr* measurements	0 – 12 m s^{-1}	1.5 m s^{-1}
b (scattering coefficient)	c(650) + bio-optical model	Measured c(650) + bio-optical model	0.2 – 0.8	Bootstrap analysis (Section 3F)
E_s	Simulated by RADTRAN [84, 111]	Satlantic HyperPro II E_d deck sensor	0.8 – 1.2× measured E_s	±0.075× measured E_s

Table 5. Summary Retrieval Statistics for Simulated Light Fields

		L_u			E_d			a_{pg}			b_b		
Chl	*Waveband*	$\bar{\psi}$	$\overline{\lvert\psi\rvert}$	ε_{RMS}	$\bar{\psi}$	$\overline{\lvert\psi\rvert}$	ε_{RMS}	$\bar{\psi}$	$\overline{\lvert\psi\rvert}$	ε_{RMS}	$\bar{\psi}$	$\overline{\lvert\psi\rvert}$	ε_{RMS}
mg m^{-3}	*Nm*	*%*	*%*	*μW cm^{-2}*	*%*	*%*	*μW cm^{-2} sr^{-1}*	*%*	*%*	*m^{-1}*	*%*	*%*	*m^{-1}*
0.01	350-700	-0.90	1.05	5.91E-02	-0.49	0.64	9.70E-01	-1.82	6.14	5.50E-05	0.12	0.35	7.50E-05
0.01	< 500	-2.09	2.35	9.02E-02	-1.11	1.31	1.47E+00	-1.15	1.85	6.90E-05	0.22	0.71	1.14E-04
0.01	> 500	0.00	0.07	3.95E-04	-0.02	0.12	1.31E-01	-2.33	9.38	4.10E-05	0.04	0.09	2.00E-06
0.1	350-700	-1.63	1.99	7.50E-02	-1.39	1.55	2.41E+00	1.33	4.35	2.31E-04	0.36	1.35	2.44E-04
0.1	< 500	-3.97	4.29	1.14E-01	-3.20	3.33	3.67E+00	-2.00	2.04	2.75E-04	1.41	2.49	3.72E-04
0.1	> 500	0.12	0.25	3.51E-04	-0.02	0.22	1.27E-01	3.83	6.09	1.92E-04	-0.44	0.48	1.30E-05
1	350-700	0.04	0.24	1.13E-03	0.00	0.20	1.09E-01	0.70	2.54	5.95E-04	-0.53	1.03	8.50E-05
1	< 500	-0.01	0.30	1.66E-03	-0.05	0.23	1.01E-01	-0.73	0.73	4.30E-04	0.56	0.60	5.30E-05
1	> 500	0.08	0.19	3.73E-04	0.05	0.18	1.14E-01	1.77	3.91	6.94E-04	-1.35	1.36	1.03E-04
3	350-700	0.05	0.21	4.60E-04	0.11	0.24	1.28E-01	0.25	1.85	1.05E-03	-1.31	1.31	1.53E-04
3	< 500	0.02	0.23	5.68E-04	0.17	0.31	1.57E-01	-0.69	0.70	9.32E-04	-0.83	0.83	1.01E-04
3	> 500	0.08	0.20	3.58E-04	0.07	0.18	1.01E-01	0.96	2.73	1.13E-03	-1.67	1.67	1.83E-04
10	350-700	0.04	0.18	2.44E-04	0.10	0.21	6.52E-02	-0.22	1.01	1.68E-03	-1.36	1.36	2.30E-04
10	< 500	0.02	0.23	2.18E-04	0.17	0.29	6.96E-02	-0.69	0.69	2.02E-03	-1.20	1.20	2.20E-04
10	> 500	0.05	0.15	2.62E-04	0.05	0.16	6.16E-02	0.13	1.25	1.37E-03	-1.48	1.48	2.37E-04

Table 6. Sensitivity coefficients computed from Monte Carlo simulations for variable radiometric error E_d, L_u at 10 m

δ	z	a_{pg}^{true}	$\overline{a}_{pg}^{est}$	$\psi_{a_{pg}}$	$\sigma_{a_{pg}} / \overline{a}_{pg}^{est}$	b_b^{true}	$\overline{b}_b^{est}$	ψ_{b_b}	$\sigma_{b_b} / \overline{b}_b^{est}$	S_{a_{pg},L_u}	S_{a_{pg},E_d}	S_{b_b,L_u}	S_{b_b,E_d}
%	m	m^{-1}	m^{-1}	%		m^{-1}	m^{-1}	%					
5	10	0.05	0.0501	0.14	0.00263	0.00585	0.00589	0.65	0.00494	1.02	1.03	1.92	1.95
10	10	0.05	0.0503	0.57	0.00528	0.00585	0.00599	2.46	0.102	1.03	1.03	1.99	1.99
20	10	0.05	0.0512	2.4	0.103	0.00585	0.00642	9.75	0.181	1.03	1.01	1.81	1.78
30	10	0.05	0.0510	2.1	0.169	0.00585	0.00659	12.7	0.326	1.10	1.09	2.12	2.10
50	10	0.05	0.0501	0.11	0.00286	0.00585	0.00725	23.86	0.725	1.38	1.12	2.88	2.83

Table 7. Sensitivity coefficients computed from Monte Carlo simulations for 5% radiometric error at various depths

z	τ	a_{pg}^{true}	$\overline{a}_{pg}^{est}$	$\psi_{a_{pg}}$	$\sigma_{a_{pg}} / \overline{a}_{pg}^{est}$	b_b^{true}	$\overline{b}_b^{est}$	ψ_{b_b}	$\sigma_{b_b} / \overline{b}_b^{est}$	S_{a_{pg},L_u}	S_{a_{pg},E_d}	S_{b_b,L_u}	S_{b_b,E_d}
m		m^{-1}	m^{-1}	%		m^{-1}	m^{-1}	%					
5	2.5	0.05	0.0501	0.16	6.258e-2	0.00585	0.005868	0.30	8.671e-2	2.44	2.42	3.39	3.36
10	5	0.05	0.0501	0.14	2.631e-2	0.00585	0.005888	0.65	4.943e-2	1.02	1.04	1.92	1.95
20	10	0.05	0.0503	0.53	1.190e-2	0.00585	0.005992	2.43	3.710e-2	0.474	0.467	1.48	1.46
50	25	0.05	0.0498	-0.48	1.525e-2	0.00585	0.005745	-1.80	5.213e-2	0.598	0.598	2.04	2.04

Table 8. Sensitivity coefficients computed from Monte Carlo simulations for variable radiometric error E_s at 10 m

δ	z	a_{pg}^{true}	$\overline{a}_{pg}^{est}$	$\psi_{a_{pg}}$	$\sigma_{a_{pg}} / \overline{a}_{pg}^{est}$	b_b^{true}	$\overline{b}_b^{est}$	ψ_{b_b}	$\sigma_{b_b} / \overline{b}_b^{est}$	S_{a_{pg},E_s}	S_{b_b,E_s}
%	m	m^{-1}	m^{-1}	%		m^{-1}	m^{-1}	%			
5	10	0.05	0.0500	-0.06	2.28e-2	0.00585	0.00583	-0.31	2.47e-2	1.24	1.35
10	10	0.05	0.0500	-0.03	4.53e-2	0.00585	0.00583	-0.27	4.90e-2	1.24	1.34
20	10	0.05	0.0499	-0.11	8.94e-2	0.00585	0.00583	-0.28	9.50e-2	1.22	1.30
30	10	0.05	0.0497	-0.62	1.22e-1	0.00585	0.00582	-0.58	1.24e-1	1.11	1.13
50	10	0.05	0.0503	0.61	1.56e-1	0.00585	0.00593	1.40	1.41e-1	0.88	0.80

Table 9. Sensitivity coefficients computed from Monte Carlo simulations for 5% radiometric error E_s at various depths

z	τ	a_{pg}^{true}	$\overline{a}_{pg}^{est}$	$\psi_{a_{pg}}$	$\sigma_{a_{pg}} / \overline{a}_{pg}^{est}$	b_b^{true}	$\overline{b}_b^{est}$	ψ_{b_b}	$\sigma_{b_b} / \overline{b}_b^{est}$	S_{a_{pg},E_s}	S_{b_b,E_s}
m		m^{-1}	m^{-1}	%		m^{-1}	m^{-1}	%			
5	2.5	0.05	0.0500	0.01	4.56e-2	0.00585	0.00584	-0.25	4.97e-2	2.54	2.77
10	5.0	0.05	0.0500	-0.06	2.28e-2	0.00585	0.00583	-0.31	2.47e-2	1.24	1.35
20	10.0	0.05	0.0502	0.39	1.05e-2	0.00585	0.00585	0.07	1.04e-2	0.580	0.578
50	25.0	0.05	0.0500	0.07	4.03e-3	0.00585	0.00585	0.05	4.08e-3	0.221	0.223

Table 10. Sensitivity coefficients computed from Monte Carlo simulations uncertainties in additional model parameters

Parameter		Fit range	$S_{a_{pg},\mathbf{b}_i}$	$S_{b_b,\mathbf{b}_i}$
$\mathbf{b}_1$	θ_s	28-60°	-0.34	-0.0064
$\mathbf{b}_2$	*cloud*	0.25-1.0	-0.066	-0.078
$\mathbf{b}_3$	U_{10}	0-12 m s^{-1}	0.0012	0.0015
$\mathbf{b}_4$	b_{pg}	0.2-0.8 m^{-1}	-0.025 - -0.12	-0.10 - -0.33

Table 11. Forward Model Parameters used for NAB08 Stations

Station	*z* *m*	*N*	θ_s *deg*	*cloud* *%*	U_{10} *m* s^{-1}	$\overline{Chl}$ *mg* m^{-3}
21	5-25	11	57	30	5	4.6
34	8-28	11	44	30	7	0.7
44	5-17	7	57	40	9	5.7
80	5-31	19	43	50	3	1.6
94	5-31	19	58	80	5	1.1
128	6-28	12	43	10	13	1.1

Table 12. Summary Retrieval Statistics for NAB08 Stations (350-555 nm)

	L_u			E_d			AC-9 a_{pg}			Spec. a_{pg}			Estimated a_{pg} uncertainty			Estimated b_b uncertainty		
Station	$\bar{\psi}$	$\overline{\lvert\psi\rvert}$	ε_{RMS}	$\bar{\psi}$	$\overline{\lvert\psi\rvert}$	ε_{RMS}	$\bar{\psi}$	$\overline{\lvert\psi\rvert}$	ε_{RMS}	$\bar{\psi}$	$\overline{\lvert\psi\rvert}$	ε_{RMS}	$\bar{\delta}_{0.95}$	$\delta_{0.95}^{440}$	$\delta_{0.95}^{555}$	$\bar{\delta}_{0.95}$	$\delta_{0.95}^{440}$	$\delta_{0.95}^{555}$
	%	%	$\mu W\ cm^{-2}$	%	%	$\mu W\ cm^{-2}\ sr^{-1}$	%	%	m^{-1}	%	%	m^{-1}	m^{-1}	m^{-1}	m^{-1}	m^{-1}	m^{-1}	m^{-1}
21	0.3	7.4	0.00638	1.9	7.4	0.654	-3.3	3.3	0.0040				0.0071	0.0058	0.0032	6.73E-04	5.43E-04	4.39E-04
34	-0.1	8.0	0.00613	-4.2	8.6	0.833	-3.5	3.5	0.0035	4.9	8.5	0.0098	0.0049	0.0076	0.0013	3.98E-04	5.86E-04	2.13E-04
44	5.6	26.9	0.00609	15.3	19.1	0.578	-3.0	3.0	0.0062				0.0294	0.0386	0.0062	2.35E-03	3.06E-03	4.11E-04
80	1.0	6.6	0.00309	4.8	6.7	0.517	-5.0	6.8	0.0077				0.0112	0.0150	0.0029	9.84E-04	1.36E-03	1.25E-04
94	0.1	1.4	0.00120	0.4	2.0	0.298	-4.1	4.1	0.0038	2.5	3.1	0.0030	0.0047	0.0040	0.0007	3.72E-04	2.68E-04	7.90E-05
128	0.4	3.7	0.00202	2.2	4.2	0.384	2.6	2.6	0.0018	-0.4	3.1	0.0036	0.0099	0.0084	0.0019	7.58E-04	6.20E-04	9.40E-05

Chapter 4

Eric Rehm, Mary Jane Perry, Eric A. D'Asaro, Estimation of inherent optical properties and phytoplankton community structure from radiometry during the North Atlantic Spring Bloom. To be submitted to Journal of Geophysical Research.

Estimation of inherent optical properties and phytoplankton community structure from radiometry during the North Atlantic Spring Bloom

Eric Rehm[1,*], Mary Jane Perry[2], and Eric D'Asaro[1]

[1]Applied Physics Laboratory and School of Oceanography, University of Washington

1013 NE 40th Street, Seattle, WA, 98105

[2]Ira C. Darling Marine Center, School of Marine Sciences, University of Maine, 193 Clark's Cove Road., Walpole, ME -4573-3397

[*]Corresponding author: erehm@earthlink.net

Key Points

1. Hyperspectral absorption is retrieved from autonomous in-water radiometry
2. Phytoplankton size class and pigments are estimated from retrieved absorption
3. Composition and evolution of a bloom are traced from autonomous measurements

Abstract

An inverse algorithm is developed to retrieve inherent optical properties from in situ radiometric measurements and thereby measure the evolution of phytoplankton community structure during the North Atlantic spring bloom continuously over 51 days from a Lagrangian float. Hyperspectral estimates of particulate plus detrital absorption are retrieved from hyperspectral

measurements of upward radiance and downwelling irradiance and beam attenuation at one wavelength. Knowledge of surface solar radiation is not necessary. The retrievals are found to be robust to spectrally-neutral biofouling. These absorption spectra are of sufficient accuracy, bandwidth, and resolution to estimate bio-optical signatures of phytoplankton community structure including overall biomass, the fraction of small phytoplankton, and the absorption due to colored detrital material. Size fraction estimates based on packaging effects on the flatness of the absorption spectrum are found to be ambiguous in the presence of vertical mixing, also a consideration for ocean satellite retrievals of this parameter. Derivative spectroscopy is employed to detect and estimate the relative contribution to absorption of individual phytoplankton pigments, specifically chlorophyll *a*, fucoxanthin and other carotenoids. The existence of mycosporine-like amino acids is detected from ultraviolet absorption peaks. The time series of these estimates show the growth of a diatom bloom which then rapidly disappears and is replaced by a community of smaller cells. This description is consistent with nearby ship-based measurements that rely on water samples and laboratory measurements. We conclude that observations of phytoplankton functional types are possible from low-power, autonomous platforms.

1 Introduction

Current knowledge of biodiversity patterns of marine phytoplankton is very limited [*Irigoien et al.*, 2004]. Maximum phytoplankton diversity is found at intermediate levels of phytoplankton biomass and minimum diversity is found during blooms. Small nano- and picoplankton dominate in low nutrient, low biomass portions of the ocean. A single phytoplankton species often dominates when phytoplankton biomass is very high. At intermediate levels of biomass, diversity and resource use efficiency is highest. Yet a mechanistic understanding of how environmental

factors may control large scale phytoplankton community structure remains elusive. Selective grazing, nutrient availability and hydrographic features (transport and mixing) all contribute to establishing and maintaining phytoplankton community diversity [*Adjou et al.*, 2012; *Margalef*, 1978].Phytoplankton participate in modifying their own physical environment by changing the spectral nature of the light field [*Sathyendranath and Platt*, 2007], in turn influencing seasonal species succession and the ocean heating rate [*Morel and Antoine*, 1994]. Phytoplankton communities depend on biodiversity for stability, e.g., the ability of a phytoplankton community to respond to damage and recover quickly. Pollution stress from toxic substances and excess nutrient input is already manifested as biodiversity loss in coastal marine environments [*Ptacnik et al.*, 2008] or as increasingly frequent blooms of single species toxic to shellfish and/or humans [*Babin et al.*, 2008]. Decadal-scale patterns of changes in phytoplankton biodiversity are already evident in the N. Atlantic. *Leterme et al.* [2005] analyzed visual estimates of silk mesh filters from Continuous Plankton Recorder (CPR) surveys of surface waters conducted in the North Atlantic and the North Sea between 1958 and 2002; phytoplankton color (a proxy for phytoplankton biomass) was assessed from four levels of greenness assigned by comparison with standard color charts while the abundance of specific phytoplankton species was assessed from microscopic cell counts. They reported overall trends of increasing phytoplankton color and dinoflagellates and a decrease of diatoms. It is possible that global warming is spatially reorganizing the N. Atlantic, with observations of a latitudinal increase of phytoplankton biodiversity in recent decades [*Beaugrand et al.*, 2010], based on a separate analysis of CPR surveys. Resolving the expected rapid and large-range shifts in organism range and changes in life cycle events is important to better determine the impacts of climate change on marine systems [*Richardson and Poloczanska*, 2008].

In addition to studying "who is where?", we are also interested in knowing "when are they there". Studies of community composition over short time frames can inform us about growth and loss processes. For example, grazing by small zooplankton can lead to increased growth of larger phytoplankton and vice versa [*Bergquist et al.*, 1985]. Long-term observations of spring bloom timing, e.g., the start of rapid increase of phytoplankton biomass, can lead to better understanding of the ecological effects of climate variability and change. For example, North Sea dinoflagellate blooms have advanced by more than 8 d per decade while diatom blooms have remained relatively fixed in time [*Edwards and Richardson*, 2004]. Such changes in synchrony may affect transfer of production to higher trophic levels such as zooplankton and larval fish [*Cushing*, 1990; *Platt and Csar Fuentes-Yaco*, 2003]. Resolving the expected rapid and large-range shifts in organism range and changes in life cycle events is important to better determine the impacts of climate change on marine systems.

Developing tools to describe, quantify, and monitor marine phytoplankton community composition and diversity at a variety of temporal (1 day to decades) and spatial (1 km to global ocean) scales is therefore of paramount importance. *In situ* assessment of phytoplankton community composition from ships, moorings, and arrays of autonomous instruments intersects with assessments from remote sensing satellites at the mesoscale (1 to 100 km). Here important biogeochemical processes and seasonal mixed layer dynamics take place that impact ocean carbon cycles [*IOCCG*, 2011].

In this study, we further develop techniques and methods that are applicable to assessing phytoplankton community composition and transitions using optical methods to assess "phytoplankton functional types", i.e., groups of organisms that have similar biogeochemical processes. Specifically, we exploit a previously developed inversion algorithm that produces

estimates of the spectral absorption and backscatter coefficients from hyperspectral radiometry [*Rehm and Mobley*, 2012]. In the present study, we use the retrieved absorption spectra to estimate the size structure [*Ciotti et al.*, 2002] and marker pigments [*Barlow et al.*, 1993] observed during the 2008 North Atlantic Bloom using *in situ* Lagrangian float observations. We compare these estimates to other measures of community composition based on other bio-optical measurements from the same float, as well as those from water samples taken on a 21 d process cruise during the bloom. We also address some challenges that result from important processes that phytoplankton undergo in the mixed layer, such as vertical mixing affecting the photoacclimation of the cells [*Lewis et al.*, 1984; *Marra*, 1978], and the cause and effect of pigment packaging on the shape of the biomass (or otherwise) normalized phytoplankton spectrum [*Bricaud et al.*, 2004; *Duyens*, 1956; *Morel and Bricaud*, 1981].

2 Data and methods

2.1 Sampling overview

A Lagrangian float was deployed at 59ºN, 20ºW near the JGOFS North Atlantic Bloom site by the *R/S Bjarni Sæmundsson* on 4 April 2008, corresponding to yearday (yd) 95 and sampled for 51 d until the end of its mission on 25 May 2008 (yd 146). The *R/V Knorr* made extensive surveys near the float between 2 to 21 May 2008 (yd 123-142). At six stations, calibration casts were made within 1 km of the float, providing accurate CTD and bottle data as well as radiometric and bio-optical profiles for bio-optical sensor intercalibration. These measurements were part of the larger North Atlantic Bloom experiment [*Alkire et al.*, 2012; *Bagniewski et al.*, 2011; *Briggs et al.*, 2011; *Cetinić et al.*, 2012; *Mahadevan et al.*, 2012]. The present work considers both float profiles and periods of float drift with sufficient vertical excursions for estimating absorption from float radiometry.

2.2 Lagrangian float

The Lagrangian float was designed and built at the University of Washington Applied Physics Laboratory, and is similar to the one described in *D'Asaro* [2003] at 1.4 m long and 12.7 cm in diameter. On each day of the mission, the float profiled to about 230 m within 1.5 h of local noon followed by satellite communication, autoballasting, and an approximately 22-h-long Lagrangian drift. During these drifts, the float accurately followed the three-dimensional motion of water within the upper ocean mixed layer, being repeatedly carried across the mixed layer by the turbulence [*Harcourt and D'Asaro*, 2010]. The float and its sensor complement are shown in Figure 3; associated sampling intervals for the sensors used here are described in Table 13. A mission software failure on yd 104 resulted in the loss of full resolution data acquired from yd 95-104. The reduced resolution data available for this period is inadequate for the radiometric inversion scheme employed here, so float results will be limited to the period yd 104 – 145 when full resolution data are available.

2.3 Float sensors and data processing

The float was equipped with two Seabird SBE 41 conductivity-temperature (CT) sensors, mounted on the top and bottom of the float. A WET Labs FLNTU mounted at the bottom of the float measured chlorophyll fluorescence *ChlF* (λ_{ex}=470 nm, λ_{em}=700 nm) and the volume scattering function at a centroid angle of 140° at 700 nm (β(140°, 700 nm)); an integral copper shutter with rubber wiper cycled once every drift measurement and once per profile to prevent biofouling. A WET Labs C-Star beam transmissometer was mounted on the side of the float, measuring beam attenuation at 653 nm (c(653)). The C-Star transmitter window was mounted facing upward and was plumbed to receive the tributyl-tin-laced exhaust from the lower CT sensor to prevent biofouling and blow off any particulate matter that may have settled on the

window. According to the details provided in *Briggs et al.* [2011], particulate backscattering at 700 nm $b_{bp}(700)$ was estimated from $\beta(140°, 700\ nm)$, and the C-Star was intercalibrated with a similar transmissometer on the *R/V Knorr*. Optical data were median filtered (12-point running median) to remove spikes associated with aggregates and other larger particles in the water column [*Briggs et al.*, 2011]. A mixed layer (ML) depth was estimated from a combination of the depth where the float-derived density exceeds the surface value by 0.01 kg m^{-3} and twice the average float depth during turbulent Lagrangian drifts, with discrepancies between these estimates resolved by eye.

In *Cetinić et al.* [2012], the co-variability of particulate organic carbon (POC) and inherent optical properties (IOPs) is statistically characterized during the NAB08 experiment, and relationships between POC and particulate beam attenuation $c_p(653)$ as well as POC and $b_{bp}(700)$ are established. Chlorophyll samples collected during the *R/V Knorr* cruise were used to convert the float's FLNTU *Chl F* measurements to derived *Chl* (mg m^{-3}) estimates using a non-linear best-fit function of temperature, photosynthetically active radiation (PAR), depth and yearday, with an error of 30-50% [*D'Asaro*, 2011]. Here, these relationships are used to estimate *Chl* and POC from fluorescence and $c_p(653)$, respectively.

The float also carried two low power, hyperspectral radiometers measuring downward spectral irradiance $E_d(z,\lambda)$ (TriOS ACC with 2-axis tilt sensor) and upward spectral radiance $L_u(z,\lambda)$ (TriOS ARC) at 3.3 nm increments from 320 to 950 nm with a spectral accuracy of 0.3 nm. Digital counts were converted to radiometric units using manufacturer-supplied radiometric calibration and immersion factors. Measurements were discarded for tilt angles > 5°. Sampling every 50-70s during profiles yielded an average of 3 m between radiometric samples. Periods

during the Lagrangian drifts, with radiometry sampled every 200 s, were selected to achieve a similar 2-3 m between samples; these selected periods had an average vertical velocity of 1.4 cm s^{-1}.

The ARC radiometer that measured upward radiance L_u can be shaded by the 1 m hexagonal drogue deployed during drift mode, the 25.4 cm diameter float end cap, or the 4.7 cm diameter sensor itself. This self-shading was corrected using equations described in *Leathers et al.* [2004] which are an extension of the work of *Gordon and Ding* [1992] to a buoy configuration where shading is modeled by a larger disk of radius r_b at a distance z_s from the sensor head of radius r_s. The result is a piecewise-nonlinear relationship between shading error ε in L_u and solar zenith angle θ_s, with a breakpoint at θ_s corresponding to the larger disk shadow passing out of the view of the sensor. Figure 4 shows shading error ε with and without the drogue for the largest value of absorption a = 0.22 m^{-1} retrieved during the deployment. The smallest solar zenith angle θ_s during the deployment is 38°. During drift mode when θ_s = 38-49°, the drogue's shadow below the L_u sensor is deeper than the depth of the float's end cap shadow; neither the float end cap nor the sensor head contributes shading beyond that of the drogue. In this case, the drogue shading is modeled as a disk with r_b = 0.5 m, z_s = 0.7 m and the corresponding L_u error ranges from ε = 0.015-0.15. Neither the drogue during drift mode periods where θ_s > 49° nor the float end cap during profiling (θ_s > 38°), modeled as a disk with radii r_b = 6.4 and 12.7 cm, contribute additional shading beyond that of the sensor head (r_s = 2.4 cm), in which results in small errors ε ≈ 0.015. Each $L_u(\lambda)$ wavelength was corrected for self-shading in two steps: 1) retrieve uncorrected absorption $a_{uc}(\lambda)$ with uncorrected $L_{uc}(\lambda)$ and 2) repeat the absorption retrieval using $L_u = L_{uc}(\lambda)/(1-\varepsilon)$, where ε is calculated from $a_{uc}(\lambda)$ and θ_s.

The 2π steradian view of the ACC E_d sensor can be partially obstructed by instrumentation on the float's top end cap (Figure 3) in some combinations of float orientation and solar zenith angle. A LI-COR 192SA PAR sensor was mounted at a different radial location on the float. To detect shading or biofouling of the ACC sensor, PAR was found by spectrally integrating $E_d(\lambda)$ and then compared to a contemporaneous LI-COR PAR reading; we assumed both sensors were never shaded or fouled simultaneously. The ACC $E_d(\lambda,z)$ spectra that were shaded compared to the LI-COR PAR sensor were removed from further analysis. Using this same method of comparison, the ACC radiometer was found to be bio-fouled during yeardays 120-140. Section 2.4 below discusses how we determined that this bio-fouling was spectrally neutral and the self-correcting nature of the absorption retrieval method for this case.

2.4 Shipboard CTD and bottle data

A single WET Labs FLNTU was used on both the *R/S Bjarni Sæmundsson* and the *R/V Knorr*; the same sensor type was deployed on the float. These measured *ChlF* and $b_{bp}(700)$. Details of the CTDs, bio-optical sensor processing, and intercalibration can be found in *Alkire et al.* [2012]. Water samples were taken at 32 stations for on-board plankton cell counts using flow cytometry (small phytoplankton, heterotrophic bacteria and heterotrophic nanoprotists) and FlowCAM (diatoms, autotrophic and mixotrophic dinoflagellates, chlorophyll *a*-containing ciliates, and other unclassified microphytoplankton). (M. Sieracki, unpublished data, 2011). Subsequently, living cell carbon for each phytoplankton group was estimated as described in *Sieracki and Poulton* [2012]. Samples were also taken for post-cruise analysis of nutrients, particulate organic carbon (POC) and phytoplankton pigments with HPLC. Additional details of water sampling processing for these products can be found in *Cetinić et al.* [2012]. Only *R.V. Knorr* cruise samples that were assessed to be in the same chlorophyll patch as the float are used in this study

[*Alkire et al.*, 2012]. At six stations, water samples were collected using the ship's CTD rosette within an hour of the float profiles and subsequently ship-board measurements of spectrophotometric filter pad absorption were carried out with ~1 nm resolution [*Kallin et al.*, 2011]. The phytoplankton absorption coefficient $a_{\phi}^{spec}(\lambda)$ was determined from the difference between the total particulate and detrital absorption coefficients using the Kishino method [*Kishino et al.*, 1985].

Phytoplankton community structure was assessed from shipboard data in three ways:

1) **Carbon:** Total autotrophic carbon was assessed by the following equation, based on the classes assigned to the results of flow cytometry and FlowCAM imaging:

$$C_{auto} = C_{diatom} + C_{coccus} + C_{dino\_auto\_mix} + C_{pnans} + C_{crypto} \quad (53)$$

where 'diatom' refers to diatoms, 'coccus' refers to *Synechococcus sp.,* 'dino_auto_mix' refers to autotrophic or mixotrophic (i.e., chlorophyll-containing) dinoflagellates, 'pnans' refers to photosynthetic pico- and nanoeukaryotes, and 'crypto' refers to cryptomonads. From this, we compute the portion of phytoplankton carbon ascribed to "small" phytoplankton (< 20 μm) as C_{pnans}/C_{auto} and the portion ascribed to diatoms as C_{diatom}/C_{auto}.

2) **Pigments:** Following the parameterization of *Uitz et al.* [2006], HPLC pigment concentrations provided an assessment of phytoplankton size class assessed as the fraction of chlorophyll *a* concentration f_{pico}, f_{nano}, and f_{micro} associated with picophytoplankton, nanophytoplankton and microphytoplankton, respectively. From this, a second assessment of "small" phytoplankton can be computed as $f_{pico} + f_{nano}$. Additionally, an assessment of diatoms alone can be made from the ratio of fucoxanthin, the diagnostic pigment for diatoms, to total Chl *a*, i.e., [fucoxanthin]/[Chl

a]. *Cetinić et al.* (manuscript in preparation, 2012) found that this assessment of the proportion of diatoms agreed well with that based on carbon, which allowed the construction of a blended product of "percent diatom domination" f_{diatom}, either as percent phytoplankton cell carbon or percent *Chl.*

3) **Bio-optical index**: According to *Cetinić et al.* [2012], the ratio of *ChlF* to $b_{bp}(700)$ (hereafter denoted *ChlF*:b_{bp}) within a 10–50 m depth range was found to co-vary with changes in the dominant plankton taxa during the 2008 North Atlantic Bloom Experiment. This assessment is valid for bio-optical measurements made from both the CTD and the Lagrangian float. High *ChlF*:b_{bp} ratios (80-180 V m) were measured in waters dominated by diatoms, based on comparisons to C_{diatom}/C_{auto} and [fucoxanthin]/[Chl *a*]. Low *ChlF*:b_{bp} ratios (20–80 V m) were measured in waters dominated by small phytoplankton, heterotrophic nanoprotists and heterotrophic bacteria and few diatoms (i.e., recycling communities). The slope of *ChlF* vs. b_{bp} can be used to diagnose a transition between these two communities.

2.5 Retrieval of hyperspectral absorption from float radiometry

An inverse algorithm is used to retrieve hyperspectral absorption coefficients from the measurements of hyperspectral radiometric measurements of $L_u(\lambda,z)$, $E_d(\lambda,z)$, and $c_p(653)$ [*Rehm and Mobley*, 2012]. The inversion procedure is based on a forward model that is an accurate solution to the radiative transfer equation (EcoLight, [*Mobley*, 2011]), which relates the in-water inherent optical properties (IOPs) to the spectral light field. The inversion procedure, via a non-linear least squares optimization routine, repeatedly solves the forward problem varying two input IOPs (absorption, backscattering) until the measured and estimated light fields ($L_u(\lambda)$, $E_d(\lambda)$) match within a given criterion. The beam attenuation $c(653)$ measurement adequately populates the null space of the otherwise ill- posed inverse problem [*Aster et al.*, 2012]. Using

this method, 3.3 nm resolution retrievals of particulate plus detrital absorption $a_{pg}(\lambda)$ are valid from 320 - 575 nm (77 wavelengths total). Retrievals at wavelengths higher than 575 nm are not possible due to the high value of pure water absorption at these wavelengths that makes the particulate absorption signal difficult to retrieve, as well as the increasingly isotropic light field due to inelastic scattering.

The inversion method assumes that IOPs are vertically homogeneous in the mixed layer and requires knowledge of $L_u(\lambda,z)$, $E_d(\lambda,z)$ and $c(653,z)$ over a range of depths, as well as the solar zenith angle θ_s, wind speed at 10 m U_{10}, cloud cover fraction *cloud*, and incident solar irradiance $E_s(\lambda)$. Latitude and longitude, interpolated from a daily GPS fix, and the time of day from an internal clock are used to estimate θ_s. Wind speed, used to describe the transfer of light across a rough sea surface, is derived from the NCEP WW3 Global Reanalysis product, http://dss.ucar.edu/pub/reanalysis/. Incident solar irradiation is estimated from θ_s and *cloud* using a solar irradiance model based on RADTRAN [*Gregg and Carder*, 1990]. However, since the float is below the surface, the cloud fraction *cloud,* and therefore the correct incident solar irradiance, are not known. Therefore, the retrieval method is modified by augmenting the retrieved parameters **m** to include the fraction of cloud cover, *cloud*, i.e., $\mathbf{m} = [a, b_b, cloud]^T$. Thus, the optimization procedure is free to control the absolute value, but not the direction or spectral composition, of incident solar irradiance over a reasonable range by varying magnitude of the direct and diffuse components of clear-sky irradiances [*Kasten and Czeplak*, 1980]. Varying the parameter *cloud* also changes the angular distribution of the incident sky radiance by changing the relative contributions of clear and overcast normalized sky radiances [*Harrison and Coombes*, 1988], which also aids in matching the directional nature of the light field that can be ascertained by $L_u(\lambda,z)$ and $E_d(\lambda,z)$.

2.6 Retrieval of phytoplankton size class from absorption

We utilize a phytoplankton absorption model based on *Ciotti et al.* [2002] in order to discover aspects of phytoplankton community size structure from the hyperspectral absorption $a_{pg}(\lambda)$ retrieved from float radiometry. Absorption $a_{pg}(\lambda)$ can be expressed as the sum of absorption coefficients for phytoplankton cells and non-algal particles (NAP) and colored dissolved organic matter (CDOM):

$$\hat{a}_{pg}(\lambda) = a_{\phi}(\lambda) + a_{NAP}(\lambda) + a_{CDOM}(\lambda), \tag{54}$$

where the subscripts ϕ represents phytoplankton. *Ciotti et al.* [2002] expressed phytoplankton absorption $a_{\phi}(\lambda)$ as a spectral mixture of two basis functions defined by laboratory absorption measurements of natural communities of microphytoplankton and picophytoplankton from surface waters, and subsequently retrieved a size parameter for phytoplankton community from high resolution (1 nm) absorption spectra as well as from multispectral SeaWIFS satellite water leaving radiances [*Ciotti and Bricaud*, 2006]:

$$a_{\phi}(\lambda) = a_{\langle\phi\rangle} \cdot \left\{ \left[S_f \cdot \overline{a}_{\langle pico\rangle}(\lambda) \right] + \left[\left(1 - S_f\right) \cdot \overline{a}_{\langle micro\rangle}(\lambda) \right] \right\}, \tag{55}$$

where the size parameter S_f is constrained to vary between 0 and 1 and specifies the relative contributions of picophytoplankton and microphytoplankton to absorption, $a_{\langle\phi\rangle}$ controls the amplitude of the spectrum, while $\overline{a}_{\langle pico\rangle}$ and $\overline{a}_{\langle micro\rangle}$ represent the area-normalized end member spectra (basis vectors) for picophytoplankton (<2 μm) and microphytoplankton (> 20 μm), respectively. Absorption due to CDOM and NAP have similar absorption spectra that can be

merged into a single term, $a_{CDM}(\lambda)$ [*Roesler et al.*, 1989] representing colored detrital material (CDM)

$$\begin{aligned} a_{CDM}(\lambda) &= a_{NAP}(\lambda) + a_{CDOM}(\lambda) \\ &= a_{CDM}(\lambda_0)\exp[-S_{CDM}(\lambda - \lambda_0)], \end{aligned} \tag{56}$$

where the exponential slope S_{CDM} and $a_{CDM}(\lambda_0)$, the concentration of CDM at λ_0 = 440 nm, are fitted parameters. Together, the four parameters $[a_{\langle\phi\rangle}, S_f, a_{CDM}(\lambda_0), S_{CDM}]$ are found by a nonlinear optimization technique that minimizes the least-squared error between the absorption estimated from radiometry $a_{pg}(\lambda)$ and that estimated bio-optical model with size parameter $\hat{a}_{pg}(\lambda)$,

$$\min \left\| a_{pg} - \hat{a}_{pg} \right\|_2^2 . \tag{57}$$

The basis vectors tabulated by *Ciotti et al.* [2002] and *Ciotti and Bricaud* [2006] are available at 2 nm resolution from 400-700 nm. Using SeaWiFS satellite ocean color data a 412, 443, 490, 510 and 555 nm, *Ciotti and Bricaud* [2006] retrieve size parameter S_f with 17.2% error compared to S_f retrievals using full resolution spectrometric data from 400-700 nm. Therefore we expect accurate S_f retrievals from 3.3 nm resolution $a_{pg}(\lambda)$ retrievals from float radiometry that are band-limited to 400-575 nm. This assumption will be tested by comparing retrievals from float radiometry to full spectrum (400-700 nm) S_f retrievals from the spectrophotometric filter pad absorption measurements from the *R/V Knorr*, where equation (55) will be applied directly to the $a_{\phi}^{spec}(\lambda)$ spectra.

2.7 Estimation of pigments from absorption spectra

Derivative spectroscopy provides a means to objectively assess the existence and concentration of the photosynthetic and photoprotective pigments that contribute to the phytoplankton absorption spectrum. Unlike Gaussian band analysis (e.g., [*Hoepffner and Sathyendranath*, 1991]), no a priori assumption is made about absorption band positions or widths. Derivative analysis has been found to minimize low-frequency background noise and resolve the overlapping contributions of component pigment spectra that give rise to peaks and shoulders in an observed absorption spectrum [*Aguirre-Gomez et al.*, 2001a; *Butler and Hopkins*, 1970; *Faust and Norris*, 1985]. We computed spectral derivatives of $a_{pg}(\lambda)$ using the Savitzky-Golay smoothing and differentiation method [*Ruffin et al.*, 2008; *Tsai and Philpot*, 1998]. The Savitzky-Golay filter is commonly used to render noisy spectrophotometric data because it (and subsequent differentiation) preserves higher-order moments in the data [*Press et al.*, 2007]. Here we used a 5-point filter length and a third degree polynomial to compute second order spectra. For higher order derivatives, a fifth degree smoothing polynomial was used. By analytical differentiation of the underlying polynomial, derivatives were computed directly from the filter coefficients rather than by repeated finite approximation of the smoothed spectra itself, so as not to introduce additional noise [*Luo et al.*, 2005]. Since differentiation cannot be applied directly at the ends of the spectrum, the differentiated spectrum is shorter than the original by the width of the filter. Absorption band center positions were distinguished from noise using the criteria of *Huguenin and Jones* [1986]

$$a_{pg}^{II}(\lambda) < 0, \quad a_{pg}^{IV}(\lambda) > 0, \quad a_{pg}^{V}(\lambda) \approx 0, \tag{58}$$

where the superscript indicates the order of the derivative. Peaks in $a_{pg}^{II}(\lambda)$ and $a_{pg}^{IV}(\lambda)$ are assessed objectively using a noise tolerant peak finding algorithm [*Yoder*, 2011]; $a_{pg}^{V}(\lambda)$ was assessed by visual inspection.

3 Results and discussion

3.1 Background

Alkire et al. [2012] and *Cetinić et al.* [2012] describe the evolution of the bloom through six periods, based on the measured physical and biogeochemical parameters (Figure 5a, Figure 6). Phytoplankton biomass, expressed as chlorophyll concentration derived from the float fluorometer, was consistently low (*Chl* < 0.5 mg m-3) during the *Deep Mixing* period (yd 95-110), characterized by a mixed layer often deeper than 100 m and active mixing to depths below 250 m (the lower depth limit of the float). During the subsequent *Early Bloom* period (yd 111-119), the upper ocean stratifies with the mixed layer shoaling to 50 m and phytoplankton biomass grew exponentially to *Chl* = 2 mg m^{-3}. The early bloom was interrupted by the *Storm* period (yd 119-127), with active vertical mixing deepening the mixed layer to 50-100 m and causing a small nitrate increase. During this period, the *R/V Knorr* arrived on site, sampling in the same patch as the float. FlowCAM observations confirmed the existence of diatoms. Subsequent HPLC analysis from water samples confirmed the existence of the accessory pigment fucoxanthin (Figure 5bc). Following the storm, the *Main Bloom* period (yd 127-134) began as the water column stratified, with the mixed layer shoaling to 30 m. During this time the float followed a well-defined patch of higher salinity water which experienced exponential growth of a diatom-dominated community up to *Chl* 4.5 mg m^{-3}. Diatom dominance is confirmed by a matching increase in fucoxanthin (Figure 5b), as well as an increase in diatom carbon

relative to pico- and nanophytoplankton carbon (pnans, Figure 5c). During this period there is also a rise in chlorophyll transformation products (pheophorbide *a* + chlorophyllide *a,* Figure 5a) and the appearance of dinoflagellates in FlowCAM results (Figure 5c) along with the detection of the dinoflagellate pigment peridinin (Figure 5b). The main bloom abruptly ended between yearday 134-135 when silicic acid was depleted causing the diatoms to almost disappear. The phytoplankton community in the patch shifted to a recycling community dominated by smaller phytoplankton, heterotrophic bacteria and heterotrophic nanoprotists, with *Chl* declining to 1 mg m^{-3} (Figure 5a), accompanied by a decline in fucoxanthin (Figure 5b) and a large increase in pico- and nanophytoplankton (Figure 5c). The *Eddy* period (yd 135-140) was characterized by relative inactivity as the float encountered a small anticyclonic eddy/front on yd 138. Following this, there is suggestion of another bloom (*Post Bloom,* yd 141-145) with *Chl* rising slightly again; the *R/V Knorr had left the study area by that time*. The float's maximum file count was unexpectedly exceeded on yd 145, terminating the science mission after 51 d of operation.

3.2 Absorption spectra retrieval from float radiometry

Absorption spectra were retrieved from 42 daily float radiometric profiles and 459 radiometric measurements during float drifts. The profile spectra typically spanned 10-30 m (1-3 optical depths) and none were rejected. Drift time periods were broken into 16.7 min subperiods to minimize errors due to varying solar zenith angle (see *Rehm and Mobley* [2012]). The radiometric sampling interval was 200 sec, yielding 5 radiometric samples per subperiod. The quality of each retrieved drift mode spectra was assessed by comparing the RMS error between the retrieved spectra and a version smoothed with a cubic Savitzky-Golay filter with an 11-point fitting window; spectra with more than 0.001 m^{-1} RMS difference were rejected. The inverse method implicitly depends on the vertical derivative of the light field by spectral matching of L_u

and E_d at multiple depths; most of the 387 rejected drift mode subperiods had insufficient vertical expression, resulting in very noisy a_{pg} spectra. The remaining 72 drift mode subperiods qualify as "vicarious" profiles, typically spanning a depth range of approximately 20 m. Subsequent results will either use the 42 profile spectra or the combined 114 profile plus drift mode spectra. Sample locations in both profile and drift mode generally fell within the 10% light level, or equivalently, within two optical depths (Figure 6),

3.3 Validation of float absorption retrievals

In previous work by *Rehm and Mobley* [2012], estimates of particulate plus detrital absorption compared well to spectrophotometric filter pad absorption carried out at three float calibration stations, with filter pad scans falling within the 95% confidence interval of the estimates. However, the $a_{pg}(\lambda)$ estimates were found to be highly sensitive to measurements of incident solar radiation $E_s(\lambda)$: a ten percent error in $E_s(\lambda)$ leads a 10 percent error in the estimation of $a_{pg}(\lambda)$. Therefore, we must first qualify the ability of the RADTRAN model and use of the cloud fraction parameter *cloud* as retrieval parameter in the optimization procedure to correctly estimate the incident solar radiation, and thereby achieve quality absorption retrievals. Matchups of spectra retrieved from simultaneous radiometric calibration casts from the *R/V Knorr*, where full hyperspectral $E_s(\lambda)$ was recorded, and that of the contemporaneous float profiles within 1 km are shown in Figure 7 (see also Figure S1 for spectra from all calibration stations). Individual matchup errors ranged from 2% (1×10^{-3} m^{-1} RMS) at Station 94 to 20% (1.5×10^{-2} m^{-1} RMS) at Station 101. Excluding Station 101, the average error in $a_{pg}(\lambda)$ retrievals for the other five stations was 4.8% (4×10^{-3} m^{-1} RMS).

All the intercalibration measurements occurred during the period of biofouling of the float's E_d sensor (yeardays 120-140). During this time, PAR integrated from float Ed

measurements decreased by up to 20% relative to the companion LI-COR PAR sensor. Since the RMS errors between the retrieved float and ship $a_{pg}(\lambda)$ spectra are small, and there is no obvious spectrally-dependent bias in the retrievals (see Figure 7 and Figure S1), we conclude that that biofouling matter was spectrally neutral. Further, we hypothesize that the time-varying reduction in $E_d(\lambda)$ by the biofouling matter was accommodated in the optimization procedure by an upward adjustment of the cloud fraction in order to match the lower measured values of $E_d(\lambda)$. Available daily, 1 km satellite cloud products were not of sufficient temporal or spatial resolution to diagnose an anomaly due to biofouling versus that of remotely sense cloud cover [*Baum and Platnick*, 2006]. If the cloud fraction is systematically increased to accommodate lower $E_d(\lambda)$ values due to biofouling, this should produce should produce anomalously low $L_u(\lambda)$ estimates. Indeed, a small 5-6% negative bias in the estimated spectra was found, larger than the negative 1% bias found in estimated $L_u(\lambda)$ spectra from ship-based profiler measurements presented in *Rehm and Mobley* [2012]. We conclude that quality absorption retrievals are possible, even in the presence of spectrally neutral biofouling, using RADTRAN-modeled $E_s(\lambda)$ and allowing the optimization procedure, within the limits of the *Kasten and Czeplak* [1980] cloud fraction model, to adjust the overall total downwelling radiance.

3.4 Relationship between absorption and chlorophyll fluorescence

In so-called Case I waters in the open ocean, phytoplankton and associated detrital material a_{pg} covary and dominate the optical properties of water [*Morel and Prieur*, 1977]. To the first order, overall absorption should increase with phytoplankton biomass approximated by chlorophyll *a* concentration [*Prieur and Sathyendranath*, 1981]. Figure 8 demonstrates that such a relationship holds for $a_{pg}(440)$ retrieved from float profile radiometry and simultaneous measurements of

chlorophyll fluorescence *ChlF* from the float's FLNTU sensor during NAB08 A log-log regression between $a_{pg}(440)$ and *ChlF*

$$a_{pg}(440) = 0.193(ChlF)^{0.562}, \qquad r^2 = 0.94 \tag{59}$$

explains 94% of the variance, where the nonlinearity expresses variability in the relationship due to changes in pigment composition and package effect during the course of the bloom. Using the value of *Chl* derived from float fluorescence, we find the relationship

$$a_{pg}(440) = 0.0718[Chl]^{0.569}, \qquad r^2 = 0.89 \tag{60}$$

holds with only a slightly lower coefficient of determination (89%). The exponent in equation (60) is close to the exponent (0.627) established between phytoplankton absorption $a_{\phi}(440)$ and *Chl* by *Bricaud et al.* [1998] for waters throughout the world's oceans, indicating that absorption by colored detrital and dissolved material is roughly proportional to $a_{pg}(440)$. Thus we find that $a_{pg}(440)$ is almost as good predictor of chlorophyll as the fluorometer during daylight hours, and maybe better during mid-day hours in surface waters where chlorophyll fluorescence suffers from non-photochemical quenching (NPQ, [*Falkowski and Kolber*, 1995]). For an autonomous mission, the absorption estimates from radiometry could be combined with an existing predictive relationship between chlorophyll and absorption to create a self-check between the radiometers and fluorometer for fouling, or more optimistically, to create an intercalibration between the sensors. (See *Xing et al.* [2011] for an more direct intercalibration approach using the downwelling attenuation coefficient $K_d(490)$ and *ChlF*.)

3.5 Retrieval of phytoplankton size parameter

The bio-optical model of equation (55) was applied to the 42 spectra retrieved from float profiles and 72 spectra retrieved from vicarious profiles during drift mode. Figure 9 illustrates a typical estimated $\hat{a}_{pg}(\lambda)$ spectra, reconstructed from picophytoplankton absorption $a_{pico}(\lambda) = S_f \cdot \overline{a}_{\langle pico \rangle}(\lambda)$, microphytoplankton absorption $a_{micro}(\lambda) = \left(1 - S_f\right) \cdot \overline{a}_{\langle micro \rangle}(\lambda)$ and colored dissolved and detrital absorption $a_{CDM}(\lambda)$. The residual spectrum $a_{pg} - \hat{a}_{pg}$ identifies spectral features not found in the original spectrum. The residual spectrum (Figure 9b) is small near the chlorophyll *a* absorption peak at ~440 nm. This is to be expected since chlorophyll *a* is present in almost all marine phytoplankton, including all the main genera or groups used to form the picophytoplankton and microphytoplankton basis vectors (see Table 2 in *Ciotti et al.* [2002]). The residuals are larger at the narrow shoulders (e.g., 412, 465, 498, and 541 nm) in the original $a_{pg}(\lambda)$ spectrum and correspond to pigment absorption peaks also identified by second derivative analysis (Figure 9c; see also section 3.6). These larger residuals and the related shoulders contain taxonomic and physiological information not present (or averaged out) in the basis vector spectra, and are likely related to accessory pigments [*Ciotti et al.*, 2002].

The time series of 114 retrievals of size factor S_f for small phytoplankton is shown in Figure 10a. A cubic smoothing spline represents the mean trend of S_f along with 90% (±1 s.d.) and 95% (±2 s.d.) confidence intervals during the various phases of the bloom. During the *Deep Mixing* and *Storm* periods, the S_f retrieval has the greatest variability and uncertainty, discussed further below. The *Early Bloom* and *Main Bloom* periods are characterized by a falling size factor and increasing amplitude $a_{\langle \phi \rangle}$, consistent increases in diatom biomass as assessed by *Chl*, HPLC pigments and flow imaging. During the latter part of the *Early Bloom period* (yd 114-

119), S_f declines from 0.9 to 0.01 indicating a large change in relative community composition from small to large phytoplankton; this change is consistent with exponential growth assessed by *Chl* derived from float fluorometry as well as POC derived from $c_p(653)$ during that time (Figure 5a). The optical index $ChlF:b_{bp}(700)$ also shifted to a higher value midway through the early bloom period [*Cetinić,* 2012, in preparation]. Entering the *Storm* period (yd 119-127), the size factor resets to a higher value ($S_f = 0.4$). The *Main Bloom* period sees a steady decline in S_f from 0.4 to 0.15 while $a_{\langle\phi\rangle}$ increases steadily from 0.03 to 0.08 m^{-1}.

The retrievals of size factor S_f from the spectrally-limited float $a_{pg}(\lambda)$ estimates (400 – 575 nm) compare well to S_f retrieved from spectrophotometric absorption $a_{\phi}^{spec}(\lambda)$ (400-700 nm), with most matchups falling within the ± 1 s.d. contour (Figure 10a, black + symbols). For example, the rise of the size factor during the *Eddy Period* is similar between the estimates. From this, we conclude that bio-optical model was able to reliably estimate $a_{\phi}(\lambda)$ from $a_{pg}(\lambda)$ using optically more complex and spectrally more limited data.

The decline in S_f during the *Main Bloom* period is bounded closely below by the fraction of chlorophyll *a* associated with pico- and nanophytoplankton, $f_{pico} + f_{nano}$, computed from HPLC pigment analysis; this HPLC-determined fraction declines from 0.1 to 0.05. The size factor S_f is bounded from above by the ratio of carbon attributed to pico- and nanoeukaryotes to total autotrophic carbon C_{pnans}/C_{auto} which declines from 0.6 to a minimal 0.28. When the bloom terminates on yd 134, all three estimates of small phytoplankton immediately increase, reaching a factor of 3-4 increase ($S_f \approx 0.45, f_{pico} + f_{nano} \approx 0.3, C_{pnans}/C_{autos} \approx 0.8$) by the end of the *R/V Knorr* cruise while *Chl* and $a_{\langle\phi\rangle}$ rapidly decrease. We conclude that the size factor S_f provides an assessment of the fraction of small phytoplankton intermediate to that explained by HPLC

(unpackaged pigments in solution), and that explained by cell counts and carbon:biovolume ratios.

When the float enters the *Eddy* period, evidence of a stable mixed community persists, with $S_f \approx 0.35$, consistent with observations of diatoms, dinoflagellates, and pnans in Figure 5c. Hints of a smaller bloom exist in the *Post Bloom* period, with small increases Chl and $a_{\langle\phi\rangle}$ and a small decrease in S_f.

During the *Deep Mixing* period (yd 105-110) and the beginning of the *Early Bloom* period (yd 111-113), rapid and large variations in S_f suggest implausibly large shifts in community structure. There are no similar changes in *Chl* or, as we will see in section 3.6, in the concentration of fucoxanthin, a photosynthetic accessory pigment found in diatoms. We suggest that these are due to variability in the light acclimatization of phytoplankton during these periods of deep mixing. *Ciotti et al.* [2002] found that their spectral mixture model explained 80% of the variability in the shape of the phytoplankton absorption spectra $a_\phi(\lambda)$. The cells in the surface samples examined by *Ciotti et al.* [2002] were all likely to be high-light acclimated, so the packaging effect exploited by their basis vectors was driven primarily by cell size; large cells have a smaller surface to volume ratio, resulting in self-shading between intracellular pigments [*Morel and Bricaud*, 1981]. However, increased intracellular pigment concentrations resulting from photoacclimation to low light also causes self-shading, resulting in the same spectral flattening as that produced by size [*Duyens*, 1956; *Falkowski and Raven*, 2007; *Morel and Bricaud*, 1981].

We hypothesize that the large variability seen in the size factor retrieval during the *Deep Mixing* and *Storm* periods is due to the mixing of low-light photoacclimated cells from below

below the 1% light level (Figure 6) into the first 10-30 m of the mixed layer used by this study's absorption retrievals, causing anomalously low S_f retrievals. To test this hypothesis, we compare the time scales of vertical mixing to the time scale of long term acclimation of phytoplankton to changes to low-light regimes. The time scale of vertical mixing can be estimated from $\tau_m \approx H/W$, where H the depth of the mixed layer estimated from daily float profiles and W is the typical vertical speed of water parcels, estimated here by RMS vertical velocity. Estimates of W have been computed from numerous float observations in the upper ocean boundary layer, and show a strong correlation between the wind speed at 10 m and RMS vertical velocity [*D'Asaro et al.*, 2011]. At the time of the *Early Bloom* period, typical NCEP wind speeds above the float are 10-15 m s^{-1}, resulting in a typical vertical velocity W of 1.5-2 cm s^{-1} (see Figure 3c in *D'Asaro et al.* [2011]). During this time, the mixed layer depth H is ≈100 m (Figure 6), leading to $\tau_m \approx H/W$ = 1-2 hours. This is far less than the typical photoacclimation time for phytoplankton pigments, estimated to be from 10-13 h [*Falkowski and Raven*, 2007; *Lewis et al.*, 1984] and up to several days [*Anning et al.*, 2000]. Thus vertical mixing can easily move dark-acclimated phytoplankton from the bottom of the mixed layer into the euphotic zone before they have time to re-acclimate to the surface layer. Also, the mixing is stochastic so many water parcels will remain deep and dark for much longer than τ_m, thus creating a continual source for dark-acclimated plankton. Once the mixed layer shallows, τ_m becomes much shorter and there is no such deep store. Therefore, during the *Deep Mixing* and start of *Early Bloom* periods, as well as the subsequent *Storm* period (yd 119-125), it is possible that low-light acclimated phytoplankton were mixed into the first two optical depths visited by the float, misinterpreted by this spectral unmixing as larger cells, causing the observed high variability in the S_f retrievals.

3.6 Retrieval of relative phytoplankton pigment concentrations

Derivative spectroscopy of a single absorption spectrum retrieved from a float profile (yd 132) is shown Figure 9c. The negative peaks $a_{pg}^{II}(\lambda) < 0$ correspond to narrow shoulders in the original $a_{pg}(\lambda)$ spectrum and the larger residuals remaining after the size factor spectral estimate $\hat{a}_{pg}(\lambda)$ is removed. In this case, these peaks occur at 412, 439, 465, 498, 508, 525 and 541 nm). All the peaks except 508 nm pass the remaining criteria, i.e., $a_{pg}^{IV}(\lambda) > 0, \quad a_{pg}^{V}(\lambda) \approx 0$. The peaks at 412 and 439 correspond to chlorophyll *a*, present in all algae of the red lineage. The peak at 465 nm is assigned to fucoxanthin, a marker pigment for diatoms, with known in vivo absorption peak in the range 460-480 nm [*Aguirre-Gomez et al.*, 2001a; *Mann and Myers*, 1968; *Roy et al.*, 2011]. The peaks at 525 and 541 nm may also be fucoxanthin [*Bidigare et al.*, 1989; *Mann and Myers*, 1968], but *Hoepffner and Sathyendranath* [1991] concluded that peaks near 536 nm may correspond to a mixture of xanthophylls and carotenes.

The results of second derivative spectroscopy applied to all the absorption spectra retrieved from float profile radiometry are presented as a spectrograph in Figure 11a. Peaks in all the spectra are identifies by black (carotenoids), green (chlorophylls) and orange (fucoxanthin, 465-478 nm). The magnitude of the second derivative $\left|a_{pg}^{II}(\lambda)\right|$ is proportional to the concentration of the pigment [*Faust and Norris*, 1985] and is shown for the chlorophyll *a* peaks $a_{pg}^{II}(412)$ and $a_{pg}^{II}(432-439)$ in Figure 11b. The trend of $\left|a_{pg}^{II}(\lambda)\right|$ for both chlorophyll peaks corresponds well to the float *Chl*, although resolution is limited of *Early* and *Main Bloom* exponential growth features and was as the diatom bloom termination.

The second derivative magnitude for fucoxanthin $\left|a_{pg}^{II}(465-478)\right|$ (n = 114) was compared to in-patch HPLC fucoxanthin values (n = 22) collected during the *Main Bloom* period of the *R/V Knorr* cruise. The relationship was linear with a correlation coefficient of 0.61. The slope of the type II regression was 785 ± 65 (mg) and a y-intercept of 0.010 ± 0.08 (mg). The resulting calibrated fucoxanthin concentration time series is shown in Figure 10b, along with the 90% and 95% confidence intervals and the HPLC samples used in the regression. The main features of the fucoxanthin pigment time series are very similar to that of chlorophyll, except for a curious 1-3 day phase lead in the float fucoxanthin time series compared to chlorophyll (Figure 10c), visible at the peak concentrations at end of the *Early Bloom*, and *Main Bloom* periods. Fucoxanthin values rise from 0.2 to 0.4 mg m^{-3} during the *Early Bloom* period and 0.4 to 1-1.2 mg m^{-3} during the *Main Bloom* period, dropping to 0.3 mg m^{-3} following the diatom bloom termination. A slight rise to 0.5 mg m^{-3} is seen in the later *Eddy* and *Post Bloom* periods. The ratio of fucoxanthin to chlorophyll during the *Early Bloom* period (~50%) is much larger than that during the *Main Bloom* period (~33%); this may indicate that other fucoxanthin-bearing organisms (e.g., dinoflagellates, prymnesiophytes, chrysophytes) may have been present in proportionally larger abundance during that time. A similar range and pattern of fucoxanthin and chlorophyll *a* concentrations from HPLC measurements was observed during the Lagrangian experiment carried out by *Barlow et al.* [1993] in the 1990 North Atlantic bloom (NAB90). Their range of NAB90 fucoxanthin concentration (0.25 – 1.5 mg m^{-3}) was similar to NAB08 (0.2 – 1.2 mg m^{-3}). While there are hints of a 1-2 d lead by fucoxanthin concentrations to HPLC Chl *a* in the NAB90 time series (see Figure 2B in *Barlow et al.* [1993]), it is not discussed.

Additional pigment peaks were detected in the second derivative spectra (Figure S2). For example, peaks detected at 330 nm are associated with absorption of mycosporine-like amino

acids (MAAs) in diatoms [*Ingalls et al.*, 2010; *Karentz et al.*, 1991]. Absorption peaks near 330 nm were also found in filter pad absorption measurements of water samples taken from the *R/V Knorr* [Kallin et al., 2011]. The biosynthesis of MAAs can be rapid, on the order of hours [*Shick and Dunlap*, 2002]; radiometric samples had insufficient temporal resolution to resolve any daily patterns of MAA production. However, from daily radiometric profiles, the occurrence and relative magnitude of MAA absorption peaks increased just prior and following bloom termination, suggesting that MAA's in this case may have played an antioxidant (rather than UV protectant) role as diatoms entered senescence and concomitant oxidative stress prior to aggregation and export [*Briggs et al.*, 2011; *Demmig-Adams and Adams III*, 2002; *Kahl et al.*, 2008].

3.7 Comparison to bio-optical community index

The third bio-optical community index, the ratio *ChlF*:b_{bp}, is derived from float measurements independent of those used for the estimation of $a_{pg}(\lambda)$ and can be thought of as a proxy for the chlorophyll:carbon ratio that takes on two modes during the portion of the NAB08 experiment covered here [*I. Cetinić et al.*, manuscript in preparation, 2012] (Figure 12a): 1) a *biomass mode* where *ChlF* and b_{bp} co-vary in a linear fashion, both being driven by biomass rather the physiological changes, and 2) a *transition mode* where *ChlF* and b_{bp} are more decoupled and independent variations in *ChlF* reflect the physiological response of phytoplankton to changes in light, nutrients and/or temperature. *I. Cetinić et al.* (manuscript in preparation, 2012) find that the *biomass mode* is valid until midway through the *Main Bloom* period (yd 104-131), with *ChlF*:b_{bp} averaging 75 Vm from yearday 95-117 and shifting to 100 V m during and after the *Storm* period. Flow imaging and microscopy carried during this period confirm that this *biomass mode* was dominated by diatoms. This was followed by a *transition mode* period (yd > 131-141) where

the community moves to a mixed assemblage coincident with the depletion of silica and the export of diatoms from the euphotic zone [*Briggs et al.*, 2011; *Martin et al.*, 2011]. Flow imaging and microscopy indicated a mixed assemblage of dinoflagellates, different diatom species, nanoflagellates, and mixotrophic ciliates [*Sieracki et al.*, 2010]. In this *transition mode,* where increases in *ChlF* are not coupled to b_{bp}, *ChlF*:b_{bp} increases to its highest value (> 150 V m) and then declines rapidly. The phytoplankton community returns to *biomass mode* with slightly lower but constant *ChlF*:b_{bp} ~ 50 V m in the *Post Bloom* period (yd > 141).

The radiometry-derived and supporting HPLC/carbon community indices provide additional information about the community composition and transitions described by the bio-optical index *ChlF*:b_{bp}. During the first diatom-dominated *biomass mode* period, the community increases from 20-50% diatoms based on the merged HPLC and carbon diatom fraction f_{diat} (Figure 12a). The size factor retrieved from float radiometry, replotted in Figure 12b as the fraction of *large* diatoms 1-S_f, indicates a growing fraction of the community dominated by large phytoplankton, with a much larger percentage of large phytoplankton (up to 90%) during the *Storm* and *Main Bloom* periods. The bio-optical index *ChlF*:b_{bp} and the size factor 1-S_f both show distinct periods before (1-S_f < 25%) and after (1-S_f ≈ 60-90%) the *Early Bloom* period. Fucoxanthin (Figure 12c) retrievals reveal two distinct *biomass mode* periods (0.1 – 0.3 mg m^{-3} before yearday 116, 0.3-1.2 mg m^{-3} afterwards), confirming a larger increase in diatoms during and after *Storm* period.

The changing slope of *ChlF*:b_{bp} marks the *transition mode* period (yd 131-141) where all other indices also change. a) The diatom dominance factor f_{diatom} from both HPLC and carbon-based assessments rise to 100%, then rapidly declines to < 20%. There is much less agreement in the final portion of the *transition mode* (yd 137-139) between the HPLC (10-90%) and carbon-

based (<25%) assessments of diatom dominance. (See also Figure 5bc.) There is evidence that fucoxanthin is destroyed by grazers to a lesser extent or otherwise degrades more slowly than chlorophyll [*McLeroy-Etheridge and McManus*, 1999; *Nunn et al.*, 2010], offering an explanation for the disparity between the fucoxanthin and carbon-based assessments of diatom dominance. b) The size factor 1-S_f decreases less dramatically from 90% to 60%, but confirms a transition to an assemblage of mixed cell size. c) The float-based fucoxanthin retrieval makes a dramatic turn, increasing from 0.75 to 1.2 mg m^{-3} from yearday 131-134, then declining to 0.2 – 0.4 mg m^{-3} by yearday 141, confirming the rapidly declining role of diatoms in this transitional period.

The float observations of the *transition mode* period end on yearday 141 as the float crosses a front into fresher water. Changes in bio-optical observations at this time may be due to lateral effects. Nevertheless, the bio-optical index indicates a return to a *biomass mode* where *Chl* and b_{bp} covary. The size factor of large phytoplankton 1-S_f is smaller than in the earlier diatom-dominated *biomass mode* (Figure 12b), yet the float-based fucoxanthin (Figure 12c) is greater than zero, indicating the continued presence of diatoms (or undegraded fucoxanthin) in the mixed assemblage.

4 Summary and Conclusions

The optical sensors (two hyperspectral radiometers, a single wavelength beam transmissometer, a single wavelength backscattering meter, and a chlorophyll fluorometer) and subsequent inversion algorithm used in this study allow us to retrieve hyperspectral absorption from 320-575 nm without the need of an incident solar irradiance sensor. With hyperspectral absorption data come more degrees of freedom than available from multispectral radiometric sensors, enabling the retrieval of a phytoplankton size factor by spectral unmixing, as well as the detection and

estimation of the concentration of several phytoplankton pigments (chlorphyll *a*, fucoxanthin and MAAs) that were large contributors to the absorption signal. While these absorption-based pigment detection techniques are not as sensitive as HPLC analysis of water samples, no a priori assumptions were made as to which pigment markers were to be assessed, nor was the use of empirical relationships between waveband ratios and optical properties required.

Together, the changes in size factor of small phytoplankton, the concentration of fucoxanthin and bio-optical index $ChlF{:}b_{bp}$ recounted the story of a diatom bloom, its termination and the transition to a new mixed-sized community assemblage no longer dominated by diatoms. Diatom existence and relative abundance over time was detected from solely from fucoxanthin absorption features. Changes in community size structure based on cell size pigment packaging effects on absorption spectra were found to be as sensitive as HPLC-based methods but were subject to aliasing by other physiological effects that also increases pigment packaging (e.g., mixing of low-light acclimated phytoplankton in the euphotic zone by storms). Such aliasing effects will also increase uncertainty in size factor retrievals from ocean color satellite observations (e.g., [*Ciotti and Bricaud*, 2006; *Mouw and Yoder*, 2010]) over waters subject to mixing below the first one or two optical depths. While the absolute value of the bio-optical index was locally interpreted, its slope was found to be useful in distinguishing between periods where first-order changes are due to biomass (abundance) and those periods of change due to physiology (pigmentation); this slope can help disambiguate the aforementioned pigment packaging aliasing.

The autonomous observations conducted during the 2008 North Atlantic Bloom experiment were supported by a suite of supporting water sample-based measurements. However, none of the optical assessments of community composition depended on these measurements in their

basic formulation: size factor estimates depended only on area-normalized absorption spectra, relative fucoxanthin concentration depended only on spectral variations in absorption, and the slope of the bio-optical index required only stable relative accuracy, but not absolute calibration, of the chlorophyll fluorescence and backscattering sensors. However, ground truth measurements were important for validating specific membership of the phytoplankton communities. If the relative composition and taxonomic succession blooming phytoplankton communities is well known, as it is in the North Atlantic, and the object of the study is the relative timing of these transitions (e.g., phenological studies), then such ground truth measurements may not be necessary. However, ground truth measurements such as those conducted during NAB08 will be required for abundance-based studies of primary productivity and carbon cycling, or in an environment where the taxonomic makeup of community transitions is paramount (e.g., harmful algal blooms).

The community transitions observed autonomously by the three methods were detected precisely in time. Long-term observations over the same period could diagnose the effects of climate and oceanic variability on spring bloom timing. Extending observation across entire annual cycle(s) in the North Atlantic would support the investigation of the role of intermittent winter blooms that sustain productivity and maintain a phytoplankton seed population [*Behrenfeld*, 2010; *Taylor and Ferrari*, 2011] as well as detect additional seasonal community transitions (e.g., summertime coccolithophore blooms with high backscattering and the marker pigment 19' –hexanoyloxyfucoxanthin) that are important to global carbon cycles [*Thierstein and Young*, 2004].

The low power requirements of these sensors allowed for a planned three-month mission on an autonomous Lagrangian platform that enabled observation of evolution of a bloom in a

vertically homogenous mixed layer, minimizing the effects of lateral mixing. With alternative or adaptive sampling schemes (e.g., additional scheduled profiles during bio-optical *transition mode* periods; bursts of increased radiometric sampling rate to increase the signal to noise ratio in the retrieved absorption spectra), more marker pigments may have been detected and/or daily variations in some pigments (e.g., MAAs) could be resolved.

Acknowledgements

E. Rehm was supported in this work by the National Science Foundation grants OCE0628379 and OCE0628107, and NASA grants NNX08AL92G and NNX-10AP29H. We wish to thank Michael Sieracki and Nicole Poulton for plankton species and cell carbon data. This work would not have been possible without the help of Emily Kallin, who assisted in the collection of NAB08 bio-optical profile data and performed the spectrophotometric measurements used here, Emmanuel Boss who loaned his Satlantic radiometric profiler, Michael Kenney and Michael Ohmart who patiently configured the bio-optical instruments on the float to our specifications, and the assistance of our Icelandic colleagues Kristinn Guðmundsson and Héðinn Valdimarsson. We wish to thank the captains and crews of the *R/V Knorr* and *R/V Bjarni Sæmundsson*.

References

Adjou, M., J. Bendtsen, and K. Richardson (2012), Modeling the influence from ocean transport, mixing and grazing on phytoplankton diversity, *Ecol. Model.*, *225*, 19-27.

Aguirre-Gomez, R., A. Weeks, and S. Boxall (2001a), The identification of phytoplankton pigments from absorption spectra, *Int. J. Remote Sens.*, *22*(2-3), 315-338.

Aguirre-Gomez, R., S. Boxall, and A. Weeks (2001b), Detecting photosynthetic algal pigments in natural populations using a high-spectral-resolution spectroradiometer, *Int. J. Remote Sens.*, *22*(15), 2867-2884.

Alkire, M., E. D'Asaro, C. Lee, M. Jane Perry, A. Gray, I. Cetinić, N. Briggs, E. Rehm, E. Kallin, J. Kaiser, and A. González-Posada (2012), Estimates of net community production and export using high-resolution, Lagrangian measurements of O2, NO3−, and POC through the evolution of a spring diatom bloom in the North Atlantic, *Deep Sea Res., Part I*, *64*, 157-174, doi:10.1016/j.dsr.2012.01.012.

Anning, T., H. L. MacIntyre, S. M. Pratt, P. J. Sammes, S. Gibb, and R. J. Geider (2000), Photoacclimation in the marine diatom Skeletonema costatum, *Limnol. Oceanogr.*, 1807-1817.

Aster, R. C., B. Borchers, and C. H. Thurber (2012), *Parameter estimation and inverse problems*, 2nd ed., Academic Press.

Babin, M., C. S. Roesler, and J. J. Cullen (2008), *Real-time coastal observing systems for marine ecosystem dynamics and harmful algal blooms: Theory, instrumentation and modelling*, UNESCO, Paris, France.

Bagniewski, W. J., K. Fennel, M. J. Perry, and E. A. D'Asaro (2011), Optimizing models of the North Atlantic spring bloom using physical, chemical and bio-optical observations from a Lagrangian float, *Biogeosciences*, *8*(5), 1291-1307, doi:10.5194/bg-8-1291-2011.

Barlow, R., R. Mantoura, M. Gough, and T. Fileman (1993), Pigment signatures of the phytoplankton composition in the northeastern Atlantic during the 1990 spring bloom, *Deep Sea Res., Part II*, *40*(1), 459-477.

Baum, B. A., and S. Platnick (2006), Introduction to MODIS cloud products, in *Earth Science Satellite Remote Sensing, Vol. 1: Science and instruments*, edited by J. J. Qu, W. Gao, M. Kafatos, R. E. Murphy and V. Salomonson, pp. 74-91, Springer-Verlag, Berlin.

Beaugrand, G., M. Edwards, and L. Legendre (2010), Marine biodiversity, ecosystem functioning, and carbon cycles, *Proceedings of the National Academy of Sciences*, *107*(22), 10120-10124.

Behrenfeld, M. J. (2010), Abandoning Sverdrup's critical depth hypothesis on phytoplankton blooms, *Ecology*, *91*(4), 977-989.

Bergquist, A. M., S. R. Carpenter, and J. C. Latino (1985), Shifts in phytoplankton size structure and community composition during grazing by contrasting zooplankton assemblages, *Limnol. Oceanogr.*, *30*(5), 1037-1045.

Bidigare, R., J. Morrow, and D. Kiefer (1989), Derivative analysis of spectral absorption by photosynthetic pigments in the western Sargasso Sea, *J. Mar. Res.*, *47*(2), 323-341.

Bricaud, A., H. Claustre, J. Ras, and K. Oubelkheir (2004), Natural variability of phytoplanktonic absorption in oceanic waters: Influence of the size structure of algal populations, *J. Geophys. Res*, *109*(C11), C11010.

Bricaud, A., A. Morel, M. Babin, K. Allali, and H. Claustre (1998), Variations of light absorption by suspended particles with chlorophyll a concentration in oceanic (case 1) waters: Analysis and implications for bio-optical models, *J. Geophys. Res.*, *103*(C13), 31033-31044, doi:10.1029/98jc02712.

Briggs, N., M. J. Perry, I. Cetinić, C. Lee, E. A. D'Asaro, A. M. Gray, and E. Rehm (2011), High-resolution observations of aggregate flux during a sub-polar North Atlantic spring bloom, *Deep Sea Res., Part I*, *58*(10), 1031-1039, doi:10.1016/j.dsr.2011.07.007.

Butler, W. L., and D. W. Hopkins (1970), Higher derivative analysis of complex absorption spectra, *Photochem. Photobiol.*, *12*(6), 439-450.

Cetinić, I., M. J. Perry, N. T. Briggs, E. Kallin, E. A. D'Asaro, and C. M. Lee (2012), Particulate organic carbon and inherent optical properties during 2008 North Atlantic Bloom Experiment, *J. Geophys. Res. (C Oceans)*, *117*(C6), C06028, doi:10.1029/2011JC007771.

Ciotti, A. M., and A. Bricaud (2006), Retrievals of a size parameter for phytoplankton and spectral light absorption by colored detrital matter from water-leaving radiances at SeaWiFS channels in a continental shelf region off Brazil, *Limnol. Oceanogr. Methods*, *4*, 237-253.

Ciotti, A. M., M. R. Lewis, and J. J. Cullen (2002), Assessment of the relationships between dominant cell size in natural phytoplankton communities and the spectral shape of the absorption coefficient, *Limnol. Oceanogr.*, *47*(2), 404-417.

Cushing, D. (1990), Plankton production and year-class strength in fish populations: an update of the match/mismatch hypothesis, *Adv. Mar. Biol.*, *26*, 249-293.

D'Asaro, E. A. (2003), Performance of autonomous Lagrangian floats, *J. Atmos. Oceanic Technol.*, *20*(6), 896-911.

D'Asaro, E. A. (2011), The 2008 North Atlantic Bloom Experiment Calibration Report #4: Calibration of the Chlorophyll Fluorometers on the Knorr CTD and Float 48, Biol. and Chem. Oceanogr. Data Manage. Off., Woods Hole, Mass., http://data.bco-dmo.org/NAB08/Chlorophyll_Calibration-NAB08.pdf.

D'Asaro, E., C. Lee, L. Rainville, R. Harcourt, and L. Thomas (2011), Enhanced turbulence and energy dissipation at ocean fronts, *Science*, *332*(6027), 318-322.

Demmig-Adams, B., and W. W. Adams III (2002), Antioxidants in photosynthesis and human nutrition, *Science*, *298*(5601), 2149-2153.

Duyens, L. N. M. (1956), The flattening of the absorption spectrum of suspensions, as compared to that of solutions, *Biochim Biophys Acta*, *19*(0), 1-12, doi:10.1016/0006-3002(56)90380-8.

Edwards, M., and A. J. Richardson (2004), Impact of climate change on marine pelagic phenology and trophic mismatch, *Nature*, *430*, 881-884.

Falkowski, P. G., and Z. Kolber (1995), Variations in chlorophyll fluorescence yields in phytoplankton in the world oceans, *Funct. Plant Biol.*, *22*(2), 341-355.

Falkowski, P. G., and J. A. Raven (2007), *Aquatic photosynthesis*, Princeton University Press, New Jersey.

Faust, M. A., and K. H. Norris (1985), In vivo spectrophotometric analysis of photosynthetic pigments in natural populations of phytoplankton, *Limnol. Oceanogr.*, *30*(6), 1316-1322.

Gordon, H. R., and K. Ding (1992), Self-shading of in-water optical instruments, *Limnol. Oceanogr.*, *37*(3), 491-500.

Gregg, W. W., and K. L. Carder (1990), A simple spectral solar irradiance model for cloudless maritime atmospheres, *Limnol. Oceanogr.*, *35*(8), 1657-1675.

Harcourt, R. R., and E. A. D'Asaro (2010), Measurement of Vertical Kinetic Energy and Vertical Velocity Skewness in Oceanic Boundary Layers by Imperfectly Lagrangian Floats, *J. Atmos. Oceanic Technol.*, *27*(11), 1918-1935.

Harrison, A. W., and C. A. Coombes (1988), An opaque cloud cover model of sky short wavelength radiance, *Solar Energy*, *41*(4), 387-392, doi:10.1016/0038-092x(88)90035-7.

Hoepffner, N., and S. Sathyendranath (1991), Effect of pigment composition on absorption properties of phytoplankton, *Mar. Ecol. Prog. Ser*, *73*(1), l-23.

Huguenin, R., and J. Jones (1986), Intelligent information extraction from reflectance spectra: Absorption band positions, *J. Geophys. Res.*, *91*(B9), 9585-9598.

Ingalls, A. E., K. Whitehead, and M. C. Bridoux (2010), Tinted windows: The presence of the UV absorbing compounds called mycosporine-like amino acids embedded in the frustules of marine diatoms, *Geochim. Cosmochim. Acta*, *74*(1), 104-115.

IOCCG (2011), Bio-Optical Sensors on Argo Floats, *Reports of the International Ocean-Colour Coordinating Group, 11*.

Irigoien, X., J. Huisman, and R. P. Harris (2004), Global biodiversity patterns of marine phytoplankton and zooplankton, *Nature*, *429*(6994), 863-867.

Kahl, L. A., A. Vardi, and O. Schofield (2008), Effects of phytoplankton physiology on export flux, *Mar. Ecol. Prog. Ser.*, *354*, 3-19, doi:10.3354/meps07333.

Kallin, E., I. Cetinić, M. J. Perry, and M. Sauer (2011), Laboratory_analysis_report-NAB08, Biol. and Chem. Oceanogr. Data Manage. Off., Woods Hole, Mass., http://osprey.bcodmo.org/dataset.cfm?id=13820&flag=view.

Karentz, D., F. McEuen, M. Land, and W. Dunlap (1991), Survey of mycosporine-like amino acid compounds in Antarctic marine organisms: potential protection from ultraviolet exposure, *Mar. Biol.*, *108*(1), 157-166.

Kasten, F., and G. Czeplak (1980), Solar and terrestrial radiation dependent on the amount and type of cloud, *Solar Energy*, *24*(2), 177-189.

Kishino, M., M. Takahashi, N. Okami, and S. Ichimura (1985), Estimation of the spectral absorption coefficients of phytoplankton in the sea, *Bull. Mar. Sci.*, *37*(2), 634-642.

Leathers, R., T. Downes, and C. Mobley (2004), Self-shading correction for oceanographic upwelling radiometers, *Opt. Express*, *12*(20), 4709-4718.

Leterme, S. C., M. Edwards, L. Seuront, M. Attrill, P. Reid, and A. John (2005), Decadal basin-scale changes in diatoms, dinoflagellates, and phytoplankton color across the North Atlantic, *Limnol. Oceanogr.*, 1244-1253.

Lewis, M., E. Horne, J. Cullen, N. Oakey, and T. Platt (1984), Turbulent motions may control phytoplankton photosynthesis in the upper ocean.

Luo, J., K. Ying, P. He, and J. Bai (2005), Properties of Savitzky–Golay digital differentiators, *Digital Signal Processing*, *15*(2), 122-136.

Mahadevan, A., E. D'Asaro, C. Lee, and M. J. Perry (2012), Eddy-Driven Stratification Initiates North Atlantic Spring Phytoplankton Blooms, *Science*, *337*(6090), 54-58, doi:10.1126/science.1218740.

Mann, J. E., and J. Myers (1968), On pigments, growth and photosynthesis of Phaeodactylum tricornutum, *J. Phycol.*, *4*(4), 349-355.

Margalef, R. (1978), Life-forms of phytoplankton as survival alternatives in an unstable environment, *Oceanol. Acta*, *1*(4).

Marra, J. (1978), Phytoplankton photosynthetic response to vertical movement in a mixed layer, *Mar. Biol.*, *46*(3), 203-208.

Martin, P., R. S. Lampitt, M. Jane Perry, R. Sanders, C. Lee, and E. D'Asaro (2011), Export and mesopelagic particle flux during a North Atlantic spring diatom bloom, *Deep Sea Res., Part I*, *58*(4), 338-349, doi:10.1016/j.dsr.2011.01.006.

McLeroy-Etheridge, S. L., and G. B. McManus (1999), Food type and concentration affect chlorophyll and carotenoid destruction during copepod feeding, *Limnol. Oceanogr.*, 2005-2011.

Mobley, C. D. (2011), Fast light calculations for ocean ecosystem and inverse models, *Opt. Express*, *19*(20), 18927-18944.

Morel, A., and L. Prieur (1977), Analysis of variations in ocean color, *Limnol. Oceanogr.*, 709-722.

Morel, A., and A. Bricaud (1981), Theoretical results concerning light absorption in a discrete medium, and application to specific absorption of phytoplankton, *Deep Sea Research Part A. Oceanographic Research Papers*, *28*(11), 1375-1393.

Morel, A., and D. Antoine (1994), Heating rate within the upper ocean in relation to its bio-optical state, *J. Phys. Oceanogr.*, *24*(7), 1652-1665.

Mouw, C. B., and J. A. Yoder (2010), Optical determination of phytoplankton size composition from global SeaWiFS imagery, *J. Geophys. Res.*, *115*(C12), C12018, doi:10.1029/2010jc006337.

Nunn, B. L., Y. S. Ting, L. Malmström, Y. S. Tsai, A. Squier, D. R. Goodlett, and H. R. Harvey (2010), The path to preservation: Using proteomics to decipher the fate of diatom proteins during microbial degradation, *Limnol. Oceanogr.*, *55*(4), 1790.

Platt, T., and K. T. F. Csar Fuentes-Yaco (2003), Marine ecology: spring algal bloom and larval fish survival, *Nature*, *423*(6938), 398-399.

Press, W. H., S. A. Teukolsky, W. T. Vetterling, and B. P. Flannery (2007), *Numerical recipes 3rd edition: The art of scientific computing*, Cambridge University Press.

Prieur, L., and S. Sathyendranath (1981), An optical classification of coastal and oceanic waters based on the specific spectral absorption curves of phytoplankton pigments, dissolved organic matter, and other particulate materials, *Limnol. Oceanogr.*, *26*(4), 19, doi:10.4319/lo.1981.26.4.0671.

Ptacnik, R., A. G. Solimini, T. Andersen, T. Tamminen, P. Brettum, L. Lepistö, E. Willén, and S. Rekolainen (2008), Diversity predicts stability and resource use efficiency in natural phytoplankton communities, *Proceedings of the National Academy of Sciences*, *105*(13), 5134-5138.

Rehm, E., and C. D. Mobley (2012), Estimation of hyperspectral inherent optical properties from in-water radiometry: error analysis and application to in situ data, *Appl. Opt.*, In press.

Richardson, A., and E. Poloczanska (2008), Under-resourced, under threat, *Science*, *320*(5881), 1294.

Roesler, C. S., M. J. Perry, and K. L. Carder (1989), Modeling in situ phytoplankton absorption from total absorption spectra in productive inland marine waters, *Limnol. Oceanogr.*, 1510-1523.

Roy, S., C. Llewellyn, E. S. Egeland, and G. Johnsen (2011), *Phytoplankton pigments: characterization, chemotaxonomy and applications in oceanography*, Cambridge University Press, Cambridge.

Ruffin, C., R. L. King, and N. H. Younan (2008), A combined derivative spectroscopy and Savitzky-Golay filtering method for the analysis of hyperspectral data, *GIScience & Remote Sensing*, *45*(1), 1-15.

Sathyendranath, S., and T. Platt (2007), Spectral effects in bio-optical control on the ocean system.

Shick, J. M., and W. C. Dunlap (2002), MYCOSPORINE-LIKE AMINO ACIDS AND RELATED GADUSOLS: Biosynthesis, Accumulation, and UV-Protective Functions in Aquatic Organisms, *Annu. Rev. Physiol.*, *64*(1), 223-262, doi:10.1146/annurev.physiol.64.081501.155802.

Sieracki, M. E., and N. Poulton (2012), Phytoplankton_Carbon-NAB08, Biol. and Chem. Oceanogr. Data Manage. Off., Woods Hole, Mass., http://osprey.bcodmo.org/dataset.cfm?id=13820&flag=view.

Sieracki, M. E., N. Poulton, E. Kallin, B. Thompson, E. A. D'Asaro, C. M. Lee, and M. J. Perry (2010), Plankton Succession and Biomass during the 2008 North Atlantic Spring Bloom, paper presented at Proceedings from the 2010 AGU Ocean Sciences Meeting, AGU, Portland, Oregon, 22-26 Feb 2010.

Taylor, J. R., and R. Ferrari (2011), Shutdown of turbulent convection as a new criterion for the onset of spring phytoplankton blooms, *Limnol. Oceanogr.*, *56*(6), 2293-2307.

Thierstein, H. R., and J. R. Young (2004), *Coccolithophores: from molecular processes to global impact*, Springer-Verlag, Berlin.

Tsai, F., and W. Philpot (1998), Derivative analysis of hyperspectral data, *Remote Sens. Environ.*, *66*(1), 41-51.

Uitz, J., H. Claustre, A. Morel, and S. B. Hooker (2006), Vertical distribution of phytoplankton communities in open ocean: An assessment based on surface chlorophyll, *J. Geophys. Res.*, *111*(C8), C08005.

Xing, X., A. Morel, H. Claustre, D. Antoine, F. D'Ortenzio, A. Poteau, and A. Mignot (2011), Combined processing and mutual interpretation of radiometry and fluorimetry from autonomous profiling Bio-Argo floats: Chlorophyll a retrieval, *J. Geophys. Res*, *116*, C06020.

Yoder, N. (2011), PeakFinder, a noise tolerant fast peak finding algorithm, MATLAB Central File Exchange, http://www.mathworks.com/matlabcentral/fileexchange/25500-peakfinder.

Tables

Table 13. Summary of measured parameters and associated sampling intervals (in seconds) of Float 48 during the 2008 North Atlantic Bloom Experiment.

Variables	**Float drift (mixed layer)**	**Float profile (0-230 m)**
$L_u(\lambda)$, $E_d(\lambda)$	200 (daylight)	50-60
PAR	50-60	50-60
$b_{bp}(700)$	50-70	50-70
Chlorophyll fluorescence	50-70	50-70
$c(653)$	200-300	50-70
Temperature, salinity	50-60	50-60

Figures

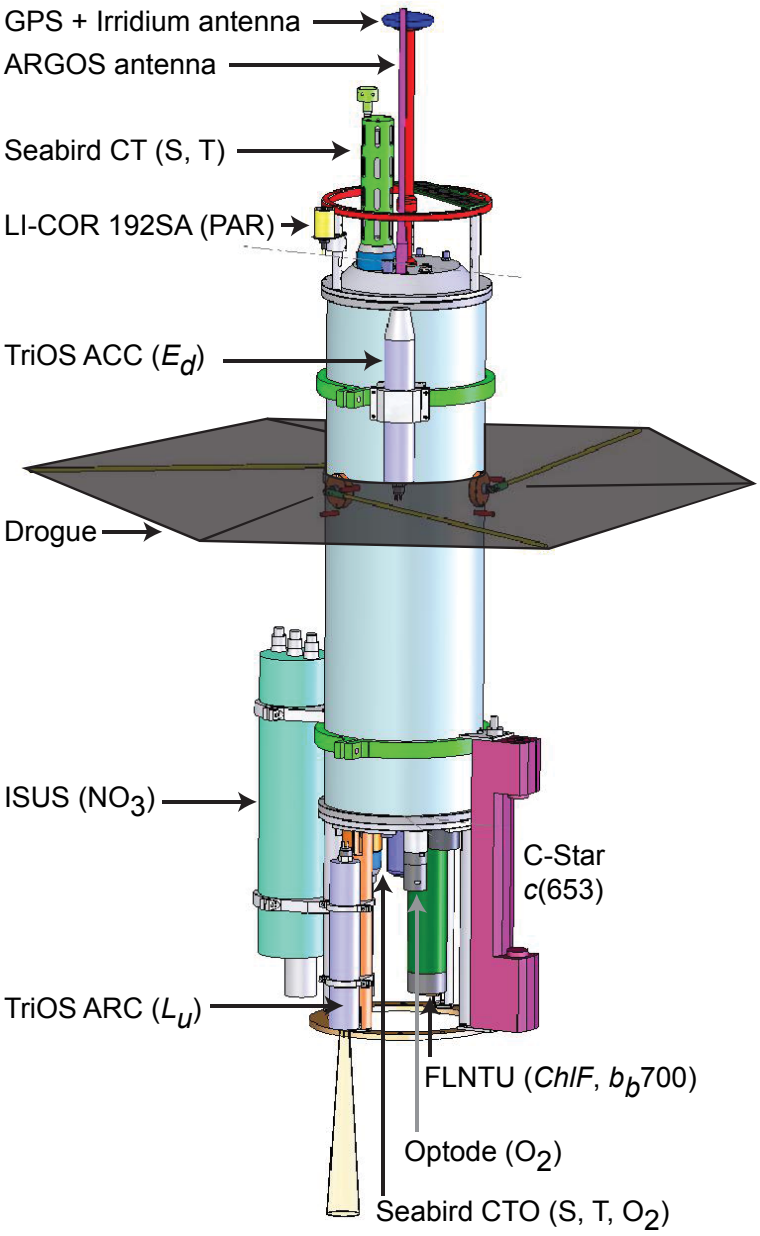

Figure 3. Mixed layer Lagrangian Float. The drogue (radius r_b = 0.5 m) was opaque black for NAB08.

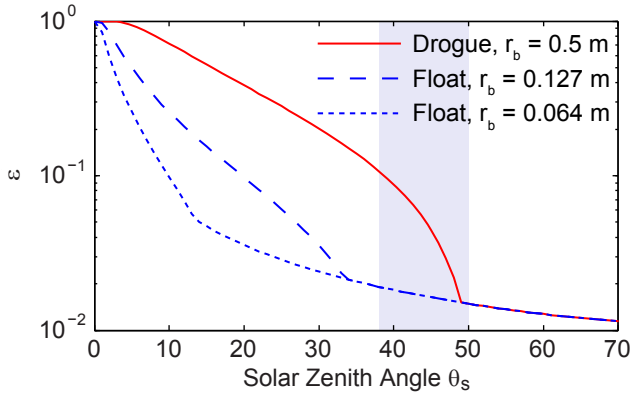

Figure 4. Shelf-shading error ε in Lu when drogue is deployed in drift mode (red) and retracted in profile mode (blue) for absorption a = 0.22 m-1 and a radius of an equivalent disk rb. Shaded region indicates the minimum solar zenith angle for yeardays 105-145. Break in curves indicates transition from shading by larger disk of radius rb (drogue or float end cap) to the smaller shading by the sensor head.

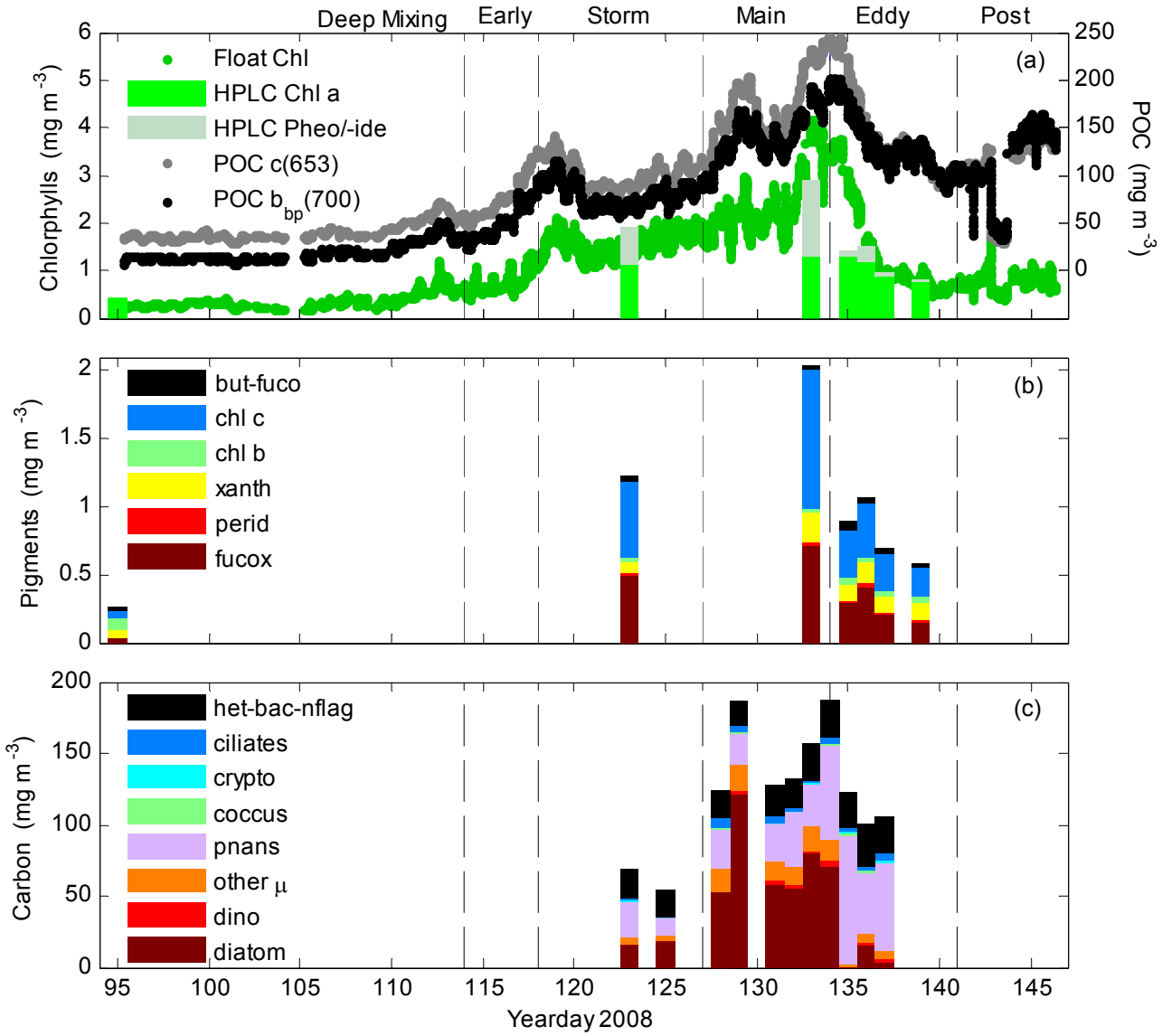

Figure 5. Changes in pigments and organic carbon during the 2008 North Atlantic Bloom reflecting the evolution of the phytoplankton community. (a) Chlorophyll and POC derived from optical proxies (ChlF, c_p(653), and b_{bp}(700)) during Lagrangian float drift mode. Also shown (bars) are HPLC measurements of total Chl *a* and chlorophyll transformation pigments (pheophorbide a + chlorophyllide a). (b) HPLC measurements of phytoplankton accessory pigments. Chl *b* includes divinyl Chl *b*. Chl *c* includes Chl *c1*, *c2*, and *c3*. Xanth includes alloxanthin, zeaxanthin, violaxanthin, diadinoxanthin, diatoxanthin, neoxanthin and lutein. (c) Phytoplankton carbon estimates from FlowCAM imaging (diatoms, auto- and mixotrophic dinoflagellates, other microplankton, heterotrophic ciliates) and flow cytometry (eukaryotic nano/picophytoplankton, cryptophytes, and prokaryotic Synechococcus spp., heterotrophic

bacteria and nanoflagellates). HPLC and flow imaging estimates are daily averages of 1-4 in-patch measurements.

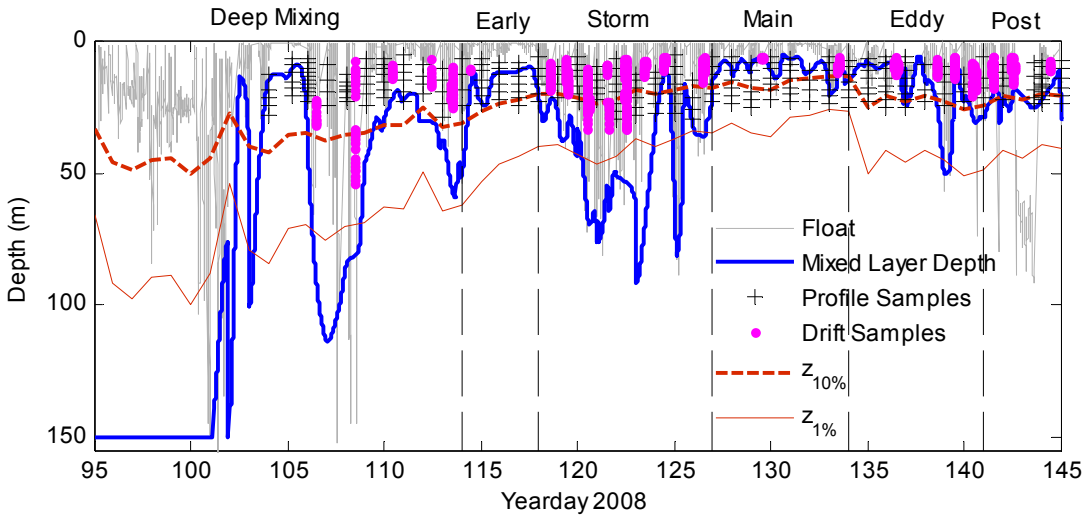

Figure 6. NAB08 float trajectory (grey) showing hyperspectral radiometric samples during profiling (+) and drift (magenta dots). Also shown are the mixed layer depth, (blue) daily average 10% (red dashed) and 1% (red thin) light levels, estimated from the diffuse attenuation coefficient K_d from daily PAR profiles.

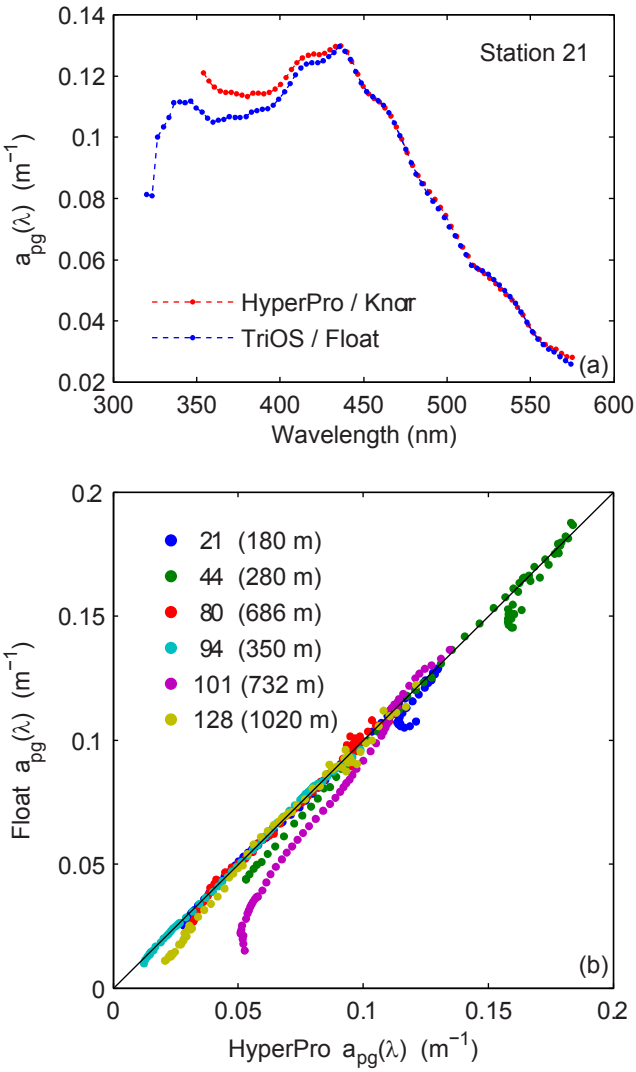

Figure 7. Matchup between absorption apg(λ) retrieved from float (TriOS) and ship-deployed (HyperPro) radiometry. (a) Station 21 (b) All stations Float-ship distance is in parenthesis.

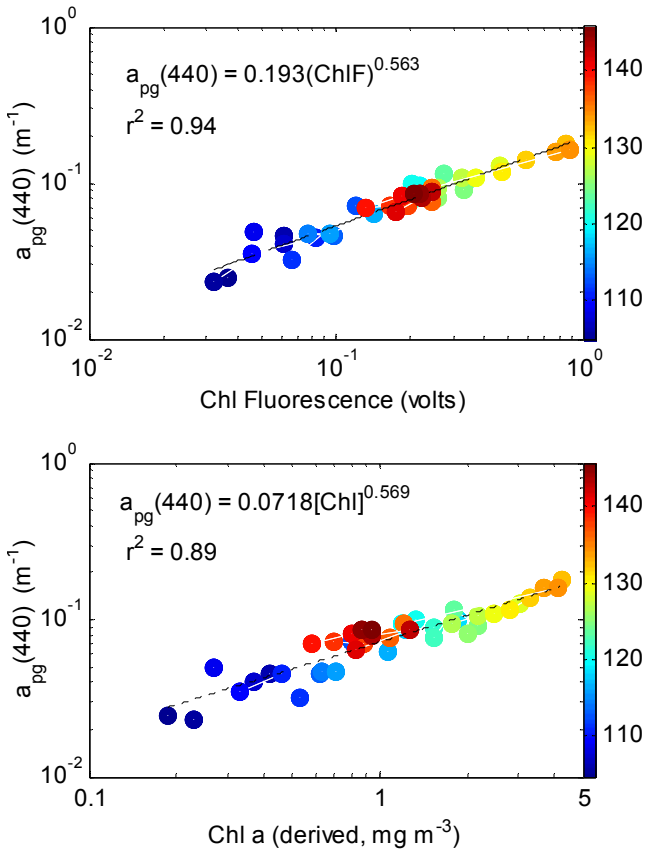

Figure 8. Relationship between absorption at 440 nm retrieved from float profile radiometry and (a) FLNTU chlorophyll fluorescence and (b) FLNTU chlorophyll fluorescence calibrated to bottle chlorophyll, PAR and temperature through regression. Dots are colored by the yearday of the retrieval. Notice log-log scale.

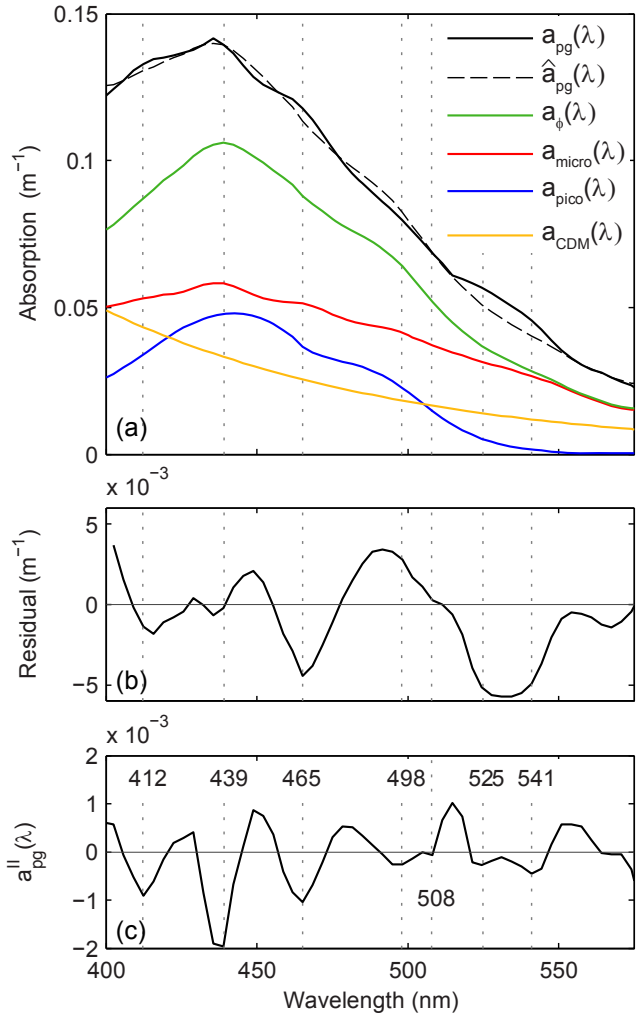

Figure 9. Estimation of size parameter S_f and pigments from absorption spectrum from float profile on yearday 132. (a) Absorption spectrum retrieved from radiometry $a_{pg}(\lambda)$ (black solid) and estimate from bio-optical model $\hat{a}_{pg}(\lambda) = a_{\phi}(\lambda) + a_{CDM}(\lambda)$ (black dashed). Constituent spectra are $a_{\phi}(\lambda) = a_{pico}(\lambda) + a_{micro}(\lambda)$ (green) yielding $S_f = 0.32$, $a_{pico}(\lambda) = S_f \cdot \overline{a}_{\langle pico \rangle}(\lambda)$ (blue), $a_{micro}(\lambda) = \left(1 - S_f\right) \cdot \overline{a}_{\langle micro \rangle}(\lambda)$ (red), and $a_{CDM}(\lambda)$ (yellow). (b) Residual spectrum $a_{pg}(\lambda) - \hat{a}_{pg}(\lambda)$. (c) Second derivative spectrum $a^{II}_{pg}(\lambda)$ has negative peaks corresponding features in residual spectrum, including fucoxanthin (465, 541 nm), other carotenoids (498, 508 nm), and additional Chl *a* variability (412, 439 nm). For all peaks, the other derivatives satisfy the conditions $a^{IV}_{pg}(\lambda) > 0, \quad a^{V}_{pg}(\lambda) \approx 0$.

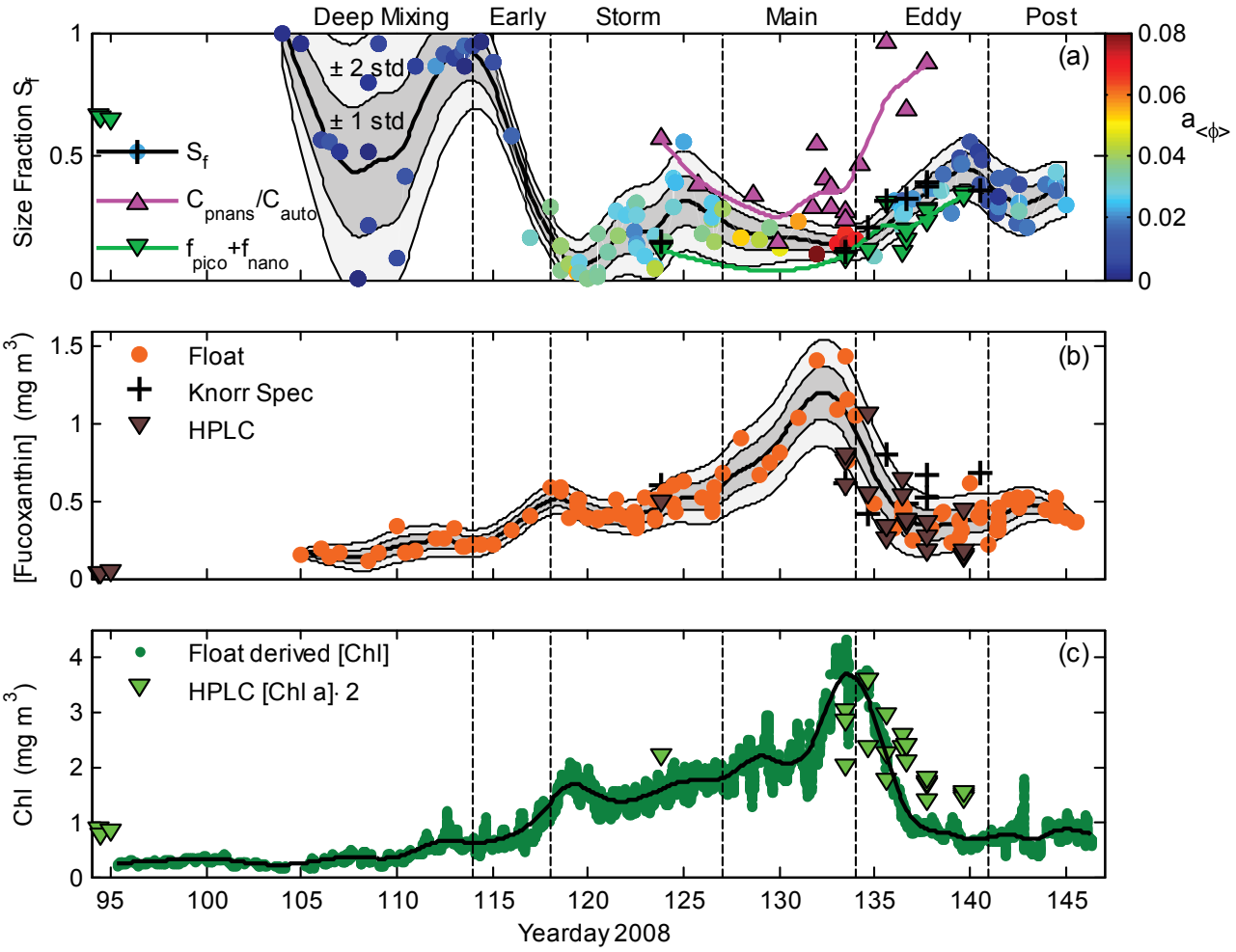

Figure 10. (a) Phytoplankton size class retrievals: Black line shows smoothed size factor estimate based on $a_{pg}(\lambda)$ retrieved from float radiometry according to equations (54) -(56); shaded area shows uncertainty as ±1 and ±2 standard deviations; colored dots and color bar represent the value of the scaling factor $a_{\langle\phi\rangle}$. Black + symbols indicate S_f retrievals from spectrophotometric filter pad measurements of $a_\phi^{spec}(\lambda)$. Magenta line and upward triangles indicated the carbon fraction for pico- and nanoplankton computed from flow cytometry. Green line and downward triangles indicate the sum of the HPLC-derived size factors for pico- and nanoplankton computed according to *Uitz et al.* [2006]. (b**)** Fucoxanthin retrievals: Black line and orange dots show fucoxanthin estimate based on 2nd derivative analysis of $a_{pg}(\lambda)$ retrieved from float radiometry, calibrated to HPLC [fucoxanthin]; shaded area shows uncertainty as ±1 and ±2 standard deviations. Black + symbols indicate fucoxanthin retrievals from spectrophotometric filter pad measurements of $a_\phi^{spec}(\lambda)$. Brown downward triangles indicate [fucoxanthin] determined by HPLC from water samples. (c) Black line and green dots show chlorophyll derived from float *ChlF*. Green downward triangles indicate HPLC total Chl *a*

samples × 2. Only HPLC and flow cytometry samples in the same patch as the float are shown in all plots.

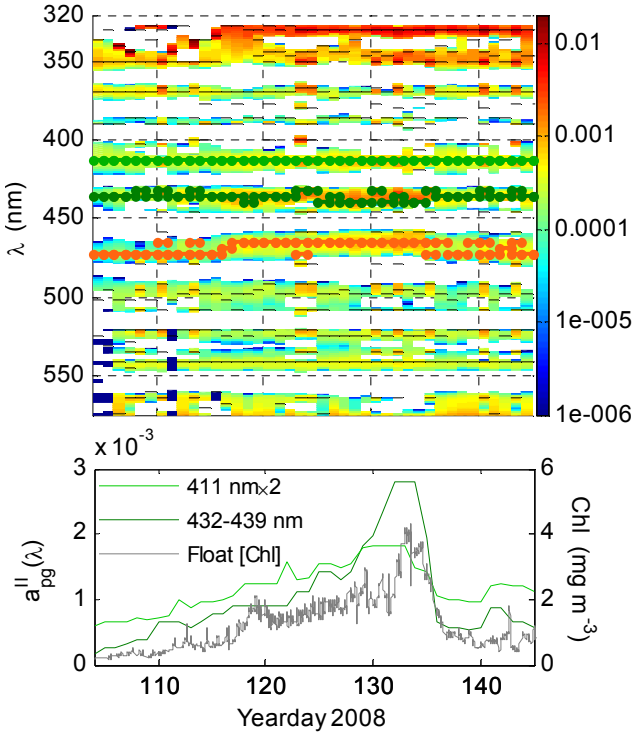

Figure 11. Derivative analysis of all absorption spectra retrieved NAB08 float profile radiometry. (a) Spectrogram of second derivative $-a_{pg}^{II}(\lambda)$. Green lines highlight Chl a peaks found at 411 nm and 432-439 nm. Orange lines indicate fucoxanthin peak found at 465-478 nm (see also Figure 10b). Color scale indicates $\left|a_{pg}^{II}(\lambda)\right|$. (b) Time series of $-a_{pg}^{II}(\lambda)$ Chl a peaks. Grey line is float chlorophyll from fluorescence.

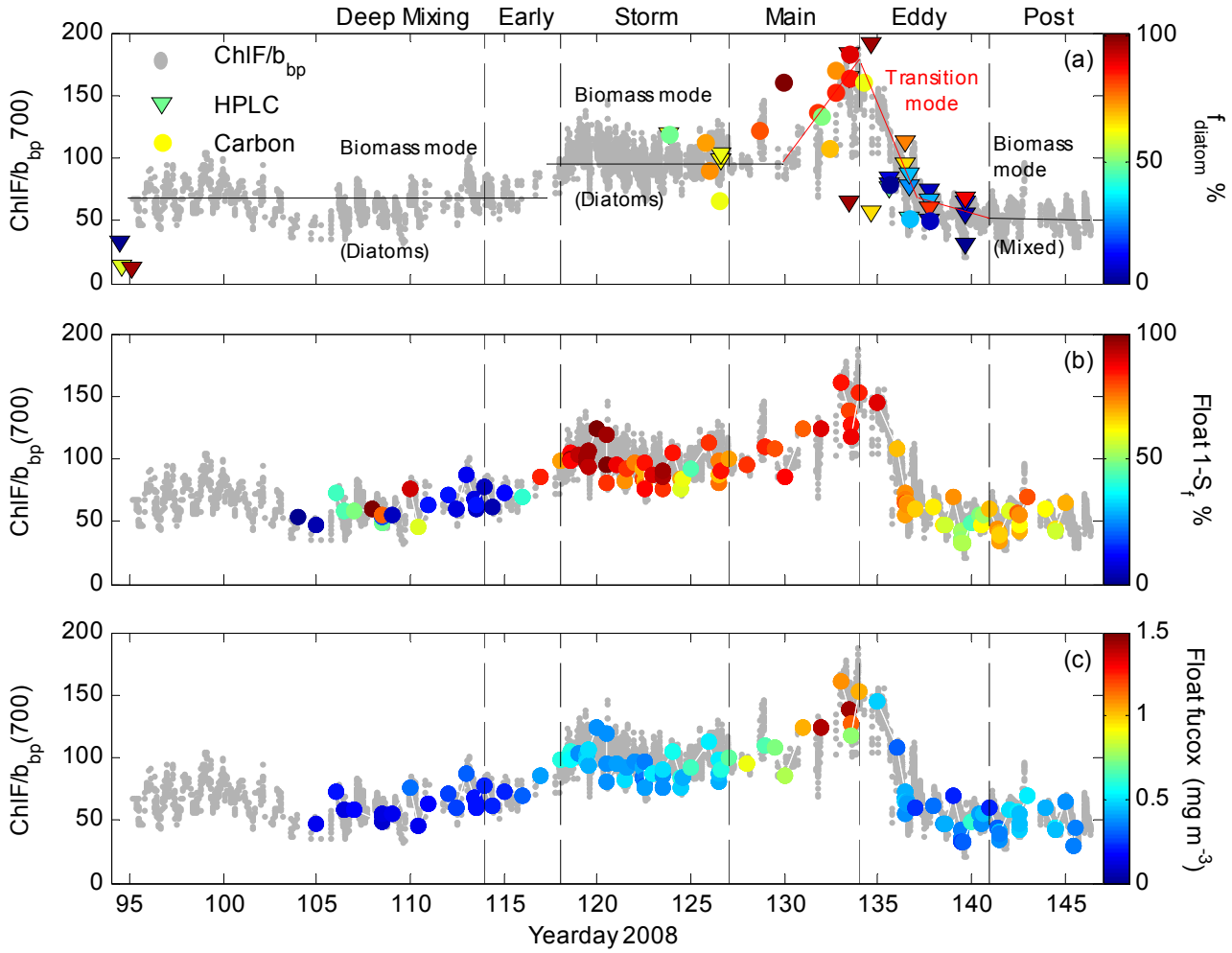

Figure 12. Community composition comparisons to bio-optical community index *ChlF*:b_{bp}(700) (background grey dots) in V m. (a) Percent diatom cell carbon from FlowCam (n=38) and percent diatom Chl from HPLC pigments (n=80), combined into a single product f_{diatom} to represent percent diatom domination (0% = minimum in our dataset, 100%-maximum in our dataset). (b) Fraction of large phytoplankton (1 – S_f), retrieved from float radiometry (c) Concentration of fucoxanthin retrieved from float radiometry, calibrated to HPLC fucoxanthin measurements.

Supporting Nonprint Material

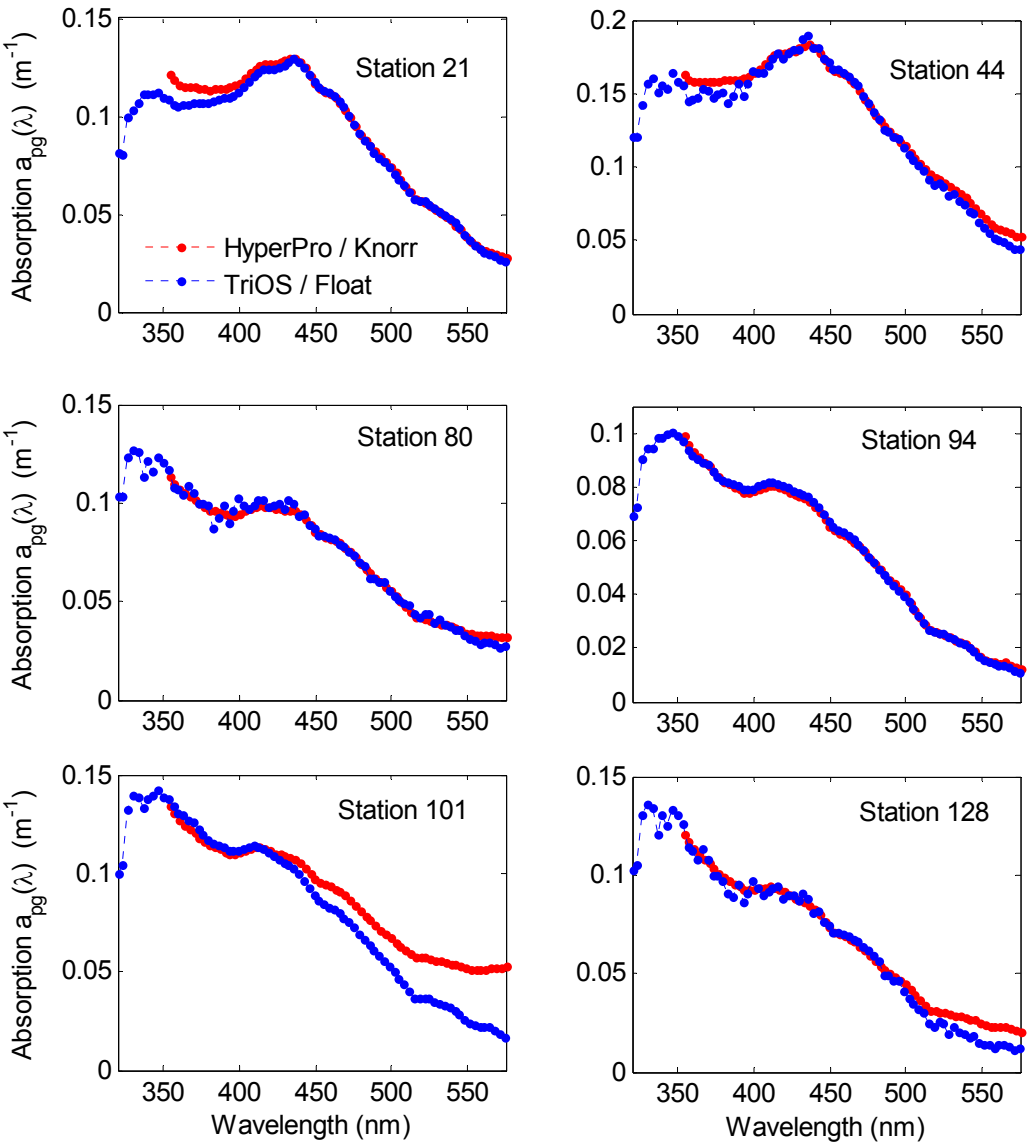

Figure S1. Matchup between absorption $a_{pg}(\lambda)$ retrieved from float (TriOS) and ship-deployed (HyperPro) radiometry for all calibration stations.

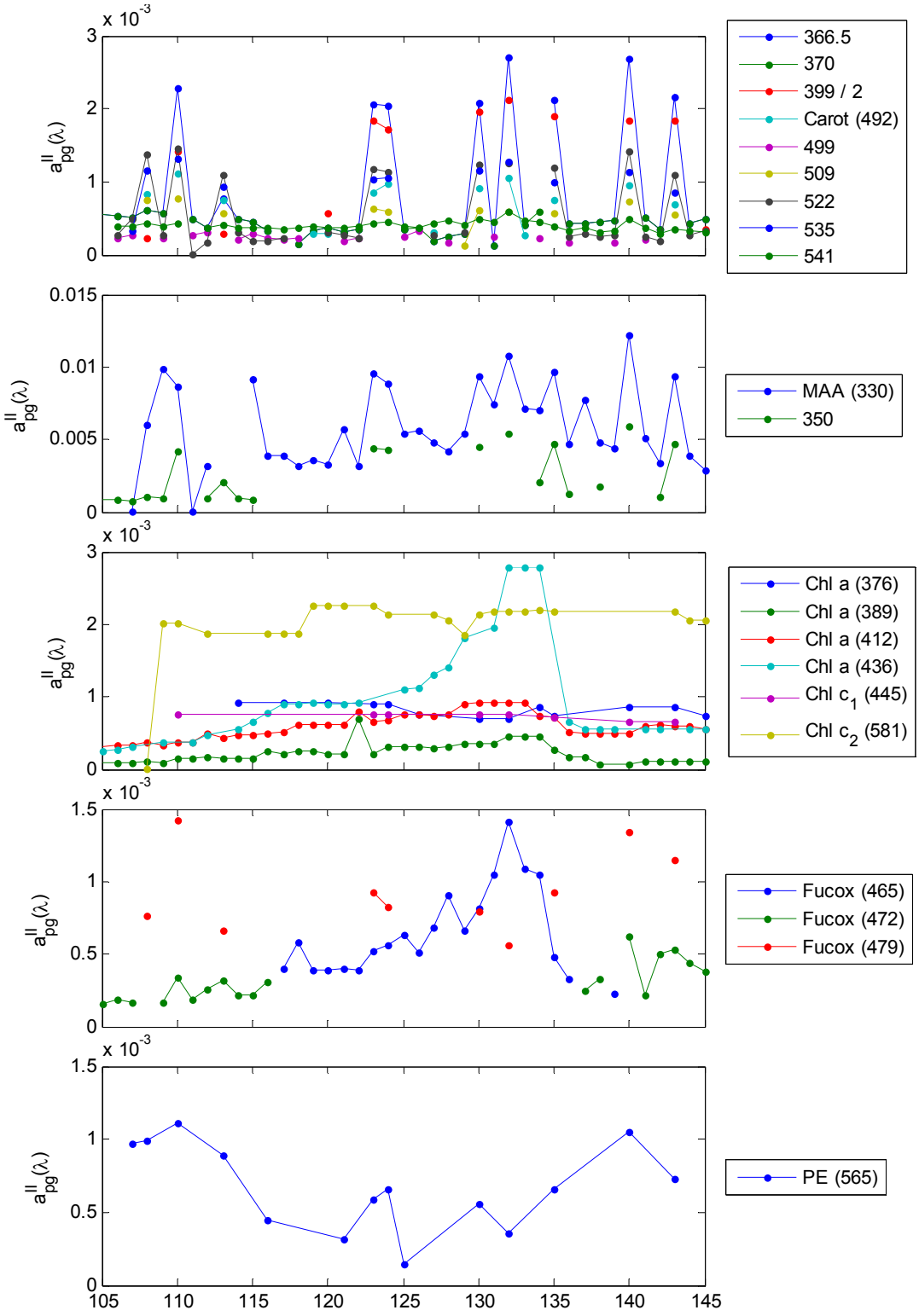

Figure S2. Time series plots of all second derivative peaks $-a_{pg}^{II}(\lambda)$ detected in float profile spectra. Putative assignments are based on *Aguirre-Gomez et al.* [2001a]; *Aguirre-Gomez et al.* [2001b]; *Roy et al.* [2011].